

University of Nottingham
UK | CHINA | MALAYSIA

ASSESSMENT OF THE ACCURACY AND THE CONTRIBUTION OF MULTI-GNSS IN STRUCTURAL MONITORING

Hussein Alwan Mahdi Msaewe

BSc Eng., MSc Eng.

Thesis submitted to the University of Nottingham for the degree of Doctor of Philosophy

October 2018

Abstract

Structural health monitoring requires precise techniques with high accuracy, due to the relatively small deformations that can be found in many structures. It has been proved that GPS is capable of detecting the characteristics of the response of flexible structures.

Although GPS can be applied for displacement monitoring, some existing constraints may limit the accuracy of the monitoring application. Some sources of these limitations are the multipath error, random noise, cycle slips and the geometry of the satellite constellation. Studies have been conducted to overcome these limitations using a combination of the GPS and other sensors: geodetic (e.g. Robotic Total Stations) or non-geodetic (e.g. accelerometer). Although these studies succeeded generally to reduce the effects of these limitations, they are still restricted on specific cases of monitoring, due to difficulties of using the accelerometer for monitoring static or quasi-static displacements and RTS due its limited range.

The introduction of the Global Navigation Satellite Systems (GNSSs), apart from GPS, such as GLONASS, BeiDou, and Galileo provides an alternative solution by combined GPS data with additional observations from other GNSS constellations to overcome GPS-only limitations. Therefore, the current study aims to develop a multi-GNSS method for structural health monitoring. The integration of different constellations contributes to improving the accuracy and availability of the solution, which allow the structural response and its characteristics effectively. The positioning performance in this study is investigated and achieved in three conducted stages:

Firstly, a series of GNSS zero baseline measurements are conducted simultaneously for 12 consecutive days in the UK and China sites to investigate the noise level of different GNSS solutions. The main aim is to investigate the correlation between the geometry of satellite constellation and the performance of the GPS-only and multi-GNSS solution. It is proved that for periods of poor GPS-only solution, due to the satellite constellation or problematic satellites, the multi-GNSS solution leads to more accurate and of higher availability solution.

Secondly, short baselines of GNSS measurements of static (1 Hz) and kinematic (10 Hz and 20 Hz) observations are collected to evaluate the precision and accuracy of different GNSS solutions. Following the same analysis approach and using the 3D best fitting of non-linear least squares adjustment models, it is proved that the multi-GNSS solution is significantly improved in comparison with the GPS-only solution for periods of weak geometry or problematic satellites. This can be attributed to the geometry improvement of the combined solution, which can reach 30% for GDOP values.

Finally, the GNSS measurements are investigated at the Severn Bridge and the Forth Road Bridge in the UK for real structural monitoring of long-span suspension bridges. The analysis was based on an assessment of workflow methodology applied in this study. The noise level of GNSS data was

assessed by zero baseline at the base station of the Severn Bridge. It was approved that the combined GPS/GLONASS solution reduced the noise level and led to more accurate results with less discontinuous time intervals. Regarding the spectral analysis, the GPS-only solution led to higer noise level of the spectrum and less easy to be detected peaks for some intervales relatively to the spectra of the multi-GNSS solution.

It was inferred from the results presented in the current study that the noise errors and discontinuity problems, as well as other limitations of the GPS-only solution, were significantly reduced and improved by combined GNSS solution. These findings are promising for many real structural monitoring applications.

Acknowledgement

There is a tremendous number of people to whom I owe my sincere gratitude, naming all of them is impossible. However, this thesis would not have been completed without the support and contribution efforts of many people who deserve to be acknowledged in the following.

Firstly, it is with great pleasure that I acknowledge my thanks to my supervisors, Dr Craig Hancock, Dr. Panos Psimoulis, Professor Gethin Wyn Roberts and Dr Lukasz Bonenberg for their encouragement, guidance, numerous support and valuable suggestions throughout my research.

I gratefully acknowledge my internal assessor Dr. Xiaolin Meng for his constructive suggestions with continuous support. Thanks to him for providing me with a required data gathered on the Forth Road Bridge with the GeoSHM system sponsored by the European Space Agency. My deepest gratitude goes also to my external examiner Mr Chris Brown for his valuable comments and feedback.

Many thanks to Mr Huib De Light and Dr. Xu Tang for collecting experimental data that carried out in Ningbo Campus at China, as a collaboration with Nottingham University in the UK. Mr Sean Ince in NGI is also acknowledged for his help.

I would like to express my great appreciation to Dr. Abbas Hameed for his continuous support and invaluable advice. Thanks also go to my colleagues Dr. Bashar Alsadik and Dr. Jareer Jaber for their help. I am grateful to Dr. Mohammed Al-Asadi for his help and all the friends who supported me.

I cannot describe my thanks to my parents for their sacrifices and encouragement along my life to get more success. A special thanks to my father who is passing away with a hope to see me getting a PhD. My most profound gratitude to my mother for her support, her tears and prayers.

My most profound gratitude to my family of my wife, my children “Zahraa, Ali and Mohammed-Ridha”, brothers and sisters for their patience, unlimited support, understanding and prayers. For my small family “my wife and my kids” who stood beside me, I owe them an apology for spending most of my time in research during my study.

I also acknowledge the financial support of my sponsor through the Iraqi Ministry of Higher Education and Scientific Research (MOHESR). I extend my thanks to the Iraqi Cultural Attaché in London for their support during the four years of my study. I would also like to introduce my gratitude to the College of Engineering at the Baghdad University for offering me the opportunity to study at the Nottingham University, in the UK.

Publication Works

- **Published Papers**

- MSAEWE, H. A., HANCOCK, C. M., PSIMOULIS, P. A., ROBERTS, G. W., BONENBERG, L. & DE LIGHT, H. 2017b. Investigating multi-GNSS performance in the UK and China based on a zero-baseline measurement approach. *Measurement,* 102**,** 186-199. http://dx.doi.org/10.1016/j.measurement.2017.02.004

- MSAEWE, H., HANCOCK, C., PSIMOULIS, P., ROBERTS, G. & BONENBERG, L. 2017a. Assessment of the Effects of Combining Multi-GNSS Constellations on the Solution Accuracy and Availability. *FIG Working Week 2017.* Helsinki, Finland, May 29–June 2, 2017.

- MSAEWE, H. A., HANCOCK, C. M., PSIMOULIS, P., ROBERTS, G. W. & BONENBERG, L. 2017. Monitoring dynamic deflections at towers of the Severn Suspension Bridge in the UK using GNSS technique. *International Symposium on GNSS, 10-13 December 2017.* Hong Kong, China.

- **Paper Under Submission**

- MSAEWE, H., PSIMOULIS, P., HANCOCK, C., ROBERTS, G. & BONENBERG. The contribution of multi-GNSS in bridge monitoring: The Severn Suspension Bridge in the UK as a case study.

Table of Contents

Abstract i

Acknowledgement iii

Publication Works v

Table of Contents vii

List of Figures xiii

List of Tables xxiii

List of Abbreviations xxv

Chapter 1 : Introduction 1

1. 1 Background 1

1. 2 Aims and Objectives 3

1. 3 Methodology 5

1. 4 Contribution to Knowledge 6

1. 5 Thesis Outlines 7

Chapter 2 : Literature Review 9

2. 1 Introduction 9

2. 2 GPS Measurements for Structural Monitoring 10

2. 3 Experimental Assessment of GPS Accuracy for Structural Monitoring 13

2. 4 GPS Measurements for Bridge Monitoring 19

2. 5 Limitations of GPS Measurements 23

2.5.1 Existing Solutions to GPS Limitations 25

2.5.1.1 Integration of GPS and Other Sensors 25

2.5.1.2 Digital Signal Processing by Filtering Techniques 28

2.5.2 The Suggested Technique of Combined GNSS to Overcome GPS Limitations 29

Chapter 3 : An Overview of the Global Navigation Satellite Systems (GNSSs) 31

3. 1 Constellations of Multi-GNSS 31

3.1.1 The Global Positioning System (GPS) 31

3.1.2 GLONASS 32

3.1.3 Galileo 34
3.1.4 BeiDou 34
3. 2 GNSS Error Sources 37
3.2.1 Satellite Orbit and Clock Errors 38
3.2.2 Atmospheric Errors 40
3.2.2.1 Ionospheric Bias 41
3.2.2.2 Tropospheric Delay 44
3.2.3 Receiver and Site Dependent Errors 46
3.2.3.1 Receiver Measurement Noise 46
3.2.3.2 Multipath 48
3.2.4 Other GNSS Errors (Satellite and Receiver Hardware) 50
3. 3 GNSS Observation Equation 52
3. 4 GNSS Relative Precise Positioning with Double-Differencing 54
3. 5 Processing of GNSS Data 56
3.5.1 Ambiguity Resolution 56
3.5.2 Cycle Slips 59
3.5.3 Dilution of Precision (DOP) 62
3.5.4 Code-Multipath Detection of MP1 and MP2 64
3. 6 The Combined Solution of GNSS Constellations 66
3. 7 Chapter Summary 67
Chapter 4 : Investigation of the Noise Level in Multi-GNSS Measurements 69
4. 1 Introduction 69
4. 2 GNSS Zero Baselines Experiments 70
4.2.1 Zero Baseline at the UK Site 71
4.2.2 Zero Baseline at the China Site 72
4. 3 Processing 74
4. 4 Preliminary Analysis 75
4.4.1 Preliminary Analysis at the UK Site 75
4.4.2 Preliminary Analysis at the China Site 80

4. 5 Data Quality Analysis 85

4. 6 Availability and Positioning Precision 89

4.6.1 Availability and Precision at the UK Site 89

4.6.2 Availability and Precision at the China Site 93

4. 7 Noise and Satellite Geometry Correlation 99

4. 8 Spectral Analysis 105

4. 9 Different Scenarios of Satellite Obstruction 107

4. 10 Chapter Summary 110

Chapter 5 : Performance Assessment of Static and Kinematic Short Baselines with Multi-GNSS Measurements 111

5. 1 Introduction 111

5. 2 Description of the Short Baselines Experiments 112

5.2.1 Short Baseline in a Static Mode 114

5.2.2 Short Baselines in a Kinematic Mode 114

5. 3 Processing the Data 115

5. 4 Results of a Static Baseline 116

5. 5 Results of the Kinematic Experiment 123

5.5.1 Accuracy and Precision of Kinematic GNSS Solutions 126

5.5.1.1 Fitting to Find the Optimum Surface 128

5.5.1.2 Mathematical Model and Assessment 130

5.5.2 Frequency Identification 134

5. 6 Summary and Conclusions 136

Chapter 6 : The Contribution of Multi-GNSS Applied in Real Cases of Bridge Deformation Monitoring 139

6. 1 Introduction 139

6. 2 Proposed Methodology 140

6. 3 Severn Bridge Monitoring 143

6.3.1 Severn Bridge Description 143

6.3.2 Monitoring Points and Measurements 143

6.3.3 Tracking Multi-GNSS Constellations 145
6. 4 Pre-Processing Analysis of the Severn Bridge Measurements 146
6.4.1 Cycle Slip Detection 147
6.4.2 Multipath Detection 149
6. 5 Processing the Severn Bridge Data 151
6. 6 Noise Assessment 153
6. 7 Analysis 155
6.7.1 Availability Analysis 155
6.7.2 Derived Displacement of the Severn Bridge Monitoring 157
6.7.2.1 Derived Displacement at Tower Stations 157
6.7.2.2 Derived Displacement at Mid-Span Stations 161
6.7.3 Frequency Response at the Severn Bridge 164
6. 8 BeiDou/Galileo Satellites in the Severn Bridge monitoring 170
6. 9 Forth Road Bridge Monitoring 173
6.9.1 Forth Road Bridge Description 173
6.9.2 Monitoring Stations on the Forth Road Bridge 173
6. 10 Pre-Processing Analysis at the Forth Road Bridge 174
6. 11 Fixed Solution Availability at the Forth Road Bridge 177
6. 12 Derived Displacement at the Forth Road Bridge 179
6. 13 Comparison of GLONASS-Only and GPS-Only Positioning at the Forth Road Bridge 187
6. 14 The Frequency Response of the Forth Road Bridge 190
6. 15 Chapter Summary 192
Chapter 7 : Conclusions and Recommendations 195
7. 1 Conclusions 195
7.1.1 The Noise Level in Multi-GNSS Measurements 195
7.1.2 Achievable Accuracy of Multi-GNSS Measurements 197
7.1.3 Bridge Deflection Monitoring with Multi-GNSS 197
7. 2 Recommendations for Future Work 198
References 201

Appendix-A: Least Squares (LS) Adjustments for Fitting a 3D Surface..... 221

A.1 Fitting a Sphere 221

A.2 Fitting a 3D Circle..... 222

A.3 Fitting a Cylinder 224

Appendix-B: Other Results of Severn Bridge monitoring 225

Appendix-C: Other Results of the Forth Road Bridge..... 231

List of Figures

Fig. 2.1 (a) Calgary Tower (Lovse et al., 1995) and (b) a high steel tower (Tamura et al., 2002). 10

Fig. 2.2 (a) Data points of 16-h measurements (1cm/30s), (b) Stuttgart TV-tower and (c) industrial chimney of Opole Power station (Breuer et al., 2002). 11

Fig. 2.3 (a) View of the Republic Plaza Building, (b) GPS results of estimated displacement and the corresponding power spectral density and (c) accelerometer results (Hristopulos et al., 2007). 12

Fig. 2.4 (a) Photo of the experimental model, (b) schematic of the test set up and (c) schematic of a full-scale of building (Celebi and Sanli, 2002). 13

Fig. 2.5 (a) Schematic of vibration test, comparison of detected displacement by RTK-GPS and actual one measured by wire displacement transducer DIS in (b) y=2 cm for different frequencies and in (c) f=2.0 Hz for different displacements (Tamura et al., 2002). 14

Fig. 2.6 (a) Schematic of experimental device of rotating rod (Im et al., 2013), (b) comparison between real and recorded orbit, plot of horizontal coordinates recorded by rotating rover versus time in (c) ideal cylinder plot, while in (d) represent some detected outliers (Nickitopoulou et al., 2006). 15

Fig. 2.7 (a) Schematic and a photo of an experimental apparatus, (b) time series of derived displacements with different frequencies and (c) frequency results by FFT (Psimoulis et al., 2008). 16

Fig. 2.8 (left) photo and details of stell pedestrian bridge and (right) time series of vertical displacement detected from GPS data (a-c), while (d) represent the recorded acceleration (Moschas and Stiros, 2011). 17

Fig. 2.9 The locations of the monitoring stations on the London Millennium Bridge (Roberts et al., 2004a)..... 20

Fig. 2.10 Schematic of the Forth Bridge and distributed points (Roberts et al., 2014)..... 21

Fig. 2.11 (left) Locations of attached monitoring stations at Forth Road Bridge and (right) the time series of 10-min mean response for vertical and lateral components (Psimoulis et al., 2017). 22

Fig. 2.12 (a) Monitoring points in Severn Bridge, (b) choke ring antenna attached to the cable, (c) time series of apparent deflection and (d) detected frequency (Roberts et al., 2015). 23

Fig. 2.13 (a) Schematic of the experiment of passing train nearby GPS antenna, (b) the derived Up time series at a specific event and (c) phase residual of observed satellites (Moschas and Stiros, 2014a)..... 24

Fig. 3.1 BeiDou system with various orbit types (Shi et al., 2013)..... 35

Fig. 3.2 Frequency bands for the four GNSS constellations (Subirana et al., 2013)..... 37

Fig. 3.3 Sketch of GNSS error sources 38

Fig. 3.4 Double difference between receivers "r" and "b" to two satellites "j" and "k". 55

Fig. 4.1 Zero baselines experiment setup (Msaewe et al., 2017b). 70

Fig. 4.2 Set up of zero baseline experiment in the UK site. 72

Fig. 4.3 (a) Leica AR-25 GNSS antenna and (b) GPS/GNSS RMS18 Splitter 8-way used in zero baseline experiment at China site. 73

Fig. 4.4 GPS time series of E-component of zero baseline using different options of AR (Leica Receiver 05/03/2015) at the UK site. 75

Fig. 4.5 GPS valid satellites tracking by Leica and Trimble receivers at the UK zero baseline along 1st h on 05/03/2015, each receiver represent the base one. 76

Fig. 4.6 GPS time series of the zero baseline records of two types of receivers for the UK site, (left) time series with Leica receivers and (right) for Trimble receivers on 05/03/2015. 76

Fig. 4.7 Autocorrelation of E, N and U components of zero baseline of GPS records of Fig. 4.6. 77

Fig. 4.8 GLONASS time series of the zero baseline records of two types of receivers for the UK site, (left) time series with Leica receivers and (right) for Trimble receivers on 05/03/2015..... 78

Fig. 4.9 Autocorrelation of E and N components of GLONASS records of Fig. 4.8. 78

Fig. 4.10 Comparison between two daily time series of GPS-only solution achieved with two pairs of Leica and Trimble collocated receivers for the UK site on 05/03/2015. 79

Fig. 4.11 (a) The visibility of BeiDou satellites that tracked by Leica receivers for 24h at the UK site on 05/03/2015 and (b) the sky-plot of tracked satellites. 80

Fig. 4.12 (a) The visibility of GPS satellites for the first hour at China site on 05/03/2015 and (b) the sky-plot of tracked satellites. 81

Fig. 4.13 GPS time series of the zero baseline records by four pairs of receivers at China site, on 05/03/2015..... 81

Fig. 4.14 Autocorrelation of E and N components of zero baseline of GPS records of Fig. 4.13. 82

Fig. 4.15 (a-c) the zero baseline components achieved with a GLONASS-only solution by Septentrio and Javad receivers, (d) comparison of a number of valid satellites and (e) the GDOP values produced for 24h at China site on 05/03/2015. 83

Fig. 4.16 (a) The visibility of BDS satellites for the first hour at China site on 05/03/2015 and (b) BDS sky-plot of tracked satellites. 84

Fig. 4.17 Time series of BDS-only solution for three components and 3D residual at China site on 05/03/2015. 84

Fig. 4.18 Autocorrelation of U-components of zero baseline of BDS records of Fig. 4.17. 85

Fig. 4.19 Time series of U-components of GPS-only at China site (a) apparent solution (b) refinement solution after excluding weak satellites. 86

Fig. 4.20 Analysis to detect the problematic and weak satellites along the interval 12:00-13:00 at China site (a) time series of U-components of GPS-only (b) valid observed satellites (c) corresponding elevations of satellites (d-e) residual analysis on L1 (f) SNR1 (g-h) residual analysis on L2 and (i) SNR2. 86

Fig. 4.21 Sequential improvement of time series of U-components of GPS-only at China site (a) apparent solution (b) Excluding G01 satellite (c) Excluding G01, G04 and G11 satellites. 87

Fig. 4.22 The time series of GPS-only at China site (top), valid satellites (middle) and elevation angles and SNR2 of valid satellites (bottom). 87

Fig. 4.23 Daily time series showing GPS-only (left), GLONASS-only (centre) and combined GPS + GLONASS (right) with Rec. UK1 receiver (UK site) on 05/03/2015. 89

Fig. 4.24 Comparison between GPS-only and combined GPS + GLONASS for 1-h duration at the UK site (Leica receivers) on 05/03/2015. 91

Fig. 4.25 Comparison between achieved precision (STD) with different GNSS solutions of Fig.5.23 on CDF analysis using the same daily data of Leica receiver on 05/03/2015. 91

Fig. 4.26 (a) Availability and (b) precision expressed as RMS at the UK site over the 12 days. 92

Fig. 4.27 Analysis the geometry of specific GLONASS intervals (left and middle) weak geometry with six satellites and (right) five satellites with good geometry in China site (05/03/2015). 94

Fig. 4.28 Sky plots of specific intervals of the weak geometry of GLONASS satellite constellation: (a) six satellites with the reference one of elevation under 50° and (b) five satellites with overlap between two of them in China site (05/03/2015). 94

Fig. 4.29 Daily time series with GPS-only (left) GLONASS-only (centre) and BeiDou-only (right) with Septentrio receivers in China site on 05/03/2015. 95

Fig. 4.30 Comparison between two daily time series of BDS-only solution achieved with two pairs of Septentrio and ComNav collocated receivers at China site on 05/03/2015. 96

Fig. 4.31 Comparison between achieved precision (STD) with different GNSS daily solutions by using CDF analysis on 05/03/2015 (a) Septentrio receivers (b) ComNav receivers. 96

Fig. 4.32 Time series of E component along the apparent daily solution of GPS-only solution for 12 consecutive days at China site with Septentrio receivers. 97

Fig. 4.33 An achieved precision expressed at the China site with different GNSS daily solutions over the 12 days (a) Septentrio receivers (b) ComNav receivers..... 98

Fig. 4.34 The daily GPS time series extracted from Leica receivers (UK site) of (a) the horizontal component, (b) the moving average of HDOP and the corresponding moving standard deviation (c) the scatter of their liner correlation, (d) the U-component, (e) the moving average of VDOP and the corresponding moving standard deviation, and (f) the scatter of their liner correlation. 101

Fig. 4.35 The daily GPS time series extracted from Septentrio receivers (China site) with details similar to Fig. 4.34 on 05/03/2015. 102

Fig. 4.36 Linear correlation between moving average of the HDOP values and the moving standard deviation of the corresponding horizontal component for GPS-only and combined GPS/GLONASS solutions for (a) the UK site and (b) China site. 102

Fig. 4.37 Two representative cases of linear correlation for GPS-only (left) well correlated and (right) no correlation at the UK site. 103

Fig. 4.38 Comparison between the linear correlation of moving HDOP values and moving standard deviation of the horizontal component of GPS-only, BDS-only and combined GPS/BDS for (a) Septentrio receivers and (b) ComNav receivers. 104

Fig. 4.39 Time series and corresponding spectra of the hourly interval (17:00-18:00) along E, N and U components for (G: GPS, R: GLONASS and combined G + R) solutions with Leica receivers in the UK site on 05/03/2015. 105

Fig. 4.40 Time series and corresponding spectra of the hourly interval (17:00-18:00) along E, N and U components for different GNSS solutions with Leica receivers in the UK site on 05/03/2015. 106

Fig. 4.41 Time series and corresponding spectra of the hourly interval with Leica receivers in the UK site on 05/03/2015. 107

Fig. 4.42 Time series and corresponding spectra at China site for (G: GPS, C: BeiDou and GC combined GPS+BeiDou with ComNav receivers on 05/03/2015. 107

Fig. 4.43 Different scenarios of blockage according to the different orientation of the blockage axis. 109

Fig. 4.44 GPS-only and combined GPS/GLONASS performance at scenarios (a) and (b). 109

Fig. 5.1 The specification of the experiment of different short baselines. 112

Fig. 5.2 The specification of the experiment of different short baselines. 113

Fig. 5.3 Time series of positioning residuals showing a comparison between GPS-only and combined GPS+GLONASS on 15/06/2016. 117

Fig. 5.4 The number of valid satellites for GPS-only, GLONASS-only and GPS+GLONASS (top) and the associated GDOP values (bottom) on 15/06/2016. 117

Fig. 5.5 The scatter graphs of distributed residuals with different GNSS positioning. 119

Fig. 5.6 Histogram of distributed residuals with GPS-only and combined GPS+GLONASS..... 119

Fig. 5.7 Time series of differences between the actual and derived length of baseline for solutions of GPS-only and combined GPS+GLONASS. 120

Fig. 5.8 Evaluation of hourly positioning of GPS-only and combined GPS+GLONASS. 120

Fig. 5.9 Time series of GPS-only and combined GPS+GLONASS with a single frequency (L1). 121

Fig. 5.10 Analysis of GPS-only with a single frequency (L1) at interval 21:00 – 23:00 GPS time. 122

Fig. 5.11 The periods of movement (top), GDOP values of individual GNSS constellations (middle) and the number of valid satellites (bottom) in the experiment of moving arm. 123

Fig. 5.12 The GPS-only time series represent the measured components of moving station Pi for the initial 20 sec of movement (left) and the whole period of the experiment (right). 124

Fig. 5.13 The traced path of the GPS-only solution at the 1st session of movement..... 125

Fig. 5.14 The time series of differences between the GPS-only solution and another GNSS positioning at the 1st session of movement. 126

Fig. 5.15 Flowchart is summarising the workflow to assess the precision and accuracy of diff. GNSS solutions. 127

Fig. 5.16 Fitting the recorded GPS data of the moving arm with surfaces of a sphere, 3D circle and cylinder with histograms of derived residuals between measured and best-fit radius in each case. 129

Fig. 5.17 The relationship between the measured and computed parameters. 131

Fig. 5.18 Results of residuals between the measured and estimated fitted positions for recording data of moving arm during the first representative session of 36 min, expressing as compared time series of GPS-only and other GNSS solutions, resulting in E, N and 3D components..... 133

Fig. 5.19 The number of valid satellites and the corresponding GDOP values (left) individual constellations (right) combined GPS with other constellations compared to GPS-only at first subset. 134

Fig. 5.20 Spectra of derived frequencies from the time series of the first dataset (10 Hz rate) with a GPS-only solution along E, N and U components. 135

Fig. 5.21 Spectra of derived frequencies from the time series of second dataset (20 Hz rate) 135

Fig. 6.1 Flowchart summarising the proposed monitoring procedure..... 141

Fig. 6.2 The Severn Suspension Bridge. 143

Fig. 6.3 Locations of monitoring points upon the Severn Bridge. 144

Fig. 6.4 The Leica AT504 choke ring antenna located on the main suspension cable..... 144

Fig. 6.5 All observed stations of monitoring Severn Bridge with operated receivers' types and their operating durations over the four days of monitoring..... 146

Fig. 6.6 Detecting cycle slips with visible satellites plot for base station (left) and monitoring tower station T3 (right) on 21 July 2015..... 147

Fig. 6.7 Time series of GPS-only for a dataset of station T2 in Fig. 6.6 (left) apparent solution (right) solution with clean data after excluding G15 on 21 July 2015. 148

Fig. 6.8 The results of detected multipath MP1 and MP2 and the corresponding SNR1 and SNR2 of GPS-only for a dataset of station T2 in Fig. 6.7 on 21 July 2015. 150

Fig. 6.9 Coordinate transformation in the local horizontal system (BCS). 152

Fig. 6.10 E, N and U noise levels and associated GDOP values obtained from the zero baseline measurements at the base station showing comparison between different GNSS solutions (a) GPS (blue) & GLONASS (red), (b) GPS & combined GPS/GLONASS (green) and (c) their achieved precision on 21/07/2015..... 154

Fig. 6.11 The availability of fixed solution for GPS-only and combined GPS/GLONASS from different bridge stations and (b) the corresponding GDOP values. 155

Fig. 6.12 Time series of derived vertical displacement at station T2 (left) the apparent solution and (right) the improved solution after excluding G30..... 156

Fig. 6.13 Comparison of derived displacement between GPS-only and combined GPS/GLO solutions during 24h (a-c) at tower points T1 and T2 and (d) the corresponding GDOP values on 21/07/2015. 157

Fig. 6.14 Analysis of derived positioning at a tower station T1 during hourly period-b at 01-02h for (a) apparent deflection (b) corresponding geometry and a number of satellites and (c) the sky plot..... 158

Fig. 6.15 (a) Different periods with discontinuity solution of GPS-only positioning (b) corresponding sky-plot and (c) improved time series of the combined solution compared to GPS-only at station T2..... 160

Fig. 6.16 Analysis of SNR and MP of GPS-only for three sessions in Fig. 6.16 at station T2 on 21/07/2015. 161

Fig. 6.17 Appearance of uncorrected cycle slips in the time series of station T2 on 21/07..... 161

Fig. 6.18 The daily time series of derived displacement obtained from GPS-only and combined GPS/GLO solutions at mid-span stations B and F on 22/07/2015..... 162

Fig. 6.19 The recorded daily data of wind loading and temperature changes at Severn Bridge on 22/07/2015 162

Fig. 6.20 Samples of derived displacements along the lateral and longitudinal direction of bridge deformations detected on mid-span station B on 22nd July 2015. 163

Fig. 6.21 The derived time series of displacements along x, y and directions of bridge deformations at mid-span stations B1 and F on 21st July 2015..... 164

Fig. 6.22 Comparison between time series of GPS-only and combined GPS/GLONASS of station B1 at period 11:00 – 12:00 on 21/07/2015..... 164

Fig. 6.23 FFT spectra of GPS data on tower station T1 at the period 17:00 – 18:00..... 166

Fig. 6.24 Analysis of movement at tower station T1 (a) displacement time series (b) logarithmic spectra of movement (c) linear spectra of the GPS-only solution and (d) linear spectra of combined GPS/GLO solution. 166

Fig. 6.25 Analysis of vertical movement at tower stations T1 and T2 at period 08:00 – 09:00 on 21st July. 167

Fig. 6.26 FFT spectra of GPS data on mid-span station B at the period 17:00 – 18:00..... 169

Fig. 6.27 The spectra of GPS-only and the combined GPS/GLONASS at mid-span station B..... 169

Fig. 6.28 The BeiDou and Galileo visible satellites observed at a base station (Rf) of monitoring the Severn Suspension Bridge. 170

Fig. 6.29 The contribution of BeiDou and Galileo observed satellites at handrail station D1 (at a period of 22:00 to 23:00. 172

Fig. 6.30 The Forth Road Bridge. 173

Fig. 6.31 Locations of monitoring stations upon the Forth Road Bridge. 174

Fig. 6.32 Detected cycle slips on visible satellites of GPS (top) and GLONASS (bottom) at the base station on 09th Jan. 175

Fig. 6.33 The analysis of observed GPS and GLONASS satellites at the base station P1 on 9th Jan. 176

Fig. 6.34 The fixing rate availability of apparent GPS-only solutions at monitoring stations (P2, P3 and P4) of Forth Road Bridge on 9th Jan. 178

Fig. 6.35 The fixing rate availability of improved GPS-only and the corresponding combined GPS/GLONASS solutions at monitoring stations (P2, P3 and P4) of Forth Road Bridge on 9th Jan. 179

Fig. 6.36 Comparison between derived results from GPS-only and the corresponding combined GPS/GLONASS solutions for (a) GDOP values with the number of satellites, (b) and (c) the derived relative displacement at monitoring stations (P2, P3 and P4) of Forth Road Bridge on 9th Jan 2016. 181

Fig. 6.37 Analysis of derived displacement in period c at (02:00 – 03:00) for GPS-only and the corresponding combined GPS/GLONASS solutions (a-c) at monitoring stations, (d) the computed geometry and (e) the sky-plot of distributed satellites at this interval on 9th Jan 2016. 183

Fig. 6.38 Analysis of derived displacement at p-period (15:00 – 16:00) for GPS-only and the corresponding combined GPS/GLONASS solutions (similar to Fig. 6.37). 184

Fig. 6.39 Analysis of derived displacement at x-period (23:00 – 24:00) for GPS-only and the corresponding combined GPS/GLONASS solutions (similar to Fig. 6.37). 186

Fig. 6.40 Comparison between derived results from GPS-only and the corresponding GLONASS-only solutions for (a) GDOP values with the number of satellites, (b) and (c) the derived relative displacement at monitoring stations (P2, P3 and P4) of Forth Road Bridge on 9th Jan 2016. 188

Fig. 6.41 Comparison between dynamic displacements derived from GPS-only and GLONASS-only at tower station P4 with the corresponding DOP values and a number of satellites in (a) period u at (21-22h) and (b) period v at (22-23h) on 09th Jan 2016..... 189

Fig. 6.42 Identified dominant frequencies at monitoring stations extracted from the time series of derived displacement in the interval (e) at (04:00 -05:00). 191

Fig. 6.43 (a) Comparison between time series of derived displacement of different GNSS solutions, (b-d) the corresponding defined frequencies by LNP technique. 192

Appendices

Fig. A.1 3D-circle with measured points 222

Fig. A. 1 (left) 2D fitting circle in E-N plane and (right) rotation between two norm 223

Fig. B.1 Comparison between displacement detected by GPS-only and combined GPS/GLONASS at T1. 225

Fig. B.2 Comparison between displacement detected by GPS-only and combined GPS/GLONASS at T2. 226

Fig. B.3 Displacement detected by GPS-only at T3. 227

Fig. B.4 Displacement detected by GPS-only at T4. 228

Fig. B.5 Analysis of movement at tower station T1 for GPS-only compared to a combined GPS/GLO solution 229

Fig. B.6 Another interval at tower station T1 for GPS-only compared to a combined GPS/GLO solution 229

Fig. C.1 Cycle slip detection at monitoring stations of Forth Road Bridge with GPS-only on 09/01/2016 231

Fig. C.2 Cycle slip detection at monitoring stations of Forth Road Bridge with GLONASS-only on 09/01/2016 232

Fig. C.3 Comparison of distributed GPS and GLONASS satellites at the Forth Road Bridge on 09/01/2016 233

Fig. C.4 Daily time series of displacement compared between GPS-only and combined GPS/GLONASS detected at Forth Road Bridge on 10/01/2016 234

Fig. C.5 Daily time series of displacement compared between GPS-only and GLONASS-only detected at Forth Road Bridge on 10/01/2016 235

List of Tables

Table 3.1 Comparison of the main characteristics of multi-GNSS implies GPS, GLONASS, Galileo and BeiDou. 36

Table 3.2 Different central Frequencies of each GNSS constellation as encoding in RINEX 3.02 (Gurtner and Estey, 2013, IGS, 2015) 37

Table 3.3 The main GNSS biases caused by satellite or receiver hardware delay, modified from (Hakansson et al., 2017)..... 52

Table 4.1 The converters used with different GNSS receivers and specifications of tracked corresponding constellations in the experiment at the China site. 73

Table 4.2 Comparison of statistical results of time series of zero baseline with GNSS solution for 24h using collocated receivers at the UK site on 05/03/2015. 79

Table 4.3 Comparison of statistical results of time series of zero baseline with GNSS solution for 24h using collocated receivers at the UK site on 05/03/2015. 81

Table 4.4 Statistical results of BDS positioning derived from zero baseline measurements for 1h (00:00 – 01:00) using collocated receivers at China site on 05/03/2015. 84

Table 4.5 Results of the daily GNSS-solutions for the UK site (Leica 24-h) on 05/03/2015. 90

Table 4.6 Results of the daily GNSS-solutions for the China site (Septentrio 24-h) on 05/03. 93

Table 4.7 Results of the daily GNSS-solutions at the China site according to achieved precision with two different sets of receivers on 05/03. 95

Table 4.8 Compared results of different scenarios when adopting GPS-only and Combined GPS+GLONASS. 109

Table 5.1 The details of the collected data by different GNSS receivers located on the two pillar stations and the platform of moving the arm on 15/06/2016..... 113

Table 5.2 The duration of the collected data at the rover station of a moving arm on 15/06/2016. 115

Table 5.3 RTKLib setting for processing of moving arm experiment. 116

Table 5.4 The statistical results of different GNSS solutions for 24-h on 15/06/2016..... 118

Table 5.5 The statistical results of different GNSS solutions for 24-h on 15/06/2016..... 121

Table 5.6 The summarised results of derived components of the baseline on the first data set according to different GNSS solutions on the experiment of moving rotating arm.(G: GPS, R: GLONASS and C: BeiDou)..... 124

Table 5.7 The achieved STD of differences between GPS-only and other GNSS solutions..... 125

Table 5.8 The adjusted elements to define the circular trajectory of the moving arm with three representative surfaces among different GNSS solutions of the first dataset..... 130

Table 5.9 The achieved precision and accuracy of different GNSS solutions for 1st session. 133

Table 6.1 Specifications of monitoring points upon the bridge. 145

Table 6.2 The initial coordinates of monitoring stations in two systems..... 152

Table 6.3 The availability of fixing rate solution for the first hourly duration for tower points T1, T2 and on 21/07 and cable points at mid-span B, F on 22/07..... 156

Table 6.4 Comparison between rates of fixed solution achieved with GPS-only and combined GPS/GLONASS in different periods at tower stations T1 and T2 on 21/07/2015..... 159

Table 6.5 The derived dominant natural frequencies by FFT and LNP at tower station T1..... 165

Table 6.6 The derived natural frequencies by FFT and LNP at cable mid-span station B. 168

Table 6.7 The derived natural frequencies by LNP at period 03:00 – 04:00 on 22nd July 2015 169

Table 6.8 The visible BDS and Galileo satellites with different GNSS solutions at handrail station D1 on 20th July..... 171

Table 6.9 The geometry of different GNSS solution represented by mean DOP values at period 22:00-23:00 on 20th July..... 172

Table 6.10 The initial coordinates of monitoring stations of Forth Bridge. 174

Table 6.11 Availability of fixing the rate at tower station P4 for every hour of a full day on 9th Jan. 178

Table 6.12 Availability of fixing rate ambiguity at a monitoring station in period c at (02:00 – 03:00). 183

Table 6.13 Availability of fixing rate ambiguity at the monitoring station at p-period (15:00 – 16:00). 184

Table 6.14 Availability of fixing rate ambiguity at the monitoring station at x-period (23:00 – 24:00). 186

Table 6.15 Extracted frequencies provided by FFT and LNP techniques. 190

List of Abbreviations

AR	Ambiguity Resolution
BDS	Chinese Navigation Satellite System (BeiDou)
CDMA	Code Division Multiple Access
DLL	Delay Lock Loop
DD	Double Difference
ECEF	Earth Centred Earth-Fixed
E, N, U	Easting, Northing and Up coordinate components
ESA	European Space Agency
FFT	Fast Fourier Transform
FEM	Finite Elements Models
FCB	Fractional Cycle Bias
FDMA	Frequency Division Multiple Access
FOC	Full Operational Capability
GIOVE	Galileo In-Orbit Validation Element
GDOP	Geometric Dilution of Precision
GEO	Geostationary Earth Orbit
GNSS	Global Navigation Satellite System
GPS	Global Positioning System
HW	Hard-Ware
HDOP	Horizontal Dilution of Precision
IGSO	Inclined Geosynchronous Satellite Orbit
ILS	Integer Least Squares
ISB	Inter-System Bias
IFB	Inter-Frequency Bias (GLONASS)
IGS	International GNSS Service
ITRF	International Terrestrial Reference Frame
ISTB	Inter-Satellite-Type Biases (BDS)
LSA	Least Squares Adjustment
LAMBDA	Least-Squares Ambiguity Decorrelation Adjustment
LNP	Lomb Normalized Periodogram

MEO	Medium Earth Orbits
OTF	On the Fly
PCO	Phase Centre Offset
PCV	Phase Centre Variation
PLL	Phase-Locked Loop
PDOP	Position Dilution Of Precision
PPK	Post-Processing Kinematic
PPP	Precise Point Positioning
RTK	Real-Time Kinematic
RTS	Robotic Total Station
RMS	Root Mean Square
SNR	Signal to Noise Ratio
SD	Single Difference
SHM	Structural Health Monitoring
RINEX	The Receiver Independent Exchange Format
TEC	Total Electron Content
TZD	Total Zenith Delay
UTC	Universal Time Coordinate
WGS84	Word Geodetic System 1984

Chapter 1 : Introduction

1. 1 Background

Engineering structures are usually designed with certain characteristics, taking into account the predicted loads. In reality, these characteristics are subjected to changes due to effects of various loadings. These loadings produce deformations in the structure, which required monitoring to ensure its performance and stability for safety purposes (Roberts et al., 2004b). The structural deformation monitoring represents an essential procedure that is based on collecting data at specific parts of the structure under loadings. The tracking of such deformation represents a vital aspect that is applied to large structures such as dams, bridges, high-rise buildings and so on.

Structural health monitoring (SHM) requires precise techniques with high accuracy. One of the conventional techniques is to analyse measurements that are taken from accelerometer readings to identify structural vibrations. However, a double integration process is required to determine relative displacements. This process might introduce bias in collected data due to the accumulated error. In addition, the accelerometer has difficulties in measuring static and quasi-static displacements (Li, 2004, Moschas and Stiros, 2011). Moreover, it is difficult to detect displacements in slow vibrated structures with a low frequency (Meng et al., 2007). Other techniques that could be used for structural monitoring are terrestrial positioning systems, laser displacement sensors (Pera and Ferrando, 2017), and photo/video imaging methods (Yu et al., 2018). Although these techniques have received attention, they are still having limitations such as short monitoring distance and weather dependency (Yu et al., 2014). Thus, the alternative technique adopted for structural monitoring is the Global Positioning System (GPS) (Im et al., 2013).

In contrast to other techniques, a GPS can measure the 3D coordinate's position directly with a very precise corresponding time tag, even feasible for real-time applications. This ability encouraged to monitor structure in a real-time domain. Different effects such as earthquakes, strong wind, moving loads, temperature variation, and other factors can excite a structure (Psimoulis and Stiros, 2008). Therefore, the excitation response could be static (permanent), semi-static or dynamic. It has been proved that the GPS is capable of measuring dynamic characteristics and static displacement in flexible structures on real-time (Im et al., 2013).

In the case of bridge monitoring, there are two distinct types of deformations; firstly the long-term displacement, which can be related to the following excitation factors; foundation settlement, bridge deck creep or stress relaxation. Secondly, the short-term movement or sometimes called a deflection which is caused by dynamic factors such as wind loading, temperature variation and traffic loading (Meng, 2002). Deflection could be categorised as (i) longitudinal, when directed along or parallel to the main bridge span, (ii) lateral deflection (orthogonal to the main axes) and, (iii) vertical deflection,

which refers to deflection in a vertical or altitudinal direction (Watson et al., 2007). Moreover, for the torsional movement of the bridge span, it could be computed depending on the vertical displacements and the distance between symmetrical stations (Guo et al., 2005).

In structural monitoring, one of the basic requirements is the selection of the sampling rate. More specifically, a particular sampling frequency should be determined, covering the desired frequency range. The frequency is generally defined by the Nyquist frequency, which states that information with a bandwidth of 'b Hz' must be sampled at a rate of '2b Hz' (Lovse et al., 1995). Therefore, the sampling rate must satisfy the limitation due to the Nyquist frequency and cover the main model/natural frequencies of the monitoring structure.

The GPS measurements are conducted in a kinematic mode to tracking the dynamic response of bridge movement. Commonly, the relative GPS positioning is applied to collect data through receivers attached to the bridge and corresponding to one or more reference stations in stable fixed location. The GPS recorded data can be either processed in real time or post-processed. In either real time or post-processed a special processing software is required (Roberts et al., 2006). Resolution of a millimetre or better can be achieved using post-processed (ibid, 2006), while the nominal accuracy of RTK technique is ±1 cm horizontally and ±2 cm vertically (Ogaja et al., 2007), with some algorithms in processing this can be improved.

Many features and restraints affect the achievable accuracy of GPS results (Meng et al., 2003). For example, the quality of GPS data is related to the number of available satellites and the geometric distribution of these satellites. Moreover, there are many causes of errors, e.g. clock and orbit errors of satellites, ionosphere and troposphere delays, multipath, etc. (Tamura et al., 2002) that should be taken into account. Therefore, the possibility of using GPS to achieve displacements precisely and meet the basic requirements of monitoring is affected by the accuracy of this technique.

Although the use of dual frequency contributes to mitigating the effect of ionospheric delay, it is a feasible tool for deflection monitoring. By using dual frequency, correct integer ambiguity resolution can be achieved (Cosser et al., 2003). On the other hand, however, the length of the baseline in structural monitoring is defined as short-baseline (i.e. < 5 km); the error sources may be the same at the two ends of baseline. Some errors (ionospheric & tropospheric delays and orbital errors) can be significantly mitigated with double differencing. For tropospheric effect, however the reference station and the rover have different heights, the effect will be insignificant due to short baseline. Some other errors, such as multipath error and random noise, cannot be removed in the differencing method because they are not the same in both ends of the baseline (Yu et al., 2014).

In bridge monitoring, even though GPS measurements can achieve displacements accurately, a number of error sources, such as multipath error, random noise, cycle slips, etc. may limit these

potentials. In addition, the limited number of visible satellites with weak geometry could reduce the precision.

To overcome these limitations and achieve high accuracy of the displacement determination, various studies have applied integration of GPS and other sensors such as an accelerometer (Meng et al., 2003, Roberts et al., 2004b, Li et al., 2006, Meng et al., 2007, Yu et al., 2014). On the other hand, other studies adopted a combination between two geodetic sensors which are GPS and Robotic Total Station (RTS) (Psimoulis and Stiros, 2008, Psimoulis and Stiros, 2012), While Moschas and Stiros (2014c) summarized a series of experiments to compare between results of GPS, RTS and accelerometer.

Although the above studies succeeded to connect between results and balance between limitations of each technique, they are restricted on specific cases of dynamic monitoring for short duration. The accelerometer has difficulties in continuous monitoring and measuring static and quasi-static displacements (Im et al., 2013, Yu et al., 2014), while the RTS in monitoring at high frequencies leads to losing some cycles of recording and delimited for short distances (few hundred meters) between RTS and reflector with clear sight (Psimoulis and Stiros, 2008).

The introduction of the satellite systems, apart from GPS, such as GLONASS, BeiDou and Galileo, provides with an alternative solution to overcome limitations, by using additional observations from the rest of the GNSS systems (GLONASS, Galileo, BeiDou and other regional systems). The integration between different constellations is contributed to improving positioning accuracy, reliability and availability (Chen et al., 2015b). Therefore, this research will adopt employing multi-GNSS for structural monitoring to estimate the accuracy improvement of GNSS kinematic coordinates and overcome the limitations when using individual constellation such as multipath error, random noise, and cycle slips.

1. 2 Aims and Objectives

The principal aim of the current study is to identify an effective positioning technique for structural monitoring that can detect the deformations in engineering structures precisely. Also, it has the potential to overcome the limitations of GPS-only positioning that mentioned in the previous section (Section 1.1) by examining the potential contribution of the recently developed or updated GNSS systems (i.e. GLONASS, BeiDou, Galileo). The main objectives, which help to achieve such aims, are outlined below;

1. To assess the impact of the satellite constellations on the accuracy of the GNSS positioning, and how the GNSS accuracy can be improved by using additional systems (i.e. GLONASS, BeiDou) for structural monitoring applications.

2. To study the impact of other GNSS satellite constellations on the performance of GPS for structural monitoring, focusing on the modelling of the noise in the GNSS measurements and how this noise can be eliminated when additional satellite systems are used.
3. To conduct the GNSS measurement focusing on the analysis and the assessment of the multi-GNSS constellations in China and the UK, in terms of achieved accuracy and reliability. Two locations were selected in order to assess the impact of the BeiDou system as well as the effect of multi-GNSS measurements for high-latitude locations, where GPS measurements are of lower quality (see Chapter 4).
4. To investigate the impact of Galileo in the satellite constellation (depending on the availability of the satellites). The investigation is focused on the bridge monitoring application, in which real GNSS monitoring data is used.
5. To test and examine the proposed methodology in real cases for monitoring the deformations of long-span bridges by comparing the GPS-only with the combined GNSS solution, which will lead to the assessment of the proposed technique.
6. To identify constellation problems/errors and to limit them by developing a method or a strategy for finding the optimum satellite constellation of GNSS, before applying it to a real structural monitoring with multi-GNSS.
7. To implement the knowledge gained from the different experiments to build a general strategy that could be applied in real structural monitoring applications.

The key questions that need to be addressed in order to achieve the aim and objectives of the current research are as follows:

1. How the use of multi-GNSS affects the GNSS data noise?
2. What is the impact of using a multi-GNSS on the availability of the solution of fixed ambiguity resolution?
3. How is the data noise correlated with the geometry of satellite constellations?
4. How is the position availability affected by different GNSS constellations?
5. How can the multi-GNSS solution improve the performance of GPS/GNSS monitoring under conditions of strong multipath or signal interference?
6. How the multi-GNSS solution is improved relatively to the GPS performance in high latitude areas?
7. How the additional multi-GNSS constellations contribute in improving the performance and the accuracy of the GNSS application for bridge monitoring?

1. 3 Methodology

In this section, a brief summary of the methodology is described (note that, the detailed methodology is discussed in relevant chapters). In order to achieve the final objectives and assess the accuracy with multi-GNSS, which is the focus of this study; their main approaches were followed as discussed below.

1. Zero-baseline experiments: in this approach, the research was focused on the processing of the simultaneous data of zero-baseline in the UK and in China to investigate the noise characteristic of these data with different GNSS constellations. The advantage of using zero-baseline measurements is that most of the GNSS/GPS error sources are cancelled, with the satellite constellation and receiver noise mainly remaining. In addition, the comparison between the results of different types of receivers for different constellations enables to identify the receiver's noise. A preliminary study of multi constellations by sky-plots provides an idea of the satellite constellation during the measurements time interval.
2. Short-baseline experiments, where the multi-GNSS performance was assessed for the positioning precision and accuracy with different GNSS solutions, under similar conditions to those of structural monitoring applications. In these experiments, the performance of GNSS measurements has been examined for static and kinematic applications, in which the monitored motion corresponds to that of flexible bridges response is measured and analysed. The main aim is to assess and evaluate the estimated movement by using multi-GNSS measurements. It will be useful to highlight the limitations to be considered in real cases with actual scale. On the other hand, the effect of combining GPS with other systems on the efficiency and reliability was also investigated.
3. Real applications of bridge monitoring, in which the GNSS measurements were assessed in terms of the availability and accuracy and their impact on the estimation of the amplitude and frequency of the response of the bridge against those estimated by using only GPS measurements were also analysed. This research is also focused on the understanding of the GPS/GNSS noise and how the GNSS measurements can be analysed to limit such noise. Furthermore, the applications are based on bridges located in high latitude areas, where the GPS performance has been proved to be of lower quality (Meng et al., 2003).

Thus, the zero baseline and short baseline are ways to assess the data and the applications on real bridges are to assess the validity of the developed workflow. In each approach, the GPS-only solution is compared with combined GNSS positioning to identify the positioning improvement with enhanced performance.

1. 4 Contribution to Knowledge

Although considerable studies have been conducted to study the positioning improvement by multi-GNSS, the majority of these studies have been focused on the Precise Point Positioning (PPP) and the improvement of the PPP multi-GNSS solution against the currently commonly used PPP GPS solution. On the other hand, most of the applied studies that are based on the use of the new constellations of BeiDou are directed to local cases. In addition, although some recommendations related to applying multi-GNSS were addressed, they are still theoretical issues.

Moreover, few attempts focused on monitoring long-span bridges in particular and/or on combining all constellation systems. This research will, therefore, be aiming to investigate and evaluate the contribution of multi-GNSS in determining accurately the GNSS relative kinematic coordinates with respect the GPS-only solution and how much be improved the accuracy and the availability of the positioning solution. This study focuses on the application of GNSS in bridge monitoring and the corresponding constraints and limitations, which are faced at this GPS/GNSS application (e.g. obstructions, multipath). Thus, the investigation of the potential contribution of multi-GNSS aims to resolve the reduced accuracy and availability of the GPS-only solution due to physical constraints of the bridge engineering application. The main contributions of this research are:

- To overcome the GPS-only limitations by combining GPS data with observations of other GNSS constellations. The combined solution improved the satellite geometry with more available satellites that contribute to obtaining the success rate of the fixed solution with more reliable results.
- The detailed analysis of the advantage of GNSS over GPS in the UK with respect the north-south component showing a significant improvement of a combined GNSS solution is achieved in Northing component along with reducing the noise level in all components.
- A new approach of correlating the noise level and satellite geometry is presented (Chapter 4). When correlating the mean DOP values and the precision of the noise that calculated by standard deviation, a higher correlation is achieved at intervals of mean DOP values higher than the daily mean corresponding values.
- The mathematical models of best fitting with related issues are derived to identify the actual parameters of caused movement.
- A new proposed methodology is presented that can be applied in structural monitoring. This strategy helps users to decide using either individual or combined GNSS solution in structure monitoring, as well as it is a useful tool for those haven’t enough GNSS knowledge to implement this strategy in monitoring.

The possibility of using the GLONASS-only solution as another alternative in structural monitoring is also investigated to highlight the expected improvement of results in relatively high latitudes area.

1. 5 Thesis Outlines

The thesis consists of seven chapters that are composed of two main groups, which are the theoretical part that is covered by the first three chapters, followed by another three chapters of practical applied aspects with analysis, the conclusions and recommendations are then given in the last chapter.

- Chapter-1: This chapter gives a brief introduction and background of structural monitoring with related issues. In addition, the research aims and objectives, a general/brief methodology and contribution to the knowledge of the current research were all addressed and discussed in this chapter.
- Chapter-2: This chapter presents the literature review focusing on utilising the GPS measurements for structural health monitoring. The previous experimental assessment studies that are evaluating GPS performance in structural monitoring are discussed in details in this chapter. The previous studies conducted on bridge monitoring are also discussed to highlight the GPS-only limitations and the adopted techniques used to overcome these limitations. Finally, the specifications of a combined GNSS as an alternative proposed technique to overcome GPS limitations are defined and addressed.
- Chapter-3: This chapter is devoted to the technical overview of GNSS constellations, which gives a concise summary of the four main GNSS constellations of GPS, GLONASS, Galileo and BeiDou. It also contains the discussion of GNSS error sources and evaluates in details some models to eliminate these errors. The observation equations and mathematical models are described. In addition, the main elements of processing GNSS data are also discussed in details, which concerning ambiguity resolution, cycle slips, DOP factors and multipath.
- Chapter-4: the investigation of the noise level in multi GNSS measurements is given in this chapter, which based on real simultaneous measurements of zero baselines with different types of pairs of receivers at two locations in the UK and China sites. The description of these experiments is provided, followed by a preliminary assessment to determine which pair of available receivers has the most reliable performance to identify the characteristics of GNSS positioning. At each location, the noise level of GPS observation is evaluated, and the contribution of other constellations to mitigate the noise level is assessed in a combined solution. Therefore, the GLONASS observations added to GPS in the UK site, while BeiDou data combined with GPS for the China site to have less noisy results. This chapter is focusing on evaluating the data quality of different GNSS constellations, and how that affected the availability of fixed solution as well as the achieved precision of these different solutions.

A new approach to correlate the noise level with the satellite geometry is presented. In addition, the spectral analysis of different GNSS solutions is discussed, then different scenarios of satellite obstruction are analysed.

- Chapter-5: The results of static and kinematic short baselines with multi-GNSS are presented in this Chapter. This includes experiments to assess the positioning precision and accuracy of different GNSS solutions. A static test is conducted on the known stations, while the rover station of the kinematic experiment is performed using a GNSS antenna attached on a rotating moving arm, to represent a simulated monitoring system. Thus, it is possible to detect the simulated movement with real data as well as to achieve the derived accuracy, which required the actual parameters of movement (real values). In this chapter, the mathematical models of best fitting with related issues are derived to identify the actually required parameters.
- Chapter-6: this chapter is dedicated to actual cases of bridge health monitoring that applied to the Severn Bridge and the Forth Road Bridge in the UK. In this chapter, the new proposed methodology is tested by adopting combined GNSS solution with a comparison to the GPS-only solution. The pre-processing analysis in the suggested methodology is based on detection cycle slips and multipath to be taken into consideration to obtain clean data. In addition, a noise assessment is presented to evaluate the noise level along with the impact of satellite geometry. In addition to utilising GLONASS observations in combined solution with GPS, a possibility of using BeiDou and/or Galileo constellation is investigated in monitoring Severn Bridge, while the potential to use GLONASS only is considered in Forth Bridge monitoring. Different durations are analysed to show the impact of implementing the proposed methodology with combined GNSS solution in detected displacements as well as the derived frequency of bridge response.
- Chapter-7: Finally, this Chapter presents the conclusions of the research and introduces some recommendations for further work on the GNSS measurements for structural monitoring.

Chapter 2: Literature Review

2. 1 Introduction

Large engineering structures are subjected to various loads, which require accurate monitoring process to secure their structural performance. Structural health monitoring (SHM) of engineering structures under loading conditions can be used to evaluate the behaviour of structure for operational safety. The evaluation is based on measurements from sensors attached to or embedded in the structure. As a consequence, the analysis of the collected reliable data will enable to assess the structures' response regarding safety, strength, integrity and the performance of the structure which allows identifying any damage or movement in the structure (Dong et al., 2010).

Traditionally, the monitoring system was based on records of a single sensor such as an accelerometer that used since 1930's (ÖNEN et al., 2014, Vagnoli et al., 2017), strain gauges, displacement transducers and anemometer, in addition to different conventional sensors that may be used for structural monitoring (Bisby et al., 2006). Moreover, the traditional monitoring techniques that based on surveying equipment (theodolite, level, total station, etc.) have also been used (Yi et al., 2013b). The significant disadvantage of conventional surveying techniques is the long durations between measurements that required a clear line of sight which can be collected without connection to real time.

This chapter discusses the literature review of GPS techniques for structural monitoring. In Section 2.2, the considerable preliminary studies of using GPS as a geodetic technique for monitoring large engineering structures are introduced. In this section, the pioneer studies to detect dynamic deformations at towers, high-rise buildings, bridges and dams are presented. To validate the GPS measurements by investigating their performance in the preliminary assessment are described in Section 2.3. The outcomes of these studies can be implemented to monitor the static and dynamic response of structures. The investigation of long suspension bridges response represents the primary focus of this study. Therefore the previous reviews to monitor bridges are conducted in Section 2.4. The monitoring of these structures by GPS-only positioning has a number of limitations; thereby Section 2.5 is devoted to describing the main limitations of GPS along with studies that adopted the techniques to overcome these limitations. There are two main techniques includes (i) integration of GPS with another sensor and (ii) digital signal processing by filtering techniques. To highlight the possible improvements that can be achieved with the combined GNSS solution, Section 2.5.3 demonstrates the improvements in these solutions. Therefore, the proposed alternative technique is to apply the multi-GNSS constellations, which will adopt in this study.

2. 2 GPS Measurements for Structural Monitoring

Although there are various monitoring techniques used in structural monitoring, Global Positioning System (GPS) has been widely used as a geodetic technique in monitoring different engineering structures. Preliminary studies have proven the technical feasibility of using GPS to monitor the continuous structural deformation of large structures. DeLoach (1989) reported that GPS has the potential to detect movements with high accuracy in three dimensions when short baseline have been used. The pioneer studies on utilising GPS in structural monitoring started in the mid-1990's (Yu et al., 2014). Lovse et al. (1995) tested a specific application of using GPS receivers to detect the dynamic deformation of the Calgary tower (160 m. high) in Canada as illustrated in Fig. 2.1a. They used two single frequency receivers relative to fixed base station collected the field observations with 1 Hz sampling rate. A differential GPS carrier-phase was used to obtain mm-level accuracy. The post-processing of the GPS data was based on the least squares method and On the Fly (OTF) technique to resolve the carrier-phase ambiguity. They found that the tower was vibrated by wind loading showing a displacement of ± 16 mm with a frequency of 0.3 Hz.

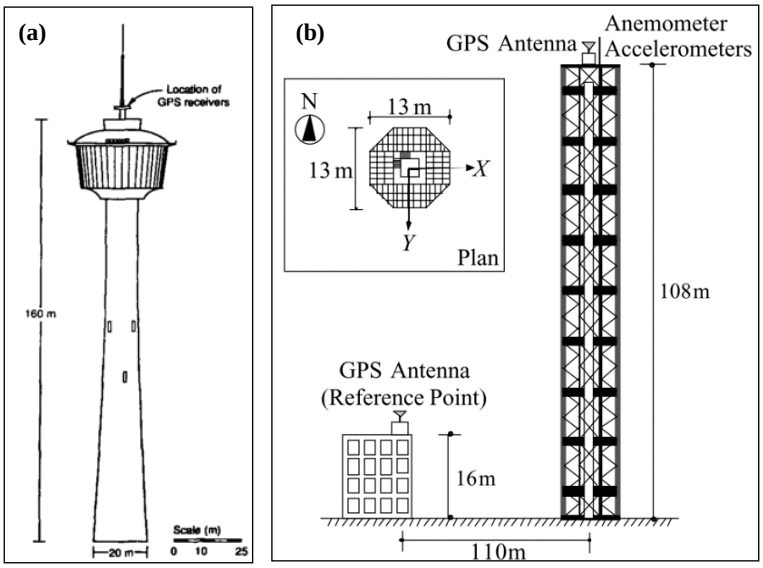


Fig. 2.1 (a) Calgary Tower (Lovse et al., 1995) and (b) a high steel tower (Tamura et al., 2002).

The wind-induced response includes a static component (i.e. mean value) and a dynamic component. It is difficult to measure the static component by the accelerometer, while GPS has the potential to measure both components efficiently. This was demonstrated by Tamura et al. (2002) when they investigated the feasibility of RTK-GPS measurements to monitor the response of building (steel tower of a 108 m high, Fig. 2.1b) under loading conditions. They reported the feasibility of 10 Hz RTK-GPS measurements to detect a 4-cm of static displacement caused by typhoon and a 4-cm deformation from temperature variations. In addition, they extracted the peak frequency of 0.57 Hz

that was detected from GPS and accelerometer data. These findings were also achieved by Li et al. (2006).

To highlight the possibilities of using GPS to detect small displacements in oscillating high-rise structures, Breuer et al. (2002) conducted two field tests before monitoring. The purpose of these tests was to evaluate the accuracy of GPS by analysing the noise of signals in a specific station. They proved that the recorded noise in the North-South direction is higher than that in the East-West direction (Fig. 2.2a), due to a limited satellite in N-S direction at (Lat. ~49°). In addition, they found that the geometry and the number of satellites are the most effective factors on the final precision. On the other hand, to achieve accurate positioning, it is better to resolve the ambiguity with minimum duration. Therefore, 100-300 data points were required to resolve the ambiguity in these tests. When monitoring Stuttgart TV tower and the industrial chimney of the Opole Power station (Fig. 2.2), they found that the recorded displacement at wind velocity of 7 m/s was 2.5 cm on both cross-wind and along-wind direction with the derived frequency of 0.2 Hz.

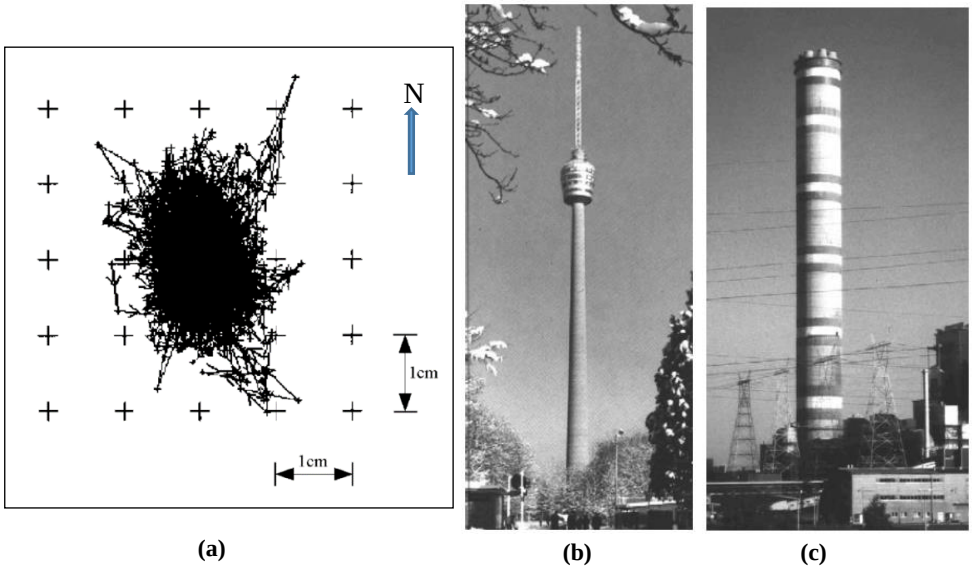
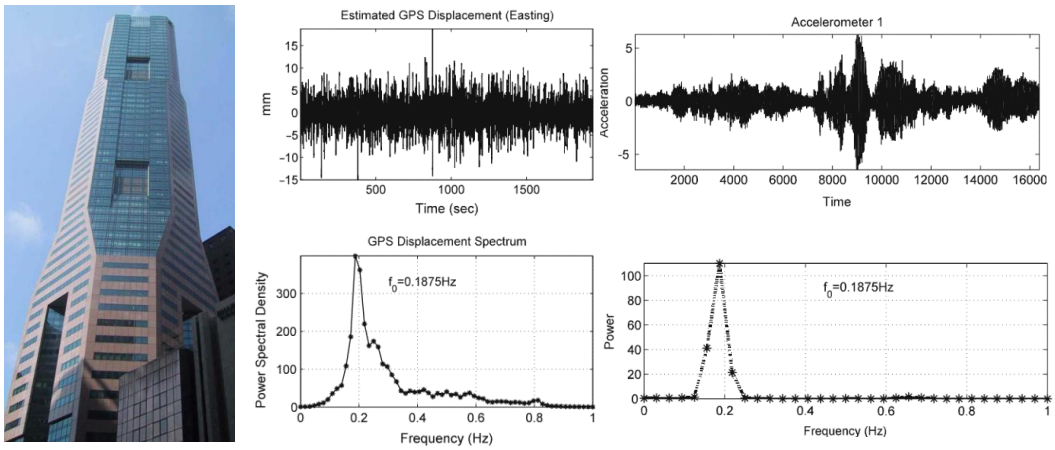


Fig. 2.2 (a) Data points of 16-h measurements (1cm/30s), (b) Stuttgart TV-tower and (c) industrial chimney of Opole Power station (Breuer et al., 2002).

The GPS measurements have been used in many studies to monitor the dynamic response of high-rise buildings and validate their performance against design criteria. For example, Brownjohn (2005) tested the capability of GPS to resolve the relatively small deflections of the dynamic behaviour of the Republic Plaza Building (280m high) in Singapore (Fig. 2.3a). He found that the GPS measurements success to identify the long-term drift in model properties of this building for long-term monitoring (between Nov 2001 and Jan 2005 (Brownjohn et al., 2005)). In the same study, Brownjohn et al. (2005) used the RTK-GPS measurements to track displacement and identified the slowly varying quasi-dynamic component of wind induced response to compare with seismic effects on this building.



(a) **(b)** **(c)**

Fig. 2.3 (a) View of the Republic Plaza Building, (b) GPS results of estimated displacement and the corresponding power spectral density and (c) accelerometer results (Hristopulos et al., 2007).

When investigate the response of the Republic Plaza Building to wind loading for a short duration (i.e. about 34 min), Hristopulos et al. (2007) indicated that the spectrum response of this building obtained from filtered GPS data shows a dominant frequency at 0.1875 Hz, which coincides with the peak frequency obtained from accelerometer data (Fig. 2.3)

GPS technique was also adopted to monitor long suspension bridges in a real-time (Ashkenazi and Roberts, 1997). They have used Kinematic GPS to monitor the deformations of the Humber suspension bridge in the United Kingdom (with a total length of 2220 m, and mid-span of 1410 m supported by two towers of 155.5 m high). Before they collected the data, the initial zero-baseline test was carried out to check receiver performance. Consequently, the resolutions of analysis were within ± 1mm and ± 3mm in horizontal and vertical directions, respectively for static data. Then the real-time monitoring was carried out with Ashtech Z-XII GPS receivers of dual frequency. The antennas were mounted on specific points at the bridge deck and the support towers as monitoring points referred to the reference station. The maximum displacement was expected at the mid-span of the bridge. To avoid the effects of passing vehicles, the deck's antennas mounted on poles. However, the vibrations of these poles by winds may also create a problem at the time of measurements in the horizontal direction. Therefore, the movement of these poles resulted in apparent accuracy within 1-2 cm for RTK, instead of a few millimetres.

From the above studies, the success in adopting the GPS technique for monitoring applications leads to extending this technique to be used in various other applications such as; recording the movements of bridges, and other engineering structures. Therefore, GPS positioning is one of the promising tools that can be effectively used in structural health monitoring applications. Monitoring structures' behaviour can also be implemented to monitor the dynamic response of long-period structures (Kijewski-Correa et al., 2006). The GPS technology has also been used to monitor the deformations in tall flexible buildings (Kijewski-Correa and Kareem, 2003, Kijewski-Correa and Kochly, 2007,

Hristopulos et al., 2007, Seco et al., 2007). It also utilised in long span suspension bridges (Nakamura, 2000) and cable-stayed bridges (Ren et al., 2005, Watson et al., 2007, Lepadatu and Tiberius, 2014, Montassar et al., 2015), as well as monitoring the displacements of large dams (Behr et al., 1998, He et al., 2004).

2. 3 Experimental Assessment of GPS Accuracy for Structural Monitoring

Originally, GPS was introduced to be used for navigation purposes. However, due to its high accuracy and reliability, it was then applied for geodetic positioning (Nickitopoulou et al., 2006). It is essential that the GPS should be validated (through simulation, to test their accuracy) before it can be deploying in full-scale applications. Considerable researches have been conducted to perform this validation such as (Celebi, 2000, Celebi and Sanli, 2002, Tamura et al., 2002).

To investigate the feasibility of implementing GPS measurements to monitor the static and dynamic response of structures; different experiments have been conducted in previous studies. These experiments focused on the assessment of GPS performance to meet the monitoring requirements through its positioning ability to record the rapid movements with high-level of accuracy, as well as the potential of GPS to detect and identify the modal frequencies of structures. Each study was based on experimental device, simulating the motions of the response of the structure, which was recorded by GPS receiver(s). The GPS data were analysed in order to assess the accuracy, precision and reliability of the GPS receivers in monitoring the amplitude and frequency of the motions.

For instance, to study the dynamic response of long-period structures, Celebi and Sanli (2002) tested a simulated model of the flexible structure before investigating the actual deployment on the tall building. The designed model consists of two stock steel bars specimens with specific dimensions (length, width and thickness as shown in Fig. 2.4 to achieve a necessary period of about 4 s in the weak direction to simulate a 30-40 story flexible building. Each bar was subjected to free vibration and excited by pulling/ releasing force.

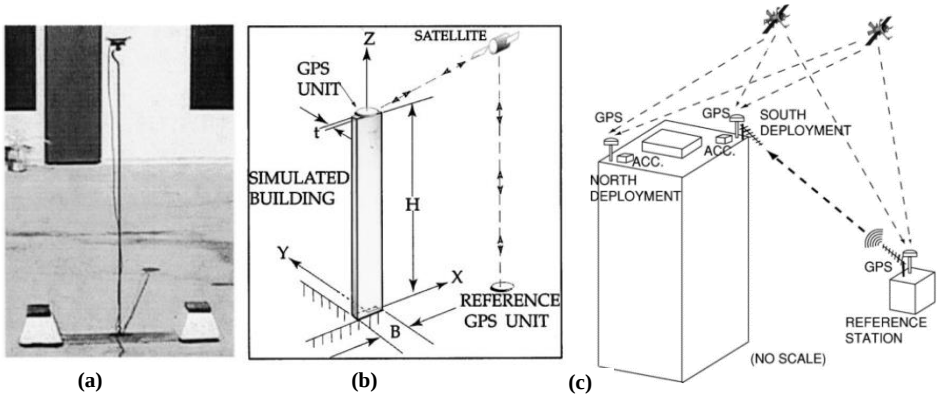


Fig. 2.4 (a) Photo of the experimental model, (b) schematic of the test set up and (c) schematic of a full-scale of building (Celebi and Sanli, 2002).

A GPS receiver was attached at the top end of each bar to record the data of vibrated bar relative to the reference receiver. The results indicate that accurate and clear displacement was derived from 10 Hz sampling rate of GPS measurements along with the identified frequency. The analysed results, which demonstrated the changes in dynamic characteristics and computed the average drift ratios. Therefore, the outcomes of this test encouraged extending monitoring to actual deployment at a 34-story San Francisco building, which was equipped with GPS units and tri-axial accelerometers deployed at two diagonal corners on the roof of the building and a reference station in other location as illustrated in Fig. 2.4.

The GPS recorded data of 10 Hz was analysed to detect the wind-induced deformation of this building. In addition, the relative derived displacement from GPS measurements agreed with the computed relative displacement from the accelerometer. The results indicated that GPS provides sufficient accurate measurements, which enable to obtain the relative displacement, and extracted the corresponding frequency response accurately.

The accuracy of GPS to measure the sinusoidal displacements was investigated by Tamura et al. (2002). They used an electronic exciter to generate sinusoidal vibrations, which occupied by RTK-GPS antenna with a wire displacement transducer to measure the actual displacement (see, Fig. 2.5).

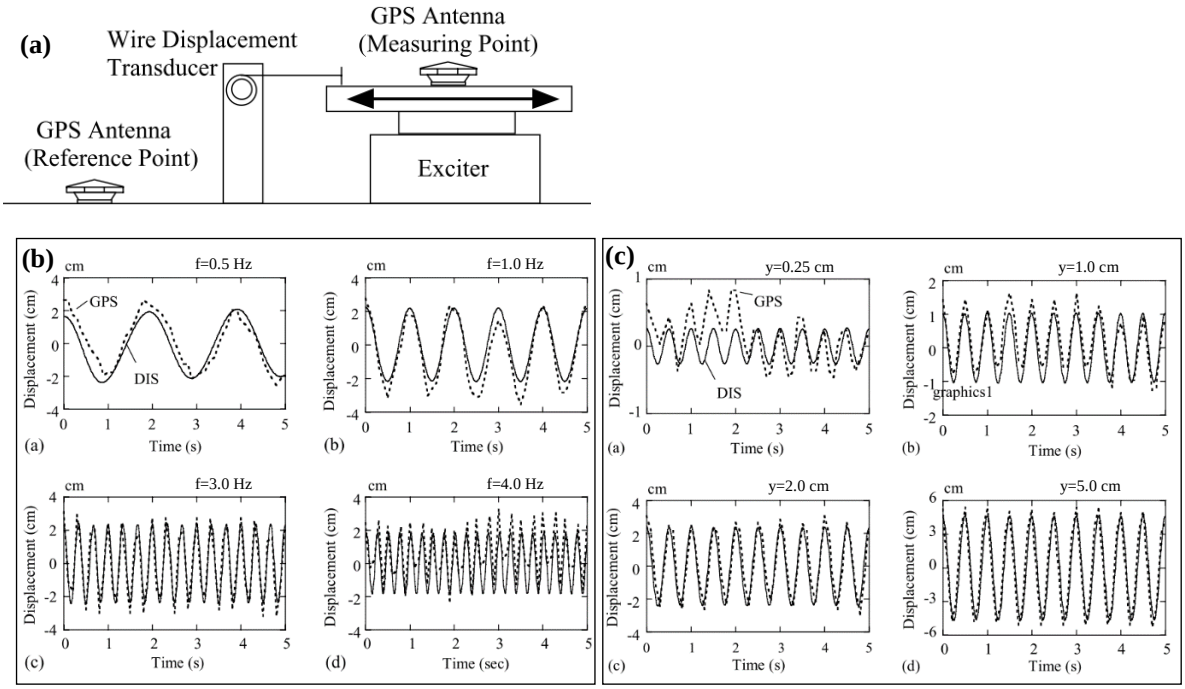


Fig. 2.5 (a) Schematic of vibration test, comparison of detected displacement by RTK-GPS and actual one measured by wire displacement transducer DIS in (b) y=2 cm for different frequencies and in (c) f=2.0 Hz for different displacements (Tamura et al., 2002).

They found that the derived displacement from RTK-GPS was identical with the actual displacement from exciter movement when the vibration frequency < 2-Hz and the vibrated amplitude > 2-cm as shown in Fig. 2.5.

To achieve the precision of kinematic GPS positioning and the dependence of baseline length, Breuer et al. (2002) tested different lengths of baseline that connected between the fixed base and moving rover points. They attached a Leica 300 GPS unit at the end of the horizontal bar that running with a constant angular velocity in a circular horizontal path (R=24.4 cm) to represent the moving rover point. They tested the tracking of kinematic positioning at different baseline lengths, from 10, 100, 250, 1 000, 5 000 to 10 000 m. They applied a sampling data of 3 min for all distances and computed the standard deviation, which was varied from 2 to 6 mm. From the investigated results, they concluded that the number and geometry of GPS available satellites affected the achieved precision, which independent from varying lengths of short baseline.

In the same manner, Nickitopoulou et al. (2006) conducted a large number of experiments to assess statistically the accuracy of kinematic GPS positioning carried out at a simple simulating monitoring system. They used prototype specimen consists of a rover GPS antenna that attached to a rotating rod moving in predetermined circular orbit to simulate harmonic movements (Fig. 2.6a).

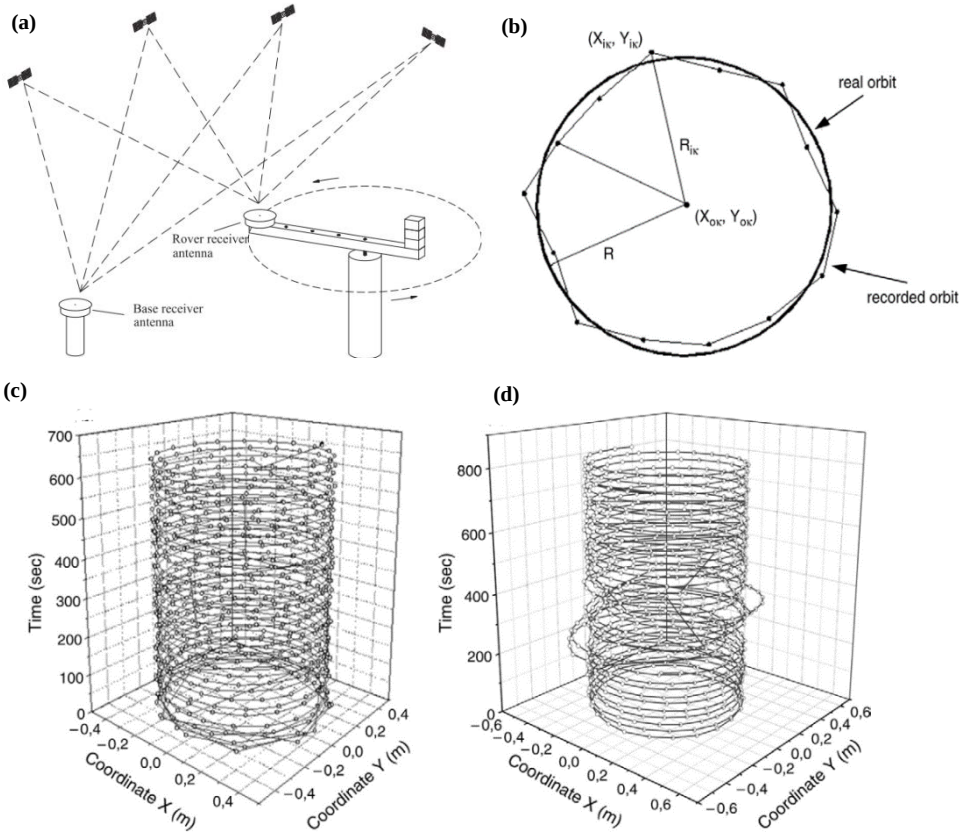


Fig. 2.6 (a) Schematic of experimental device of rotating rod (Im et al., 2013), (b) comparison between real and recorded orbit, plot of horizontal coordinates recorded by rotating rover versus time in (c) ideal cylinder plot, while in (d) represent some detected outliers (Nickitopoulou et al., 2006).

To confirm the determined accuracy, the outlier GPS measurements (at 1.5% outlier level) were detected, and the results showed that GPS data could identify displacement of harmonic motion

at a standard accuracy of up to 15-mm and 35-mm in horizontal and vertical coordinates, respectively. In addition, they reported that the harmonic frequencies could be successfully determined in the range of 0.1 Hz and 0.5 Hz. The validated GPS results could help in modelling various dynamic and quasi-static flexible engineering structures. Similarly, Casciati and Fuggini (2009) investigated the accuracy of GPS measurements for static and dynamic tests by comparing the real and recorded displacements, which caused by a linear movement of GPS antenna (generated by an electromagnetic motor) along with a longitudinal direction. The researchers concluded that the GPS detected displacements at the millimetre level of accuracy with frequency motion up to 2 Hz. These findings agree with the achieved results presented in (Breuer et al., 2008).

The GPS technique has been successfully applied to monitor and study the dynamic response of large flexible structures with primary model frequencies <1 Hz (Ogaja et al., 2003, Kijewski-Correa and Kareem, 2003, Kijewski-Correa et al., 2006). To investigate the potential of GPS to define the model frequencies of oscillation structures (> 1 Hz), Psimoulis et al. (2008) designed an experimental apparatus permitting computer-controlled oscillations (Fig. 2.7) to study the frequency response of GPS records.

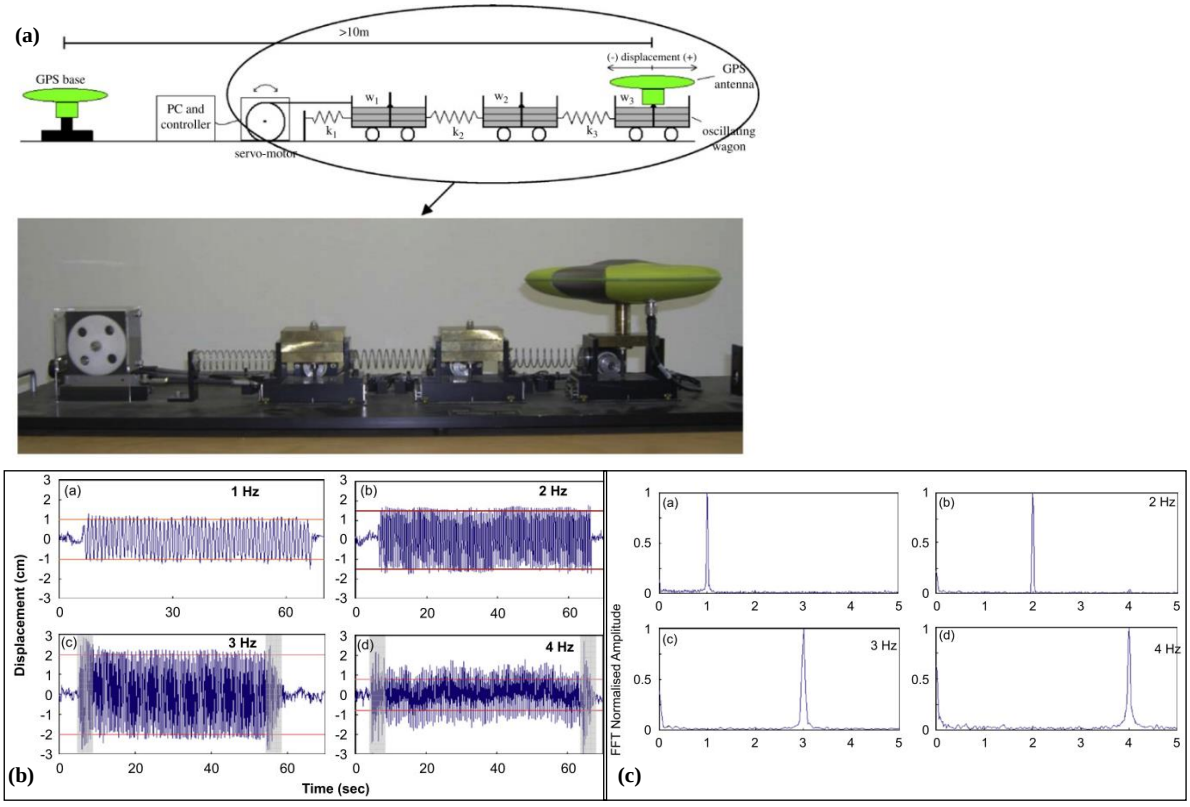


Fig. 2.7 (a) Schematic and a photo of an experimental apparatus, (b) time series of derived displacements with different frequencies and (c) frequency results by FFT (Psimoulis et al., 2008).

They attached the antenna of GPS rover receiver (having a sampling rate of 20 Hz) on the top of the oscillation part of the apparatus. The PC-computer was used to determine the known characteristics of oscillation (i.e. frequency, amplitude, etc.), which allow to compare them with the results of

collected GPS data during oscillation. The outcomes of this study demonstrated that GPS is capable of identifying the dynamic characteristics up to 4 Hz, which can be used to analyse the response of relatively rigid structures. Also, they found that the results are more accurate when achieved up to 2 Hz and the displacement ≥ 5mm (Fig. 2.7). Then Psimoulis and Stiros (2008) performed a further analysis using the same experimental apparatus by adding both GPS and robotic total station (RTS) technique, to assess the accuracy of each technique in order to detect and identify the characteristics of oscillations. They compared the predefined characteristics (amplitude and frequency) with the results of simultaneous recording of both GPS and RTS. The analysis showed that GPS could identify oscillations and a minimum amplitude of 4 Hz and 5-10 mm respectively (with an accuracy of few mm). On the other hand, RTS technique is capable of recording peaks oscillations with an accuracy of sub-mm to a few mm; however, some cycles could be lost at high frequencies.

To assess the possibility of GPS technique to identify the dynamic displacement in monitoring stiff structures (in applications where the model frequency is greater than 4 Hz), Moschas and Stiros (2011) presented a study to analyse the collected GPS data in a steel short-span pedestrian bridge. The bridge of 40 m length (Fig. 2.8) has the model frequency of 4.3 Hz and approximately 6 mm oscillation amplitude. During their experiment, the GPS and accelerometer data were collected when the load exerted by a group of pedestrians excited the mid-span of the bridge.

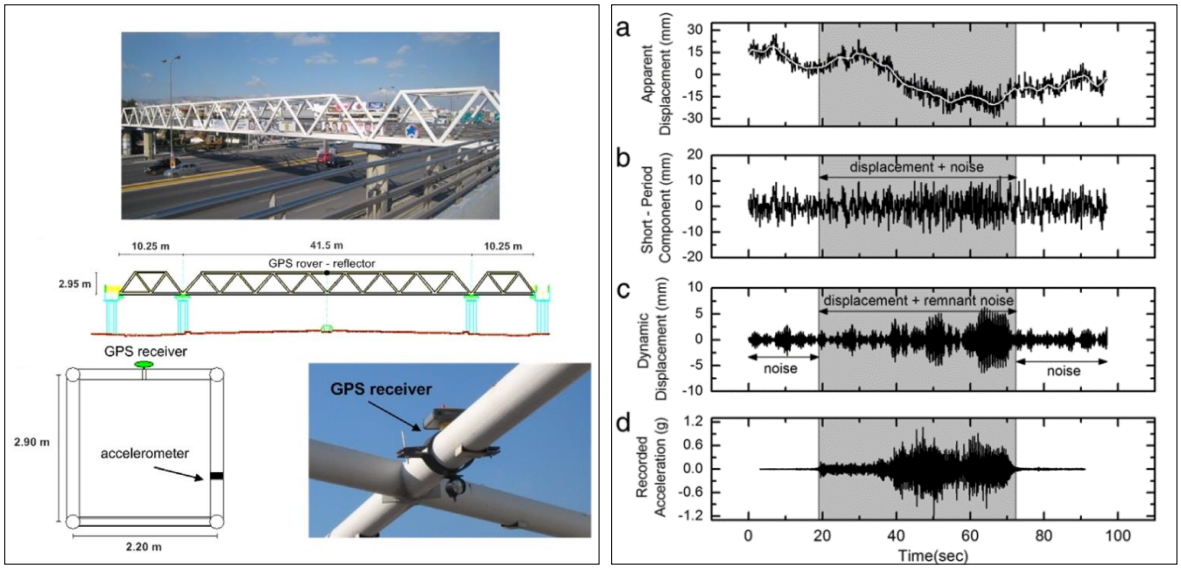


Fig. 2.8 (left) photo and details of stell pedestrian bridge and (right) time series of vertical displacement detected from GPS data (a-c), while (d) represent the recorded acceleration (Moschas and Stiros, 2011).

However, the GPS measurements are contaminated by noise; de-noising these geodetic measurements can achieve the more reliable and accurate results. Therefore, they presented a new technique to reconstruct the waveform of the detected dynamic displacement of the oscillating

bridge. Their method was based on digital filtering of oscillated 10 Hz GPS data as illustrated in Fig. 2.8. Each filtering process was constrained and tested by independent accelerometer data. They filtered the introduced time series of apparent vertical displacement to obtain the dynamic response by sequential procedures. Firstly, they derived the long-period component (by moving average) that represent the semi-static displacement, followed by extracted the short-period component by applying supervised learning-derived filtering (1^{st} level). The resulted short period represented the dynamic displacement with noise. To assess the validity of filtering, the derived frequency of GPS data was compared with that derived from the accelerometer. Then, to identify the dynamic displacement alone, a Chebyshev band-pass filter was applied to the time series of apparent displacement (2^{nd} level), which also assessed with accelerometer records. They extracted the model frequency from filtered GPS data to be 4.28 Hz, which has a close agreement with accelerometer data. From the outcome of this study, they confirmed the possibility of using GPS for monitoring stiff structures.

Moschas and Stiros (2013) continued their studies to analyse the noise characteristics of GPS measurements by conducting a series of experiments based on different types of stationary, collocated and identical GPS receivers. They collected GPS data of 10 Hz along short duration (<100 s), and they found that the significant noise level that is affecting 10 Hz GPS, is mainly based on the instrument itself even when same instruments are used. By investigating the spectral analyses of recorded data, they reported that the coloured noise was dominant for frequencies below 0.2 Hz, which was decaying and resulting to the white noise being dominant for frequencies above 2.5 Hz.

In structural monitoring for some applications (e.g. stiff structures), the monitoring process required collecting data with high sampling rate. One of the primary development in GPS receivers is increasing the sampling recording rate up to 100 Hz (Haberling et al., 2015, Bischof and Schön, 2016), which enhance the ability to analyse the recorded GPS measurements conducted in concerned structures. To investigate the reliability and operating performance of GPS records with the high sampling rate, Yi et al. (2013a) performed experiments by adopting two types of GPS receivers (NovAtel-50 Hz and Javad-100 Hz). They aimed to assess the performance and characteristics of GPS high rate recordings. Therefore, they attached the receivers and accelerometer (Lance LC0161A) on a controlled steel frame model and collected high-rate data when the frame was vibrated. They concluded that the high-rate GPS records could detect the sensitive displacements, which can be then implemented to investigate the dynamic response of bridge structure.

Although the GPS receiver can record data with the high sampling rate, it is expected to increase the noise level. Therefore, Moschas and Stiros (2014b) investigated the impact of increasing the bandwidth of phase-locked loop (PLL) on the noise and their effect on correlated GPS measurements at 100 Hz. They processed the collected data with different modes according to various PLL

bandwidth values. They found that the increase in the PLL bandwidth reduces the correlations and leads to increase in the frequency noise of 100Hz. Therefore, they suggested a combining of a band-pass filter with a pre-set PLL bandwidth to obtain more optimal results.

To validate the use of high rate GPS sampling and expand their ability to detect the dynamic deflections of stiff structures (> 6Hz), Moschas and Stiros (2015) succeeded to monitor stiff Footbridge by 100-Hz GPS records. However, the derived vertical deflection was contaminated with noise; they extracted the 6.5 Hz to be the natural frequency of the bridge.

It can be summarised from the above experimental studies that the GPS is a promising accurate technique, which can be used in structural monitoring as reported by different researchers.

2. 4 GPS Measurements for Bridge Monitoring

Bridges are one of the main infrastructures that require monitoring as an essential part of Structural Health Monitoring (SHM). The bridges are subjected to various external dynamic loadings such as the wind (Han et al., 2016), temperature variation (Montassar et al., 2015) and traffic loading (Karoumi et al., 2005), resulting in their response, which can be recorded by different techniques employing various sensors.

Among different monitoring sensors, the GPS technique has been used to monitor the behaviour movements of structures under loading. The main advantages of GPS are the ability to provide (i) direct 3D displacement of the monitoring points, in an independent coordinate system (Psimoulis et al., 2008, Haberling et al., 2015) and (ii) sampling rate which can reach up to 100Hz (Yi et al., 2013a, Moschas and Stiros, 2015, Haberling et al., 2015). In addition, the continuous GPS measurements can be taken in all weather conditions (Im et al., 2013).

Several experimental studies (see, Section 2.3) have proved that accurate GPS measurements can be used to monitor the dynamic motion of a few mm amplitude (i.e. 4-5 mm; (Roberts et al., 2000, Psimoulis and Stiros, 2008, Moschas and Stiros, 2014c). In addition, GPS has the potential to estimate the motion frequency of the bridges up to 4-5 Hz (Psimoulis et al., 2008, Moschas and Stiros, 2011), and thus it meets the requirements for monitoring the dynamic response of structures. Therefore, it can be adopted for short and long-term monitoring systems (Meng et al., 2003, Kaloop et al., 2017).

Many studies have been conducted, where GPS has been used successfully to measure not only the dynamic response but also the static and semi-static behaviours (Moschas and Stiros, 2015). For example, after the success monitoring of Humber Bridge by Ashkenazi and Roberts (1997), further studies were carried out to study the bridge response. One of those studies focused on assessment of the GPS data to monitor the twist and deflection of the bridge (Roberts, 1999) as well as the height deflection (Roberts et al., 2000). During the latter study, the derived deflections from GPS

measurements showed a close agreement with those predicted by Finite Elements (FE). The results were achieved when five fully loaded Lorries (weighing about 160 tons) passed through the bridge to detect deflections under loading conditions. Five receivers related to the reference station were used to collect the data at a rate of 5 Hz. The precision of the processing procedure was within a few millimetres. When they analysed 3D deflections and converted to distances, the deflection at mid-span was 420 mm with GPS while it was predicted by finite element to be within 440 mm. Similar trend about validation of GPS results and finite element analysis was proved by (Brown et al., 1999).

After opening London Millennium Footbridge (330 m length with mid-span of 144 m) in June 2000, unpredicted lateral vibrations occurred by crowed pedestrians loading led to close this bridge for extra treatment by placing dampers, and it was monitored again in November 2000. Thus, Roberts et al. (2006) studied and monitored 'London Millennium Footbridge'. They analysed the vibration of the bridge by using five receivers connected to Leica AT504 choke ring antennas (at 10 Hz rate) that are placed on the bridge handrail as illustrated in Fig. 2.9. The results showed good agreement between the computed natural frequencies from GPS data and the predicted natural frequency by finite elements models (FEM). The predicted frequencies of lateral dynamics at the mid-span are 0.5 and 0.95 Hz, while the actual frequencies from GPS are 0.55 and 0.95 Hz. The strange output was found that the longitudinal deflection is larger than the lateral deflection. They attributed this to the limitation of GPS geometry in the north-south direction (Roberts et al., 2004a).

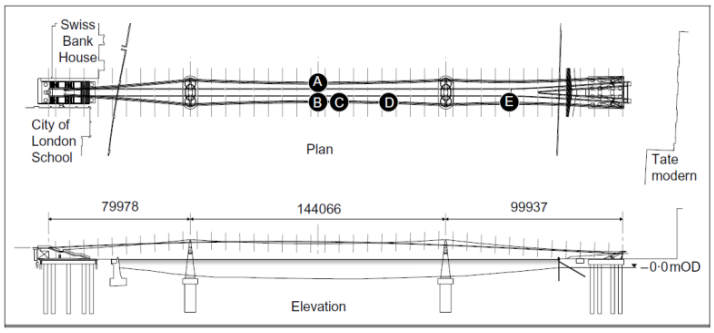


Fig. 2.9 The locations of the monitoring stations on the London Millennium Bridge (Roberts et al., 2004a).

To illustrate displacements in bridge structure for an extended period, Guo et al. (2005) have studied Humen Bridge in China for five months period by RTK GPS. They investigated the vertical displacement as a result of temperature variation and lateral displacement caused by wind loads. Moreover, they applied the spectral analysis to estimate the frequency characteristic of that bridge. As a result, the frequencies that computed by GPS are identical to that calculated by finite elements (FE). The torsional displacement was also calculated at the symmetrical points on the deck of the bridge.

The Forth Road Bridge in Scotland (a bridge that is used as the main case study for the current research) was another bridge that monitored with several trials. In February 2005, continuous 46

hours gathered data depending on two adjacent reference receivers outside the bridge and seven receivers distributed upon the bridge in desecrating points were investigated (Roberts et al., 2005), as illustrated in Fig. 2.10.

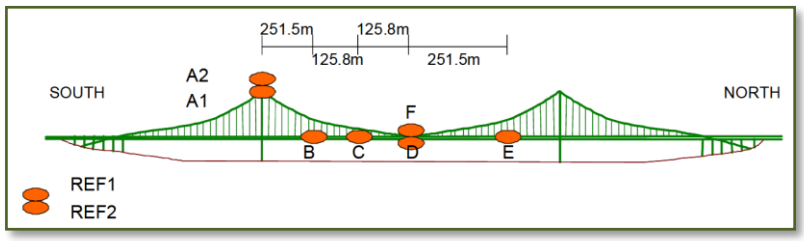


Fig. 2.10 Schematic of the Forth Bridge and distributed points (Roberts et al., 2014).

In their study, two monitoring points were placed on the top of the bridge tower while the other two locations were attached on both sides of mid-span. The rest of the monitoring points were located in distances divided along the mid-span at ¼, ¾, and 3/8 of the mid-span length. Leica 530, 510 and GPS1200 receivers were used with 10Hz sampling rates of recording data. Metrological data of wind, temperature, and other factors were collected besides traffic loading. In the early hours of the morning when the traffic was less congested, it was an excellent opportunity to pass two 40 tonne lorries along the bridge to detect controlling loading effect. 400 mm deflected the bridge from 80-tonne loading and the two symmetric mid-span points deflected by different magnitudes due to torsional movement. The precision of the gathered data was within millimetres and post-processing technique used was 'on the fly' (OTF) technique (Roberts and Brown, 2010). The data of deflection components of the bridge was analysed and filtered by the pass-band filter using both Fast Fourier Transform (FFT) and the Lomb Normalized Periodogram (LNP). The spectral analysis of FFT was related to 0.08, 0.275 and 0.34 Hz at frequencies in the lateral direction, and 0.10, 0.20, and 0.26 Hz in the vertical direction, while it was 0.17 Hz in the longitudinal direction. These results are identical with that computed by LNP technique (Pytharouli et al., 2006). For more information on derived frequencies, refer for example to (Brown et al., 2007, Roberts et al., 2012, Wang et al., 2015b).

Currently, the Forth Road Bridge has permanent structural health monitoring established as part of a Geo-SHM project that sponsored by ESA (Meng et al., 2016). This project implies the use of GNSS records, Remote sensing data and environmental information for effective integrated assessment of concerned structure (ibid). The GNSS data are collected by four Leica receivers (two attached at the mid-span and one at the top of bridge's tower relative to reference one) as shown in Fig. 2.11. From available collected data, it can correlate the response of the bridge with loading effects as well as the environmental conditions to study the behaviour of the bridge. Therefore, Psimoulis et al. (2017) implemented the GPS recorded data over a long duration (between 20/07/2016 and 21/08/2016) to define the characteristic behaviour of the bridge response. They analysed the collected data at mid-span stations by evaluating the response for every 10-min (compute the mean and standard deviation)

during the long duration. They found that the daily cycle response was detected with the vertical component of movement caused by variations in temperature and traffic. In contrast, the daily cycle response did not exist in the lateral component, which showed the resulting response from the wind load.

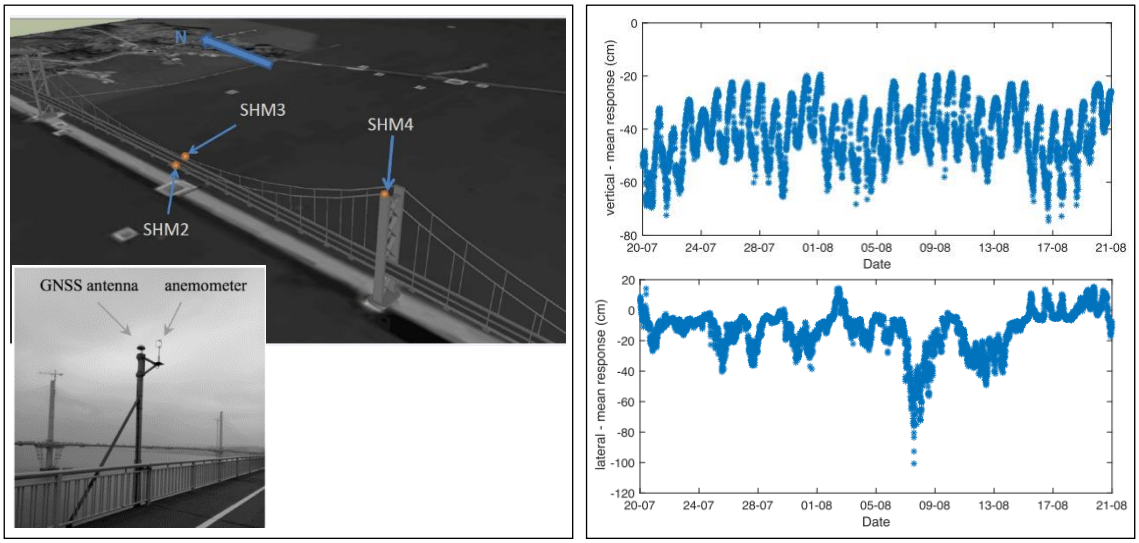


Fig. 2.11 (left) Locations of attached monitoring stations at Forth Road Bridge and (right) the time series of 10-min mean response for vertical and lateral components (Psimoulis et al., 2017).

Likewise, Chen et al. (2018) analysed the GPS data collected at the monitoring station (SHM4 in Fig. 2.11) of the southern tower of Forth Bridge. They investigated the vertical deformation of this tower derived from GPS data (for every 10-min) during 33-months along with metrological data of 15 months, in order to detect the mechanism of vertical deformation. They reported that the subsidence rate was within 4.7 mm/year, with the uncertainty of 0.1 mm.

M48 Severn Bridge in the UK (the second case study in the current research) was monitored by Roberts et al. (2014). They monitored the suspension cable of the bridge by attached several antennas directly onto the suspension cable. During three days in March 2010, nine receivers referring to two reference stations collected GPS data. The sampling rate was 20 Hz for 5 points on cables and 10 Hz for four tower points as illustrated in Fig. 2.12.

Different types of receivers were used including; Leica 530, Leica 1200, Leica SR510 and Leica Viva receivers connected to Leica chock ring antennas. Because of the high resolution of the GNSS carrier phase and implementation of chock ring antennas, the predicted precision will be within millimetres. Moreover, the post-processing used was OTF technique. They found that the vertical deflection could reach 0.3 m due to the mass of traffic in a specific point (Fig. 2.12). From their analysis, the fundamental frequency was around 0.146 Hz derived from the vertical displacement of mid-span station. Furthermore, the results showed the changes in external factors that affecting the natural frequencies values.

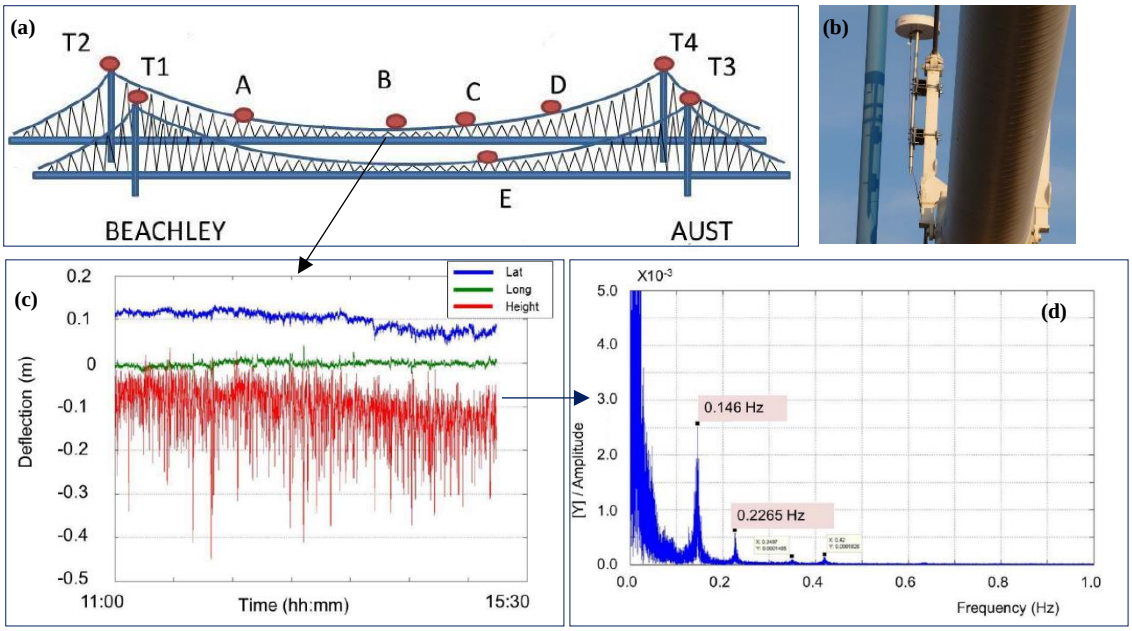


Fig. 2.12 (a) Monitoring points in Severn Bridge, (b) choke ring antenna attached to the cable, (c) time series of apparent deflection and (d) detected frequency (Roberts et al., 2015).

2. 5 Limitations of GPS Measurements

Many studies have been conducted, where GPS has been used successfully to measure the response of different engineering structures. More specifically, GPS is used to measure the deflection of the top of the tall structures, while for the case of the long-span bridges it is mainly applied to the top of the towers and other critical points at the main span (e.g. midspan). Even though, the response of the suspension bridges is at least of cm-level, which is detectable with GPS measurements.

Although it is possible to meet the requirements of structural monitoring with GPS, some limitations will affect the efficiency of this technique. The limitations are due to biases and errors that contaminated the GPS measurements such as multipath, noise, cycle clips, ionospheric delay, etc. In addition, the limited number of visible observed satellites is another limitation may lead to weak geometry that introduced a low quality of derived positioning or no solution in some cases. Most of these limitations can exist in conducted GPS measurements at a particular monitored structure along different durations, which consequently affect achieving precise characteristics of the movements as well as identifying accurate response with correct interpretation.

In bridge deflections monitoring by GPS, it is challenging due to multipath effects from towers, cables and passing vehicles on the bridge as well as obstructions causing cycle slips in measurements (Raziq and Collier, 2007), resulting in additional coloured noise and biases errors (Moschas and Stiros, 2013). Additionally, the monitoring of the vertical response, which is crucial for the evaluation of the bridge behaviour is often challenging due to the lower accuracy of GPS in the

vertical component in comparison to the horizontal components (Meng et al., 2003, Raziq and Collier, 2007).

Regarding multipath, the complexity of site environment that influenced by surrounding reflective features with the limitation of the selected site make multipath a dominant unavoidable error source in GPS measurements (Dodson et al., 2001). Since the GPS measurements of pseudorange and carrier phase are contaminated by receiving direct and indirect reflected signals (i.e. multipath), the accuracy and reliability of required precise positions will be degraded. Thus, the multipath effect could maximise the amplitude of detected deformation to vary from several millimetres up to several centimetres or even meters (Dodson et al., 2001). Different studies have been conducted as an attempt to eliminate the effect of multipath in order to achieve accurate positioning as well as to improve the detection of structural movement, such as (Roberts et al., 2002, Meng et al., 2004, Ogaja and Satirapod, 2007, Moschas and Stiros, 2014a, Peppa et al., 2018). To illustrate the effect of dynamic multipath, Moschas and Stiros (2014a) carried out experiments to investigate the impact of multipath caused by passing trains nearby stations occupied by GPS antennas. They found that the derived GPS time series was biased by errors caused by temporary blockage of some satellites and dynamic multipath during the interval of passing trains (see Fig. 2.13). They concluded that the dynamic multipath looked to be affected by satellite geometry and caused a shift in the derived time series. Multipath has a systematic effect over a short time interval (few seconds) and periodic effect for a longer time (i.e. many minutes) (Amiri-Simkooei and Tiberius, 2007).

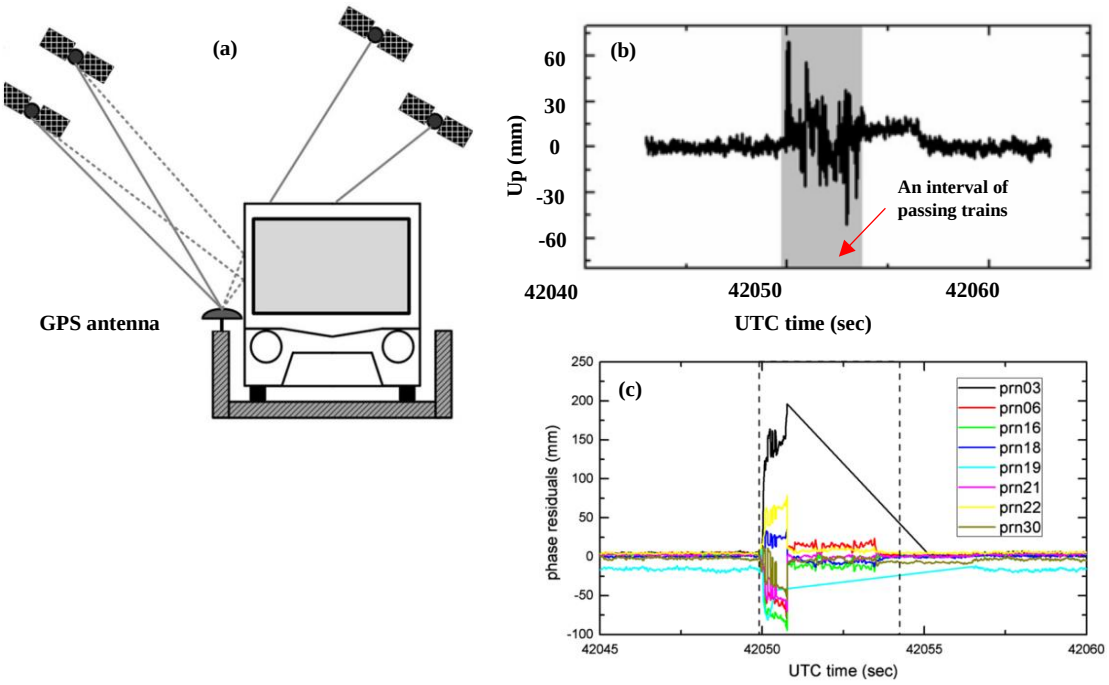


Fig. 2.13 (a) Schematic of the experiment of passing train nearby GPS antenna, (b) the derived Up time series at a specific event and (c) phase residual of observed satellites (Moschas and Stiros, 2014a).

The second limitation of the GPS measurements is the noise that degrades the quality of derived positioning. As a proper receiver gathers the GPS data, each receiver is characterised by a specific type of noise that contaminated the measurements. Therefore, the derived displacement of structural deformations always masked by different levels of noise, which affect the precision of derived results. In addition, the accuracy of GPS positioning can also be affected by satellite availability and their geometry, the quality of observations and resolution of integer ambiguity (Rabbou and El-Rabbany, 2015).

Even with the presence of the limitations mentioned above, GPS can be used in structural monitoring by adopting methods and techniques to limit the GPS measurement errors and improve its performance to achieve high precision positioning. The implemented methods and techniques can be grouped into two main categories of considerable studies including (i) integration of GPS with another sensor (e.g. accelerometer, Robotic Total Station RTS, Pseudolite or Locata) and (ii) adopting different digital signal processing by filtering methods. In addition, the combined GNSS observations as a suggested technique in this study.

2.5.1 Existing Solutions to GPS Limitations

2.5.1.1 Integration of GPS and Other Sensors

For specific applications that require high-rate sampling with high accuracy, GPS alone is not able to provide accurate and reliable results. The accelerometer is used for dynamic monitoring, with the high sampling rate (several hundred Hz), but with the requirement of a double integration of the acceleration to derive displacement. Also, the acceleration reading will drift over time and cannot detect low frequencies which is another limitation (Roberts et al., 2004b). Furthermore, the accelerometer readings are insensitive to detect movements of long duration in monitoring deformations of long-span bridges (Han et al., 2016). Therefore, the integration of GPS and acceleration data is a common solution (Meng, 2002). The use of an accelerometer as a supplementary could enhance the GPS data analysis and improve the quality of the GPS time series (Moschas and Stiros, 2015). This integration will surpass limitations regarding improving the overall system reliability and performance.

Many studies have been applied to this technique in dynamic monitoring. (Meng et al., 2003) developed the hybrid system consisting of a GPS system and triaxial accelerometer. To have a correct alignment of the accelerometer, one of its axes should be aligned with a known direction. Usually, the bridge central axis and that was done manually by theodolite. The monitoring test applied to Nottingham Suspension Footbridge under wind and pedestrian loading. The collected field data were synchronised between accelerometer and GPS by a cross-correlation algorithm, with a rate of 10 Hz for GPS and 200 Hz for the accelerometer. Finally, the model frequency was extracted by spectrum analysis after post-processing. The hybrid system contains Leica CRS100 and SR530 GPS dual-

frequency receivers combining with Kistler triaxial accelerometer. This procedure reflects the possibility of utilising the integrated system to monitor deformations in small bridges with high frequency providing millimetre accuracy. A set of trials demonstrated on this bridge to check the validity of monitoring by integrated GPS and accelerometer (Meng et al., 2007).

Other studies for assessing the performance of utilising GPS and accelerometer had been performed by (Li, 2004, Li et al., 2006, Moschas and Stiros, 2011). Recently, Yu et al. (2014) repeated monitoring the Wilford Bridge in Nottingham by applied three GNSS data processing modes, which are Real-Time Kinematic (RTK), network RTK and post-processing Kinematic (PPK). They used multimode adaptive filtering (MAF) that combining the adaptive filter with Chebyshev highpass filter to mitigate the GNSS measurement errors and to identify the dynamic displacements of the bridge. They assessed the differences between measured displacements from two approaches either GNSS or from the double integration of accelerometer data. Statistically, the standard deviation of displacements differences between two approaches is less than 1mm, which satisfy monitoring purposes. The results from GNSS data related to the sub-millimetre level of accuracy with an amplitude of less than 8 mm and the model frequency were 1.690 Hz, in close agreement with the accelerometer results. It could be concluded that the GNSS technique could detect the model frequency less than 2 Hz with a sampling rate of 20 Hz.

Another geodetic technique could be integrated with GPS is Robotic Total Station (RTS). The RTS has been combined with GPS in order to reduce the error of GPS data, mainly for dynamic motion of a few mm amplitude or semi-static displacement (Psimoulis and Stiros, 2008, Psimoulis and Stiros, 2012) and mitigate the impact of the multipath effect in GPS time series (Moschas et al., 2013).

Psimoulis and Stiros (2008) proposed this type of combination to identify dynamic characteristics of relatively rigid structures (model frequencies are up to 3-4 Hz) by simultaneous recordings of both GPS and RTS. In their study, dual frequency receivers were used with a sampling rate of 20 Hz while sampling rate of RTS was 10 Hz to supplement the missing data of GPS. The cross-correlation was used to resolve the phase difference between both independent records. The resulting time series were analysed to determine the amplitude and frequency of oscillation by implementing Spectral analysis. It was found that the noise seems to increase when frequency increased, and cycles were lost from RTS recordings in high frequencies. The precise quality of results obtained when getting higher amplitudes and lower model frequencies.

For high-frequency oscillations of civil engineering structures, Psimoulis and Stiros (2012) developed a computer-based algorithm that computes the mean amplitude of small scale. This algorithm is based on a peak-picking filter, which is a function of the oscillation frequency. This algorithm minimises the noise of high-frequency GPS and RTS recordings. The application of this method could be demonstrated in monitoring short-span bridges.

However, inconsistencies between GPS and accelerometer data (Psimoulis et al., 2015), and the main weaknesses of RTS, such as non-constant sampling rate (Stiros et al., 2008) or monitoring distance up to few hundred meters (Psimoulis and Stiros, 2013), reduce the applicability of integrating GPS with other sensors. Thus, the combination of GPS with other sensors cannot improve the achievable accuracy of GPS positioning which partly depends on the number of valid satellites and their geometry.

Pseudolite is another possibility to augment GPS signals and aiming to improve the satellite geometry (Dai et al., 2002). The pseudolites (i.e. pseudo-satellites) transmit signals from the ground, which can provide additional and continuous signals (pseudorange and carrier phase) to GPS users (Saka, 2008). Thus, the added signals contribute to improving the geometry and positional accuracy, especially in urban canyons and other applications with limited available satellites.

Barnes et al. (2003) have demonstrated that the positioning precision of the vertical GPS component can be improved by implementing pseudolites with GPS. They conducted a trial to monitor the Wilford suspension Bridge in Nottingham, UK. They reported that a sub-cm level of accuracy could be achieved in both horizontal and vertical positioning components by applying this integrated technique.

In the same context, a Locata is another terrestrial positioning technique that emerged from the concept of psedolite. This technique can be integrated with GPS to overcome the limitation of GNSS under challenging areas (i.e. urban canyons) and provide cm level accuracy (Bonenberg et al., 2011). Also, it can be used in the same difficult areas to solve the challenges of dense multipath (Montillet et al., 2009).

Meng et al. (2003) have also used pseudolite that integrated with GPS and accelerometer to develop a hybrid monitoring system that can be used to detect the bridge deflections. When they monitored the deformations at Wilford Bridge, they investigated the impact of GPS satellite geometry on the achieved derived precision. They demonstrated that a hybrid monitoring system was feasible to perform a millimetre 3D positioning precision.

Meng et al. (2004) have continued their study by analysed the 3D GPS positioning accuracies for monitored structure into horizontal and vertical directions. They have mentioned that installed pseudolite on the northern side can reduce the limitation of northing GPS component due to limited satellites in N-S direction for areas (φ>45°).

However, the location of pseudolite with respect to the antenna of GPS receiver can be critical, which required optimisation approach to achieve the aimed improvement. Furthermore, the selection of cut-off elevation angle can be a constraint in the location of pseudolite (Saka, 2008, Shan et al., 2013). In addition, the pseudolite transmitted signal has frequency similar to that of GNSS, which requires licences to use (Hancock et al., 2016).

2.5.1.2 Digital Signal Processing by Filtering Techniques

Another approach to reduce GPS limitations and improve its performance with more precise positioning is applying digital signal processing based on filtering techniques. Several types of filters can either be used to time series of GPS-only results or implemented to results of integrated GPS with another sensor (as discussed in the Section mentioned above).

In structural monitoring, the multipath noise could appear as a low-frequency movement (Dodson et al., 2001). Therefore, filtering techniques can be used to mitigate the multipath errors. Dodson et al. (2001) have investigated the adopting of spectrum analysis to detect the characteristics of multipath and applied an adaptive filter (AF) to mitigate the effect of multipath. They have analysed the results of Wilford footbridge monitoring and separated the real bridge deflections from multipath and receiver noise. Similarly, Roberts et al. (2002) have developed an adaptive filter to isolate the multipath effect from the derived contaminated GPS time series of detected displacement, which was also used by (Cosser et al., 2003, Cosser et al., 2004). Further studies were implemented an adaptive filter to mitigate the multipath effect in structural monitoring such as (Meng, 2002, Chan et al., 2005, Yu et al., 2014).

The wavelet transform filter can be used to decompose GPS positioning data and mitigate the noise errors, which leads to more accurate GPS data and estimation of frequencies (Mosavi and EmamGholipour, 2013). The more precise data is essential to obtain a correct interpretation of structure movement and reduce the events of false alarm (Ogaja et al., 2003).

Yu et al. (2006) have used wavelet analysis to eliminate the high-frequency noise in the results of dynamic GPS deformation data of bridge monitoring (bridge on the Yangtze River in Wuhan, China). They reported that the noise was effectively removed from the derived time series of bridge deformations with wavelet, and the frequency response was extracted (0.25 Hz).

Souza et al. (2009) have constructed a mathematical model based on Kalman Filter to eliminate most of GPS errors, and they applied wavelet technique to mitigate the multipath error.

Kaloop and Li (2011) have analysed the using of GPS observations, and wavelet transforms to study the movements and damage detection in cable-stayed Yonghe Bridge, China. They found that the GPS measurements with wavelet analysis were a reliable tool for damage detection technique. It has been proved that wavelet filtering is effective as de-noising procedure (Kaloop and Kim, 2016).

In GPS measurements, as the errors are cover up the required signals, the apparent displacement may not show the dynamic response. In this case, the de-noising of the derived displacement can lead to extract the dynamic movement. Moschas and Stiros (2011) have adopted a sequential filtering procedure with external constraints in each step. As explained in Fig. 2.8, they applied two steps to extract the final dynamic response of the stiff structure. They based on the supervised-learning

derived filter (from the high-pass filter), then used a Chebyshev band-pass filter. They assessed the validity of filtering in each step according to accelerometer records. From the resulting time series, they identify the dynamic characteristics.

Moving average is an ideal filter to reduce the long period noise of GPS measurements, which also preserve the whole trend of time series that represent the deflection in structural monitoring (Moschas and Stiros, 2015).

However, different filtering techniques may enhance the results; they might lead to excluding real signals that are essential to define the actual response of monitored structure or introduced biases in some cases (Psimoulis et al., 2008). Therefore, the alternative technique is a combined GNSS observation.

2.5.2 The Suggested Technique of Combined GNSS to Overcome GPS Limitations

The introduction of other Global Navigation Satellite Systems (GNSS) such as the Russian GLONASS, European Galileo and Chinese BeiDou provides an alternative and complementary solution to overcome GPS limitations and enhance the positioning solution. The combination of GPS with other GNSS constellations is contributed in improving satellite geometry because of increasing number of valid satellites (Truong and Ta, 2013, Yu and Gao, 2017, Abd Rabbou et al., 2017). This will contribute to improving positioning accuracy (Cai and Gao, 2013, Li et al., 2015a, Cai et al., 2015), reliability and availability solution for deformation monitoring. The derived GNSS data can be used to identify the permanent displacements of the structure and evaluate its dynamic response (Lepadatu and Tiberius, 2014).

A number of studies have generally shown that the contribution of combined GNSS constellations improves the positional accuracy and increase the rate of fixing ambiguity solution (Teunissen et al., 2014, Zhao et al., 2014). For example, according to Cai and Gao (2007), they have assessed the positional accuracy and reliability of integrated GPS and GLONASS observations in a combined solution. They have indicated that an improvement in the positional accuracy was achieved with combined GPS/GLONASS solution as compared with GPS-only positioning. This improvement was realised when satellite geometry improved. Grelier et al. (2007) demonstrated the geometry improvements with simulated results of combined GPS with BeiDou and/or Galileo.

Ong et al. (2009) have investigated the expected positional improvement when adding GLONASS measurements to GPS observations in a combined RTK solution. They indicated that the horizontal accuracy of single frequency combined solution was better than that achieved with the dual frequency of GPS-only solution (1 cm vs 2 cm RMS). In addition, the dual frequency combined solution

provided more accurate results than GPS-only with dual frequency. They also reported that the combined solution enhance the positioning availability in urban canyon areas.

While the BeiDou system was in its initial stage, Yang et al. (2011) conducted a simulation study to assess the contribution of the BeiDou constellation for both local and global positioning performance. The combined GPS/BDS results showing enhancement in the satellite visibility, the availability and the DOP values. They reported that GDOP and PDOP factors were improved by 50% when including BeiDou data to GPS observations.

For real data of GPS/BDS combination, He et al. (2014) have analysed the conducted data of RTK positioning at a short baseline of 8 km. They found a significant improvement of the combined solution in comparison with a GPS-only solution, which permitted enhance the fixing rate and reliability of ambiguity resolution. The improvement in positioning accuracy of RTK combined solution relative to individual GPS positioning was 23% and 4% with two trials of short baselines respectively.

Thus, since the signals of multi-GNSS became available, different studies have been conducted to analyse the performance of combined GPS and other GNSS constellation, which compared with a GPS-only solution to illustrate the expected positional improvements. The results of considerable studies can be addressed for both precise relative positioning as well as absolute precise point positioning (PPP). The presented results of combined GNSS positioning systems can be found in (Teunissen et al., 2014, Deng et al., 2014, Paziewski and Wielgosz, 2014, Tokura et al., 2014, Gao et al., 2016, Liu et al., 2016, Odolinski and Teunissen, 2016, Paziewski and Sieradzki, 2017, Paziewski et al., 2018) and others for relative positioning. Whereas the results of combined GNSS positioning for PPP were presented in (Anquela et al., 2013, Cai and Gao, 2013, Cai et al., 2015, Wang et al., 2015a).

However, there is a limited improvement can be realised when a sufficient number of GPS satellites with proper geometry are available (Alkan et al., 2015).

Although the combined GNSS has been applied in different positioning applications, there has been a limited number of studies using combined GNSS solution for structural monitoring. Therefore, the current study aims to investigate the improvements of combined GNSS to overcome the GPS limitations and enhance the positioning performance towards an efficient monitoring technique.

Chapter 3: An Overview of the Global Navigation Satellite Systems (GNSSs)

3. 1 Constellations of Multi-GNSS

Global Navigation Satellite System (GNSS) is the collective term for those navigation systems that providing positions by orbiting satellites (Groves, 2013). These systems include; GPS, GLONASS, Galileo and BeiDou. GPS and GLONASS received full attention in the past, and they are currently in full operation, while Galileo and BeiDou are still under development and would be expected to be fully global coverage/operation in 2020. This development of the GNSS constellations focuses, for example, on introducing additional frequencies along with increasing the number of operating satellites, improving instantaneous positioning and evaluating the reliability of the system (Wu et al., 2015, de Lacy et al., 2011).

Each GNSS system comprises three distinct segments: (i) Space segment, (ii) Operational Control segment and (iii) User segment. The space segment consists of a number of operating satellites, which broadcasting radio signals to the user. The control segment operates the system by a network of ground facilities that monitor the status and health of satellites, track the satellites in their orbits, and responsible for determining the required data of predicted ephemerides and clock corrections transmitted by the satellites. The users receive the transmitting signals from the satellites, thereby the ranges between the user's receiver and the simultaneously observed satellites can be determined to obtain the positioning. The position is calculated from recorded GNSS observations and broadcast data. In addition to the 3D Position, the GNSS technique can provide Velocity and Time information (PVT). For more details, the interested reader can refer to textbooks such as (Misra and Enge, 2006, Hofmann-Wellenhof et al., 2008) and (Xu and Xu, 2007).

3.1.1 The Global Positioning System (GPS)

The Global Positioning System (GPS) is a space-based radio navigation system developed by the U.S. Department of Defence. The first satellite of Block-I generation was launched in Feb. 22, 1978 and reached Full Operational Capability (FOC) in July 1995 (Kaplan and Hegarty, 2005, Hofmann-Wellenhof et al., 2008). Through the developments of the GPS, several sets of Blocks (i.e. Block II, IIA, IIR and so on) have been established over a few decades. The modernised GPS constellation has more satellites that broadcast newly improved signals with the more efficient transmission. However, the initial GPS constellation was designed to include 24 evenly distributed satellites across six orbital planes; the current constellation consists of 32 satellites (Su et al., 2018). The GPS uses a Medium Earth orbits (MEO), which are arranged in equally separated by 60° planes at the equator, and each orbital plane inclines 55° concerning the Earth's equator. The GPS satellites are placed in their orbits

at an altitude of 20,200 km. The nominal semi-major axis of GPS satellites' orbit is about 26,560 km from the centre of the Earth. One complete orbit takes about 11h 57min 28s or almost one-half of a sidereal day. Therefore after two rotations, each satellite rises roughly from the same original location, which means repeated geometry period, but approximately four minutes earlier than the day before (Bhatta, 2011). These satellites broadcast ranging signals and navigation data message to the users.

Even with more than 24 GPS satellites, the possibility of a limited number of satellites can occur at specific regions. Although the best coverage of the GPS constellation can be expected at mid-latitudes, the less coverage could be at the poles and higher latitudes due to the GPS design (Subirana et al., 2013).

Each GPS satellite transmits signals of data centred on two microwave frequencies: (L1=1575.42 MHz) and (L2=1227.60 MHz) in addition to the third frequency (L5=1176.45 MHz) transmitted by several satellites. Gao et al. (2009) mentioned that the first GPS satellite with L5 was launched in March 2009. As the value of the fundamental frequency is (f_o=10.23 MHz), therefore, the frequencies are derived by multiplying the fundamental frequency by 154, 120 and 115, respectively (Xu and Xu, 2007). The GPS uses Code Division Multiple Access (CDMA) technique with a unique code for every satellite to send different signals at the same frequency.

For time system, the GPS uses the GPS reference time (GPST), which is a continuous timescale to avoid leap seconds (T. Takasu, 2013). It is related to the atomic time system and is referenced to Universal Time Coordinated (UTC) as maintained by the U.S. Naval Observatory, UTC (USNO) that considered the 6th Jan 1980 the initial epoch of this system (Hofmann-Wellenhof et al., 2008). To define the positions, the GPS adopts the Word Geodetic System 1984 (WGS 84) as a reference coordinate system, in which the positions are represented in Cartesian components concerning ECEF (earth centred earth-fixed) system. The broadcast ephemerides and clocks parameters of GPS are given in navigation messages as Keplerian elements of the orbit and correction elements (Hofmann-Wellenhof et al., 2008, T. Takasu, 2013). Therefore, the GNSS receivers can decode, detect and process the signals received from satellites in order to produce the data which include the code, phase and Doppler observables (Xu and Xu, 2007).

3.1.2 GLONASS

GLONASS is the Russian counterpart of the American GPS that uses Frequency Division Multiple Access (FDMA) technology. In other words, each satellite transmits signals at a particular frequency within the band of the centre frequency. The first GLONASS satellite was launched on October 12, 1982, and then reached full operation in January 1996 (i.e. less than one year later than GPS). The GLONASS system consists of 21 satellites placed in three MEO orbital planes, with three on-orbit spare satellites (i.e. 24 satellites in total). An eight satellite will occupy each of the orbital planes,

which are separated by 120° and inclined at 64.8° to the equator (this criterion enables GLONASS to offer better coverage than GPS in higher latitudes areas)(Subirana et al., 2013).

The GLONASS satellites operate in nearly circular orbits with a radius of 25,510 km. This implies that the GLONASS orbit is lower than that of GPS by 1,100 km. Also, the nominal orbit of GLONASS is at an altitude of 19,100 km, and each satellite completes an orbit in 11h 15min 44s (Hofmann-Wellenhof et al., 2008). The repeated ground track of the same satellites required about eight sidereal days (i.e. a period of 17 orbits) to repeat the same geometry (Subirana et al., 2013).

Unlike the GPS, the GLONASS satellites transmit signals in the same code, but in a different range of sub-band frequencies of FDMA technique. At present, the GLONASS system transmits FDMA signals at two microwave L-band frequencies (denoted by G1 and G2), in addition to the third CDMA signals obtained from some of the existing modernised GLONASS satellites with the L3 band (denoted G3). In FDMA mode, each GLONASS satellite transmits on its own channel or sub-band, which can be derived using the expression (1602 + n × 0.5625 MHz for L1 band) and (1246 + n × 0. 4375 MHz for L2 band), where the channel number, n= -7, -6, -5… 5, 6 (Geng and Bock, 2016). Consequently, the sub-band of L1 spanning two sides of the nominal centre frequency of 1602.0 MHz, resulting range of frequencies from 1598.0625 to 1605.3750 MHz channelised with a spacing of (9/16 or 0.5626 MHz). While, the nominal centre frequency of L2 is 1246.0 MHz, and the sub-bands are ranged from 1242.9375 to 1248.6250 MHz, which are channelised with a spacing (7/16 or 0.4375 MHz).

Due to a limited number of frequencies (i.e. 14 frequency channels), every two satellites at antipodal slots (separated by 180°) in the same orbit transmit the same frequency. However, it is impossible to observe at a single station any pair of GLONASS satellites sharing the same frequency at the same time (Henkel and Kiam, 2013). This will enable the receiver to detect and separate the incoming GLONASS signals.

In comparison between GPS and GLONASS, the transmitted broadcast ephemerides and clock parameters in GPS is the Keplerian elements while the navigation message of GLONASS is transmitted as geocentric Cartesian coordinates and their derivations, velocity and acceleration of satellites in ECEF (PZ90.02) system (T. Takasu, 2013). In addition, the coordinate and time systems used in the GLONASS are different from that used with GPS. The GLONASS time is based on Universal Coordinated Time, Soviet Union (UTC-SU), which is a Russian national reference timescale and includes leap seconds (Lewandowski and Arias, 2011). The GPS, on the other hand, is based on GPST. For the reference coordinate system, the GLONASS uses the Earth Parameter System 1990 (PZ-90) which differs from WGS84 that used in GPS. For more details of characteristics of PZ-90, see (Kaplan and Hegarty, 2005).

3.1.3 Galileo

In parallel to GPS and GLONASS, the European Union (EU) and European Space Agency (ESA) have developed an independent GNSS of Galileo for civilian use. The development of Galileo took place in three phases. The first phase of Galileo system starts by launching two experimental satellites; (i) GIOVE-A: Galileo In-Orbit Validation Element (which was brought into orbit in December 2005) and (ii) GIOVE-B (which was launched on April 2008). For the second phase, a pair of operational satellites were placed in their orbit on October 2011, while the next couple launched on October 2012 and placed in the second orbit (Subirana et al., 2013). After the In-Orbit Validation (IOV) phase, the Galileo system moved forward to the deployment of the last stage with Full Operational Capability (FOC), which will be expected to be in 2020.

The full operating features of Galileo constellation will consist of 27 satellites and 3 inactive spares distributed in three MEO orbit planes, which are separated by 120° and inclined by an angle of 56° concerning the equator (Galileo-ICD, 2010). The nominal semi-major axis of Galileo orbit will be 29,600 km (3,000 km higher than GPS); the satellites are placed in their orbits with an altitude of 23,222 km above the Earth, which makes the orbital period Consequently, the repeated track with the same geometry will take about 10 days (Subirana et al., 2013).

The Galileo System Time (GST) is adapted to be the reference time scale of Galileo constellation. It starts at the epoch of 00:00:00 UTC on 22nd August 1999 as a continuous time scale that does not introduce any leap seconds (T. Takasu, 2013). The difference between the GST relative to GPST is defined as the Galileo-GPS Time Offset (GSTO) (Afifi and El-Rabbany, 2015). The coordinates are expressed in Galileo Terrestrial Reference Frame (GTRF), which designed to be compatible with the International Terrestrial Reference Frame (ITRF2008).

Galileo navigation signals are transmitted in four frequency bands denoted by E1, E5a, E5b, and E6 (besides to E5, which is sub-divided into E5a and E5b). The Galileo's E1 and E5a frequencies coincide with GPS' L1 and L5 respectively. Also, the signals transmitted in CDMA technique that permit interoperable with GPS. The Galileo ephemeris parameters are Keplerian-like orbital elements as in GPS ephemeris. Also, Galileo aimed to offer five different services to various users (Galileo-ICD, 2010).

3.1.4 BeiDou

The fourth system of the GNSS constellations is the Chinese Navigation Satellite System (CNSS) known as BeiDou (BDS), which is currently under development and intended to reach the full global operation by 2020 (CSNO, 2013a). When BeiDou becomes with an entire operation, it will consist of five Geostationary Earth Orbit (GEO) satellites, three Inclined Geosynchronous Satellite Orbit

(IGSO) satellites, and twenty-seven Medium Earth Orbit (MEO) satellites (CSNO, 2013b, Bhuiyan et al., 2014).

The construction of BeiDou system followed three stages, which are the initial demonstrated stage, the regional stage and eventually the Global coverage stage. The initial phase completed in 2003 relied on the first generation of BeiDou-I satellites (2 GEO with one backup satellite) (Grelier et al., 2007). Then, the regional stage was introduced with the launch of the first MEO satellite in April 2007, followed by a number of satellites placed in their orbits to provide local services with the generation of BeiDou-II (or Compass) (Yang et al., 2011, Montenbruck et al., 2013). The end of 2012 has completed the second stage (consisted of 5 GEO, 5 IGSO and 4 MEO satellites) (Li et al., 2014, He et al., 2014). Since the BeiDou system introduced the third stage of development strategy, additional satellites will be launched to its constellations that is foreseen to reach global operational capability until 2020.

In contrast to other GNSS constellations, the BeiDou system is consist of three orbit types implied three different sets of satellites as above stated (see Fig. 3.1). All GEO satellites are placed in a single Geosynchronous Equatorial Orbit by an altitude of 35,786 km and located at fixed longitudinal positions at 58.75°E, 80°E, 110.5°E, 140°E and 160°E, respectively (Yu and Gao, 2017). The altitude of the IGSO plane is as GEO plane of 35,786 km, while the inclination of IGSO is 55°, which is similar to that of MEO planes. The orbital period of IGSO is 23h 56min, which repeats the ground track shaped like a symmetric figure of eight shapes (CSNO, 2013a). The third set of MEO satellites are operating with an altitude of 21,528 Km in their orbits that incline with 55° to the equator and complete an orbital period of 12 h 53 min. After a period of 13 rotations, the same constellation is repeated within seven days (CSNO, 2013a).

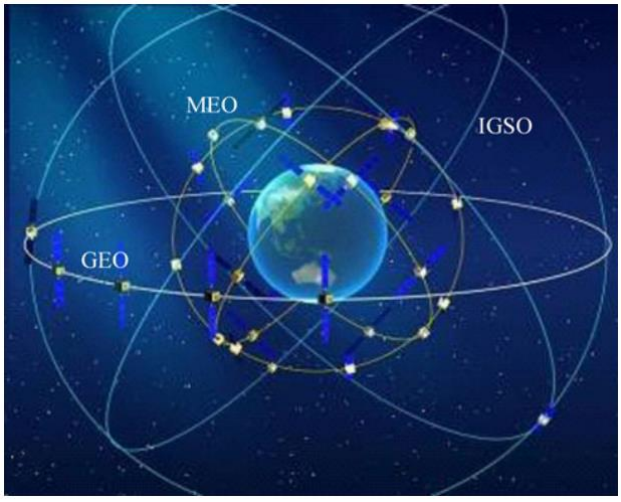


Fig. 3.1 BeiDou system with various orbit types (Shi et al., 2013)

The mixed orbits of BeiDou constellation structure can introduce a better observation geometry for positioning compared to the current GPS and GLONASS, and future Galileo, especially in China and the Asia-pacific regions. Referring to time, the BeiDou Navigation Satellite System Time (BDT) is used as the reference time, which is a continuous time scale without leap seconds. The reference epoch of BDT is starting at 00:00:00 UTC on 1st Jan 2006 to have zero second difference with UTC (T. Takasu, 2013). The coordinate reference system that used in BeiDou is the China Geodetic Coordinate System 2000 (CGCS2000) (Yang, 2009), which has the similar characteristics of Galileo reference system (Deng et al., 2014).

The BeiDou satellites broadcast navigation signals and messages within three frequency bands, which are B1:1561.098 MHz, B2:1207.14 MHz and B3:1268.52 MHz. The transmitted signals are based on Code Division Multiple Access (CDMA) technique similar to that of GPS and Galileo. In addition, the nature of broadcast ephemerides is also provided with Keplerian elements.

The BeiDou satellites broadcast navigation signals and messages within three frequency bands, which are B1:1561.098 MHz, B2:1207.14 MHz and B3:1268.52 MHz. The transmitted signals are based on Code Division Multiple Access (CDMA) technique similar to that of GPS and Galileo. In addition, the nature of broadcast ephemerides is also provided with Keplerian elements.

To summarise the characteristics of each GNSS constellation and the main differences between them, Table 3.1 presents such differences. Regarding full operational capacity, the Galileo and BeiDou are still under development and would be expected to be fully functioning in 2020.

Table 3.1 Comparison of the main characteristics of multi-GNSS implies GPS, GLONASS, Galileo and BeiDou.

Characteristic	GPS (G)	GLONASS (R)	Galileo (E)	BeiDou (C)
First launch	Feb. 22,1978	Oct. 12, 1982	Dec. 28, 2005	April, 2007 (MEO)
Full operational capability	July 17, 1995	Jan. 18, 1996	Expected 2020	Expected 2020
Signal separation	CDMA	FDMA	CDMA	CDMA
Number of satellites	32	24	Planned:27+ 3 active reserves	Planned:27 MEO +3 IGSO +5 GEO
Orbital planes	6	3	3	3 (MEO)
Orbit inclination	55°	64.8°	56°	55° for (MEO)
Semi-major axis of orbit	26,560 km	25,508 km	29,601 km	27,878 km (MEO)
Altitude of Satellites	20,200 km	19,100 km	23,222 km	21,528 km
Orbit plane separation	60°	120°	120°	120° (MEO)
Complete orbital period	11h 57min 28s	11h 15min 44s	14h 04min 45s	12h 53min (MEO)
Repeated same geometry	1 sidereal day	About 8 days	About 10 days	Within 7 days
Geodetic Reference	WGS-84	PZ-90.02	GTRF	CGCS2000
Time system	GPS time, UTC (USNO)	GLONASS time, UTC(SU)	Galileo System Time (GST)	BeiDou System Time (BDT)
Leap seconds	No	Yes	No	No
Broadcast Ephemerides	Keplerian elements, correction coeffic.	Satellite position, velocity, acceleration in ECEF system	Keplerian elements, correction coeffic.	Keplerian elements, correction coeffic.

In CDMA: Code is different for every satellite, while in FDMA: Frequency is different for every satellite, modified from (Hofmann-Wellenhof et al., 2008).

Regarding the frequency bands, each GNSS constellation has its frequency range, as illustrated numerically and graphically in Table 3.2 and Fig. 3.2, respectively. It is clear from Fig. 3.2 that, B1, L1 and E1 are sharing the same frequency band but with a different central frequency. In addition, an overlap in frequency might occur as in L2 and G2.

Table 3.2 Different central Frequencies of each GNSS constellation as encoding in RINEX 3.02 (Gurtner and Estey, 2013, IGS, 2015)

GNSS Const.	Details	Frequencies				
		1st	2nd	3rd	4th	5th
GPS (G)	Freq. Band/Freq. Observations.*	L1: 1575.42 C1, L1, D1, S1	L2: 1227.60 C2, L2, D2, S2	L5: 1176.45 C5, L5, D5,S5		
GLONASS (R)	Freq. Band/Freq. Observations.*	G1: 1602+k*9/16 C1, L1, D1, S1	G2: 1246+k*7/16 C2, L2, D2, S2	G3: 1202.025 C3,L3, D3, S3		
Galileo (E)	Freq. Band/Freq. Observations.*	E1:1575.42 C1, L1, D1, S1	E5a:1176.45 C5, L5, D5,S5	E5b: 1207.14 C7,L7, D7, S7	E5(E5a+E5b): 1191.795 C8,L8, D8, S8	E6: 1278.75 C6, L6…
BeiDou (C)	Freq. Band/Freq. Observations.*	B1:1561.098 C1, L1, D1, S1	B2:1207.14 C7,L7, D7, S7	B3:1268.52 C6,L6, D6, S6		

Observations.* which are Pseudo Range (C), Carrier Phase (L), Doppler (D) and Signal Strength (S).
For GLONASS k= -7…..+6, which is the satellite's frequency channel number.

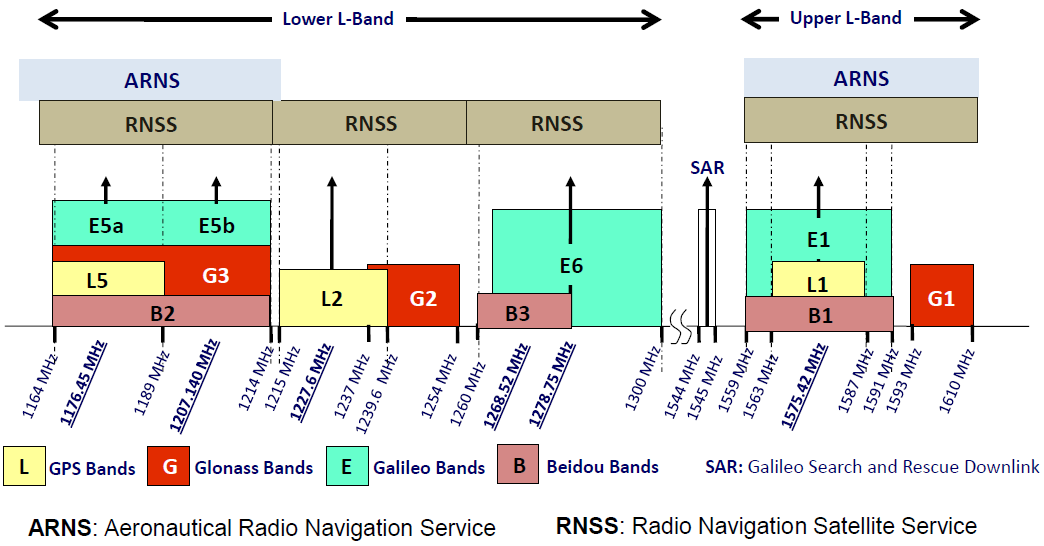


Fig. 3.2 Frequency bands for the four GNSS constellations (Subirana et al., 2013).

3. 2 GNSS Error Sources

The fundamental principle of GNSS positioning depends on the measured ranges between the antenna of GNSS receiver and a number of GNSS satellites, which in turn differentiate from differences between the times of transmitted and reception of GNSS signals. These ranges are

subjected to different effects that caused a number of random errors and systematic biases. Therefore, to achieve the required accurate positioning, it is necessary to identify the various error sources and implement the proper technique to reduce them or cancel out. As the transmitted signals broadcast from satellites to the user's receiver through an atmospheric propagation medium, it can be categorised the GNSS error sources into three main sets (as illustrated in Fig. 3.3), which implies the satellite-related errors, propagation medium and receiver related part, which will be discussed in the following sections.

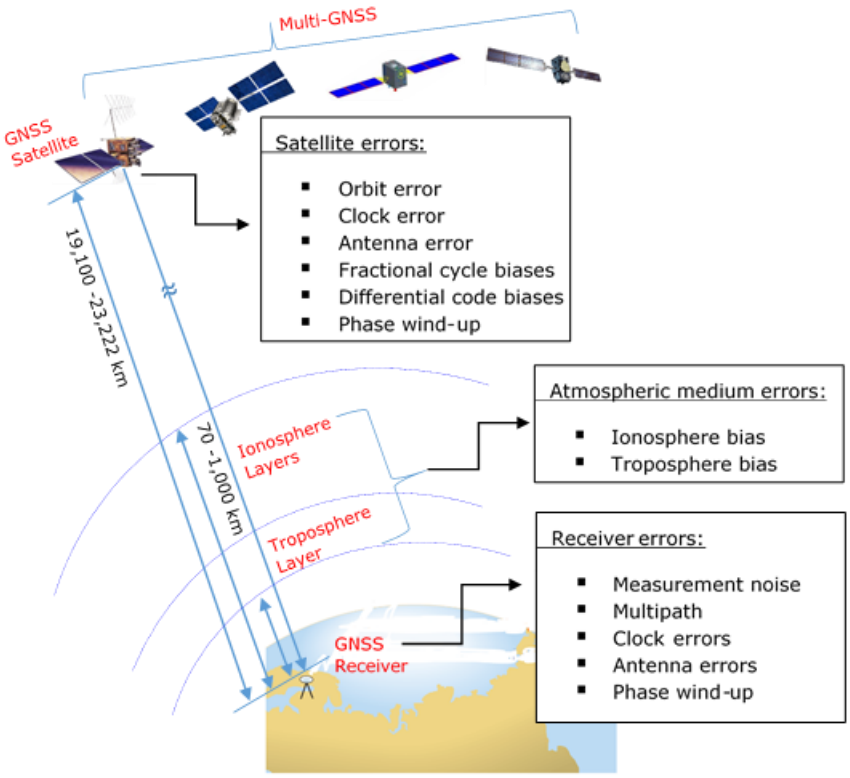


Fig. 3.3 Sketch of GNSS error sources

3.2.1 Satellite Orbit and Clock Errors

The GNSS ephemerides and clock corrections are calculated and predicted by the ground control segment, then uploaded to satellite constellations periodically to be delivered continuously as navigation messages to the users in real time. Therefore, the GNSS receiver can estimate the predicted satellite's position in real time from broadcast navigations. Thus, the deviation between the predicted and the actual pre-calculated position of satellite represents the satellite position error, which has an impact on the accuracy of the derived solution. The satellite position differences are defined relative to the satellite orbit in three orthogonal components, which are radial, cross-track and along-track components (Nicolini and Caporali, 2018).

Based on the global network of receivers, the information of satellite orbit and clock corrections can be estimated and distributed by the provider (e.g. the International GNSS Services IGS or others) to the users with different levels of accuracy (Dow et al., 2009). For example, the IGS determines the satellite positions in orbit for every 15 min; thereby the location of the satellite at transmission time can be determined by interpolation.

As above mentioned in Section 3.1, that the navigation message for each GNSS constellation of GPS, Galileo and BeiDou are given in Keplerian orbit elements and clock correction parameters. Based on these broadcast parameters, three elements can be calculated which are (i) satellite position in ECEF system, which represent the antenna phase centre position of the satellite, (ii) the satellite clock bias and (iii) the clock drift. In contrast to other GNSS, the navigation message of the GLONASS system is broadcast the satellite position, velocity and acceleration in EFEC of PZ90.02.

Recently, the quality of GNSS broadcast ephemerides of orbit and clock products have been improved with the developing of new generations of GNSS constellations and their new signals, especially with remarkable progress with GPS and GLONASS observations (Montenbruck et al., 2015, Griggs et al., 2015). This is reflected in increasing the ground monitoring stations of control segment by established newly sites that provide better global distribution, in addition, to increasing the frequently updated information along the day (Montenbruck et al., 2017). Furthermore, to enhance the accurate position of satellites at the time of signal emission, the broadcast corrections from Satellite Based Augmentation Systems (SBASs) in geostationary orbits such as (WAAS and EGNOS) can be used along with the navigation ephemerides to reduce the measurement errors.

The other parameter is the satellite clock bias, which defined as the difference between the in-satellite clock and the reference GNSS time-scale, due to clock synchronisation errors. The corrections of satellite clock are given in the form of polynomial coefficients related to reference epoch (t_o) in the broadcast navigation message, which can be expressed in clock model as (Qing et al., 2017):

$$\delta t^s = a_o + a_1(t - t_o) + a_2(t - t_o)^2 \qquad (3.1)$$

where a_o, a_1 and a_2 are the polynomial coefficients describing the clock phase offset, frequency offset (drift) and linear frequency drift (drift rate) respectively.

In CDMA systems (i.e. GPS, Galileo and BeiDou), the coefficients of second order polynomial are given with a_o, a_1 and a_2 . For GLONASS only considered a first order polynomial, which including the clock offset (a_o=-τ_n) and the relative frequency offset (a_1=γ_n) (Subirana et al., 2013, T. Takasu, 2013). However, the broadcast time transmitted by satellite will be with the order of nanoseconds, while the satellite clocks of precise GPS and GLONASS constellations are within 0.1 ns or less (i.e. the error of 1 ns can caused error range of 30 cm). For more details about the precise orbits and clocks verification see (Hadas and Bosy, 2015).

When comparing the broadcast ephemerides with the precise orbit (final orbit) and clock products provided by IGS for all available GNSS constellations, Montenbruck et al. (2015) assessed the accuracy of broadcast ephemerides by analysing the signal-in-space ranging errors (SISREs) for data of one year period with a near-global receiver network. They found the global average of SISRE values for every GNSS constellation to be (0.7 ± 0.02 m for GPS), (1.5 ± 0.10 m for BDS), (1.6 ± 0.30 m for Galileo) and (1.9 ± 0.10 m for GLONASS). These results reflect the progress and development of the modernised performance of GNSS constellations.

- **Other Satellite-Receiver Errors**

In addition to above-discussed errors that related to satellite effect, other errors need to consider into account to provide precise positioning. The satellite's antenna is identified with two variables to express the antenna phase centre errors contain a satellite Phase Centre Offset (PCO) and satellite Phase centre Variation (PCV) (IGS, 2015). The PCO represents the offset between the phase centre of GNSS satellite and their centre of mass, while PCV term related to variation dependent upon the direction between the satellite and the relative station include the azimuth and nadir angles (T. Takasu, 2013). Both PCOs and PCVs are corrected by the IGS08 absolute antenna model (Guo et al., 2017), which also provided the ANTEX file by IGS (international GNSS service).

Similarly, at the receiver side, The incoming GNSS signal is received at a specific point of the antenna phase centre, an error of antenna *phase centre offset* ($\boldsymbol{d}_{r,pco}$) can be produced when the antenna phase centre does not coincide with the geometric centre of the antenna. The magnitude of this error is depend on the antenna type.

The Fractional Cycle Bias (FCB) errors are mainly related to satellite and receiver hardware biases over a network of reference stations, which affected fixing the ambiguity resolution in Precise Point Positioning (PPP) (Geng and Bock, 2016). However, for precise relative positioning, the FCBs are cancelled by double differencing (Ge et al., 2008). In PPP solution, the FCB is well defined with CDMA signals, while it is complicated with GLONASS FDMA signals (Geng and Li, 2016).

The antenna phase wind-up is another error caused by the relative rotational motion between the satellite and the receiver antenna that created a change in phase measurements (Dilssner et al., 2011). Most of these errors are significant for PPP applications or precise global network adjustments. Therefore the detailed discussion of these effects is beyond the scope of this study.

3.2.2 Atmospheric Errors

The GNSS signals from a satellite to a receiver propagate with the constant speed of light in a vacuum passing different atmospheric layers that affect the velocity of propagated signals (speed and direction). Due to the variation in physical properties of these layers of gases, the atmosphere refracts

the GNSS signals through the *ionosphere* of charged particles and at the neutral atmosphere with water vapour of the *troposphere*. In signal path, the ionosphere represents the upper part of Earth's atmosphere that affects the characteristics of GNSS signals, while the troposphere is the lower layer that influences the GNSS signals. As above mentioned that the GNSS positioning depends on range measurements that derived from accurate transit time with constant speed, thereby the velocity of propagated GNSS signals will be changed at the atmospheric part. This consequently introduces systematic errors (biases) in GNSS measurements due to the effects of the non-homogenous physical medium.

3.2.2.1 Ionospheric Bias

The ionosphere is the upper part of the atmosphere's region that situated between 70 and 1,000 km above the Earth's surface. This region of the dispersive medium consists of ionised particles that affect the GNSS signals in frequency dependent and cause a significant range error. Solar radiation causes the ionisation when ultraviolet and x-ray radiation emitted from the sun interact with the gas molecules resulting in free negatively charged electrons and positively charged particles (Kaplan and Hegarty, 2005).

The behaviour of the propagated GNSS signal through the ionospheric medium depends on the refraction index (n) of that medium, which defined as a proportional ratio of speed of light in the vacuum (c) to the speed of light in that medium (v) as expressed in equation (3.2) (Subirana et al., 2013).

$$n = c/v \tag{3.2}$$

When the propagated GNSS signals passing the dispersive medium of the ionosphere, the change in velocities of these signals will differ according to observables type measurements. For the code pseudorange measurements, the ionosphere delays the signal propagating velocity from the speed of light in a vacuum (group delay); while the velocity of propagated signal advances in the carrier-phase measurements (phase advancement). These effects resulting from two refractive indices n_p and n_g, for carrier-phase and code measurements, respectively, which can be represented by (Kaplan and Hegarty, 2005):

$$n_p = 1 + \frac{I_1}{f^2} + \frac{I_2}{f^3} + \frac{I_3}{f^4} + \cdots_. \tag{3.3}$$

$$n_g = 1 - \frac{I_1}{f^2} - \frac{I_2}{f^3} - \frac{I_3}{f^4} + \cdots_. \tag{3.4}$$

Where the coefficients I_1, I_2 and I_3 are a function of electron density (N_e) along the range path of transmitting signal from the satellite to user receiver, where f is the frequency of transmitted GNSS

signal. It is clear that the two factors (i.e. electron density (N_e) and the frequency of the GNSS signals) affected the magnitude of ionospheric delay. In addition, I_1 represents the first-order ionospheric effect, while I_2 and I_3 are the second and third order ionospheric effect, respectively.

By taking the first-order term, it can compute the approximate index of the ionosphere by the following expression (Hofmann-Wellenhof et al., 2008)

$$n_p \approx 1 + \frac{40.3}{f^2} . N_e \tag{3.5}$$

$$n_g \approx 1 - \frac{40.3}{f^2} . N_e \tag{3.6}$$

N_e is the local electron density and given in units of electrons per cubic metre (e^-/m^3)

From definition in equation (3.2), and the approximate value of refraction index in equations (3.5) and (3.6), it can compute the velocity of the propagated signal in the ionosphere medium as:

$$n = \frac{c}{v} \quad then \quad v_p = \frac{c}{1 + \frac{40.3}{f^2} * N_e} = c.(1 + \frac{40.3}{f^2} * N_e)^{-1} \tag{3.7}$$

$$n = \frac{c}{v} \quad then \quad v_g = \frac{c}{1 - \frac{40.3}{f^2} * N_e} = c.(1 - \frac{40.3}{f^2} * N_e)^{-1} \tag{3.8}$$

From equations (3.7) and (3.8), it has been proven that the phase velocity of the propagated signal v_p in ionosphere medium is exceeding to be faster than the speed of light in vacuum, whereas the code velocity v_g of the code measurements slows down by the same amount. Consequently, the satellite-receiver distance of carrier-phase will be shorter than the actual distance, while the vice versa manner will be with the code distance.

Hence, it is possible to estimate the ionospheric bias from phase advance (I_p) or code delay (I_g), which are in the same amount with opposite signs. By taking the integration of the excess phase velocity over time and its variation along the signal transmitting path, which can be given in metres by (Kaplan and Hegarty, 2005):

$$I_p = -\frac{40.3 * c}{f^2} * \int_{path} N_e \; ds = \; -\frac{40.3 * TEC}{f^2} \tag{3.9}$$

where TEC denotes the Total Electron Content. The TEC referred to the number of free electrons (electron density) contained in a unit area (1 m^2) normal to the path of the GNSS signals under consideration. It is used to calculate the effect of the ionosphere on these signals and expressed in units of electrons per square metre (e^-/m^2) or TEC units (TECU) that equal to $10^{16}\, e^-/m^2$.

The TEC is affected by the solar activity, diurnal and seasonal variations, and the earth magnetic field (Hofmann-Wellenhof et al., 2008) along with the user location and satellite elevation angle.

From above equation 3.9, it can define the following characteristics of the ionospheric bias:

It is determined from the first-order ionospheric term, which represents 99.9% of the total ionospheric delay (Yang et al., 2016).

The ionospheric bias is in direct proportional to the number of free electrons (TEC), and it is proportional to the inverse of the squared frequency. Therefore, the ionosphere less affects the GNSS signals of high frequencies. For the same reason, the L2 has more delay than L1.

It will be in a negative value for carrier-phase measurements.

It will be expected a large ionospheric delay for low elevated satellites, due to crossing long distances. Typically the magnitude of delay ranging between 1 to 50 m (Kedar et al., 2003), which can reach more than 150 m for periods of extreme solar activity (i.e. midday and near the horizon)

For single frequency users, the ionosphere delay can be reduced by applying an ionospheric delay model (e.g. Klobuchar ionospheric model (Klobuchar, 1987, de Ponte Müller et al., 2013). This model can reduce 50-60 % of the ionospheric delay (Paziewski et al., 2013). To calculate the ionospheric path delay, the broadcast navigation data of GNSS constellations contain the Klobuchar ionospheric model parameters that can be formulated (e.g. for GPS and QZSS (T. Takasu, 2013), as well as for BeiDou (Bhuiyan et al., 2014)). In addition to corrections for the ionospheric delay that broadcast by SBAS data.

The ionospheric bias can be eliminated substantially in the GNSS signal measurements when applying dual-frequencies and form a linear combination (LC) of ionosphere-free (IF) in data processing for the same receiver at the same station. This could be valid for both the code and carrier phase measurements (Dach et al., 2007).

For example, when using observables of dual frequencies f_1 and f_2 belonging to any GNSS system, it can be formed ionosphere-free observables of frequency f_3 as given by (T. Takasu, 2013):

$$P_{r,3}^{s} = C_1 P_{r,1}^{s} + C_2 P_{r,2}^{s} \tag{3.10}$$

$$\Phi_{r,3}^{s} = C_1 \Phi_{r,1}^{s} + C_2 \Phi_{r,2}^{s} \tag{3.11}$$

$$C_1 = \frac{f_1^2}{f_1^2 - f_2^2} \quad , \quad C_2 = \frac{-f_2^2}{f_1^2 - f_2^2} \tag{3.12}$$

Where $P_{r,1}^{s}$, $P_{r,2}^{s}$ are the pseudorange observables for f_1 and f_2 ,respecti vely.

$\Phi_{r,1}^{s}$, $\Phi_{r,2}^{s}$ denote the carrier-phase observables for f_1 and f_2 , respectively.

$P^s_{r,3}$, $\Phi^s_{r,3}$ are pseudorange and carrier-phase of ionosphere-free, respectively.

C_1, C_2 are coefficient of the linear combination (LC) of ionosphere-free.

Since the system is represented by a first order system, approximately 99.9% of the ionosphere effects can be reduced by applying the ionosphere-free model (equations 3.10 to 3.12). (Hofmann-Wellenhof et al., 2008). Although the ionosphere-free model eliminates the ionospheric bias, it magnifies the noise level.

The utilisation of triple frequencies of GNSS measurements can mitigate the first and second order ionospheric delays by forming a linear combination of triple frequency in data processing (Hoque and Jakowski, 2008) and also contribute in cycle-slip detection.

3.2.2.2 Tropospheric Delay

In GNSS aspects, the lowest part of Earth's neutral atmosphere is commonly referred to as the *troposphere*, which is a non-dispersive region (non-ionised and frequency independent medium). The troposphere is extended between Earth's surface and an altitude of about 60 km (Subirana et al., 2013). The travelled GNSS signals along satellite-receiver distance will be subjected to the tropospheric delay. Therefore, the speed of the propagated signals in the troposphere becomes lower than that in a vacuum. This effect caused an excess in the observed length of satellite-receiver range and resulting in a range error in the same magnitude of delay for both code and carrier-phase measurements. The effect of the tropospheric delay is considered to comprising two components:

(i) The *hydrostatic* (dry) delay component, which represents about 90% of tropospheric delay at any given site that caused by the majority of dry neutral gases. The dry component can be modelled accurately by predicted models such as Saastamoinen, Hopfield and other models (Misra and Enge, 2006). For satellite at zenith and the user at sea level, the magnitude of the tropospheric delay is about 2.3 to 2.4 m, which increases with the increase of zenith angle to track satellite to be within 25 m for a satellite at about 5° elevation angle (Kaplan and Hegarty, 2005).

(ii) The wet delay component that contributes about 10% of tropospheric delay that mainly caused by the atmospheric water vapour. Unlike the dry delay, it is not easy to model the wet delay due to the variation in the density of water vapour and its dynamic distribution (Rohm et al., 2014). The magnitude of this delay varies from few mm in the polar region to 40 cm in the tropical region estimated at zenith direction (Zheng et al., 2018).

The Total Zenith Delay (TZD) is computed as a sum of a common effect of both hydrostatic and wet delays at the local zenith direction. The GNSS signals from low elevated satellites take a longer path through troposphere than those of high elevation angle. Consequently, the troposphere delay is minimised at the user's zenith and maximised near horizon (Xia et al., 2013). Thus, the elevation

angle of the observed satellite plays a fundamental role on the magnitude of tropospheric delay when the GNSS signal penetrates the troposphere. To describe how the oblique (slant) troposphere delay differs concerning satellite elevation angle; a mathematical expression of a mapping function can be used (i.e. to convert a zenith delay into slant path delay). Different formulations are expressing the mapping functions that achieve the tropospheric delay, which is beyond the scope of this study. For example, a separate mapping function for dry and wet delays are given in (Misra and Enge, 2006) or (Xu and Xu, 2007). It can be noted that either a proper mapping function can be used in modelling of ionosphere or troposphere delays, due to both delay effects are dependent upon the elevation angle of observed satellites.

- **Tropospheric Delay Modelling**

A number of tropospheric delay models have been proposed, which are different in the assumptions made on the refractivity profiles of zenith direction and the mapping functions. They can classify into two main groups (Subirana et al., 2013): geodetic oriented (i.e. Saastamoinen, Hopfield and others) and navigation oriented. Although the geodetic models are more accurate, they are more complex and required surface metrological data. Therefore, the achieved accuracy is affected by the quality of metrological data. In contrast, the navigation models are not needed metrological data that provide less accurate results.

The simplest and most common model for the tropospheric delay is the Saastamoinen model, which have been used in this study to investigate the tropospheric effect in structural monitoring (see Section 6.4). Therefore, the details of this model are given here to be an example of tropospheric models.

The assumption of Saastamoinen model depends on the change in refractivity from gas laws regarding the change in pressure, temperature and humidity with height (Hofmann-Wellenhof et al., 2008). The metrological data can be applied in the standard model from the nominal set or can be obtained from actual surface measurements. As the RTKLIB is the main tool for processing in this study, thereby the mathematical expressions of this software are used here.

The standard atmospheric model can be expressed as (T. Takasu, 2013):

$$P = 1013.25 * (1 - 2.2557 * 10^{-5} h)^{5.2568} \tag{3.13}$$

$$T = 15.0 - 6.5 * 10^{-3} h + 273.15 \tag{3.14}$$

$$e = 6.108 * exp\left\{\frac{17.15T - 4684.0}{T - 38.45}\right\} * \frac{h_{rel}}{100} \tag{3.15}$$

where P is the total pressure (in hectopascal units (hPa)), T is the absolute temperature (in Kelvin (K)), h is the geodetic height above Mean Sea Level (MSL), e is the partial pressure (hPa) of water vapour and h_{rel} is the relative humidity.

The *Saastamoinen model* to calculate the tropospheric delay T_r^s (in m.) can be expressed with P, T and e derived from the standard atmosphere as (T. Takasu, 2013):

$$T_r^s = \frac{0.002277}{\cos z}\left\{P + \left(\frac{1255}{T} + 0.05\right)e - tan^2 z\right\} \tag{3.16}$$

where z is the zenith angle in (rad) as ($z = \frac{\pi}{2} - El_r^s$), El_r^s is the satellite angle between the line of sight (receiver-to-satellite) and the receiver local horizon. In addition, there is also an expression of a *modified Saastamoinen model* T_r^{s*}(Xu and Xu, 2007) by adding corrections of B that depend on the height of the station (H) and δR term based on z to be:

$$T_r^{s*} = \frac{0.002277}{\cos z}\left\{P + \left(\frac{1255}{T} + 0.05\right)e - Btan^2 z\right\} + \delta R \tag{3.17}$$

Eventually, the tropospheric delay errors have to be taken into account for most GNSS measurements, which mainly affects the height component of the solution (Xia et al., 2013).

3.2.3 Receiver and Site Dependent Errors

The GNSS measurements obtained by the geodetic receiver are subjected to errors due to the imperfection of a receiver and the connected antenna, in addition to the multipath effect that produced by the site environment where the receiver antenna is located. Practically, the most inherent errors that affected GNSS measurements are the receiver's noise and the multipath effect. Furthermore, receiver clock offset, the antenna phase centre offset, variation inherent inter-channel biases, and phase wind-up can also be considered as relatively minor GNSS errors. Moreover, for some applications that required more precise positioning, additional corrections should be applied, which are related to site displacement errors that including ocean loading, solid earth tides and polar tides. (Banville and Langley, 2010)

3.2.3.1 Receiver Measurement Noise

The GNSS receivers cannot measure the code and carrier-phase measurements correctly with infinite precision (Langley, 1997) due to the imperfection of these devices. In other words, the receiver could not follow the changes that might occur in signals/waveforms in a perfect way in which there are considerable delays and distortions at each epoch (Misra and Enge, 2006). This will introduce a certain level of random noise in addition to other error sources that affect the precision of these measurements. Although the major cause of the noise error comes from the receiver itself, other error sources (such as connected antenna and cables) also exist.

After the reception of incoming GNSS signal and acquisition at the antenna receiver front end, the sensed signal is converted from analogue to digital form by the AD converter. The signal processor in the receiver is responsible for generating the code and carrier replica signals and performing the necessary correlations, in addition to time synchronisation and other functions. Therefore, the GNSS receiver provides the pseudorange measurements as an output of code tracking loop that entitled the Delay Lock Loop (DLL), while the carrier-phase observations are obtained from the tracking loop called Phase lock loop (PLL) (Aquino et al., 2009). The DLL continuously adjusts the alignment between the local replica code and the received satellite signal, and try to reduce the estimation error of the delay between them (Hofmann-Wellenhof et al., 2008, Tran et al., 2018). In addition, the PLL tracking aims to match the phase of the incoming carrier with the locally generated carrier. Thus, the receiver noise error is the result of delay and distortion in GNSS tracking loop. The source of this noise is typically thermal noise jitter, and in some cases occurred from radio interference (Kaplan and Hegarty, 2005).

The noise error is influenced by different factors that are varying from receiver to another depending on receiver design and its performance. These factors include the signal strength, the antenna design and the adopting method to convert the GNSS signal from analogue-to-digital form, the characteristics of the receiver detector and correlation process. This makes the randomly fluctuating noise from GNSS measurements to be independent for each receiver and each signal, which is inevitable and cannot be cancelled by differential techniques (Subirana et al., 2013). Therefore, each receiver is characterised by a specific type of noise called "*self-noise*" (Moschas and Stiros, 2013).

The tracking of GNSS signals represents the primary factor in determining the position of the receiver (i.e. receiver's antenna) and other parameters (e.g. user time and velocity), which are contaminated by noise with a certain level of accuracy. When estimating the position and by applying a proper technique in processing (i.e. Kalman filter or Least Squares), the noise level could be reduced to achieve highly accurate positioning. It is worth mentioning that the precision of the pseudorange and carrier-phase measurements can be specified by either carrier-to-noise density ratio (C/N_o) or signal-to-noise ratio (SNR). These parameters are used to measure the receiver signal tracking performance.

The noise level of code measurements is expected to be much higher than that of the phase measurements. Therefore, the noise level of code measurements can be reduced by combining the code and carrier-phase measurements in carrier smoothing with no cycle slips (Xu and Xu, 2007). A detailed discussion of smoothing is beyond the scope of this study. However, for more details see for example (Amiri-Simkooei and Tiberius, 2007) and (Zhang et al., 2017).

The modernisation of GNSS constellations with new signal structure leads to the development of GNSS receivers with a lower noise level to meet the user requirements (Borio, May 2017). The common assumption is to consider the receiver noise to be white noise and Gaussian in data

processing, which means the noise is not correlated with time from epoch to another. White noise can be measured efficiently by zero baseline test. In addition, to evaluate the noise level with different receivers among various GNSS solutions, the most precise way is to perform zero baseline test, which will be analysed in more details in Chapter 4. In zero baseline, a single antenna is connected to splitter via cables into two or more GNSS receivers, to evaluate the noise level as well as to identify the receiver performance and assess the effect of receiver noise on the precision of different GNSS solutions. Ideally, the utilising of a single antenna with Double-Difference approach should lead to the solution of zero length. However, the detected time series could show some differences/fluctuations indicating the existence of noise in the system.

Short baseline test can also be used to evaluate the actual field performance of GNSS positioning to account the noise components. In this test, the derived residuals might contain multipath errors, in addition to positioning noise. Moschas and Stiros (2013) reported that the spectra of noisy records could be characterised by coloured noise in low-frequency bands (<0.2 Hz) for the duration of short recording, as well as white noise at a higher frequency. However, the long duration of GNSS records could be free from coloured noise, which will be useful to study the dynamic effects of structural monitoring (Moschasa and Stiros, 2012). For these applications, it is expected that the noise increases with increasing excitation frequency (Psimoulis et al., 2008).

One of the remarkable developments in GNSS receivers is increasing its ability to record with high sampling rate, e.g. 100Hz (Haberling et al., 2015). Analysing the behaviour of noise with the higher sampling rate, for example, Moschas and Stiros (2014b) found that with increasing PLL bandwidth, the observation noise level of GPS-only measurements is also increased.

3.2.3.2 Multipath

Multipath occurs when a signal from a specific satellite arrives an antenna via two or more paths. This might, but not need to, include a direct signal (line of sight). The indirect path is introduced when the satellite transmitted signal diffracted and reflected by a specific obstacle (i.e. reflecting the structure, water surface, and ground) in the site where the antenna is located. Thus the antenna receives both direct and indirect signals from the same satellite. The reflected signal is usually delayed, attenuated and takes a longer path. Consequently, the interference by different arrival paths of direct and reflected signals is generated, which increase the effective noise and reduced the signal strength (C/N_o) (Kaplan and Hegarty, 2005). It is worth mentioning that the obstacle sometimes might block the direct path of the signal and the antenna receives the only weak reflected signal, this caused poor GNSS positioning of None-line-of-sight (NLOS) (Groves et al., 2013).

The multipath error depends on signal frequency and structure that affects both the code and carrier-phase measurements, which degrades the accuracy of GNSS positioning. Therefore, the multipath effect is a limiting factor to achieve high-precision positioning. For code measurements, the

multipath error can be in the order of meters, while the theoretical maximum value for carrier-phase measurements can be within a quarter of the wavelength, which means about 5 cm for L1 or L2 of GPS signals. However, in the relative positioning of short baseline, multipath affects carrier-phase measurements typically within 1 cm error with proper satellite geometry (Hofmann-Wellenhof et al., 2008).

The magnitude of multipath in any GNSS measurements depends upon the reflecting environment surrounding the GNSS antenna, the type of antenna used and its gain pattern, the receiver hardware and firmware as well as the satellite/antenna geometry and signal characteristics (Su et al., 2018). The more effective factor in geometry is the satellite elevation angle, where most reflected signals are received from low elevated satellites, which are more vulnerable to multipath.

Due to different causes of multipath (i.e. surrounding antenna, low elevation satellite, SNR and design of antenna and receiver), it is difficult to model them at the same time (Wang et al., 2016). Notwithstanding the multipath cannot be removed by differencing observations or adopting the model, but it would be possible to detect and mitigate its effect.

Different techniques can be used to mitigate multipath effect such as; (i) antenna-based mitigation, (ii) the hardware of receiver or (ii) processing techniques (Ray et al., 1999). For antenna design, a choke-ring antenna can be used to mitigate the multipath near or below the horizon of the antenna station (Ray et al., 1999). By adopting a specific receiver structure with hardware correlator technique, it is possible to limit the multipath (e.g. Narrow correlator, MEDLL approach and others) (Irsigler, 2010). Regarding processing, the multipath can be reduced by digital filtering using wavelet analysis (Satirapod and Rizos, 2005), Kalman filtering or other filters (Dong et al., 2016). Although different methods have been developed to mitigate multipath, they are still limited and not ideal (Su et al., 2018).

In precise static GNSS positioning, the observation times are relatively long; the interrupted short periods of contaminated multipath may not affect the results. However, in a kinematic positioning, the multipath is affected by the stability of the reflecting surface. When the diffracted signal received from moving reflecting surface (e.g. passing vehicle) that caused randomisation of high-frequency multipath that takes few seconds, up to 2-3 min (Ogaja and Satirapod, 2007), this can be identified as dynamic multipath (Moschas et al., 2013). The dynamic multipath is dependent upon the geometry of satellites (Moschas and Stiros, 2014a). However, the stationary antenna received contaminated multipath signals from the stable reflecting surface leads to a very slow frequency fluctuation that characterises the multipath error. For example, in bridge structural monitoring (i.e. as in the current study), the multipath occurred from gradual changes in the satellite geometry is characterised by frequencies <0.05 Hz (Moschas and Stiros, 2014a).

In modernisation of GNSS signal structure to reduce the multipath effect, the GPS signal transmitted from L5 has higher power than that of L2 with a greater bandwidth which in turns, contributes to improving multipath resistance. For Galileo, new modulation process called Alternate Binary Offset Carrier Modulation (AltBOC) and Multi Binary Offset Carrier Modulation (MBOC) have been used to enable better distribution of the signal over the bandwidth. This can be achieved by modulating E5a and E5b onto a single E5, which reduce the influence of multipath and tracking noise signal (Subirana et al., 2013, Guo et al., 2017).

In severe cases of multipath such as urban canyons environment, highly reflective surfaces can cause loss of lock or prevent fixing the ambiguity resolution, particularly when the single independent GNSS constellation is implemented. For this reason, there is a real need to observe satellites using multi-GNSS constellations, not to improving the availability only but also to improve the accuracy (Truong and Ta, 2013).

3.2.4 Other GNSS Errors (Satellite and Receiver Hardware)

In GNSS positioning, the limitations in satellite and receiver hardware lead to biases. These biases are introduced when the delay occurred between two events that supposed to be instantaneous in an ideal situation. For instance, the timing delay between L1 and L2 of dual frequency transmission produces bias originating in the satellite. In addition, the receiver should receive the two signals instantaneously, however, due to the bias error, there will be a delay in receiving signals. Such biases have an impact on the derived position and would affect other calculated quantities (Hakansson et al., 2017).

The imperfect synchronise between transmission of different signals through the satellite hardware to the satellite antenna might produce this delay, which can be related to satellite code bias or satellite phase bias depending on their observables (Kaplan and Hegarty, 2005).

In the same manner, the delay could occur in the travelling signal between the antenna and the receiver hardware, which, in turns, caused the *receiver code bias* and the *receiver phase bias*. This delay will be the same for all signals simultaneously received from different satellites; therefore, these biases could be eliminated in relative positioning.

For GLONASS with FDMA approach, each received signal from a specific satellite has its unique frequency that processed differently in the receiver channels and causing different delays in the receiver according to different frequencies (Hakansson et al., 2017). Because of each signal received from GLONASS has its frequency dependent-delay, an additional error might be introduced (i.e. the clock errors which are scaled by different frequencies). This error is known as GLONASS *inter-frequency biases* that relate to both code and carrier-phase observables, which depend on the firmware of receiver type and antenna used (Reussner and Wanninger, 2011). Unlike the carrier-

phase inter-frequency bias that can be modelled in a linear function, the code inter-frequency biases are a non-linear character and more challenging to handle (ibid). The Carrier-phase inter-frequency biases are very similar (identical) on homogenous receivers (i.e. for the same type or the same manufacturer), which cancelled out in relative positioning (Wanninger, 2012). On the other hand, it is complicated to fixing the integer ambiguity resolution for heterogeneous receivers of different types (Wanninger, 2012, Al-Shaery et al., 2013). For more details of IFBs, see (Hakansson et al., 2017, Sleewagen et al., 2012).

For GLONASS compatible receiver, the channel design requires a wider bandwidth in order to accommodate various GLONASS frequency ranges. This will produce noisy observations, which has a negative influence on fixing the ambiguity resolution.

The emergence of new GNSS constellations encouraged adopting a combined GNSS solution to improve positioning performance. In a combined solution, the observations are belonging to different GNSSs, which required transformation between these systems (i.e. varying in reference frames and time scales), to represent a solution in one positioning system. In addition, the receiver-specific biases of interoperability of different GNSS need to be calibrated (Nicolini and Caporali, 2018). The most significant part of Inter-system Bias (ISB) between receivers with different constellations is related to receiver hardware that is dealing with various signal structures. For example when combined GPS and Galileo systems, it is possible to form double differencing between receivers by differencing Galileo code as well as the phase observations relative to the counterpart observations of GPS reference or pivot satellites (Odijk and Teunissen, 2013). The impact of ISB on fixing the ambiguity was investigated by Odijk and Teunissen (2013). They reported that the ISB could only be effective when different receiver types in relative positioning (i.e. heterogeneous configuration) are used, while the corresponding ISBs are insignificant with homogeneous receivers. These findings agree with (Paziewski and Wielgosz, 2015).

When employing relative combined solution between different systems of identical frequencies, the differential ISBs can be calibrated by selecting one common pivot satellite for inter-system ambiguity resolution at that specific frequency (Odijk et al., 2017). Odijk et al. (2017) used multi-GNSS with a single frequency and compared fixing the ambiguity resolution of the combined solution with pivot satellite and with independent reference satellite for each system. They found that the fixing results were improved when applying common pivot satellite.

For BeiDou system (BDS), the receiver detecting various BDS signals from three types of BDS satellites that contain GEO, IGSO and MEO satellites. Nadarajah et al. (2013) studied the receiver-dependent biases among the three types of BDS satellites. They assumed the existence of delays/biases caused by receiving different BDS signals by different receiver types of what they named “inter-satellite-type biases” ISTBs. They analysed the impact of these biases on mixed

receiver attitude determination by using real data from zero-baseline experiments. It was observed that the ISTBs could affect fixing the ambiguity resolution when using mixed receivers. The occurrence of these biases is expected when GEO is combined with either IGSO/MEO BDS satellites (Odijk et al., 2015). It is worth mentioning that the adopting of homogenous receives with double-difference DD technique could minimise the effect of these biases as discussed in details in the following chapters.

To summarise the GNSS biases mentioned above, Table 3.3 listed the main biases that introduced as a result of the delay in satellite or receiver hardware.

It can be noticed from Table 3.3 that most of the biases are related to receiver hardware delay, which can be eliminated with relative positioning technique (the technique used in this study). Although these biases are creating and affecting fixing the ambiguity when implementing different receiver types in relative positioning, they are eliminating and cancelling out with relative positioning with identical receivers.

Table 3.3 The main GNSS biases caused by satellite or receiver hardware delay, modified from (Hakansson et al., 2017)

Bias type	Origin HW*	Relative positioning	Other Effect
Satellite code bias	Satellite HW	Eliminated	
Satellite phase bias	Satellite HW		
Receiver code bias	Receiver HW		
Receiver phase bias	Receiver HW		
GLONASS Inter-Frequency bias (IFB) code	Receiver HW	Eliminated for receivers of the same type	Has an impact on fixing the ambiguity when employing different receiver types.
GLONASS Inter-Frequency bias (IFB) phase	Receiver HW		
Inter-system bias (ISB) code	Receiver HW		
Inter-system bias (ISB) phase	Receiver HW		
BeiDou inter-satellite type bias (ISTB) code	Receiver HW		
BeiDou inter-satellite type bias (ISTB) phase	Receiver HW		

HW*: Hardware delay

3. 3 GNSS Observation Equation

The GNSS observations provided by the receiver represent the measurement of apparent geometric range from the satellite to the receiver that embedded by several errors and biases. The apparent geometric range can be expressed either as a pseudorange for code measurements or phase-range for carrier-phase measurements. Therefore, the relationship between the errors mentioned above and the measurements can be modelled by the general observation equations given below (Hofmann-Wellenhof et al., 2008, T. Takasu, 2013):

For Pseudorange;

$$P_{r,i}^{s} = c(t_r - t^s) \tag{3.18}$$

$$P_{r,i}^{s} = \rho_r^s + c[\delta t_r - \delta t^s] + I_{r,i}^{s} + T_r^s + M_{r,i}^{s} + Q_{r,i}^{s} + B_{r,0,i} - B_{0,i}^{s} \quad : \varepsilon_p = M_{r,i}^{s} + Q_{r,i}^{s} \tag{3.19}$$

And, for the phase-range;

$$\phi_{r,i}^{s} = \phi_{r,i}(t_r) - \phi^s{}_i(t^s) + N_{r,i}^{s} + \varepsilon_\phi \tag{3.20}$$

$$= \frac{c}{\lambda_i}(t_r - t^s) + \frac{c}{\lambda_i}[\delta t_r - \delta t^s] + [N_{r,i}^{s} + b_{r,0,i} - b_{0,i}^{s}] + \varepsilon_\phi \tag{3.21}$$

$$\Phi_{r,i}^{s} = \lambda_i \phi_{r,i}^{s} \tag{3.22}$$

$$= \rho_r^s + c[\delta t_r - \delta t^s] - I_{r,i}^{s} + T_r^s + \lambda_i(N_{r,i}^{s} + b_{r,0,i} - b_{0,i}^{s}) + m_{r,i}^{s} + q_{r,i}^{s} \quad : \varepsilon_\Phi = m_{r,i}^{s} + q_{r,i}^{s} \tag{3.23}$$

where:

(i) : is the satellite index for a specific frequency (f_i).

$P_{r,i}^{s}$: is the pseudorange distance between receiver-r and satellite-s (m).

$\phi_{r,i}^{s}$: is the carrier-phase measurements of a signal (cycle).

$\Phi_{r,i}^{s}$: is the carrier-phase measurements of a signal (m).

c : is the speed of light (i.e. 299792458 m/s).

t_r : is the time of the received signal at the receiver (s).

t^s : is the time of the transmitted signal from satellite (s).

ρ_r^s : is the geometric range of satellite-receiver antennas (m).

δt_r : is the receiver clock offset at time t (s).

δt^s : is the satellite clock offset at time t (s).

$I_{r,i}^{s}$: is the ionospheric delay (m).

T_r^s : is the tropospheric delay (m).

ε_p : represents the measurement errors of pseudorange (m).

ε_ϕ : represents the measurement errors of carrier-phase (cycle).

ε_Φ : represents the measurement errors of carrier-phase (m).

$M_{r,i}^{s}$: is the multipath error for code measurements on frequency f (m).

$m_{r,i}^{s}$: is the multipath error for carrier-phase measurements on frequency f (m).

$Q_{r,i}^{s}$: is the noise error for code measurements on frequency f (m).

$q_{r,i}^{s}$: is the noise error for carrier-phase measurements on frequency f (m).

$N_{r,i}^{s}$: is the carrier-phase integer ambiguity (cycle).

λ_i : is the carrier wave length (m).

$B_{r,0,i}$: represent the receiver code bias (m).

$B_{0,i}^{s}$: represent the satellite code bias (m).

$b_{r,0,i}$: is the receiver Fractional cycle bias (FCB) (cycle).

$b_{0,i}^{s}$: is the satellite Fractional cycle bias (FCB) (cycle).

3. 4 GNSS Relative Precise Positioning with Double-Differencing

Two main techniques can be applied to determine the precise GNSS positioning with a certain level of accuracy. The first technique is the absolute precise point positioning (PPP) which depends on undifferenced measurements from an adequate number of satellites to a single receiver. The second technique is the precise relative positioning, in which the unknown position is determined at the rover receiver with respect (i.e. relative) to another base receiver that occupied at a reference station with known coordinates. In other words, the base and rover receivers recorded simultaneous observations to similar tracked satellites, and the differencing measurements approach typically implemented to improve the positioning accuracy.

In most applications, there is a single reference station, which almost fixed and stationary, while one or more rover stations could be in static or kinematic manner. One of the main factors that affect the achieved accuracy is the length of the vector between the base and rover stations (i.e. the length of the baseline). The precision of short-baseline lies in the order of centimetres or even better when using carrier phase measurements, depending on the correct fixing of ambiguity resolution.

To achieve precise positioning, the carrier-phase measurements as well as the code observables are performed, which might contain several errors as discussed in Section (3.3). The typical approach in relative positioning to eliminate these errors is to implement Double Difference (DD) technique, where the observables are linearly differenced in data processing.

Double differencing involves a linear combination of four undifferenced observations as shown in Fig. 3.4, forming by two receivers (base '*b'* and rover *r*) to two satellites (*j* and *k*). The DD represents

a pair of Single Differences (SD) (i.e. between two receivers to single satellite), which can be then subtracted from each other to minimise the common error.

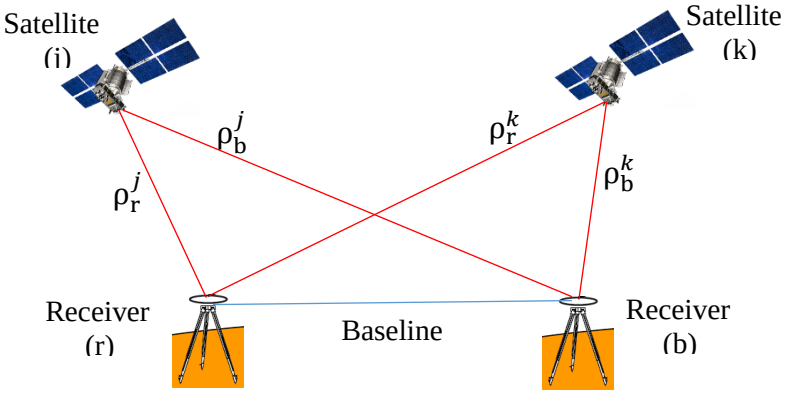


Fig. 3.4 Double difference between receivers "r" and "b" to two satellites "j" and "k".

As a consequence of the DD in relative positioning, the common biases and errors are eliminated from the observation equation. When the distance between the rover and the base station is short enough (<10 km) (T. Takasu, 2013), it can be assumed that the simultaneous observations collected at the base and rover stations affected by similar magnitude when tracked at the same satellites. In more specific, the residuals of DD-ionospheric, DD-tropospheric and orbit errors are small after differencing. However, the correlated errors (i.e. orbit errors, tropospheric and ionospheric errors) can be eliminated, while the uncorrelated errors (i.e. noise and multipath) cannot be reduced.

According to Equations (3.19) and (3.23) in Section 3.3, the single difference can be formed between two receivers b and r to single satellite j (as shown in Fig. 3.5), which can be defined for code and carrier observables as:

$$SD_{rb,i}^{j}(.) = (.)_{r,i}^{j} - (.)_{b,i}^{j} \tag{3.24}$$

$$\begin{aligned} P_{rb,i}^{j} &= P_{r,i}^{j} - P_{b,i}^{j} \\ &= (\rho_r^j + c[\delta t_r - \delta t^j] + I_{r,i}^j + T_r^j + M_{r,i}^j + Q_{r,i}^j) - (\rho_b^j + c[\delta t_b - \delta t^j] + I_{b,i}^j + T_b^j + M_{b,i}^j + Q_{b,i}^j) \\ &= (\rho_r^j - \rho_b^j) + c(\delta t_r - \delta t_b) + (I_{r,i}^j - I_{b,i}^j) + (T_r^j - T_b^j) + (M_{r,i}^j - M_{b,i}^j) + (Q_{r,i}^j - Q_{b,i}^j) \\ &= \rho_{rb}^s + c(\delta t_{rb}) + \cancel{I_{rb,i}^j} + \cancel{T_{rb}^j} + (M_{r,i}^j - M_{b,i}^j) + (Q_{r,i}^j - Q_{b,i}^j) \end{aligned} \tag{3.25}$$

$$\Phi_{rb,i}^{j} = \Phi_{r,i}^{j} - \Phi_{b,i}^{j} \tag{3.26}$$

$$\begin{aligned} &= \{\rho_r^j + c[\delta t_r - \delta t^j] - I_{r,i}^j + T_r^j + \lambda_i \left(N_{r,i}^j + b_{r,0,i} - b_{0,i}^j\right) + m_{r,i}^j + q_{r,i}^j\} - \\ &\quad \{\rho_b^j + c[\delta t_b - \delta t^j] - I_{b,i}^j + T_b^j + \lambda_i \left(N_{b,i}^j + b_{b,0,i} - b_{0,i}^j\right) + m_{b,i}^j + q_{b,i}^j\} \end{aligned}$$

$$= \left(\rho_{rb}^{j}\right) + c(\delta t_{rb}) - \cancel{I_{rb}^{j}} + \cancel{T_{rb}^{j}} + \lambda_i(N_{r,i}^{j} - N_{b,i}^{j}) + \left(m_{r,i}^{j} - m_{b,i}^{j}\right) + (q_{r,i}^{j} - q_{b,i}^{j}) \quad (3.27)$$

where $SD_{br,\mathrm{i}}^{j}(.)$ denotes the single difference SD for a specific frequency (i), $P_{rb,\mathrm{i}}^{j}$ is the SD-pseudorange and $\Phi_{rb,i}^{j}$ is the SD-carrier phase. It can be noticed that the satellite clock error is cancelled after single differences between receivers. In addition, the fractional cycle biases are removed in carrier-phase observable.

Applying the same SD technique between two receivers and satellite k allows the forming pair of SD to be subtracted from each other. As a result, the DD can be obtained. The DD is expressed by;

$$DD_{rb,i}^{jk}(.) = SD_{rb,i}^{j}(.) - SD_{rb,i}^{k}(.) \quad (3.28)$$

$$\begin{aligned} P_{br,i}^{jk} &= P_{rb,i}^{j} - P_{rb,i}^{k} \\ &= \rho_{rb}^{jk} + c(\delta t_{rb}^{jk}) + I_{rb,i}^{jk} + T_{rb}^{jk} + (M_{r,i}^{jk} - M_{b,i}^{jk}) + (Q_{r,i}^{jk} - Q_{b,i}^{jk}) \end{aligned} \quad (3.29)$$

$$\begin{aligned} \Phi_{br,i}^{jk} &= \Phi_{rb,i}^{j} - \Phi_{rb,i}^{k} \\ &= \left(\rho_{rb}^{jk}\right) + c\left(\delta t_{rb}^{jk}\right) - \cancel{I_{rb}^{jk}} + \cancel{T_{rb}^{jk}} + \lambda_i(N_{rb,i}^{j} - N_{rb,i}^{k}) + \left(m_{r,i}^{jk} - m_{b,i}^{jk}\right) + (q_{r,i}^{jk} - q_{b,i}^{j}) \end{aligned} \quad (3.30)$$

where $\mathrm{DD}_{\mathrm{rb,i}}^{\mathrm{jk}}(.)$ is the double difference between two sets of observables.

It is evident that the receiver clock offsets are cancelled in DD as well as the satellite clock errors at SD. In addition, for short baseline between the base and rover stations, it can be assumed that the atmospheric conditions are similar thereby the ionosphere and troposphere are cancelled. Also, the fractional cycle biases are cancelled.

To determine the unknown positions and related quantities in relative approach, the observation equations at each epoch are forming by differencing the simultaneous measurements of satellites. This differencing can be performed by subtracting the measurement of each satellite in view from the common reference satellite. The latter is defined as a satellite of the maximum elevation angle at each epoch, which is automatically selected by RTKLIB software. In addition, this software does not choose one common reference satellite for combined GNSS solution. As discussed in Section 3.4.2, to prevent the effect of ISBs (inter-system biases), there is one reference satellite belonging to each independent navigation system (T. Takasu, 2013).

3. 5 Processing of GNSS Data

3.5.1 Ambiguity Resolution

The observations of precise carrier-phase measurements are essential to achieving the high accurate GNSS positioning (Teunissen, 1995). The computed range of measured phase represents the number of carrier-phase cycles between the satellite and receiver (Teunissen, 2003). Consequently, the receiver can measure the fractional part of this range, while the integer part of full cycles (i.e. exact

number of multiple wavelengths) along the phase range is unknown, due to the presence of biases in carrier-phase measurements (as discussed in Section 3.2.4). The entire unknown number of full cycles is referred to as an integer phase of ambiguity. Therefore, to achieve a highly accurate positioning, the ambiguities of the phase measurements should be resolved. The resolving of ambiguity to correct integer values is called an integer phase of ambiguity resolution (AR), which requires fixing before implementing the measurements of carrier-phase in model equations of precise positioning.

To resolve the ambiguity resolution (AR), the procedure includes three sequential steps (Teunissen, 1998, Teunissen, 2003): (i) estimating the float ambiguities as real values along with estimated position; (ii) estimating the ambiguities resolution as integers, and their validation; and (iii) adjusting the estimate positions to improved values.

In GNSS precise relative positioning, the first step of ambiguity is to compute the float solution through differenced measurements (SD then DD). The model of equations is solved by a proper approach such as the Least squares or Kalman Filter. The obtained solution gives the estimated real–value of ambiguities and the estimated position of rover antenna through the computed baseline components, in addition to the corresponding variance-covariance matrices of float solution. The estimation will be more effective when applying less noisy parameters, which helps in defining estimate values close to the final most probable values. Although the ambiguities are related to phase measurements, the code measurements are also needed to determine the estimated values. This is a limiting factor in estimating ambiguity, due to less accurate results of code measurements.

The second step involves an estimation of the integer ambiguity from the results of previous float estimation by applying a mapping function (Ong, 2010). The conversion from the real-valued float ambiguities to integer-valued fixed ambiguities needs to deal with the real part of the estimated value for each satellite (i.e. required to rounding to the nearest integer). This means that the float solution gives the initial search space for the integer ambiguities, which implies different sets of float ambiguities that used to map one set of integer ambiguities. For this purpose, the Integer Least Squares (ILS) method can be used as an optimal method, which can achieve the best-estimated set of integer ambiguities. The defined set must have the minimum weighted sum of squared ambiguity residuals (Teunissen, 2000).

To solve the ILS problem and find the most probable values of ambiguities, the Least-Squares Ambiguity Decorrelation Adjustment (LAMBDA) and modified-LAMBDA (MLAMBDA) (Chang et al., 2005) are employed (T. Takasu, 2013). The LAMBDA represents the well-known efficient strategy that applies a combination of a linear transformation in order to minimise the integer vector of search-space and skilful tree-search procedure (Teunissen, 1995, T. Takasu, 2013).

The most important part is to check the validation of the defined integer vector of ambiguity solution, to accept or reject that fixing. For validation, there is a simple Ratio-Test (R) computed as the weighted sum of the squared residual (WSSR). Therefore, R can be expressed as the ratio of the second best solution $\check{N}_2$ to the double difference integer ambiguity, $\grave{N}$, (T. Takasu, 2013):

$$R = \frac{(\check{N}_2 - \grave{N})^T Q_N^{-1} (\check{N}_2 - \grave{N})}{(\check{N} - \grave{N})^T Q_N^{-1} (\check{N} - \grave{N})} > R_{thres} \tag{3.31}$$

where $\check{N}_2$ denotes the vector of the second best solution of ambiguity resolution, $\grave{N}$ is the double difference integer ambiguity and their covariance Q_N, while $\check{N}$ is the most appropriate integer vector obtained by solving ILS. In data processing, the value of the validation threshold R_{thres} can control the acceptance of fixed solution (i.e. from experience, it is recommended to set the minimum value of the threshold to be 3) (Yamada et al., 2010). When the computed ratio less than the threshold value, the output will be a float solution. For more details see (Verhagen, 2004, Verhagen, 2005).

Once the integer ambiguity with its validation is defined, the fixed improved position (from the estimated one) of the rover antenna (which represents the third step of the solution) can be easily obtained. Eventually, with fixing the ambiguity (by following the above technique), the carrier-phase measurements became unambiguous and can achieve high precision outcomes.

The defined integer ambiguity resolution is remain constant since the phase lock is preserved (i.e. there is no occurrence of cycle slips). In general, to update or resolve the ambiguity, the estimated ambiguity and position in float solution (i.e. the first step in resolving resolution procedure) can constrain in a proper filter (e.g. Kalman Filter), especially in kinematic applications.

The ambiguity resolution in RTKLIB software (an essential software used in the current study), can be processed in three different techniques including; (i) instantaneous (ii) continuous and (iii) fix-and-hold. After calculating the float solution, the estimated integer ambiguity resolution is then calculated and resolved in the best vector of fixed solution ambiguity. Consequently, the integer-phase difference between the estimated and fixed ambiguity resolution is an integer number of cycles that need to be added to the measured carrier-phase to have the correct range.

The integer ambiguity, which has been estimated and resolved by ILS for every epoch, is related to instantaneous mode (also known as a single epoch). While, both the continuous and fix-and-hold techniques use the Kalman Filter in a different way for estimating the ambiguity of the successive epochs. In other words, in the continuous mode the integer-phase difference is updated based on the next float solution, while the fix-and-hold method uses the valid derived AR of the current stage to feed the next epoch by applying the Kalman Filter (i.e. the ambiguities are tightly constrained to the resolved values) (T. Takasu, 2013). Within Kalman filter, the estimated ambiguities and positions converge to adjusted values when noise is reduced.

When using GLONASS-only or combined GPS/GLONASS solution, the challenge will be how to fix the GLONASS ambiguity in carrier-phase measurements. The reason for that is the multiplexing technique of FDMA GLONASS signals transmitted with different frequencies (as explained in Sub-section 3.1.2). Therefore the fixing of GLONASS ambiguity resolution is more complicated than GPS (Petovello, 2009). When constructing the SD then the DD of GPS or any other CDMA systems (with the same frequency), most of the error sources can be mitigated. For GLONASS the receiver clock errors cannot be eliminated with ordinary DD (Quan et al., 2016). To overcome this challenge, several methods have been presented by (Ong, 2010). One of the most effective techniques is a process of scaling the carrier-phase measurements of GLONASS into distances, equivalent to wavelengths (by considering the inverse of frequency) (Leick, 1998, Takasu and Yasuda, 2009, Al-Shaery et al., 2013).

Although the DD of scaling method eliminates receiver clock errors, the obtained resulting integer ambiguity is non-integer. Takasu and Yasuda (2009) used a transformation matrix to overcome this problem. Therefore, the transformation matrix is used to convert the SD integer ambiguities to DD form before implementing LAMBDA strategy to solve the ambiguity resolution. Thus, the scaling method is adopted by RTKLIB software to tackle the problem of fixing GLONASS ambiguity resolution.

3.5.2 Cycle Slips

When receiver starts tracking the GNSS signals, the initial integer ambiguity of carrier-phase required fixing to define the correct integer number of cycles for each satellite-receiver pair as above mentioned. The fixed integer ambiguity will be constant for all epochs of continuous tracking. However, when receiver losses tracking due to signal interruption, a phenomenon of cycle slips occurs. In this event, the integer part shows a sudden apparent jump in the instantaneous accumulated phase by an integer number of cycles (Hofmann-Wellenhof et al., 2008). The occurrence of cycle slips causes discontinuities in phase measurements; thereby the integer ambiguity is lost, and a correct number of counted cycles is miscounted, which has to be initiated again (Xu and Xu, 2007) or calculated precisely the value of cycle slips to be correctly repaired (Banville and Langley, 2010).

Obstructions that prevent receiving satellite signals may cause the loss of signal, a low SNR (due to multipath or bad ionospheric activity), interference or receiver signal processing. In addition, cycle slips can be occurred due to either the setting in satellite oscillator or receiver software failure (Kaplan and Hegarty, 2005). The presence of cycle slips with few cycles can add a constant bias to all following observations that affect the estimated parameters and subsequently degrade the achieved precision, which is a problematic issue in precise applications (Kim and Langley, 2001).

Cycle slips should be detected and corrected before estimating the position to attained high precision results (Bisnath and Langley, 2000). However, many techniques have been developed to identify and

repair cycle slips; they can be classified into four main methods (Chen et al., 2015a). These main methods including (i) undifferenced based (Banville and Langley, 2010) , (ii) double difference dependent (Chen et al., 2015a), (iii) triple-frequency (de Lacy et al., 2011, Huang et al., 2015) and (iv) sensors aided (Du and Gao, 2012). The details of these methods are beyond the scope of this study.

For single receiver positioning the detection of cycle slip can be carried out regarding geometry-free combinations of measurements at single or different frequencies. The geometry-free provides a linear combination that affected by the ionospheric refraction and the ambiguity parameters (Xu and Xu, 2007). For single-frequency, both code and carrier-phase measurements are required in computation, while with different frequencies the combination is forming by carrier-phase observables only. Thus, the comparing code and phase observables can be applied for single frequency measurements, while differencing two carrier-phase observables is suitable for dual or multi frequencies (Subirana et al., 2013).

For dual frequency (e.g. L_1 and L_2) at epoch (t_j), the geometry-free by differencing two carrier-phase measurements can be formed by (Xu and Xu, 2007):

$$\lambda_1 \phi^s_{r,1}(t_j) - \lambda_2 \phi^s_{r,2}(t_j) = \lambda_1 N_1 - \lambda_2 N_2 - \Delta I^s_{r,1,2}(t_j) + \Delta\varepsilon_\phi \tag{3.32}$$

For single frequency (i) at epoch (t_j), the geometry-free by comparing the phase-code observables (which also used in wide lane ambiguity computation) can be written as (Xu and Xu, 2007):

$$\lambda_i \phi^s_{r,i}(t_j) - P^s_{r,i}(t_j) = \lambda_i N_i - 2I^s_{r,i}(t_j) + \Delta\varepsilon_{\phi P} \qquad i = 1, 2, 5 \tag{3.33}$$

where $\phi^s_{r,i}$: is the carrier-phase measurements of a signal (cycle), index *i* for a specific frequency.

$P^s_{r,i}$: is the pseudorange distance between receiver-r and satellite-s (m).

λ_i : is the carrier wave length (m).

$N^s_{r,i}$: is the carrier-phase integer ambiguity (cycle).

$I^s_{r,i}$: is the ionospheric delay (m).

$\Delta I^s_{r,i}$: is the difference in ionospheric delay between two carrier frequencies (m).

$\Delta\varepsilon_\phi$: represents the remaining errors of carrier-phase (m).

$\Delta\varepsilon_{\phi P}$: represents the remaining errors of carrier-phase and pseudorange (m).

From the above combinations, it can be considered the simultaneous difference at each epoch, and then it is possible to compare the consecutive epochs. The change in two successive epochs (t_j) and (t_{j-1}) can be as below:

$$\lambda_1 \Delta_t \phi^s_{r,1}(t_j) - \lambda_2 \Delta_t \phi^s_{r,2}(t_j) = \lambda_1 \Delta_t N_1 - \lambda_2 \Delta_t N_2 - \Delta_t \Delta I^s_{r,1,2}(t_j) + \Delta_t \Delta \varepsilon_\phi \quad (3.34)$$

$$\lambda_i \Delta_t \phi^s_{r,i}(t_j) - \Delta_t P^s_{r,i}(t_j) = \lambda_i \Delta_t N_i - 2\Delta_t I^s_{r,i}(t_j) + \Delta_t \Delta \varepsilon_{\phi P} \qquad i = 1, 2, 5 \quad (3.35)$$

where Δ_t is the time difference operator, $\Delta_t \Delta I^s_{r,1,2}$ and $\Delta_t I^s_{r,i}$ are the ionospheric residuals (Xu and Xu, 2007). When comparing the current and previous epochs, the change will give an indication of the occurrence of cycle slips or not.

If there are no cycle slips, the ambiguities N_1 and N_2 are constant, which leads to no differences between successive ambiguities (i.e. ΔN_1 and ΔN_2 equal zero), otherwise there is might existence of cycle slips. In other words, for two adjacent epochs, the minimum ionospheric residual should be achieved. Any unusual change of ionospheric residual may indicate cycle slips in one or two phases. When cycle slips detected, the repairing should be applied by correction model or repeating the ambiguity resolution fixing.

The cycle slips detection by phase-code measurements might suitable for big jumps of cycle slips, due to high noisy code measurements compared to phase ones, thereby it is not operative for correct small cycle slips (e.g. 1-2 cycles) (Liu, 2011). Therefore, the phase-phase ionospheric residual method is more effective. However, there are other methods can be used to detect cycle slips that contain Doppler integration and differential phases of time (Xu and Xu, 2007).

In RTKLIB, there are two techniques can be used to detect and correct the cycle slips. The methods being the loss-of-lock indicator (LLI) and the linear geometry jump (LG Jump). These techniques use the observation data from a single receiver, which not required differencing between receivers. The first technique is based on single frequency and evaluating the RINEX observation data by comparing range residuals from differences between consecutive carrier phase and code measurements. While, the second technique can be used when dual frequencies are available to form a linear combination (LC) of geometry-free (T. Takasu, 2013).

Although the cycle slip may be detected, accurate correction may not be valid. This can result in a temporary gap in carrier-phase observables. However, the presence of cycle slip in data of a single satellite can affect the estimated position; it will be better to exclude that contaminated data to keep estimation with clean data. The latter issue will be more efficient with the combined GNSS solution that offers a redundant available satellite.

3.5.3 Dilution of Precision (DOP)

The expected precision of GNSS positioning is affected by the precision of the measured quantities and the geometric configuration of observed satellites. Accordingly, the measurement's precision evaluated statistically by the variance (or standard deviation), while the satellite geometry is expressed by scalar factors referred to Dilution of Precision (DOP) values (Subirana et al., 2013).

Thus, the DOP parameters represent an important factor that has an impact on achieving high-quality results (Hofmann-Wellenhof et al., 2008). It depends on the number of observed satellites and their distribution with a geometric orientation to each other concerning the antenna receiver. That means the strength of geometry will vary according to the change in separated angles between distributed satellites and their locations. Therefore, the DOP can visualise as a volume of polyhedron created by the intersection of receiver-satellite vectors with the unit sphere (ibid). As the volume increases, a better geometry with decreased DOP magnitude is achieved, which indicates that the small DOP values can lead to results that are more precise and vice versa. Due to the relative movement of satellites, their positions are changed within time; thereby an instantaneous geometry can be achieved.

The mathematical definition of DOP factors can be derived from computations of single-point positioning with code-range measurements. The position of the receiver (r) can be determined when observed a sufficient number of visible satellites (S_1, S_2, S_3, .., S_m) at a specific epoch of time. Consequently, the computed pseudoranges between the receiver and each satellite are expressed by Eq. (3.19), then the vector x of unknowns and vector y of pseudorange measurements can be given as follows:

$$\mathrm{x} = (\mathrm{r_r^T}, \mathrm{c\delta t_r})^{\mathrm{T}} \tag{3.36}$$

$$\mathrm{y} = (\mathrm{P_r^1}, \mathrm{P_r^2}, \mathrm{P_r^3}, \ldots., \mathrm{P_r^m})^{\mathrm{T}} \tag{3.37}$$

where x is the vector of unknown parameters of (4*1) dimensions, which contains three positioning components (r_E, r_N, r_U) of receiver coordinates (r_r^T) and one component for clock offset $c\delta t_r$. The P_r^s represents the Pseudorange distances, which can be defined as normal pseudorange or Ionosphere-free LC one. As a result, the measurement equations can be constructed and the partial derivative can be given as (T. Takasu, 2013):

$$\mathrm{h(x)} = \begin{pmatrix} \rho_r^1 + c\delta t_r - c\delta t^1 + I_r^1 + T_r^1 \\ \rho_r^2 + c\delta t_r - c\delta t^2 + I_r^2 + T_r^2 \\ \rho_r^3 + c\delta t_r - c\delta t^3 + I_r^3 + T_r^3 \\ \vdots \\ \rho_r^m + c\delta t_r - c\delta t^m + I_r^m + T_r^m \end{pmatrix}_{(m*1)} \qquad \mathrm{H} = \begin{pmatrix} -e_r^{1\,T} & 1 \\ -e_r^{2\,T} & 1 \\ -e_r^{3\,T} & 1 \\ \vdots & \vdots \\ -e_r^{m\,T} & 1 \end{pmatrix}_{(m*4)} \tag{3.38}$$

where ρ_r^s represents the geometric range (physical distance between the satellite antenna and receiver antenna), and e_r^s denotes the independent vector of the line of sight (LOS) from receiver to the satellite specified by ECEF coordinates (e_E, e_N, e_U). It is obvious that the number of observed satellites (m) will specify the number of observation equations. The required position of each satellite and satellite-clock biases are given in the GNSS satellite ephemerides, while the troposphere and ionosphere effects are modeled. Consequently, the set of observation equations can be solved to determine the receiver position and receiver clock bias.

In RTKLIB, after estimate the initial receiver position and clock offset, the final estimated vector is determined by employing an iterated weighted Least Square Estimation (LSE), for more details see (T. Takasu, 2013).

Generally, the unknown vector is determined by:

$$x = (H^T H)^{-1} H^T (y - h(x)) \tag{3.39}$$

$$Q = (H^T H)^{-1} = \begin{pmatrix} q_{EE} & q_{EN} & q_{EU} & q_{Et} \\ q_{NE} & q_{NN} & q_{NU} & q_{Nt} \\ q_{UE} & q_{UN} & q_{UU} & q_{Ut} \\ q_{tE} & q_{tN} & q_{tU} & q_{tt} \end{pmatrix}_{4*4} \tag{3.40}$$

where Q represent the symmetric cofactor matrix (Hofmann-Wellenhof et al., 2008) (also represent the inverse of the normal matrix or the geometry matrix in litriture). Based on the Q matrix, typical dilution metrics can be computed from the digonal elements of this matrix as given below:

$$\begin{aligned} GDOP &= \sqrt{q_{EE} + q_{NN} + q_{UU} + q_{tt}} \\ PDOP &= \sqrt{q_{EE} + q_{NN} + q_{UU}} \\ HDOP &= \sqrt{q_{EE} + q_{NN}} \\ VDOP &= \sqrt{q_{UU}} \end{aligned} \tag{3.41}$$

The $GDOP$ factor is the geometric dilusion of precision that comprises the effect of geometry in 3D position and time, which calculated from the square root of the trace components of the cofactor matrix. The $PDOP$ indicates the position dilution of precision that effected by 3D position geometry, while HDOP (horizontal DOP) and VDOP (Vertical) represent the effect geometry in 2D horizontal position and vertical position, respectively.

However, the dilution of precision can also be defined from the covariance matrix of the errors in the computed values, which represent the product of (i) geometry and (ii) an expected precision in measured values as above mentioned (Kaplan and Hegarty, 2005). As the pseudorange observations

represent the measured values, the usual assumption is evaluating the measured quantities by the variance of User Equivalent Range Error (UERE), thereby the covariance can be expressed as :

$$\mathrm{cov(x)} = (\mathrm{H^T H})^{-1}\,\sigma^2_{\mathrm{UERE}} \qquad (\mathrm{H^T H})^{-1} = \frac{\mathrm{cov(x)}}{\sigma^2_{\mathrm{UERE}}} \tag{3.42}$$

It is clear from Eq. (3.42) that the parameters of DOP (from Q), are defined as the ratio factor between coverance and the precision of measurements. However, the geometry is only influnced by the receiver-satellite ranges, therefore the Root Mean Square Error (RMSE) can be defined by (Subirana et al., 2013):

$$\mathrm{RMSE} = \sqrt{\mathrm{tr(cov(x))}} = \sigma\sqrt{\mathrm{tr(Q)}} \tag{3.43}$$

It can be seen from Eq. (3.43) that the trace of the Q matrix represent a scale factor on σ , the standard devation of measured values.

For more specific, the estimated computation of the expected accuracy can be given as a common effect between the DOP values and the precision in measurements. This reflects the importance of DOP values to show the impact of errors in measurements onto the errors in positioning. Therefore, the analysed DOP values will be a helpful tool in interpreting the processed data, which is also a more efficient factor in assessing the performance of different GNSS solutions (Wang and Huang, 2014).

The DOP values can be improved by increasing the number of observed satellites, which represent the most significant benefit that promotes to adopt the combined solution (Miaoyan et al., 2008), especially in environments of limited available satellites. For example, Anquela et al. (2013) have reported that a combined GPS/GLONASS solution improved the satellite geometry by reducing PDOP values by 27% in comparison with a GPS-only solution and the improvement will be 80% better than the GLONASS-only solution. Similarly, Cai and Gao (2013) found that adding GLONASS satellites to GPS increase the number of observed satellites from eight to fourteen will lead to a reduction in PDOP values from 2.5 to 1.7, which leads to improving the RMS values of assessed position. Also adding BDS satellites also have the remarkable effect of improving the geometry (Yang et al., 2011). Furthermore, the combination of more than two constellations of multi-GNSS will contribute in providing more robust geometry (Cai et al., 2015, Li et al., 2015b). It can be concluded that the observing of more satellites will reduce the uncertainty in the estimated position and minimise the related standard deviation.

3.5.4 Code-Multipath Detection of MP1 and MP2

As explained in Section 3.5, that the multipath effect represents the significant error that limiting the achievement of highly accurate positioning. Although the double-differencing technique is used to

cancel and reduce many of correlated error sources (i.e. Troposphere, ionosphere, others), the multipath and receiver noise are still cannot be cancelled and removed in GNSS observations using such technique. In addition, no general model can determine multipath precisely, due to the variable geometrical conditions between satellite and receiver regarding time and location. However, the multipath effect can be detected and estimated by applying a linear combination between code and carrier-phase dual frequency measurements (Hofmann-Wellenhof et al., 2008). The main assumption assumes that both code and carrier-phase measurements are affected by the similar magnitude of correlated errors.

According to Equations (3.19) and (3.23) for code and carrier observables, the difference between them can be written as given in Eq. 3.44 (Xu and Xu, 2007). For the same satellite at the same epoch, the difference between code and carrier-phase observables can be related to the relationship between the differenced observables' errors as expressed by equation (3.44).

$$P_{r,i}^{s} - \Phi_{r,i}^{s} = 2I_{r,i}^{s} + \lambda_i\left(N_{r,i}^{s}\right) + \left(M_{r,i}^{s} - m_{r,i}^{s}\right) + \left(Q_{r,i}^{s} - q_{r,i}^{s}\right) \tag{3.44}$$

Where $(P_{r,i}^{s} - \Phi_{r,i}^{s})$ represent the difference between code and carrier observables, $I_{r,i}^{s}$ is the ionospheric delay, λ_i is the wavelength, $N_{r,i}^{s}$ is the integer ambiguity parameter, $\left(M_{r,i}^{s} - m_{r,i}^{s}\right)$ is the difference between code multipath and phase multipath, and $(Q_{r,i}^{s} - q_{r,i}^{s})$ is the difference between code and phase noise errors.

To exclude the effect of the ionosphere, the difference will apply to ionosphere-free pseudorange and carrier observables as given in Equations (3.9) and (3.12), then form the corresponding differences (Hofmann-Wellenhof et al., 2008). The resultant difference removes effects from geometry, clocks, troposphere and ionospheric delay. When the impact of phase multipath and noise are neglected compared with that of code measurements and considering ionospheric-free ambiguity to be constant when there is no occurrence of cycle slips. The remaining effect can reflect the code multipath (i.e. which also contain the code noise and hardware delay) as given in (Estey and Meertens, 1999), which can be expressed with the following:

$$MP1_{r}^{s} = P_{r,1}^{s} - \frac{f_1^2 + f_2^2}{f_1^2 - f_2^2}\Phi_{r,1}^{s} + \frac{2f_2^2}{f_1^2 - f_2^2}\Phi_{r,2}^{s} \tag{3.45}$$

$$MP2_{r}^{s} = P_{r,2}^{s} - \frac{2f_1^2}{f_1^2 - f_2^2}\Phi_{r,1}^{s} + \frac{f_1^2 + f_2^2}{f_1^2 - f_2^2}\Phi_{r,2}^{s} \tag{3.46}$$

where $MP1$ and $MP2$ are code estimated multipath computed in meters for frequencies f_1 and f_2 belonging to specific satellite (^{s}) of GNSS constellation to a single receiver ($_{r}$). It is clear that each equation contain the pseudorange observable of a single frequency and phase measurements of dual frequency (Shi et al., 2013, Wang et al., 2016).

The expression of MP1 or MP2 can be implemented for each satellite at each epoch. Therefore, it is possible to represent a time series of MP1 and MP2 for each observed satellite during observation duration, which gives a quality check for the observed data and the contaminated multipath observations can be distinguished. From this analysis, the satellites affected by extensive multipath are identified, which can be excluded to achieve accurate positioning results with clean GNSS data.

3. 6 The Combined Solution of GNSS Constellations

With the availability of different GNSS constellations, it is possible to improve the positioning performance by adopting a combined GNSS solution. However, each satellite system is characterised by its independent parameters, which are varied from system to another (as discussed in Section 3.2). Therefore, the implementing of various observations belonging to different systems requires transformation between these systems to identify the positions in a single uniform system.

The effective combined solution can be achieved by identifying the parameters that contribute to interoperability of the different GNSSs (Nicolini and Caporali, 2018). These parameters are represented by differences in (i) coordinate reference frame to define the positions, (ii) the time-scale between different systems and (iii) different signal multiplexing technique. In addition to generated errors and biases related to each system as well as the differences in ephemeris data.

For instance, when combining the GPS and GLONASS observations, the above three major differences between systems should be determined. Firstly, the reference frame of GPS is a WGS-84 system, which differs from a PZ-90.02 system that adopted for GLONASS computations, thereby an offset distance between origins of two systems is introduced apart with differences in scale and orientation of two systems. The integration of GPS/GLONASS has to be computed in WGS-84 for example, which means transform GLONASS datasets to WGS-84 by utilising the 7-parameters transformation (Dach et al., 2007, Hofmann-Wellenhof et al., 2008). For this purpose, the orbital positions will represent in the unique reference frame.

Secondly, the time-scale for the two systems needs to be aligned, where the GLONASS time has an exact offset of 3-hours from UTC, while the GPS based on UTC with no offset. The instantaneous time scale difference between them can be determined, which enables one to transform one system to another. Thirdly, it can be dealing with the different signal multiplexing techniques (i.e. CDMA and FDMA) that used by two systems by considered the scaling carrier phase observables of GLONASS into distances as explained in Section 3.5.3 for fixing the ambiguity. Furthermore, the introduced biases (as discussed in Section 3.2.4) have to be calibrated. In this case, the combined GPS and GLONASS offers redundant measurements.

Likewise, the above considerations can be applied when combining other GNSSs. The positioning coordinates of any GNSS constellation can be expressed in the Cartesian system. In addition, the

time in each GNSS constellation is based on the UTC system. Therefore the relationship between the coordinate systems as well as the time systems of different GNSSs can be determined, which leads to the potential of transformation between these systems (Xu and Xu, 2007).

3. 7 Chapter Summary

This chapter was dedicated to a technical overview of GNSS constellations. It starts by giving a review of the current four available GNSS constellations, which implies GPS, GLONASS as full operation systems, then Galileo and BeiDou as other under developments satellite systems. This could provide a general understanding of the main specification of these systems and illustrate the main differences between them regarding the orbital planes, number of satellites, geodetic reference frame and time systems. As the fundamental principle of GNSS positioning is based on measured ranges, which are subjected to different error sources, a detailed discussion of the GNSS errors were given in this chapter, which characterised in three main groups that contain (i) satellite error sources, (ii) propagation media effect (i.e. ionosphere and troposphere) and (iii) receiver related part. In addition, other GNSS errors that related to hardware biases were discussed, which have an impact on fixing ambiguity and in turn, affected achieve correct positioning.

The GNSS observation equations were discussed for code and carrier phase measurements; then the emphasis was given to relative positioning along with DD technique to mitigate most of the error sources, which will be used in this study. This was followed by describing and analysing in details the main elements of processing GNSS data that implies the ambiguity resolution; cycle slips detection, Dop values and multipath effects. Finally, the basic required transformations between different system were discussed to achieve the final combined GNSS solution. All these aspects to cover the theoretical part in this study.

Chapter 4: Investigation of the Noise Level in Multi-GNSS Measurements

Part of this chapter has been published as:

MSAEWE, H. A., HANCOCK, C. M., PSIMOULIS, P. A., ROBERTS, G. W., BONENBERG, L. & DE LIGHT, H. 2017b. Investigating multi-GNSS performance in the UK and China based on a zero-baseline measurement approach. *Measurement,* 102**,** 186-199.

MSAEWE, H., HANCOCK, C., PSIMOULIS, P., ROBERTS, G. & BONENBERG, L. 2017a. Assessment of the Effects of Combining Multi-GNSS Constellations on the Solution Accuracy and Availability. *FIG Working Week 2017.* Helsinki, Finland, May 29–June 2, 2017.

4. 1 Introduction

GPS is the positioning tool of choice for a wide variety of applications where accurate (cm level or less) positions are required. However, the measurements of GPS, as well as other GNSS constellations, are susceptible to a variety of errors (as described in Chapter 3) that degrade both the quality of the position solution and the availability of these solutions. Additional satellites from other GNSS constellations offer the possibility of improving the positioning performance when combined with GPS observations. To investigate the potential of each positioning solution, it is necessary to use measurements with an ability to mitigate most of the error sources. This requirement can be achieved by applying zero baseline measurements, which eliminate most of the common errors of the GNSS measurements, which are due to satellite orbits, clock errors, atmospheric delays (i.e. ionosphere and troposphere effects) and multipath (Chen et al., 2015a, Deng et al., 2014). Thus, the remaining error of the GNSS solution is due to the geometry of the satellite constellations and the noise of the GNSS receiver (Dróżdż and Szpunar, 2012).

Since the noise assessment is one of the main research objectives (see Chapter 1), a series of field experiments were conducted, to assess the GPS-only solution compared to the combined solution of GPS with either GLONASS or BeiDou constellations. This will reveal the impact of using GLONASS with GPS and evaluate the contribution of the BeiDou satellite systems with regard to the positioning quality. The expected improvement will be analysed regarding the positional precision and fixed solution availability. When evaluating the positional precision, it is possible to investigate whether the combination of the satellite systems can limit the noise level of the GPS-only solution. Therefore, noise reduction is also analysed.

For these purposes, a series of measurements of multi-GNSS zero-baselines carried out, using different pairs of receivers (each pair of the same type) for 12 consecutive days, simultaneously in the UK and China. The handling of different pairs of receivers was to select the pair of receivers with the most reliable, consistent function and characterised by relatively low receiver noise, to achieve the positioning of different GNSS solutions.

In this chapter, the experimental results to evaluate the GPS-only solution compared to the combined solution of GPS with either GLONASS or BeiDou constellations are discussed and analysed. The effect of this combination on the noise level is also examined.

4. 2 GNSS Zero Baselines Experiments

For the zero baseline measurements, two or more GNSS receivers are connected to a single antenna via a signal splitter. The zero baseline measurements are usually conducted to assess the performance of the GNSS receivers. In the current study, the aim is to evaluate the positioning quality of various multi-GNSS solutions. In addition, what is the performance enhancement relative to the GPS only solution, using the zero-baseline measurements. Therefore, the GNSS measurements have been carried out simultaneously at two locations in the UK and in China, utilising pairs of collocated GNSS similar receivers at each site as displayed in Fig. 4.1, which shows both antennas mounted in open sky environments.

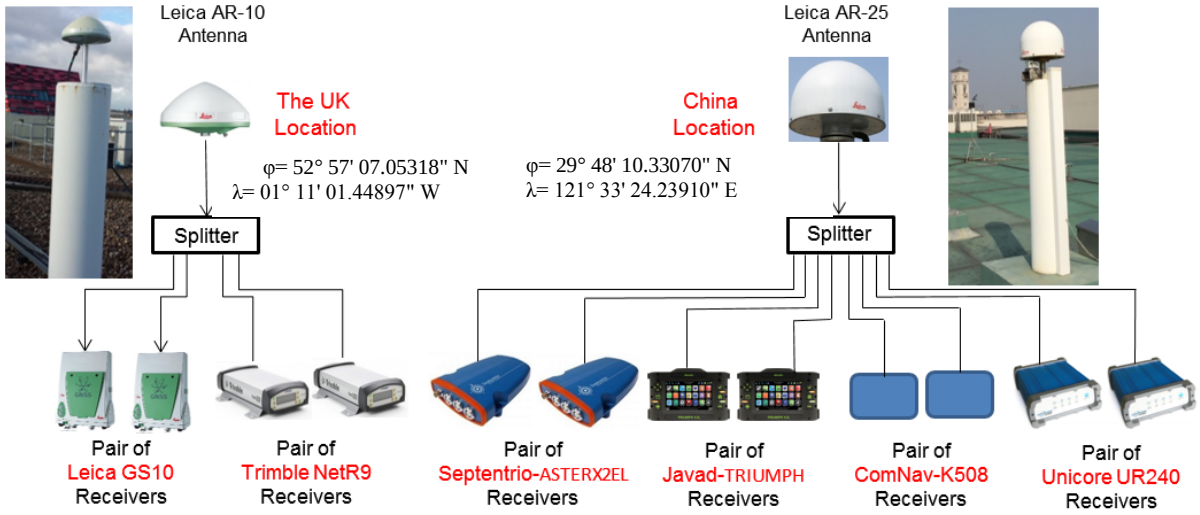


Fig. 4.1 Zero baselines experiment setup (Msaewe et al., 2017b).

The measurements have been conducted over 12 consecutive days, between the 5th and 16th March 2015, with a 1-second sampling rate; hence each day should have been recorded 86400 epochs. The two sites in the UK and China considered as representative cases to reflect the enhancement of the positioning solution by using multi-GNSS constellations. The main reasons are (i) the relatively high latitude of the UK site (i.e. $\varphi \approx 53°$), which leads to reduced accuracy in the northern component of

the GPS-only solution (Meng et al., 2004) and (ii) the low latitude of the China site (φ≈ 29.8°), which corresponds to robust constellation of the BeiDou system, due to the presence of the Mid Earth Orbiting (MEO) satellites with Inclined Geosynchronous Satellites Orbit (IGSO) and Geostationary (GEO) satellites (Teunissen et al., 2014).

The daily solution of multi-GNSS constellations depends on the characteristics of the measurements and the satellite systems used in the solution. More specifically, the GPS constellation repeats every sidereal day (23 h and 56 min), and the GLONASS constellation requires about 8 days to repeating the same constellation. For BeiDou, the MEO satellites need approximately seven days to replicate the same geometry (Winit, 2013). Therefore, the long duration of zero-baseline measurements, i.e. in this study 12 days, is required to investigate different GNSS solutions, in order to assess the occurrence of potential events or problems with periodic repetition (e.g. daily repetition).

For this study, measurements of GNSS zero-baseline were carried out, using pairs of identical receivers. The GNSS data was processed using Double-Difference (DD) technique to eliminate most of the GNSS error sources. In this case, both receivers theoretically have the same errors caused by multipath, satellite orbits and clocks and atmospheric delay, thereby double differencing between receivers cancels these errors. However, for the case of differential positioning using GLONASS, it is required a pair of the same receivers (i.e. for base and rover station) to fix the ambiguity resolution (Al-Shaery et al., 2013), as the different types of receivers have inter-frequency bias (IFB) which cannot be eliminated by Double Differencing (DD) process.

Furthermore, the potential impact of BeiDou inter-satellite-type biases (ISTBs) between different types of BeiDou satellites occurs in the case of using different GNSS receivers, also affecting the ambiguity resolution of the GNSS records process (Nadarajah et al., 2013), which is not in the case of these measurements since, identical receivers are used for each pair.

In this study, the contribution of the Galileo constellation was not assessed, due to the limited number of available satellites, since there were only three satellites (E11, E12, and E19) functioning reliably at the time of the experiments. Other constellations such as QZSS and SBAS have limited contribution to the three main examined systems (GPS, GLONASS, and BeiDou) and they were not included in the study.

4.2.1 Zero Baseline at the UK Site

The first series of zero baseline experiments were set up at a station on the UK site, where a Leica AR10 GNSS antenna mounted on a pillar of control point with known coordinates, on the roof of Nottingham Geospatial Institute (NGI) at the University of Nottingham. This radome antenna designed for optimal signal quality and multipath suppression. With a dedicated low noise cable, the antenna connected via a splitter (GPS RMS18 splitter) to two pairs of multi-GNSS receivers, these

being the Leica-GS10 and Trimble-NET9 (Fig. 4.2). For simplicity, they called ‘Leica’ and ‘Trimble’ receivers.

Each receiver was continuously connected to the power supply and was recording with 1-second sampling rate. Furthermore, the receivers of both types (i.e. Leica and Trimble) can track multiple GNSS constellations; however, the Trimble receivers could not record the signal of the BeiDou satellites. To process the GNSS records, they were converted to RINEX format version-3. For the Leica receivers’ records (files.M00), the Leica Infinity 2.1.0 software was used to convert the raw data into a RINEX data format (version 3.2), while Trimble RINEX convertor 4.5.6 software used to convert the raw data of Trimble receivers (files.T02) to RINEX of 3.2 version. The converted data consist of observation files with navigation message files of each tracked GNSS constellation, for more details see (Gurtner and Estey, 2013).

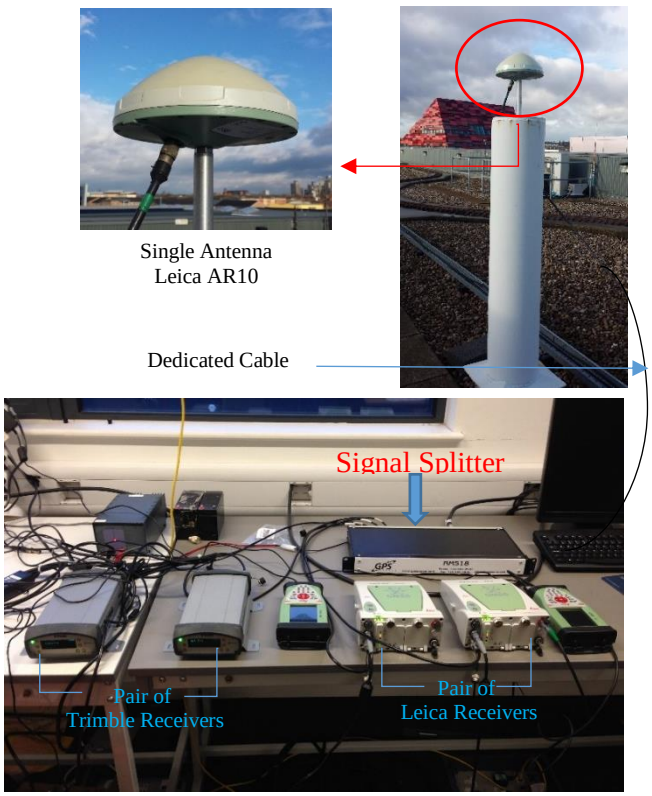


Fig. 4.2 Set up of zero baseline experiment in the UK site.

4.2.2 Zero Baseline at the China Site

The second set of zero baseline measurements was set up on a pillar of known coordinates on the roof of the Faculty of Science and Engineering building, at the University of Nottingham Ningbo China. At this site, a Leica AR-25 GNSS antenna (LEIAR25R4) was connected via a splitter (GPS+GNSS RMS18 Splitter 8-way, Fig. 4.3) to four pairs of GNSS receivers, consisting of Javad-

TRIUMPH, ComNav K508, Unicore UR240 and Septentrio ASTERX2EL receivers. Refer to receivers' specifications of each receiver type for more details.

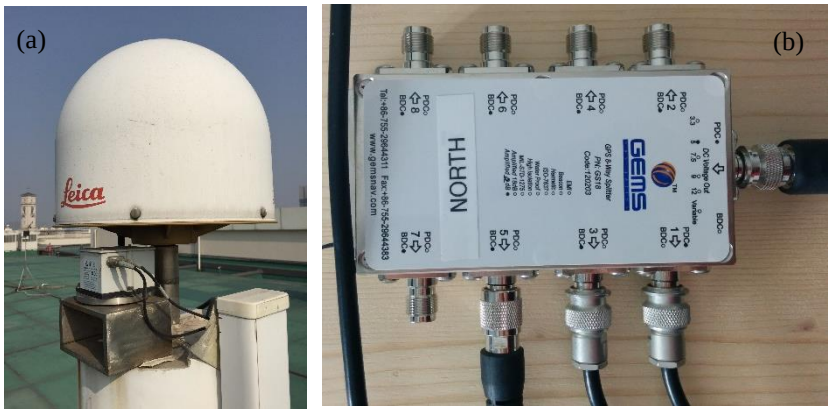


Fig. 4.3 (a) Leica AR-25 GNSS antenna and (b) GPS/GNSS RMS18 Splitter 8-way used in zero baseline experiment at China site.

The GNSS receivers at the China site recorded at a 1-s sampling rate, in order to have consistency with the UK site GNSS records. For each receiver, the raw data were saved in internal receiver memory and then were converted into RINEX files. Due to different receivers manufactures, each receiver type required an appropriate converter. For example, the GNSS raw measurements from Javad receivers required "JPS2RIN v.2.0.0.99" software to convert to RINEX files. The recorded data of ComNav receivers in binary format (*.cnb) employed "CRU- Compass Receiver Utility v1.5.5" for this conversion. Table 4.1 presents the different converters used to convert into RINEX files from the GNSS receivers records and illustrates the specifications of the recorded signals of varying GNSS constellations recorded by these receivers.

Table 4.1 The converters used with different GNSS receivers and specifications of tracked corresponding constellations in the experiment at the China site.

Types of receivers	Type of Raw files	Converter used	Constellation recorded by receivers					
			GPS	GLO	Gal	BDS	QZSS	SBAS
1) Javad-TRIUMPH-VS	JTR*.jps	JPS2RIN v.2.0.0.99	√	√	√	√	√	√
2) Septentrio ASTERX2EL	ssn*.15_	RX tool- SBF convertor	√	√	√	√	√	√
3) ComNav K508	*.cnb	CRU- v.1.5.5 Compass Receiver Utility	√	√		√		
4) Unicore UR-240	*.cdtlog	U-converter	√			√		

However, some satellites have tracked with triple frequency; the required measurements to present investigations will be with the dual frequency of GPS (L1, L2), GLONASS (G1, G2) and BeiDou (B1, B2). Since the GPS-only solution represents the primary demand in GNSS positioning, the combination of GPS with other GNSS constellation will investigate, especially when GPS performance is degraded. Consequently, the observed data of each set of receivers will process with GPS-only and compared to other GNSS solutions.

4. 3 Processing

The GNSS records were post-processed, using RTKLIB v2.4.2, in the kinematic mode to assess the precision of the position for each epoch using DD solutions, having one receiver of the zero-baseline as the reference and the other as a rover. The cutoff angle of 15° was selected in order to (i) limit potential cycle slips which are possible to occur at lower cutoff angle (Huang et al., 2015), and (ii) obtain GNSS data of better quality than that of low-elevated satellites, as the low-elevated satellites are more susceptible to multipath effect (Wang et al., 2016). However, the option of a 10° cutoff was also examined for the GNSS measurements, to investigate potential improvement in the achieved availability or precision of the GNSS solutions.

To attain precise GNSS positioning results, the ambiguity resolution (AR) should be fixed to their integer values. RTKLIB offers three strategies to achieve this fixing, which are; (i) Continuous, (ii) fix-and-hold and (iii) instantaneous (T. Takasu, 2013). Both continuous and fix-and-hold methods use a Kalman filter to estimate the carrier phase ambiguity of the successive epochs. Whereas in continuous mode, the updating of fixing the ambiguity is estimated depending on the float solution and resolved into integer values, the fix-and-hold method uses the valid derived AR of the current stage to feed the next epoch by applying the Kalman filter. The instantaneous method uses integer Least Square method. For the GNSS records of this study, the selection of the appropriate strategy of fixing the ambiguity depended on the fact of the relatively long duration of the records and the kinematic processing mode. For this purpose, a sample data set collected by Leica receiver on the UK site for a session of 16h between (00:00 -16:00 GPS time) can be used as the representative period to assess the different strategies of fixing the ambiguity as shown in Fig. 4.4.

It was found that fix-and-hold technique occasionally has some problems, occurred when a period of sudden change in data quality corrupted the ambiguity resolution after fixing of long duration. This was observed in the period between 14:00 – 15:00 is such as an example (Fig. 4.4b). The time series was interrupted by cycle slips occurred due to the loss of lock, which produced an apparent jump in the carrier phase ambiguity, and forcing the Kalman filter state in RTKLIB to reset. This can arise as a gap interval effect on the final availability of fixed solution. Therefore, the availability of a fixed solution achieved by Fix-and-hold was 98.6%. The use of an instantaneous mode (Fig. 4.4c), leads to a time series with a large number of outliers as a result of incorrect fixing of ambiguity when they are achieved epoch by epoch, using integer Least Square method (T. Takasu, 2013), and also this technique reduces the availability to be 97.2%.

Finally, in continuous mode, the phase-bias is updated depending on the next float solution, which provides a less noisy estimate of the phase biases for solutions of this type of recorded data and it was selected for the kinematic processing of the GNSS records (Fig. 4.4a).

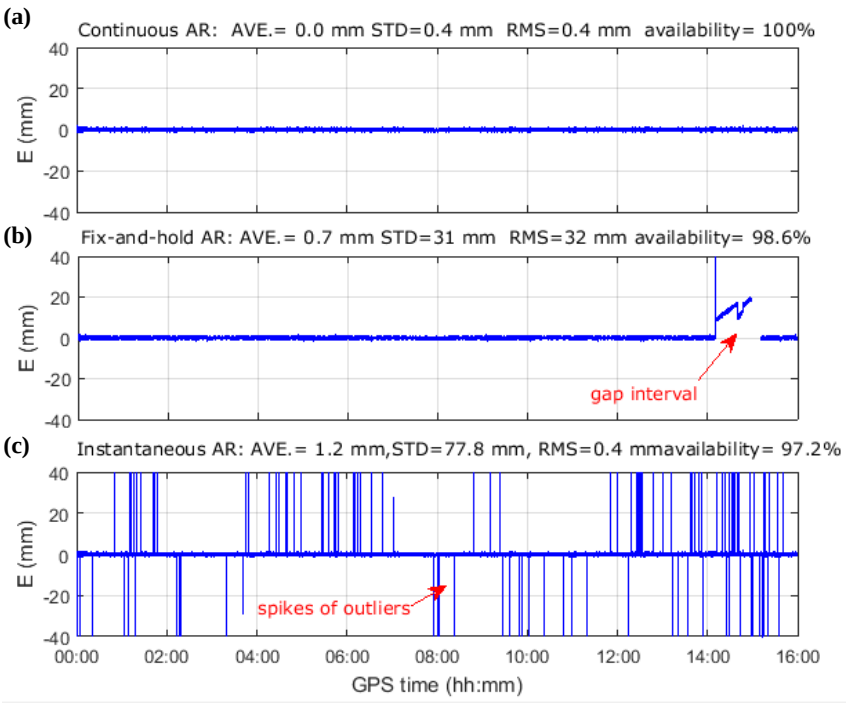


Fig. 4.4 GPS time series of E-component of zero baseline using different options of AR (Leica Receiver 05/03/2015) at the UK site.

Furthermore, it can be noticed that for short duration, the results of continuous AR are identical with the corresponding solutions that processed with Fix-and-hold that leads to similar precision. However, the Fix-and-hold strategy cannot hold the same ambiguity for a long duration of GNSS records. Based on the main elements of processing configuration (i.e. kinematic mode, 15° cut-off elevation angle, continuous mode for AR, etc.) the GNSS records of the zero-baseline measurements were processed.

4. 4 Preliminary Analysis

In the initial analysis of the GNSS records, an assessment was made to determine which pair of the available receivers had the most reliable performance, characterised mainly by uncorrelated data, giving a representative picture of the contribution of the GNSS constellations. The preliminary analysis was made between the collocated receivers for the UK and China sites.

4.4.1 Preliminary Analysis at the UK Site

For the preliminary investigation at the UK site, the positioning quality derived from zero baselines where the precision of the Leica receivers was compared against that of the Trimble receivers. Since the main focusing is on GPS performance, among several sessions of 1-h positioning duration, the 1-h session from 00:00 to 01:00 (GPS time) on 05/03/2015 was selected, as this period was free from data gaps and cycle slips, and with the collocated receivers tracking the same satellites, presented in Fig. 4.5, leading to similar results.

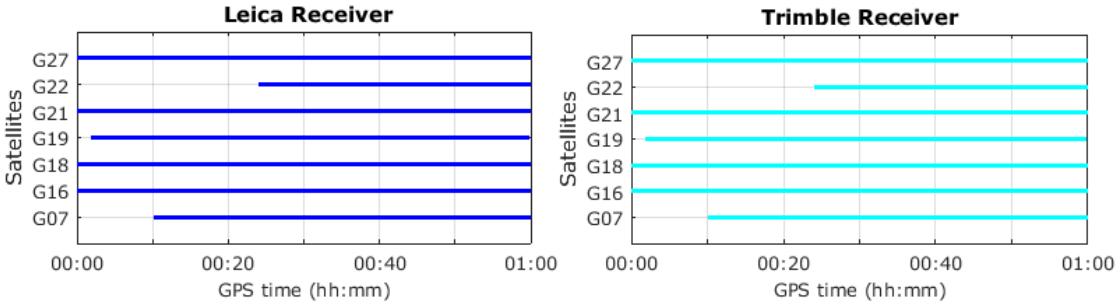


Fig. 4.5 GPS valid satellites tracking by Leica and Trimble receivers at the UK zero baseline along 1st h on 05/03/2015, each receiver represent the base one.

The time series of the components of zero baseline solution in E, N and U represents the deviation (the residual) of the positioning solution at each epoch from the known coordinates of the occupied station, expressing practically the precision of the positing solution at each component (Fig. 4.6). From all plots in Fig. 4.6, there was a period of noisy results at the first 10 min where a limited number of satellites (4 to 5) was available. For each set, the statistic characteristics of the average, standard deviation (STD) and Root Mean Square (RMS) of every component was computed, resulting to the estimation of the precision of the GNSS receivers.

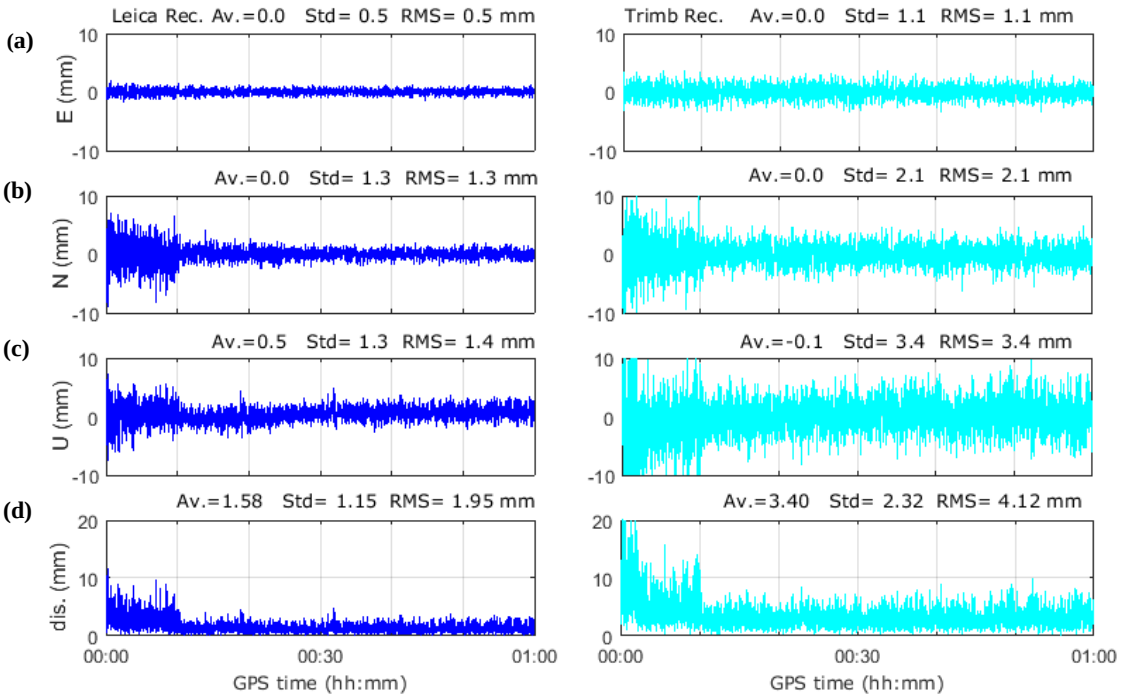


Fig. 4.6 GPS time series of the zero baseline records of two types of receivers for the UK site, (left) time series with Leica receivers and (right) for Trimble receivers on 05/03/2015.

The RMS with Leica receivers was 0.5mm, 1.3mm and 1.4 mm for E, N and U components of zero baseline, respectively, while the corresponding precision of the Trimble receivers was 1.1mm, 2.1mm and 3.4 mm for E, N and U components, respectively.

Additionally, the investigation can be assessed by comparing the achieved precision of GPS data from a zero baseline computed as 3D distance, whereas the precision with Leica receivers was (RMS = 1.95 mm) compared to the corresponding precision with Trimble receivers (RMS = 4.12mm) as shown in Fig. 4.6d. This indicates that Trimble receiver is nosier than Leica.

Furthermore, in order to evaluate the quality of the GNSS data, the autocorrelation analysis was applied (Bona, 2000), which expresses potential correlation of the time series data and reveals whether the time series are contaminated only by white noise (Amiri-Simkooei and Tiberius, 2004). Mainly, the white noise process has a zero mean and no correlation between its values at different times. The derived correlogram describes the autocorrelation coefficients versus time lag (the time interval between samples). When the lag is 0, the value of the correlation coefficient will be 1 from the definition, while other values of lag showing the behaviour of time correlation (Amiri-Simkooei and Tiberius, 2007). The autocorrelation function in Matlab was applied to zero baseline components. The results of the autocorrelation of the GPS time series at the UK site are presented in Fig. 4.7, which showing uncorrelated data.

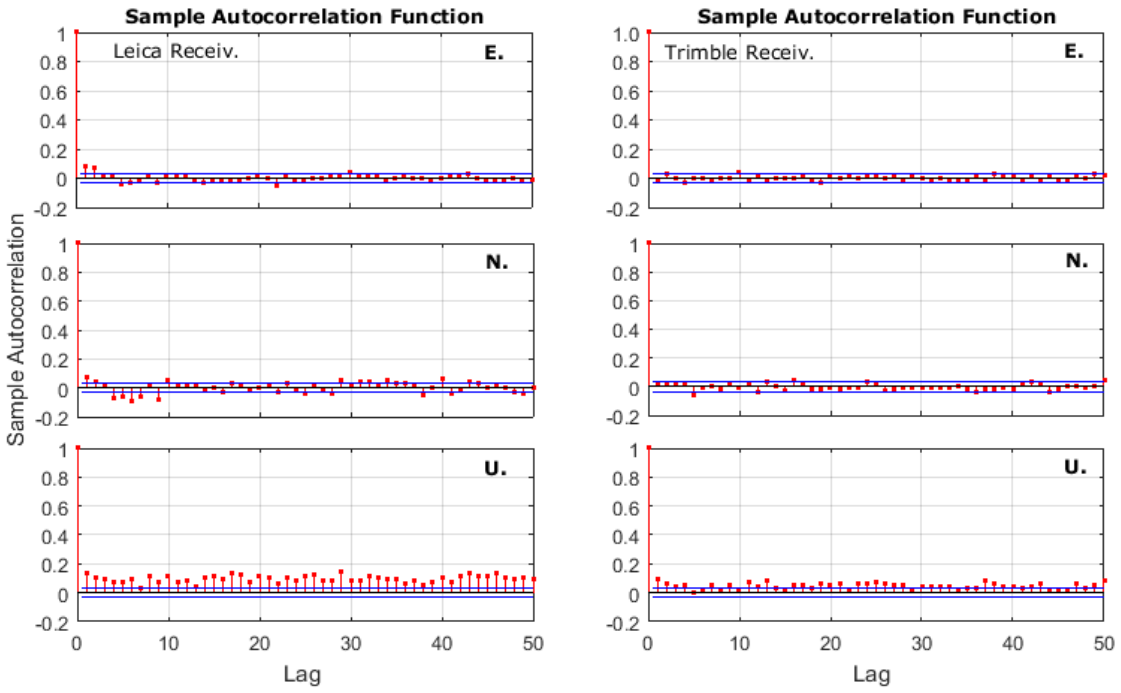


Fig. 4.7 Autocorrelation of E, N and U components of zero baseline of GPS records of Fig. 4.6.

The resolution of the time lag was defined by the 1-s sampling rate of the GNSS records. It is evident that the GPS data are uncorrelated and express mainly white noise for zero baseline components for both of the collocated receivers, as the autocorrelation coefficient is ranging randomly around zero, for all the time lag values. In addition, it is observed that most of the horizontal components are uncorrelated while the vertical components have a slight bias. This bias is a systematic effect caused by a slight offset in the mean of the residuals series.

The same analysis was made for the GLONASS solution using the same 1h period. The RMS values of the GLONASS-only solution are 0.5mm, 0.8mm and 5.7mm for the E, N and U components, respectively for the zero baseline of Leica receivers, while the achieved RMS with Trimble receivers are 0.9mm, 1.3mm and 6.9mm for the E, N and U, respectively as presented in Fig. 4.8.

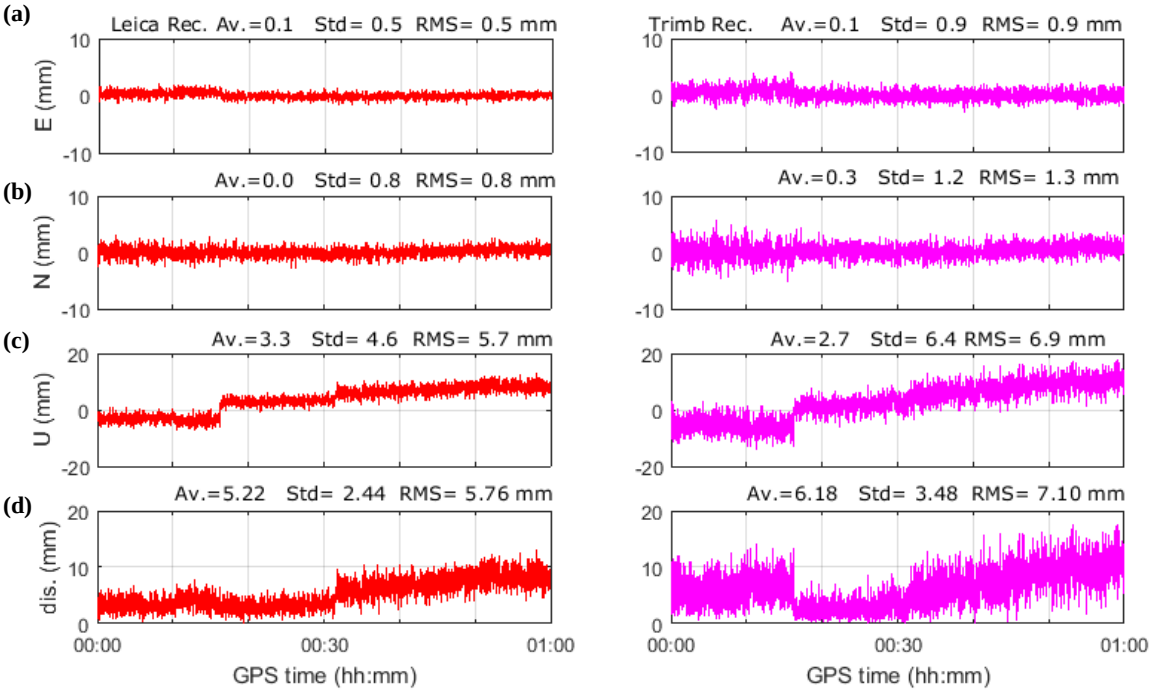


Fig. 4.8 GLONASS time series of the zero baseline records of two types of receivers for the UK site, (left) time series with Leica receivers and (right) for Trimble receivers on 05/03/2015.

In this case, the 3D RMS precision with Leica was 5.76mm compared to 7.10mm with Trimble receivers. Moreover, when applying the autocorrelation analysis to these data, the results of both receivers tend to have the same behaviour. Where the horizontal components are showing slight biases (Fig. 4.9), while the vertical components were correlated. Nevertheless, the GLONASS positioning results with Leica receivers is less noisy than that with Trimble receivers (Fig. 4.8).

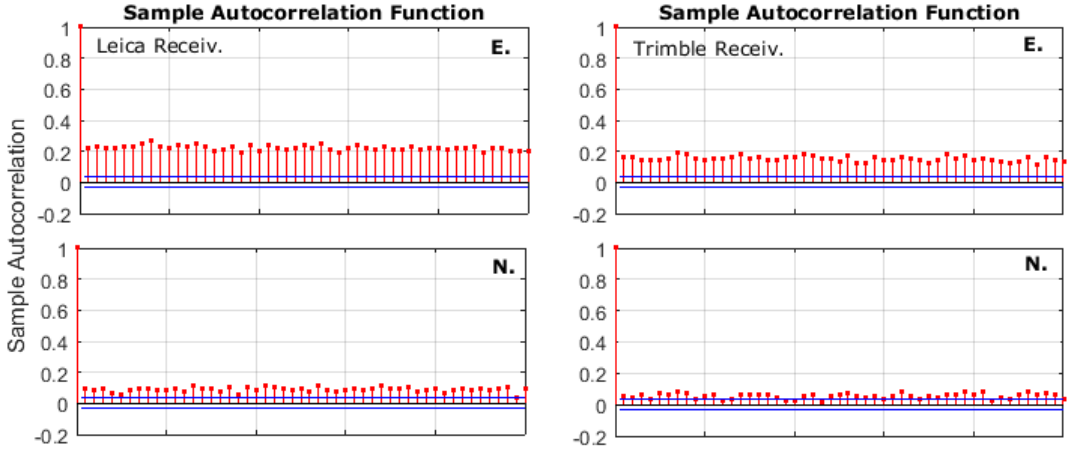


Fig. 4.9 Autocorrelation of E and N components of GLONASS records of Fig. 4.8.

However, a 1h duration of GNSS measurements would be insufficient to give a representative picture of the relative noise level of the receivers; therefore, a comparison of the accuracy of the measurements of the receivers for 24h duration was also made.

Figure 4.10 illustrates the GPS-only positioning on 05/03/2015 with Leica receivers compared to the corresponding positioning with Trimble receivers. It is evident that the amplitude of the time series of the Leica receivers, which express the noise level, is a lower level than that of the Trimble receivers along 24h, which is compatible with the analysed results of 1h for a GPS-only solution. Likewise, the comparison between the positioning time series of the GLONASS-only solution for the two sets of receivers leads to similar trends of noise level, with the Leica receivers proved to be less noisy (Table 4.2).

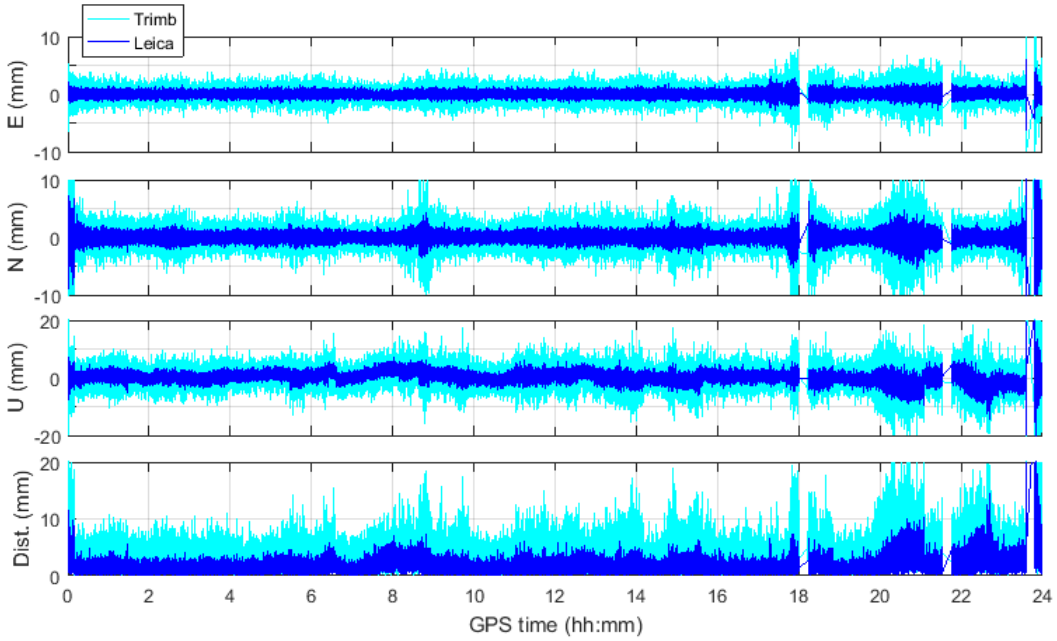


Fig. 4.10 Comparison between two daily time series of GPS-only solution achieved with two pairs of Leica and Trimble collocated receivers for the UK site on 05/03/2015.

Table 4.2 Comparison of statistical results of time series of zero baseline with GNSS solution for 24h using collocated receivers at the UK site on 05/03/2015.

		Leica Receivers			**Trimble Receivers**		
Const.	Comp	Ave. (mm)	STD (mm)	RMS (mm)	Ave. (mm)	STD (mm)	RMS (mm)
GPS	E	0.0	0.5	0.5	0.0	1.2	1.2
	N	0.0	0.9	0.9	0.0	2.4	2.4
	U	0.1	1.8	1.8	0.1	3.8	3.8
	S	1.64	1.26	2.07	3.61	2.91	4.63
GLONASS	E	0.0	0.7	0.7	0.0	1.2	1.2
	N	0.0	0.8	0.8	0.0	1.3	1.3
	U	0.7	4.3	4.4	0.7	5.6	5.7
	S	3.65	2.66	4.52	5.0	3.21	5.94

For other constellations, although the Leica receivers observed the BeiDou constellation on the UK site, due to the limited number of visible satellites (MEOs and IGSOs satellites; Fig. 4.11) with 15° cut-off elevation angle, the positioning with current BeiDou satellites has a marginal effect on the UK site.

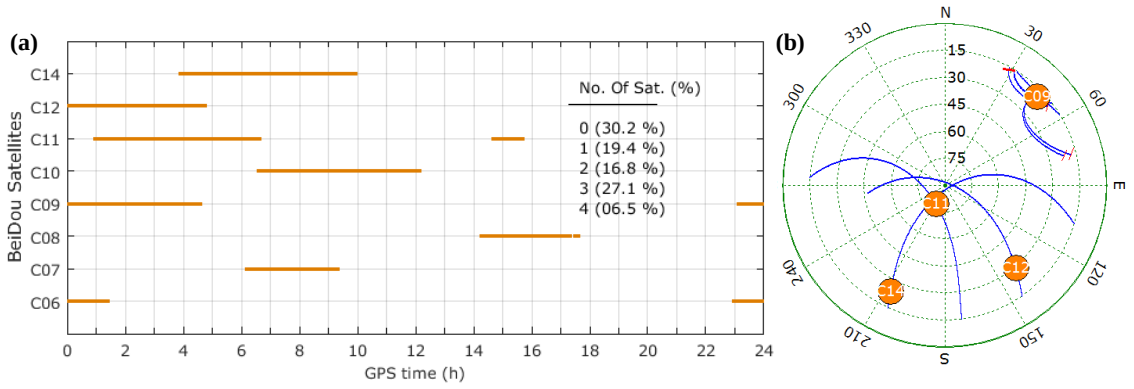


Fig. 4.11 (a) The visibility of BeiDou satellites that tracked by Leica receivers for 24h at the UK site on 05/03/2015 and (b) the sky-plot of tracked satellites.

Along the whole day, the maximum number of valid satellites appeared at the time of observation was four satellites which constitute 6.5% for 24h, while 30.2% of no satellites appeared on the UK site for the same daily duration as shown in Fig. 4.11a. Furthermore, it is observed the weak coverage of BeiDou satellites in the northern sky as illustrated in Fig. 4.11b. In addition, a limited number of Galileo satellites was operating at the time of the experiment, which cannot perform autonomous positioning. Thus, the GNSS assessment will analyse and evaluate for GPS and GLONASS at the UK site.

In general, the statistical results as expressed in Table 4.2, show that the pair of Leica receivers has lower noise level for all the components (i.e. N, E, U) and solutions (i.e. GPS, GLONASS) for the zero baseline. Therefore, the Leica receivers were used at the UK site for the investigation of the performance of GNSS positioning.

4.4.2 Preliminary Analysis at the China Site

The China site offers the option to track more GNSS constellations than that for the UK site, depending however on the ability of receivers to track the available signals. Apart from the analysis of the positioning solutions using GPS and GLONASS constellations, as in the UK site, in China site could also be analysed the accuracy of the positioning using BeiDou system and the contribution of other GNSS measurements provided from Galileo, QZSS and SBAS.

To examine the positioning performance over different receivers, four pairs of receivers were used at China site (Fig. 4.1). Following the same procedure as the UK site, from the four pairs of receivers, it was defined the pair of receivers with the most reliable measurements and overall lower noise level.

Firstly, to perform the comparison of the GPS-only solution with zero baseline measurements at this site, the same interval of 1h at this site was chosen to coincide with that for the UK site. The four pairs of receivers observed the identical GPS satellites (Fig. 4.12) and their solutions are represented in time series (Fig.4.13), while the statistical comparison between their results is summarised in Table 4.3.

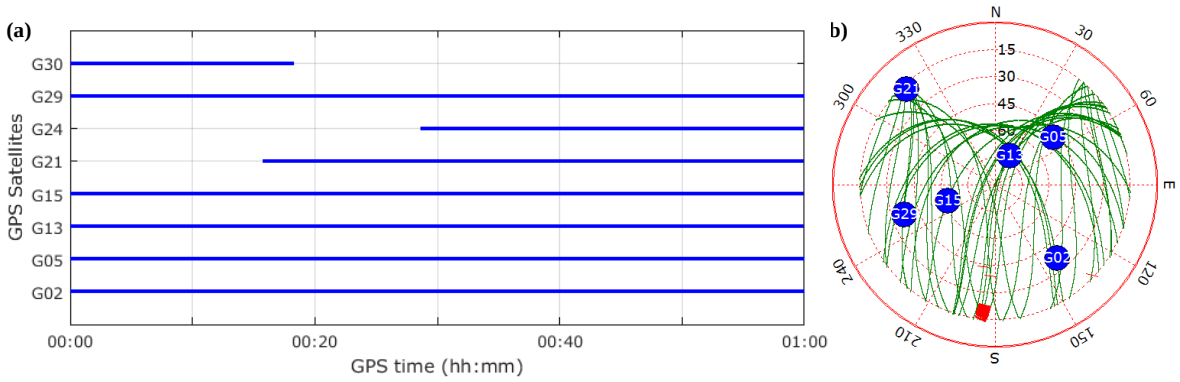


Fig. 4.12 (a) The visibility of GPS satellites for the first hour at China site on 05/03/2015 and (b) the sky-plot of tracked satellites.

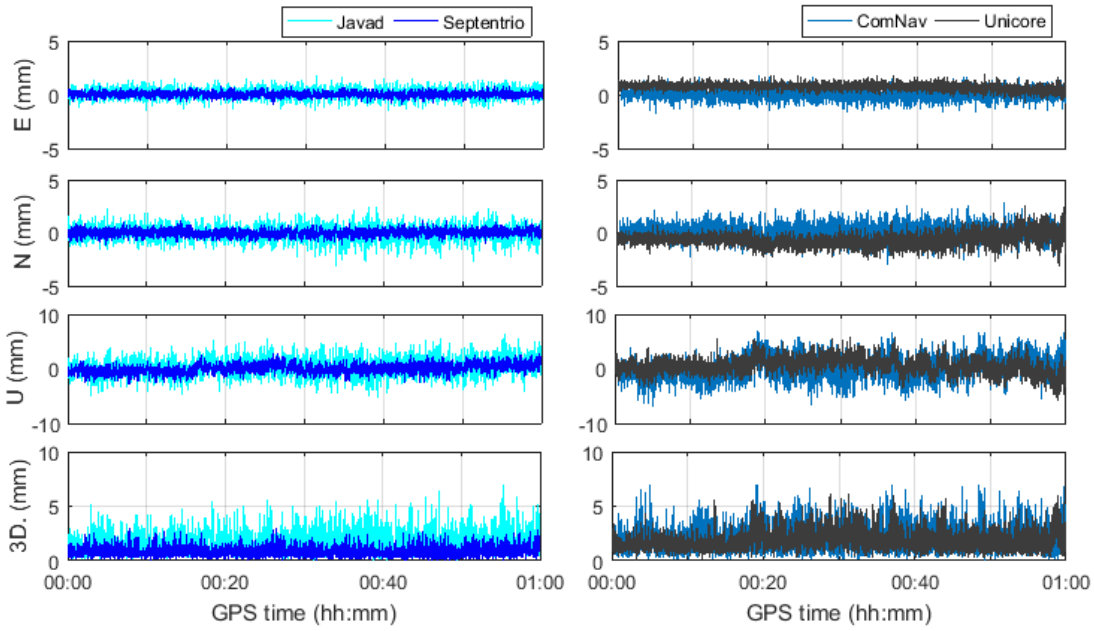


Fig. 4.13 GPS time series of the zero baseline records by four pairs of receivers at China site, on 05/03/2015.

Table 4.3 Comparison of statistical results of time series of zero baseline with GNSS solution for 24h using collocated receivers at the UK site on 05/03/2015.

Receiver type	Mean (mm)				STD (mm)				RMS (mm)			
	E	N	U	S	E	N	U	S	E	N	U	S
Septen.	0	0	0	0.85	0.2	0.3	0.9	0.48	0.2	0.3	0.9	0.98
Javad	0.1	0	0.3	1.63	0.5	0.7	1.7	0.99	0.5	0.7	1.7	1.91
ComNav	0	0	0.1	2.00	0.5	0.8	2.1	1.21	0.5	0.8	2.2	2.34
Unicore	0.7	-0.6	0.6	1.86	0.3	0.7	1.6	0.94	0.8	0.9	1.7	2.09

The comparison of the four receivers for the positioning using the GPS-only solution in China site indicates a weak performance of the Unicore receivers. More specifically, the time series of all three components (i.e. N, E, U) of the Unicore receivers are significantly noisy, with their mean averages deviated from zero. On the contrary, the Septentrio receivers show the least noisy performance, from all the receivers in this site, with the minimum standard deviation of N, E and U components relative to the other receivers. Further analysis of the time series was made by applying the autocorrelation function to diagnose the systematic effects in measurements (Craymer, 1999).

Figure 4.14 presented the results of the autocorrelation analysis for each pair of receivers for horizontal components. The correlogram shows the uncorrelated results of the three pairs of receivers and expresses mainly white noise, while data of Unicore receivers have slight biases. The latter reinforces the above observation that the processed data of GPS-only with Unicore receiver is inappropriate for the zero-baseline measurements.

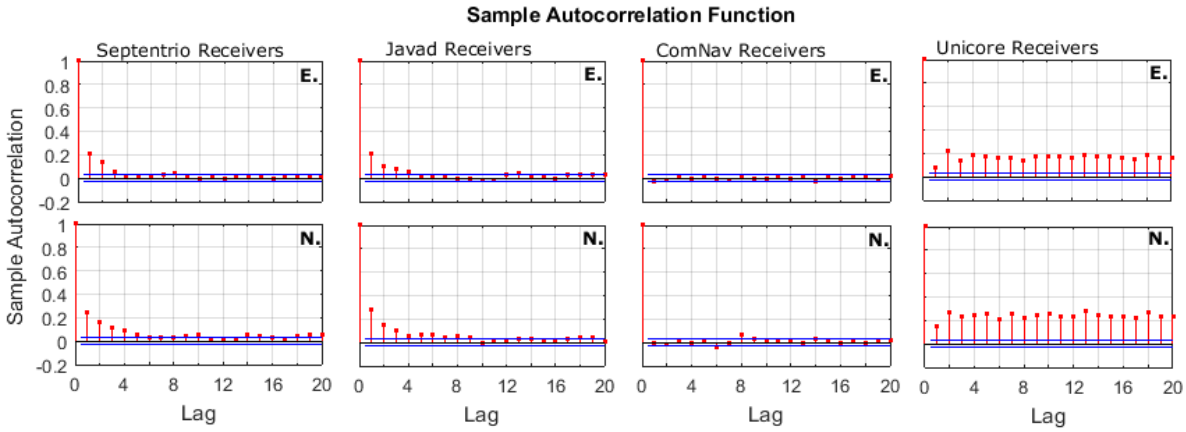


Fig. 4.14 Autocorrelation of E and N components of zero baseline of GPS records of Fig. 4.13.

The positioning of the second autonomous GNSS constellation that can be analysed in China site is GLONASS. Septentrio, Javad and ComNav receivers recorded GLONASS satellites signals. However, the ComNav receivers failed to fix the ambiguity resolution for the GLONASS-only solution due to inter-frequency biases between the two ComNav receivers. Thus, the performance of GLONASS positioning will be assessed with both pairs of Septentrio and Javad receivers.

At the China site, the GLONASS only solution suffers from a weak geometry along several intervals, and that leads to the variable performance of each pair of receivers. Therefore, an interval of 1h is insufficient to assess the performance of the positioning time series of these pairs of receivers. The 24h-period solution for the GLONASS-only process shows the problematic noisy periods, which occur when the satellite geometry is weak, and the no solution intervals, which occur when the number of satellites less than 4 or the GDOP values are more than 30 (Fig. 4.15).

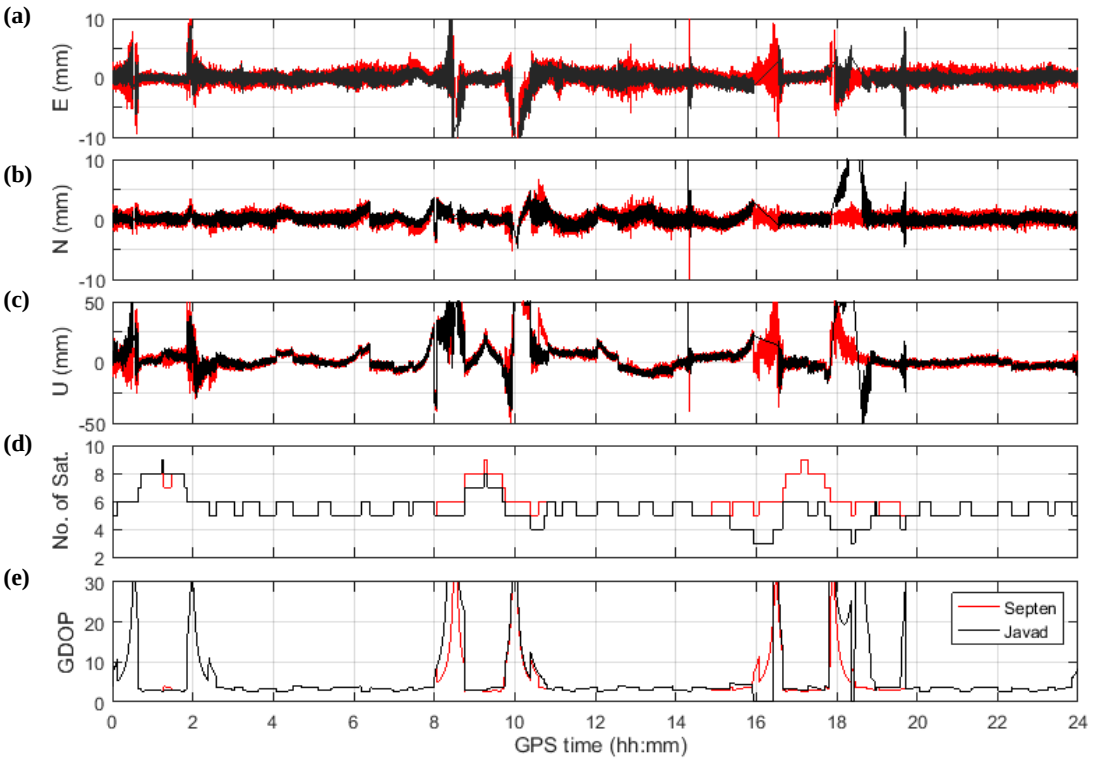


Fig. 4.15 (a-c) the zero baseline components achieved with a GLONASS-only solution by Septentrio and Javad receivers, (d) comparison of a number of valid satellites and (e) the GDOP values produced for 24h at China site on 05/03/2015.

Along the 24h with 1 Hz recording data, the total number of epochs should be 86400 (100%). However, the positioning solution of Septentrio receivers resulted in 84811 epochs (98.16%), while the Javad receivers resulted in 81386 epochs (94.20%). The loss of computed positions is a result of this weak geometry of GLONASS in China Site. Moreover, the overall RMS values for the whole 24h period of a GLONASS-only solution of the Septentrio receivers are 1.3mm, 0.9mm and 13.1mm for the E, N and U components of the zero baseline, respectively, while for the Javad receivers are 1.4mm, 1.3mm and 15.9mm, respectively. These results indicate that the GLONASS solution of the Septentrio receivers is less noisy and reliable, which can be used for the analysis of the multi-GNSS performance.

The other dominant GNSS constellation available at the China site is BeiDou. To assess the precision of a BeiDou-only positioning solution across the four pairs of receivers the same approach as the other constellations were followed. For a short duration of 1h, there were ten BDS satellites visible in total, and all receivers observed eight of them, while other two (grey colour) were only observed by Unicore receivers (Fig. 4.16).

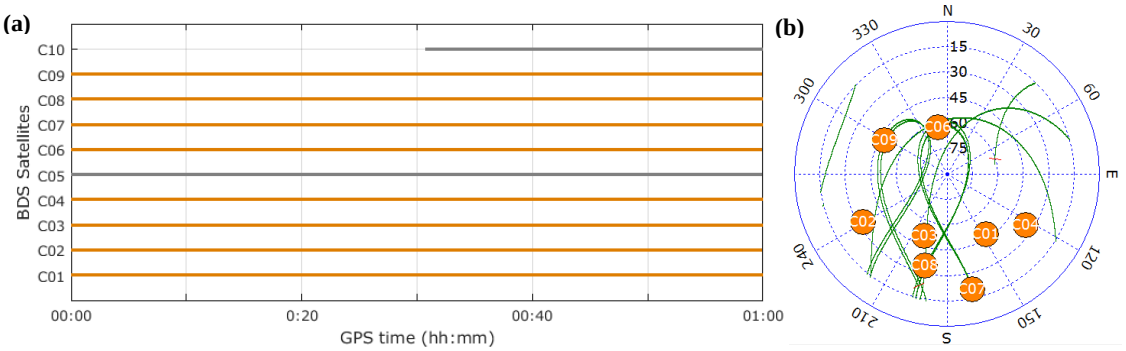


Fig. 4.16 (a) The visibility of BDS satellites for the first hour at China site on 05/03/2015 and (b) BDS sky-plot of tracked satellites.

To have comparable results, only the eight observed satellites undertaken in this evaluation. Table 4.4 presents the statistical results to compare the BDS positioning quality for all four pairs of receivers. From this table, it is clear that the minimum RMS values were achieved with the Unicore receivers followed by the ComNav receivers, while both the Septentrio and the Javad receivers have more substantial noise levels as represented in Fig. 4.17.

Table 4.4 Statistical results of BDS positioning derived from zero baseline measurements for 1h (00:00 – 01:00) using collocated receivers at China site on 05/03/2015.

Receiver type	Mean (mm)				STD (mm)				RMS (mm)			
	E	N	U	S	E	N	U	S	E	N	U	S
Septen.	0	-0.1	3.3	5.25	0.4	2.2	4.8	3.38	0.4	2.2	5.8	6.24
Javad	0	0	4.2	5.40	1.0	1.1	4.5	3.36	1.1	1.1	6.2	6.36
ComNav	0	0	3.4	3.69	0.5	0.6	2.5	2.13	0.5	0.6	4.2	4.26
Unicore	0	0	2.9	2.93	0.2	0.2	1.7	1.66	0.2	0.2	3.4	3.36

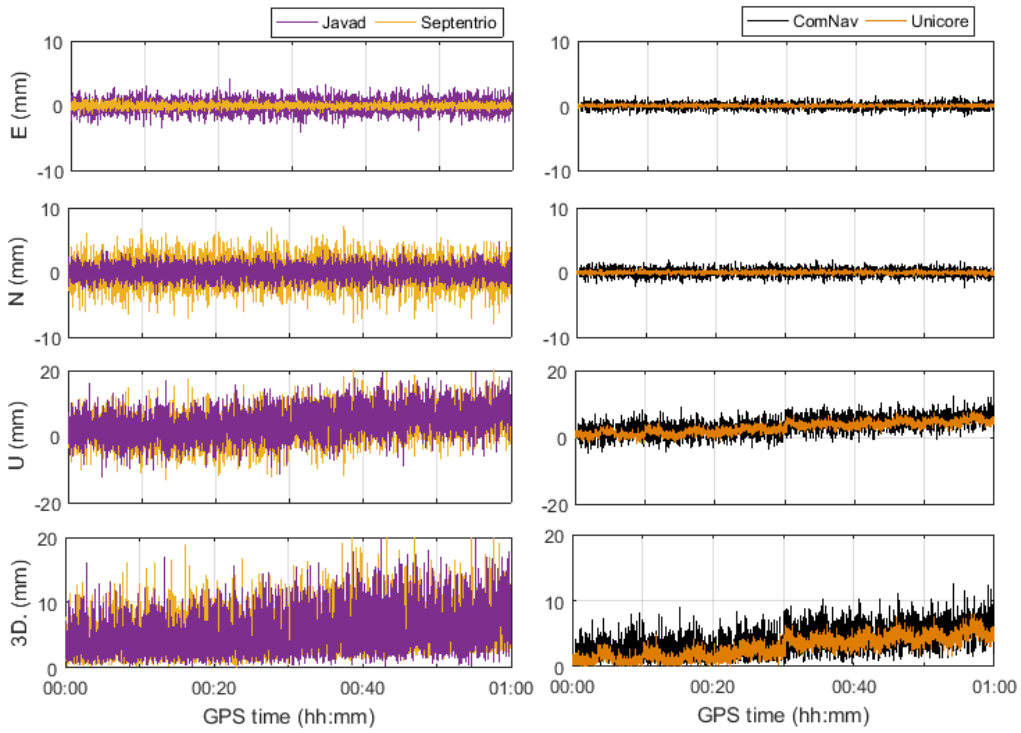


Fig. 4.17 Time series of BDS-only solution for three components and 3D residual at China site on 05/03/2015.

To verify the quality of the BDS data autocorrelation analysis was applied. Based on the autocorrelation analysis it is proved that the horizontal components for each pair of receivers are uncorrelated, while for the U components, the Unicore receivers, which have the lowest RMS, proved to be highly correlated (Fig. 4.18).

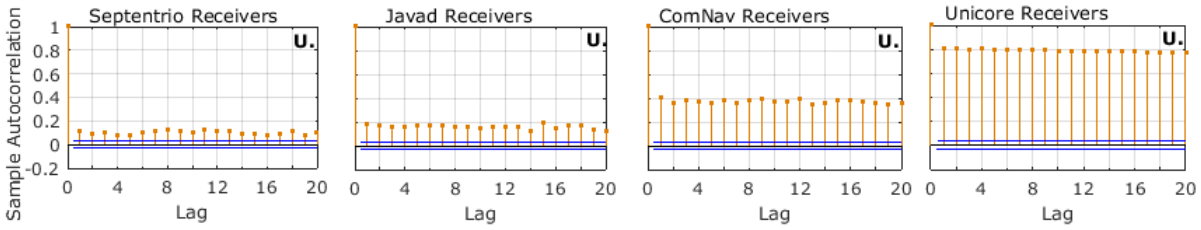


Fig. 4.18 Autocorrelation of U-components of zero baseline of BDS records of Fig. 4.17.

This means that the Unicore receivers reduce the noise level, but the noise is correlated having characteristics of coloured noise. On the contrary, the Septentrio receivers, which have the highest RMS, are characterised by the lowest correlation (Fig. 4.18).

For the performance of other constellation such as Galileo, QZSS and SBAS, due to the limited number of their satellites, they were only analysed in combined solutions.

Finally, the results of the preliminary analysis indicate that the data of Septentrio receivers can be adapted to investigate the GNSS performance for GPS, GLONASS and their combination. As a BeiDou constellation is receiver dependent, it can analyse the dataset of Septentrio receivers in comparison to other ComNav receivers to assess BeiDou performance and its combination with GPS solution. The derived solution from the selected receivers may contaminate by outliers due to some events of cycle slips or jumps. To diagnose all these effects and exclude them, the data quality analysis is required to have clean data for assessment.

4. 5 Data Quality Analysis

In general, the quality of the observed data is affected by the multipath and obstruction conditions of the surrounding environment, which has a significant influence on the derived position and their accuracy (Mosavi and EmamGholipour, 2013). However, in zero-baseline measurements, those error sources are expected to be eliminated (Zhang and Teunissen, 2016). Thus, the errors, which remain in the residuals, are errors due to noise effect with the impact of satellite geometry.

In some cases, the residuals of the GNSS process diverge significantly from the mean residuals trend, expressing higher noise level due to observations of poor quality or the impact of problematic satellites, which may lead to cycle slips, etc. To detect the problematic satellite or low-quality observations, the Signal-to-Noise ratio (SNR) of the satellite signals and the residuals are analysed. For example, when processing the data for the time interval between 07:00 to 14:00 on 05/03/2015 at China site, the time series of apparent solutions was characterised by outliers, represented as

"spikes" and sudden jumps in specific intervals as shown in Fig. 4.19a. These outliers are caused by problematic or weak satellite(s), which can be excluded in processing to have clean data as illustrated in (Fig. 4.19b); (Tokura et al., 2014).

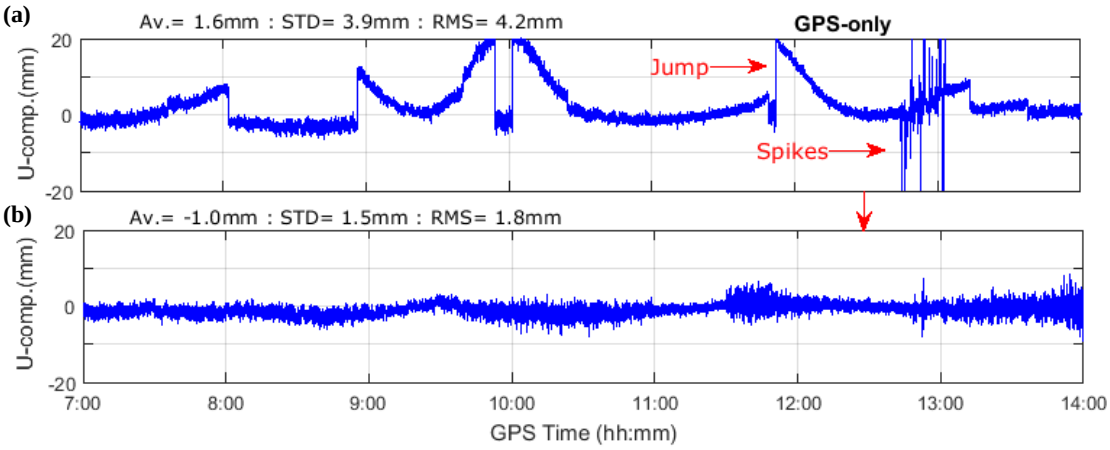


Fig. 4.19 Time series of U-components of GPS-only at China site (a) apparent solution (b) refinement solution after excluding weak satellites.

It can be noticed that the achieved precision was improved after removing the effect of these outliers. The RMS of the apparent solution was 4.2mm, while it becomes 1.8mm after refinement of the time series from these outliers. To explain the refinement of the outliers in above observed data, the time interval between 12:00 to 13:00 can be analysed as representative example of many spikes characterise the U-component (Fig. 4.20a).

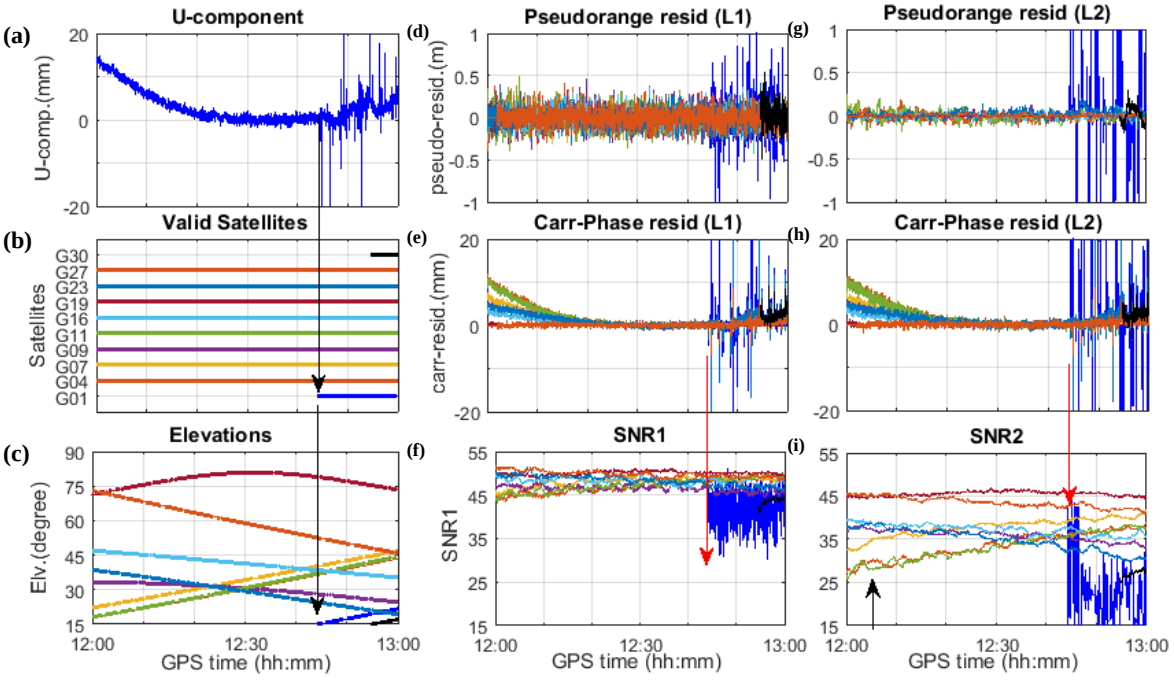


Fig. 4.20 Analysis to detect the problematic and weak satellites along the interval 12:00-13:00 at China site (a) time series of U-components of GPS-only (b) valid observed satellites (c) corresponding elevations of satellites (d-e) residual analysis on L1 (f) SNR1 (g-h) residual analysis on L2 and (i) SNR2.

The analysis of residuals and SNR of the satellites revealed that these spikes occur when satellite G01 is introduced to the solution. G01 is a rising satellite with low SNR on both L1 and L2 (Fig. 4.20f and i) which caused multiple cycle slips, appearing as outliers in the time series. Probably, the receivers lost the lock on this satellite leading to the cycle slips (Chen et al., 2015a).

Due to the adequate availability of satellites, excluding G01 can improve the results especially in U-component, with the elimination of the outliers and the computed RMS of U-component being reduced to 4.5mm from the initial 4.9mm (Fig. 4.21b).

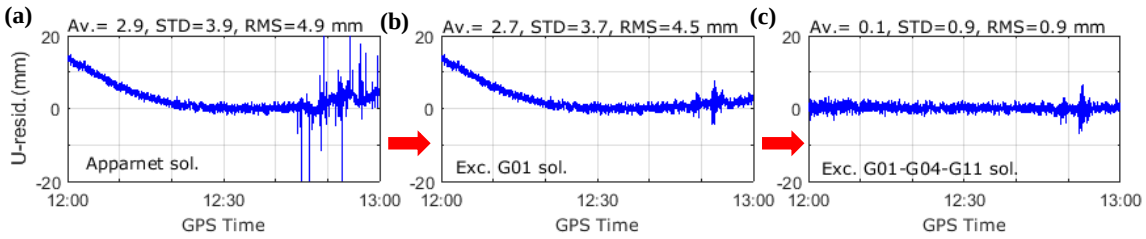


Fig. 4.21 Sequential improvement of time series of U-components of GPS-only at China site (a) apparent solution (b) Excluding G01 satellite (c) Excluding G01, G04 and G11 satellites.

However, the spikes are removed; the trend of time series still diverges from the mean value, which required another refinement. From the analysed data, it was observed that both G04 and G11 (Fig.4.20) were of relatively low elevation, expressed through the low SNR on (L2), affecting the derived time series. By excluding these two satellites and G01, the RMS is reduced even more to 0.9mm (Fig.4.21c).

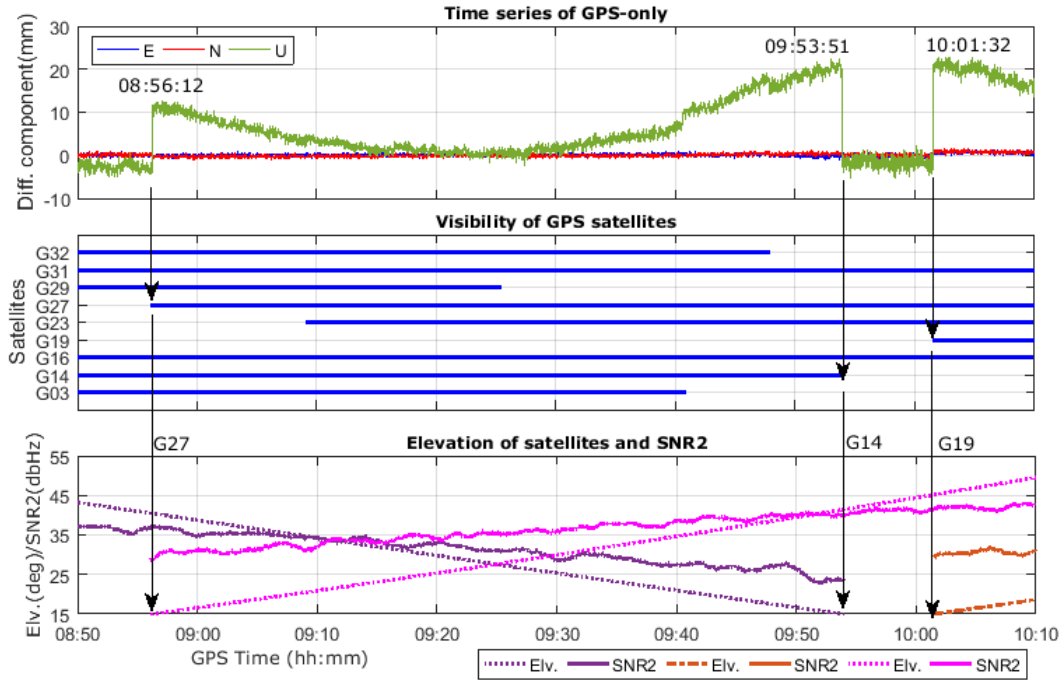


Fig. 4.22 The time series of GPS-only at China site (top), valid satellites (middle) and elevation angles and SNR2 of valid satellites (bottom).

Regarding the jumps in the positioning solution, these are likely due to the sudden change in the number of valid satellites and the quality of the satellite signal. For instance, the introduction or exclusion of an ascending or descending satellite, of low elevation angle and/or low Signal-to-Noise ratio (SNR) may lead to a jump in the derived time series as shown in Fig. 4.22.

From this figure, it is apparent when the rising satellite G27 with an elevation angle of 15° and low SNR2 introduce to a solution; this jump occurs at 08:56:12. Similarly, when descending satellite of G14 departs the solution at 15° elevation angle with deteriorating SNR2, the jump appears in the time series of the solution as well as for G19 at the next event. It can be noticed that these jumps affect the vertical component more than the horizontal ones in the derived solution (Fig. 4.22) due to satellite geometry.

Likewise, jumps also occur when the state of the ambiguity resolution is changing from fixed to float, indicating the introduction of observations (e.g. new satellite in the solution) which produces an inconsistency into the Kalman filter solution (Zhao et al., 2014). These jumps can be removed by excluding certain satellites of lower SNR during the occurrence periods, which improves the RMS of the derived solution. Meanwhile, the introduction of the new satellites with better quality of the signal (i.e. higher SNR) does not cause jumps, as well as when there are enough redundant satellites.

The same methodology can be followed with other GNSS constellations to improve the derived time series. However, the enhancement of the solution by excluding one or more satellites occurs when a sufficient number of valid satellites are available. In the case of a limited number of satellites, though, the exclusion of one or more satellites affects the availability of the final solution, due to the reduction of the total number of available satellites and/or the degradation of the satellite constellation. For example, it was found in the time series of the UK site that the satellite G25 causes cycle slips for many epochs during the interval between (17:15 – 17:30) on 05/03/2015, and by excluding this satellite from GPS only solution, the percentage of final fixed positioning will be degraded.

For these cases, when a problematic GPS satellite suffers from weak SNR that affects the final GPS-only solution and caused spikes along the derived time series, the combined GPS with other GNSS constellation will remove the effect of these spikes without excluding any GPS satellite. This is attributed to increasing the number of valid satellites and improving the satellite geometry. As the number of the satellites increases, this will enlarge the dimension of the observation equation and limits the impact of the problematic satellite. For the same reason, when the effect of the problematic satellite is caused by cycle slips that lead to apparent spikes in the time series, the combined solution of GPS with other GNSS will reduce the effect of this problematic satellite as a result of improved solution. To remove this effect, the affected problematic GPS satellite needs to be excluded and the solution compensated by other satellites from another GNSS constellation through a combined solution. Hence, the application of combined solution leads to (i) limit the impact of the problematic

satellite, (ii) eliminate the effect of cycle slips, (iii) retain the availability and provide a fixed solution of potentially improved precision.

4. 6 Availability and Positioning Precision

The availability of a fixed solution is defined as the percentage of the number of epochs that have a valid fixed solution to the total number of observed epochs (T. Takasu, 2013). By following the same methodology of the preliminary analysis, the availability and positioning precision was investigated for different combinations of multi-GNSS solutions at the UK and China sites for time-period of the 12 consecutive days.

Thus, the differencing between the derived GNSS coordinates of observed station and its true values represent the residual at each epoch, which can be express as time series of E, N and U components for different GNSS combinations. Those time series were used to assess the performance of the different constellations, through the positional precision and fixed solution availability.

4.6.1 Availability and Precision at the UK Site

For the UK dataset, three different GNSS solutions were examined: (i) GPS only, (ii) GLONASS only and (iii) combined GPS+GLONASS. When implementing these different solutions along the daily data set on 05/03/2015, it is obvious that gaps characterise the GPS-only solution in three-time separate intervals (Fig. 4.23).

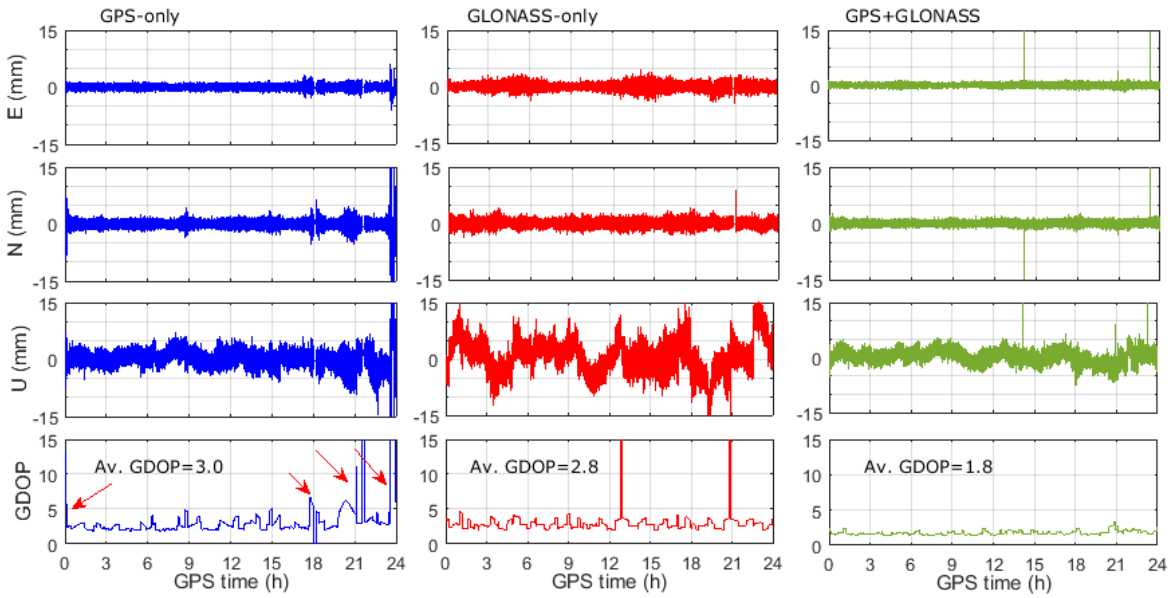


Fig. 4.23 Daily time series showing GPS-only (left), GLONASS-only (centre) and combined GPS + GLONASS (right) with Rec. UK1 receiver (UK site) on 05/03/2015.

The first gap interval along the GPS time series was caused at the time interval between (18:00:01 – 18:14:00) as a result of a limited number of valid satellites, whereas only three satellites were available during this interval when the cut-off elevation angle is 15°. The other gap intervals occur

at periods of (21:32:47 – 21:45:36) and (23:37:04 – 23:48:15) due to high DOP values (i.e. >30). On the other hand, there are two gap intervals along the GLONASS time series observed at intervals (12:52:02 – 12:55:46) and (20:46:17 – 20:55:45) due to available of only four satellites at these intervals which leads to high DOP values.

The availability of a GPS fixed solution was 97.4%, while there are significantly fewer gaps in the corresponding GLONASS-only time series with an availability of 99.1% (Table 4.5). By using a combined solution of GPS and GLONASS, the availability increases up to 100%. The enhanced availability of the combined GNSS solution proved that the increasing number of valid satellites could overcome problematic periods, where gaps characterise the GPS-only or GLONASS-only solutions.

Table 4.5 Results of the daily GNSS-solutions for the UK site (Leica 24-h) on 05/03/2015.

GNSS Solution	No. of total epochs	No. of fixed epochs	No. of unfixed epochs (gaps)	Percentage of fixed solved solution (%)	RMS of positional precision (mm)		
					E	N	U
GPS-only	86,400	84,129	2,282	97.4	0.5	0.9	2.0
GLONASS-only	86,400	85,610	790	99.1	0.7	0.8	4.4
GPS+GLONASS	86,400	86,400	0	100	0.4	0.5	1.7

Regarding the precision of the positioning, it is observed that the GPS-only solution is more accurate than the GLONASS-only solution in the E and U components, while the GLONASS-only solution proved to be more precise for the N component (Table 4.5).

In this dataset, the GPS + GLONASS combination gives the more accurate solution for all components. Therefore, it can be concluded that the combined GPS with other GNSS solution can improve the availability of a fixed solution and enhance the positional precision with clean data (Liu et al., 2016).

The combination of GPS and GLONASS leads to enhanced satellite geometry, which is expressed through the reduction of the DOP values (Odolinski et al., 2015, Odolinski and Teunissen, 2016), improving the achieved precision. Furthermore, all outliers in the individual solutions due to poor satellite coverage (e.g. Fig. 5.23, at 18:00–18:30 or 20:00–21:00, marked by red arrows) are removed, with the mean of the GDOP being improved by 60%; e.g. the GPS + GLONASS solution provides mean GDOP of 1.8, while for GPS- only and GLONASS-only solution are 3.0 and 2.8, respectively.

From the above results (Fig. 5.23 and Table 4.5), it can be noticed that the combined solution has a slight improvement over the daily solution. However, the obvious improvement of the combined solution can be identified over relatively short durations when GPS-only is noisy. For example, the hourly duration of the GPS-only solution at the interval between (20:00 – 21:00) was noisy especially in the N and U components, while the results of combined GPS+GLONASS solution achieving more accurate results than the GPS only solution, as shown in Fig. 4.24.

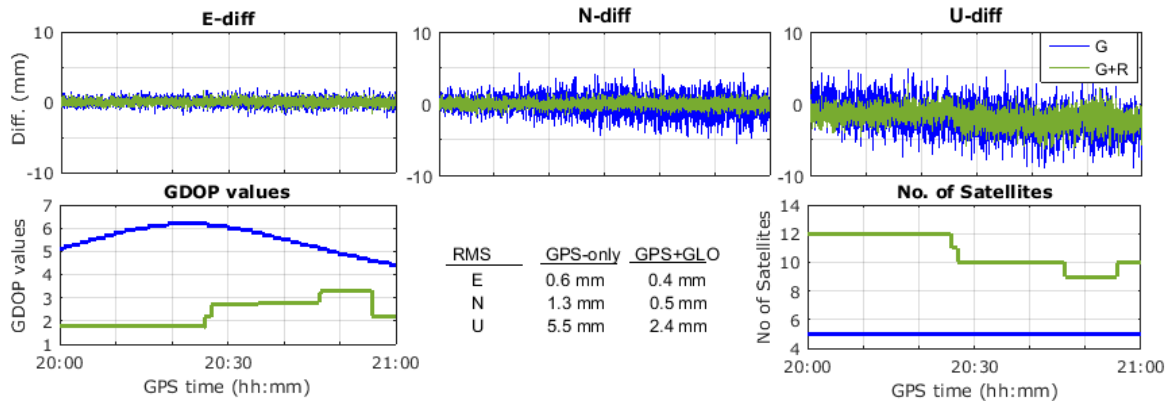


Fig. 4.24 Comparison between GPS-only and combined GPS + GLONASS for 1-h duration at the UK site (Leica receivers) on 05/03/2015.

The achieved precision of the combined GPS+GLONASS solution at this 1-h period is (0.4, 0.5 and 0.4mm), while the corresponding precision with the GPS-only solution is (0.6, 1.3 and 2.1mm) for E, N and U components, respectively.

The small differences in the achieved results (i.e. positions and their precision) between the solutions of different combinations and the existence of some outliers result in differences between the achieved precision. Therefore, to present the achieved precision of different GNSS solutions in the further statistical analysis, a Cumulate Distribution Function (CDF) can be used to visualise the distribution of achieved results by their cumulative distribution (Pianosi and Wagener, 2015).

A CDF assess visually the "*proportion of data less than or equal to (x) values as a function of (x), which computes by assigning the probability 1/x to each of x observations in a data sample (Salós et al., 2010).* Thus, the values along the y-axis are equivalent to cumulative probability from zero to one. The results of the GNSS mentioned above solutions are achieved in kinematic mode by determining the position at every epoch by computing the evaluated precision along every component of E, N and U. The visual comparison between the achieved precision of this different GNSS solution can display by generated the belonging CDF plots. Therefore, the CDFs of achieved STDs of GPS-only, GLONASS-only and combined GPS+GLONASS solutions on 05/03/2015 are represented in Fig 4.25.

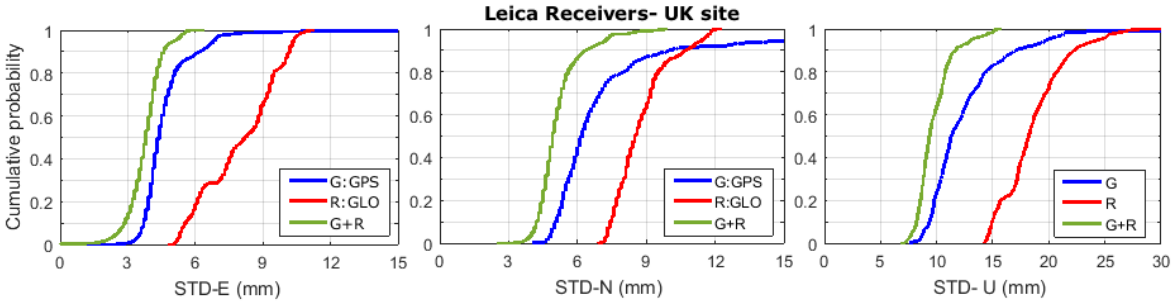


Fig. 4.25 Comparison between achieved precision (STD) with different GNSS solutions of Fig.5.23 on CDF analysis using the same daily data of Leica receiver on 05/03/2015.

The represented CDF results indicate that the combined solution has achieved the minimum STD along all components. At the same time, the CDF graphs show more accurate results of GPS along E and U components, while the results of N component with GLONASS is better. These findings agree with the previous analysis that relies on the achieved RMS for every GNSS solution.

For a GPS-only solution at this site, it can be noticed that the E-component is more accurate than the N-component. This may attribute to the number of satellites in an N-S direction at the UK site is less than that of E-W direction (Meng et al., 2003, Cosser et al., 2003). As the inclination angle of GPS orbit is 55°, this enables to track the majority of satellites in the area between 55°N and 55°S with fewer satellites beyond this area. As the UK is site located within 53°N, few satellites can be tracked in the North. On the other hand, the distribution of GLONASS satellites at the UK site in N-S direction is better than that of GPS due to the design of GLONASS with an inclination angle of 64.8°. For this reason, there is a slightly outperforming N-component of GLONASS than that of GPS.

To assess the performance of different GNSS solutions along other days, the observations of 12 consecutive days between the 5th and 16th March were analysed to evaluate the availability and precision of each GNSS daily solution. For availability of fixed solution, it is clear that the GLONASS-only solution has (in general) slightly better availability than the GPS-only solution, due to a fewer data gaps with GLONASS compared to the GPS solution (Fig. 4.26a).

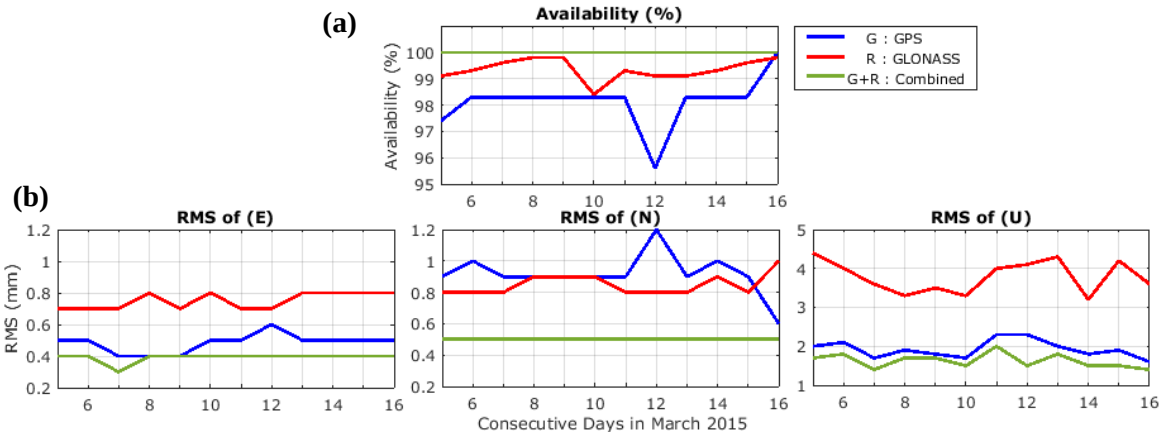


Fig. 4.26 (a) Availability and (b) precision expressed as RMS at the UK site over the 12 days.

The gaps are the results of the weak geometry of the valid satellites when the solution corresponds to extremely high DOP values (i.e. GDOP > 30), which are excluded from the final solution by the software, or fundamentally there is no solution due to a limited number of satellites (<4) at these intervals. This leads to a more considerable difference in GPS availability corresponding to ~50 min during the daily records (i.e. 12th March). Therefore, the combination of GPS + GLONASS solution increases the number of valid satellites and gives the highest availability reaching up to 100% for the entire examined period.

Regarding the analysed precision, the GPS-only solution tends to be more accurate than the GLONASS-only solution for the E and U components as observed along the entire 12-days period (Fig. 4.26b), while GLONASS-only solution proved to be more accurate though for the N component, due to the GLONASS constellation design as mentioned above.

4.6.2 Availability and Precision at the China Site

The GNSS records of the dataset in China were analysed following the same approach as for the GNSS records of the UK site, with the only difference being the additional constellation of BeiDou and all the possible combinations of it with GPS and GLONASS. When analysing daily different GNSS solutions as summarised in Table 4.6, the results of independent constellations on 5th March showing that both GPS and BeiDou have an optimum availability of 100% fixed solution, which indicates a perfect coverage due to the adequate number of satellites.

Table 4.6 Results of the daily GNSS-solutions for the China site (Septentrio 24-h) on 05/03.

GNSS Solution	No. of total epochs	No. of fixed epochs	No. of unfixed epochs (gaps)	Percentage of fixed solved solution (%)	RMS of positional precision (mm)		
					E	N	U
GPS-only	86,400	86,400	0	100	0.3	0.4	2.4
GLONASS-only	86,400	84,744	1,656	98.1	1.3	0.9	13.1
BDS-only	86,400	86,400	0	100	0.7	1.8	4.4
GPS+GLONASS	86,400	86,400	0	100	0.3	0.3	2.3
GPS+BDS	86,400	86,400	0	100	0.5	1.1	2.9
GPS+GLO+BDS	86,400	86,400	0	100	0.4	0.8	2.4

Regarding the GLONASS-only solution, the corresponding availability of a fixed solution is slightly lower (i.e. 98.1% on 5th March). This is the result of a few weak periods, where enough GLONASS satellites are available but with weak geometry.

The weakness of GLONASS geometry is caused during a couple of intervals, which repeated within eight hours along the whole day as shown in Fig. 4.27. During these couple of intervals extremely high DOP values occur, which can reach more than 30 even with the existence of six satellites in those epochs. When analysing the valid satellites at these intervals, it was found that the elevation of the reference GLONASS satellite was lower than 50°. The geometry was improved during periods when the number of satellites was more than six as shown in the first period of Fig. 4.27. On the other hand, when five GLONASS satellites are available, and the reference one among them has a high elevation, the low DOP value can achieve as shown in the third period of Fig. 4.27.

For other specific periods, it was observed when the GLONASS constellation consisted of five satellites with two of them being very spatially proximate, resulting in a constellation of practically four satellites, which was also reflected in high DOP values (Fig. 4.28b).

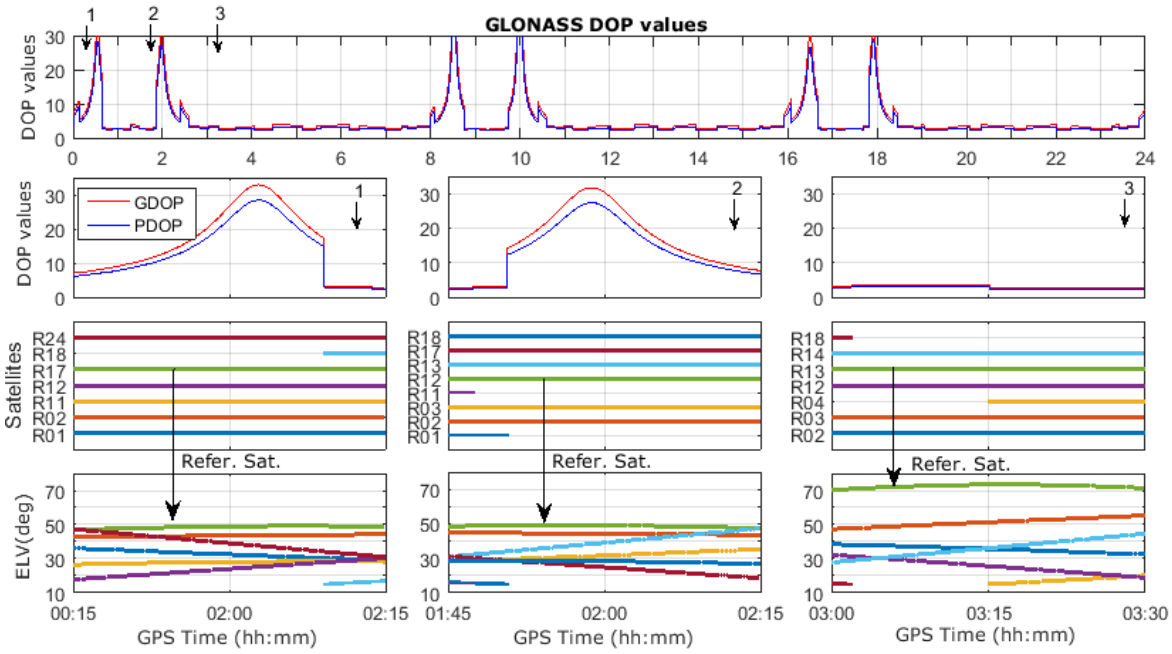


Fig. 4.27 Analysis the geometry of specific GLONASS intervals (left and middle) weak geometry with six satellites and (right) five satellites with good geometry in China site (05/03/2015).

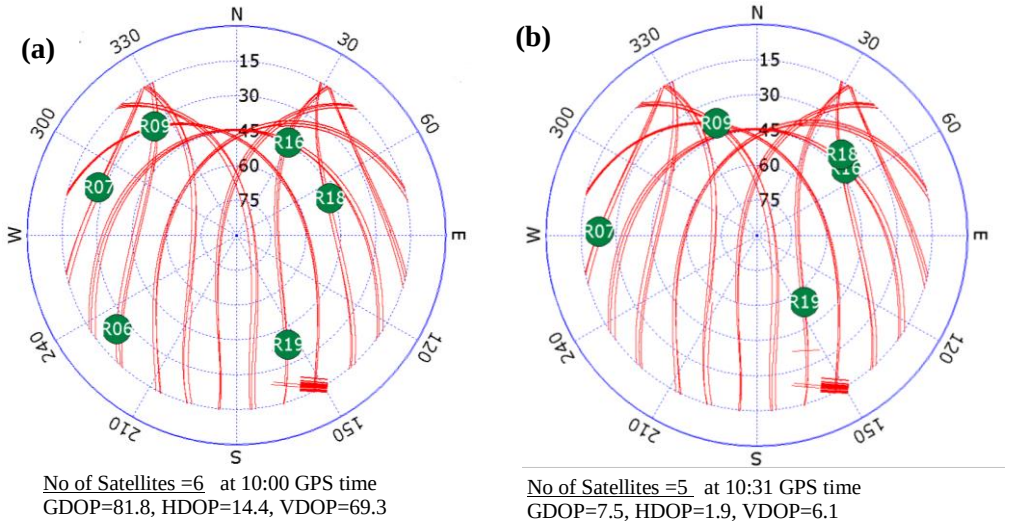


Fig. 4.28 Sky plots of specific intervals of the weak geometry of GLONASS satellite constellation: (a) six satellites with the reference one of elevation under 50° and (b) five satellites with overlap between two of them in China site (05/03/2015).

According to the achieved precision, the GPS-only solution in China has a similar precision to that of the UK site, with a significant improvement of RMS though in the North component (~0.4 mm in China versus 0.8–0.9 mm in the UK), due to the improved constellation (Fig. 4.29).

Regarding the high values of RMS (i.e. 1.3 mm, 0.9 mm and 13.1 mm for E, N and U respectively; Table 4.6) of the GLONASS only solution, these are mainly due to the periods of poor satellite constellation (as related above) with the weak satellites geometry.

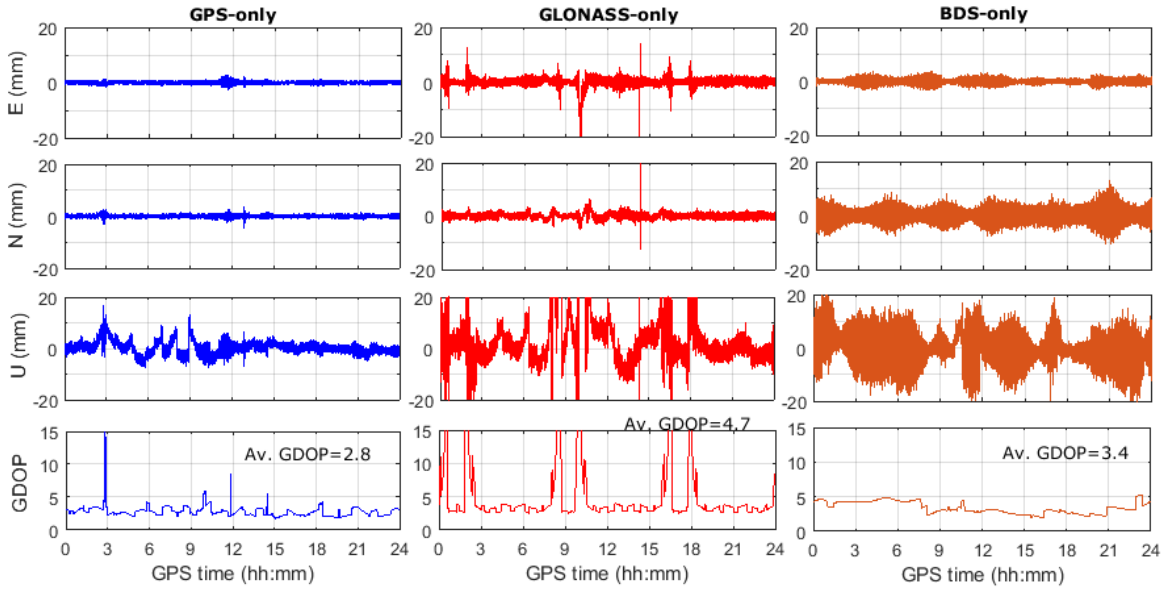


Fig. 4.29 Daily time series with GPS-only (left) GLONASS-only (centre) and BeiDou-only (right) with Septentrio receivers in China site on 05/03/2015.

The GLONASS-only solution is of similar accuracy in North component with that of the UK site. However, the E and mainly U components have significantly worse accuracy than that of the UK, with the RMS in U component reaching up to 13 mm (Table 4.6). The variation of the RMS of E and U components is of similar pattern, indicating that probably both are affected by the GLONASS poor constellation, with a more significant impact on the U component.

Regarding the BeiDou-only solution, the achieved precision of the solution proved to be receiver dependent (Fig 4.29). Although the comparison between different receivers led to the selection of Septentrio receiver, as it achieved the minimum level of noise for both GPS and GLONASS constellations, however, the corresponding BeiDou solution was very noisy. On the contrary, the Chinese receiver (ComNav) led to less noisy of BeiDou solution (Fig.4.30), while the corresponding GPS solution was of high noise level (Table 4.7).

Table 4.7 Results of the daily GNSS-solutions at the China site according to achieved precision with two different sets of receivers on 05/03.

Receiver type	GPS-only RMS (mm)			GLONASS-only RMS (mm)			BDS-only RMS (mm)			GPS+GLONASS RMS (mm)			GPS+BDS RMS (mm)		
	E	N	U	E	N	U	E	N	U	E	N	U	E	N	U
Septen.	0.3	0.4	2.4	1.3	0.9	13.1	0.7	1.8	4.4	0.3	0.3	2.3	0.5	1.1	2.9
ComNav	0.6	0.7	3.0	---	---	---	0.4	0.6	2.7	---	---	---	0.3	0.4	2.1

Therefore, the positional precision of GPS-only, BeiDou-only were investigated using these two receivers, with the corresponding results being summarised in Fig. 5.30 and Table 4.7. The significantly improved precision of the ComNav receiver for the BeiDou-only solution is probably

due to the compatibility of the receiver with the BeiDou system and the better quality of decoding of the signal from the BeiDou satellites relatively to that achieved by the Septentrio receivers.

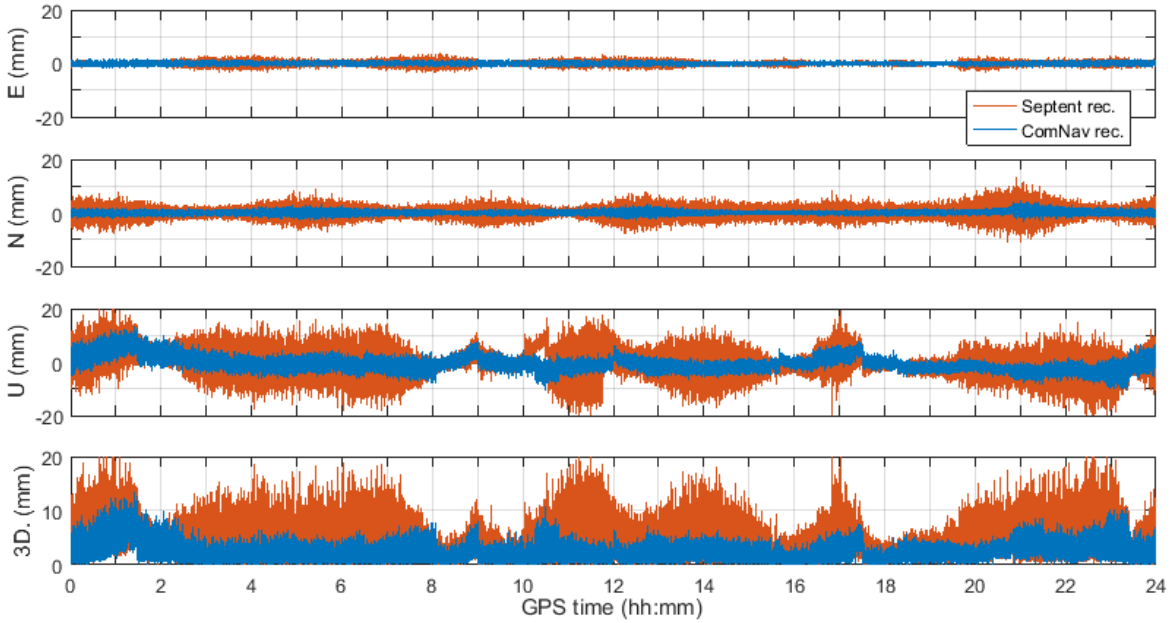


Fig. 4.30 Comparison between two daily time series of BDS-only solution achieved with two pairs of Septentrio and ComNav collocated receivers at China site on 05/03/2015.

The assessment of the precision of the combined solution of GPS and GLONASS was based on the Septentrio records; while for the combined GPS and BeiDou solution, it was used the ComNav records. Figure 4.31 presents the consistency between the trends of achieved results by the two receivers, by applying the CDF analysis. The results indicate that any combined GNSS solution achieved higher precision than any other independent solution for any of the three components.

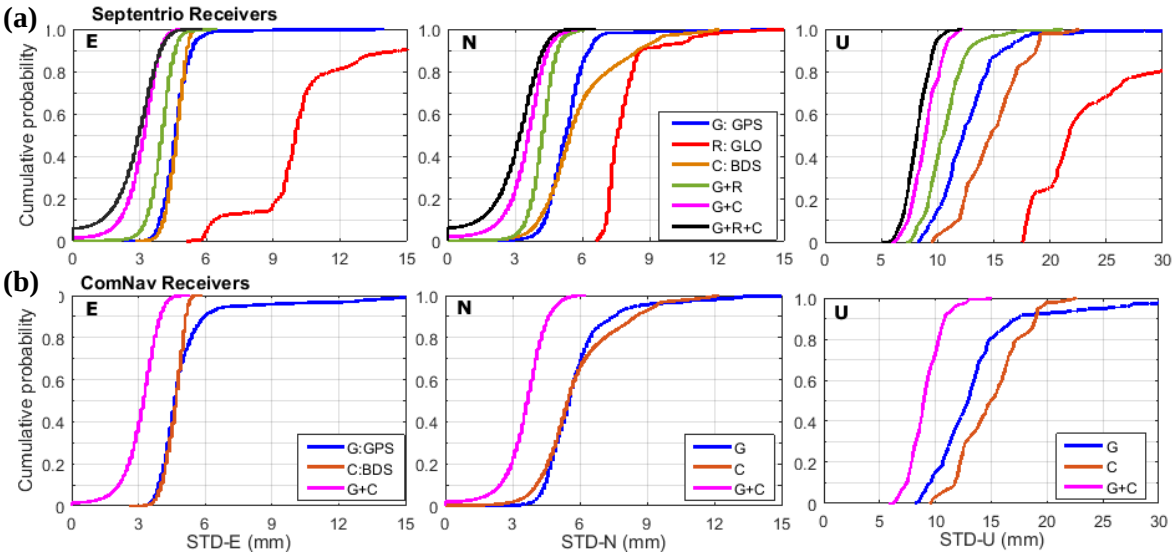


Fig. 4.31 Comparison between achieved precision (STD) with different GNSS daily solutions by using CDF analysis on 05/03/2015 (a) Septentrio receivers (b) ComNav receivers.

Based on the analysis of the independent solutions, it is observed that the GLONASS-only solution achieved the least accurate results for all three components (Fig. 4.29). The more accurate results at N and U components are achieved for the GPS-only solution, while the E component seems to be at the same level of precision with a GPS-only and BeiDou-only solution.

For combined GPS with other observed constellations such as Galileo, QZSS and SBAS at this site. However, a number of Galileo satellites (E11, E12, E18, E19 and E20) were observed at the time of experiments; there is no navigation data available to perform a final solution. The combined GPS with single QZSS satellite related to the same solution of GPS-only, which means no contribution of QZSS in the ultimate solution. For Augmentation Geostationary satellites SBAS, three satellites with single frequency were observed which beyond to present in this analysis. Therefore, the analysis devoted to studying GPS, GLONASS, BeiDou and their combinations.

It is worth mentioning that the daily availability of all potential GNSS solutions along 12 consecutive days are within the optimum availability of (100%) except for GLONASS, which has daily availability fluctuated from 96% to 98% during this period. The analysis of the time series of the independent constellations (GPS, GLONASS and BeiDou) solutions reveal precision similar to that achieved on 05/03/2015 with slight differences. These differences vary from day to another depending on the changing effect of repeated events such as cycle slips on the daily GPS time series, low SNR or due to differentiation of the satellite constellation (e.g. GLONASS, which required eight days to repeat the same constellation). It can be noticed as an example, the effect of repeated events along the daily time series of E component on the apparent GPS-only solution, as shown in Fig. 4.32.

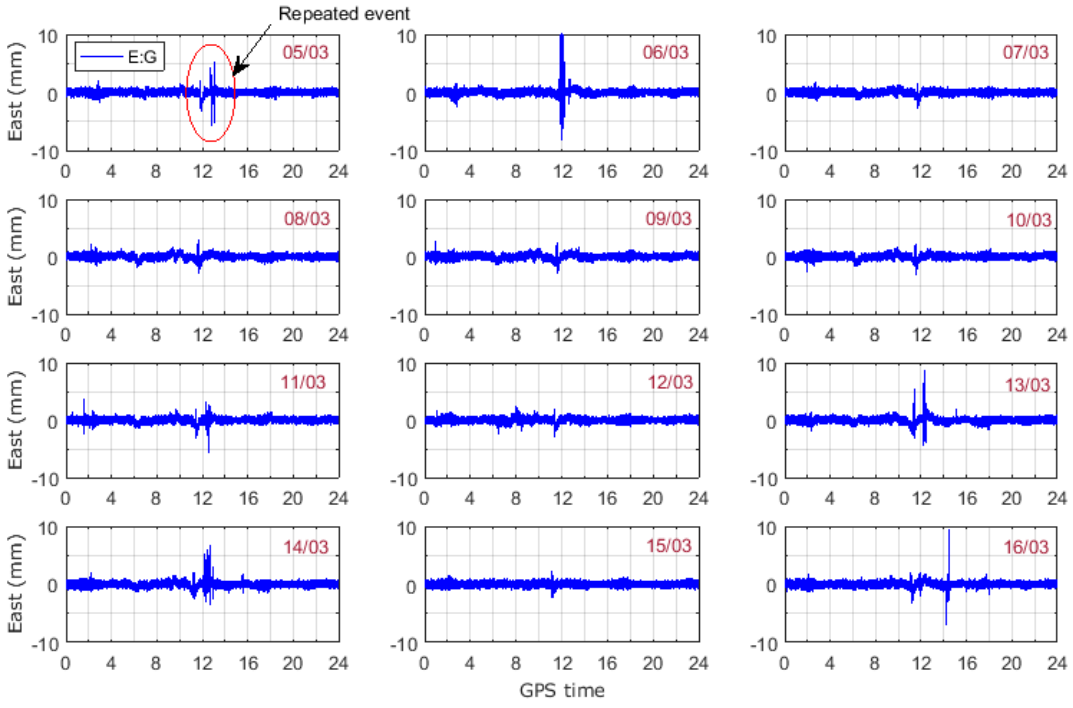


Fig. 4.32 Time series of E component along the apparent daily solution of GPS-only solution for 12 consecutive days at China site with Septentrio receivers.

The existence of these events (caused by problematic satellites) will affect the final precision in the independent solution, while their effect can be reduced or removed in a combined GNSS solution.

More specifically, for the Septentrio receivers' records, the combined GPS+GLONASS solution results to coordinate time series of slightly lower noise level relative to the GPS-only solution. However, the main improvement is for the time-intervals where the GPS-only solution is characterised by outliers or gaps, for which the combined GPS+GLONASS solution overcome this problem resulting in time series with no gaps and of the lower noise level. In addition, there is a significant improvement in the precision of the coordinate time series by the combined GPS+GLONASS solution relative to the GPS-only and GLONASS-only solution. Thus, the combined GPS+GLONASS leads to GNSS time series of improved precision and reduced noise level, expressed through the RMS.

Regarding the BeiDou contribution, it seems to be again receiver dependent as for Septentrio receivers. More specifically, the BeiDou-only solution is noisier than the GPS-only solution, while the combined GPS+BeiDou leads to a solution of worse precision than the GPS-only solution, but still, it is better than the BeiDou-only solution. For the case of ComNav receivers, the GPS+BeiDou combined solution leads to improved coordinate time series precision-wise relatively to the GPS-only and BeiDou-only solution (Fig. 4.33b).

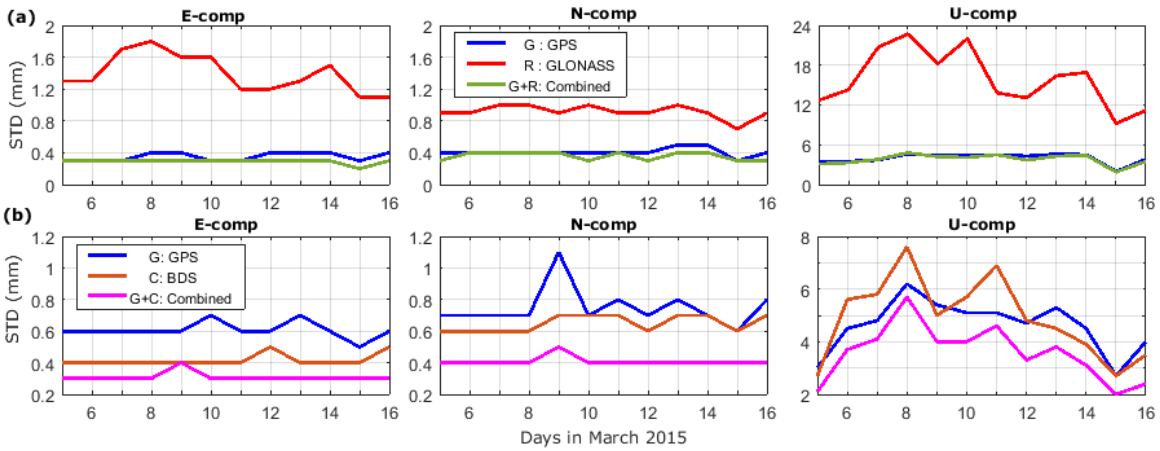


Fig. 4.33 An achieved precision expressed at the China site with different GNSS daily solutions over the 12 days (a) Septentrio receivers (b) ComNav receivers.

Finally, the contribution of BeiDou seems to be more significant relative to that of GLONASS at this site when combined with GPS (Rabbou and El-Rabbany, 2015, Odijk et al., 2015), as the combined GPS+GLONASS solution is noisier than that of GPS+BeiDou in China.

4. 7 Noise and Satellite Geometry Correlation

After investigating the precision and the availability for different GNSS systems combinations based on the daily solution, the next step was the analysis of the impact of the geometry of these constellations, expressed through the DOP values, on the precision of the GNSS solutions. The DOP values define a relationship between the geometric distribution of satellites and the positioning precision, which also describe the propagation of random errors of the measurements into the computed positions (Yang et al., 2011). It is also evident that the DOP values improve with the positional precision and vice versa. To quantify the impact of the geometry of the satellite constellation on the precision of the GNSS positioning, a linear-correlation analysis was made between the DOP values and the standard deviation of the GNSS solutions, with the latter expressing the precision of the results. The horizontal component of the GNSS measurements, derived from E and N components, corresponds to the HDOP (Horizontal DOP), while the vertical component U corresponds to the VDOP (Vertical DOP).

For the correlation of the standard deviation and the DOP values of the 24-h time series, the standard deviation and the DOP values were computed for consequent segments of the time series using a moving window. Thus, the moving standard deviation of the GNSS time series and the moving average of the corresponding HDOP and VDOP values were computed using a moving window of width k with an overlap between the adjacent windows m. The moving standard deviation σ_{Un} of the U-component U_i and the moving average μ_{VDOP} of the *VDOP* values are given from the following formulae:

$$(\sigma_U)_n = \sqrt{\frac{1}{k-1}\sum_{i=nm}^{nm+k}(U_i - \bar{U})^2} \tag{4.1}$$

$$(\mu_{VDOP})_n = \sum_{i=nm}^{nm+k}\frac{VDOP_i}{k} \tag{4.2}$$

where U_i and $VDOP_i$ are the U-component and VDOP values for the epoch i, while $\bar{U}$ is the mean of U-components at that window.

Likewise, the moving standard deviation σ_{En}, σ_{Nn} of E, N components were computed, with their sum resulting in the moving standard deviation of the horizontal component σ_{Hn}, which was correlated with the moving average of HDOP μ_{HDOP} as in the following equations:

$$(\sigma_E)_n = \sqrt{\frac{1}{k-1}\sum_{i=nm}^{nm+k}(E_i - \bar{E})^2} \quad (4.3)$$

$$(\sigma_N)_n = \sqrt{\frac{1}{k-1}\sum_{i=nm}^{nm+k}(N_i - \bar{N})^2} \quad (4.4)$$

$$(\sigma_H)_n = \sqrt{(\sigma_E)_n{}^2 + (\sigma_N)_n{}^2} \quad (4.5)$$

$$(\mu_{HDOP})_n = \sum_{i=nm}^{nm+k}\frac{HDOP_i}{k} \quad (4.6)$$

In order to represent a smooth time series with representative moving DOP values, different values for *k* and *m* were tested. It was found that the optimum values of *k* and *m*, which achieve a smooth and representative pattern of the STD and DOP values, are 100 and 50, respectively.

The main aim of these correlations is to examine whether an additional constellation of satellites can improve the noise level of the GPS only time series, by focusing on the general constellation and not on specific satellites. To assess whether the precision of the GPS solution is strongly correlated with the satellite constellation, the linear correlation between the noise level of the GPS time series, expressed through the moving standard deviation of the time series, and the moving DOP values, which expresses the satellite constellation, was computed resulting in the R-square coefficient (R^2). The latter was taken as an indication to examine the effectiveness of the correlation. For the GPS time series of zero baseline in the UK (Fig. 4.23), the moving standard deviation of the horizontal *(*σ_H*)* and vertical *(*σ_U*)* components and the moving average of the corresponding DOP values (μ_{HDOP} and μ_{VDOP}*)* were computed, which then were used to correlate the two components (Fig. 4.34).

In the GPS coordinate time series, a few time-intervals of gaps were observed (i.e. of 38 min total duration), apart from the time-intervals of significantly amplified noise level (indicated and numerically marked in Fig. 4.34a), due to poor satellite geometry, which was also reflected on the increased DOP values. As a result, the computed correlation coefficient R^2 was 0.92 when correlating the moving average of DOP values μ_{HDOP} with the corresponding STD of the horizontal component σ_H of the time series. On the other hand, the R^2 was 0.85 for the vertical correlation.

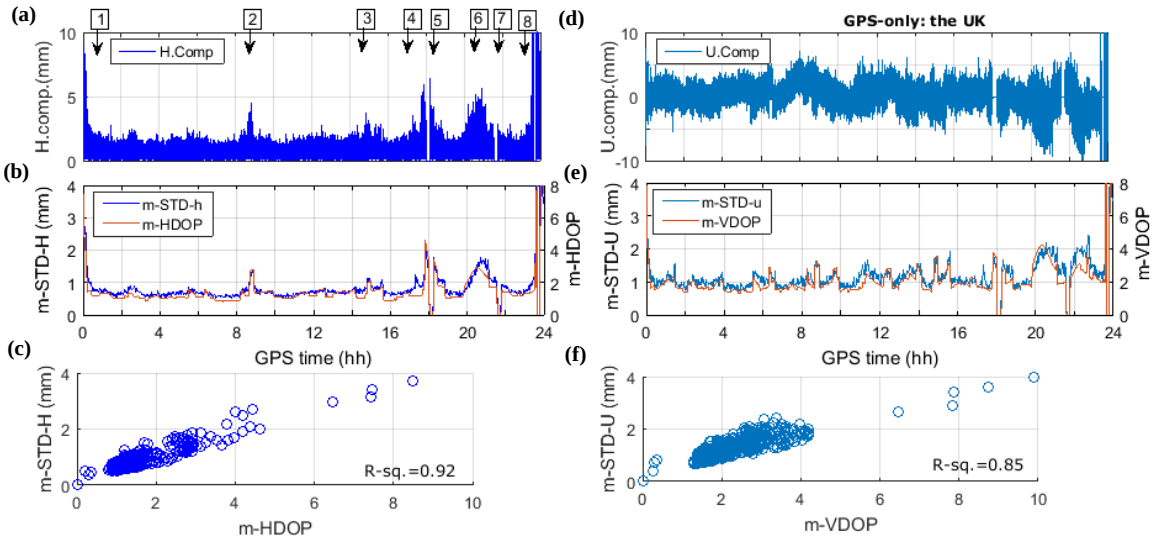


Fig. 4.34 The daily GPS time series extracted from Leica receivers (UK site) of (a) the horizontal component, (b) the moving average of HDOP and the corresponding moving standard deviation (c) the scatter of their liner correlation, (d) the U-component, (e) the moving average of VDOP and the corresponding moving standard deviation, and (f) the scatter of their liner correlation.

The correlation process reveals that GPS measurements corresponding to DOP values above (5) are extremely noisy and can be considered as outliers. By rejecting these measurements, the correlation coefficient R^2 decreases to 0.81 and 0.68 for the horizontal and vertical components, respectively. Furthermore, to test the effectiveness of this correlation mathematically, a cross-correlation between the moving STD and the moving DOP values (for HDOP < 5) was used, the coefficient of the horizontal and the vertical components for lag = 0 were 0.90 and 0.82.

Regarding the GPS time series in China, the correlation between the moving standard deviation of horizontal and vertical components and the moving average of the corresponding DOP values resulted in correlation coefficients of 0.85 and 0.51, respectively (Fig. 4.35). The differences between the two sets in the UK and China are due to the different noise level and the different satellite constellation for the two locations.

However, to better identify time-intervals of the high correlation between the noise and satellite constellation geometry for different solutions, we analyse correlation for 1-hour segment between GNSS time series and DOP values for the different combination of satellite constellations.

The plots presented in Fig. 4.36 present the correlation results for 1-hour interval of the GPS-only solution for the UK and China sites. This can detect the change in correlation when looking at the GPS-only solution and the corresponding solution of the combined solution.

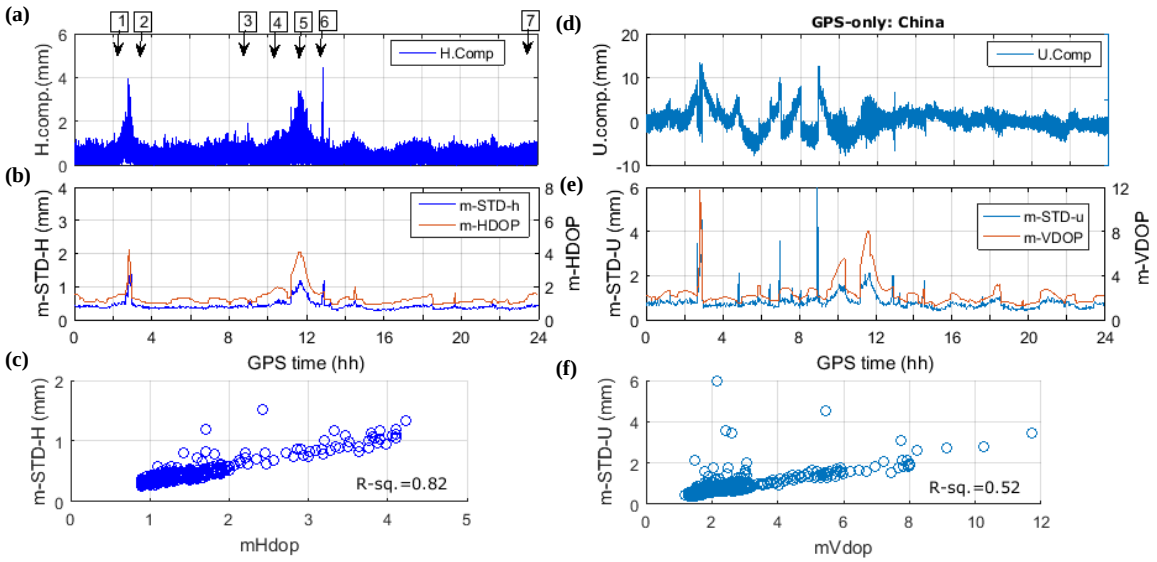


Fig. 4.35 The daily GPS time series extracted from Septentrio receivers (China site) with details similar to Fig. 4.34 on 05/03/2015.

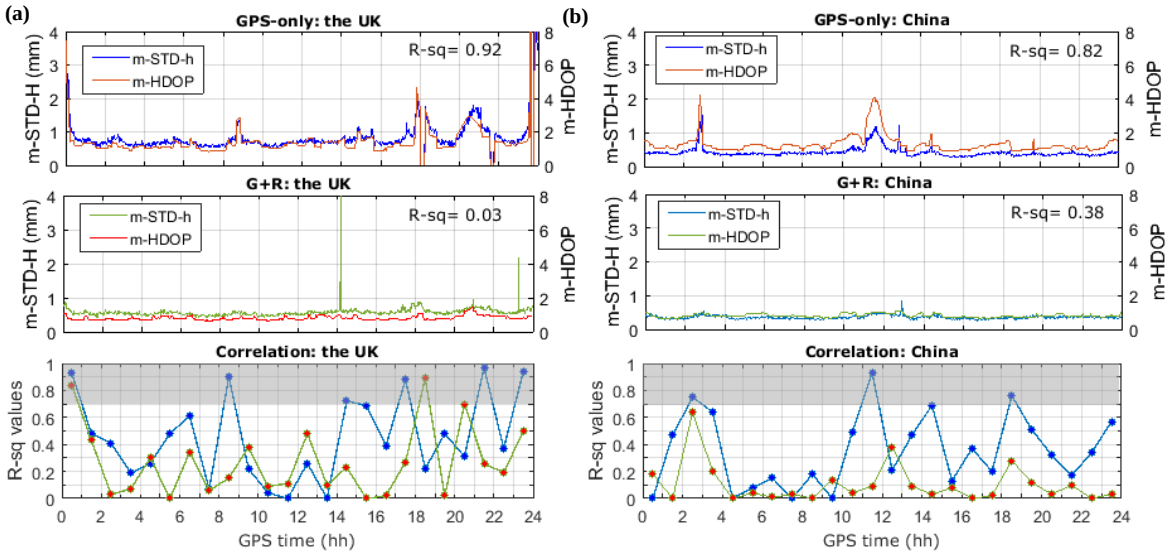


Fig. 4.36 Linear correlation between moving average of the HDOP values and the moving standard deviation of the corresponding horizontal component for GPS-only and combined GPS/GLONASS solutions for (a) the UK site and (b) China site.

It is evident that for the GPS-only solution, the well-correlated intervals (i.e. $R^2 > 0.7$; in the grey-shaded area of Fig. 36) occur for a period of high DOP values, larger than 1.4, and noisy data, where the standard deviation is larger than 0.8 mm, following the waveform of the DOP value. To investigate the relationship between them, the mean value of HDOP was 1.4 for the daily data at the UK site, beside STD of 0.8 mm. For the low-correlated intervals ($R^2 < 0.7$), on the other side, the DOP value is below 1.4 and the GPS solution of high precision (i.e. STD<0.8).

In Fig. 4.37, the first interval (08:00 – 09:00) has mean HDOP of 1.6 which is greater than 1.4 the mean HDOP along the whole day, at the same time the evaluated STD of the horizontal component

was 0.86mm which is greater than 0.80mm of the daily solution. Therefore, there is a high correlation between the geometry and the noise level in this interval (R^2 = 0.90). On the other hand, the second representative case at the interval (10:00 – 11:00) does not correlate for the same above reasons (Fig. 4.37).

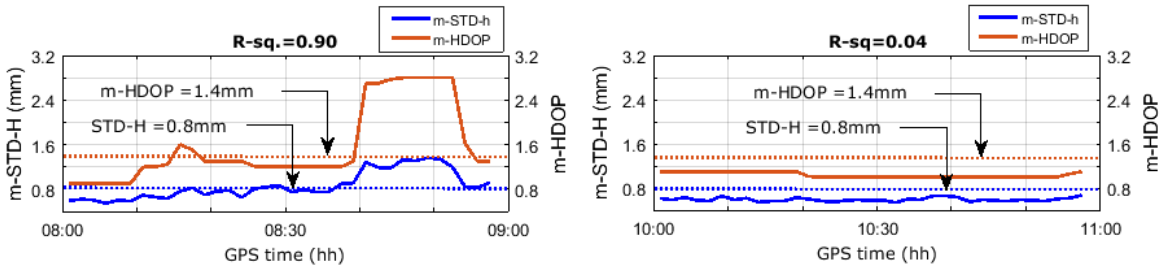


Fig. 4.37 Two representative cases of linear correlation for GPS-only (left) well correlated and (right) no correlation at the UK site.

The impact of the poor geometry of the GPS-only solution at the China site is well defined at some intervals. Due to the high precision of GPS-only solution as a result of proper geometry with sufficient satellites (apart from some weak intervals), the correlation coefficient at China site was less than the corresponding one on the UK site. This means the relatively worse constellation leads to a generally less accurate GPS-only solution.

Thus, for highly correlated intervals the satellite constellation has significant impact on the precision of the GNSS solution, which means that any improvement in satellite constellation (DOP values), would improve the precision of the GNSS solution, while for low correlated values (i.e. $R^2 < 0.7$) the precision is practically independent of the satellite constellation (i.e. DOP values).

Regarding the correlation of the combined GPS+GLONASS solution as illustrated in the above Fig. 4.36. It is clear that the noise level of the combined solution is smaller than that of the GPS-only solution, as the correlation coefficient between the noise and geometry is usually lower than the corresponding computed coefficient for the GPS-only solution. However, this reduction in correlation is detected in most of the hourly intervals; some other intervals produce correlation coefficient of combined solution larger than the corresponding one of the GPS-only solution, such as intervals of (18:00 – 19:00) or (20:00 -21:00).

When analysing the belonging satellites at these intervals, it can be observed the impact of noise at specific GLONASS satellites that added to the final solution that affects the correlation. In addition to the sudden change in a number of valid satellites and their effect on the achieved DOP values. For example, at the interval (18:00 -19:00), two GLONASS satellites (R13 and R17) lead to achieved high correlation coefficient. By excluding these two satellites, the correlation coefficient will reduce.

These results indicate that the addition of GLONASS constellation reduces the impact of the satellite geometry in the GNSS solution significantly, with the DOP values being relatively low in the UK and China (i.e. <1.4) and the standard deviation ranging below 0.8 mm.

Finally, the main contribution of the GLONASS constellation is for the cases of strong correlation between the GPS geometry and the low precision of the GPS-only solution, whereby adding the GLONASS satellites results to GNSS solutions of high precision and uncorrelated with the low DOP values.

For the contribution of BeiDou constellation in the precision of the GNSS solution, the data of Septentrio and ComNav were used. Although, the computed mean of DOP values for a BeiDou-only daily solution was similar for the two receivers (i.e. mean HDOP is 1.40, and the mean of VDOP is 2.4), the corresponding standard deviation, expressing the noise level of the two receivers was different. As it was analysed in Section 4.4.2, the Septentrio receiver was less noisy than ComNav for the GPS-only solution, while the ComNav solution was less noisy for the BeiDou-only solution (Fig. 4.30).

However, the Septentrio receivers' records were used for the correlation analysis, since the Septentrio receivers seem to result in less noisy GNSS solution (Fig. 4.13).

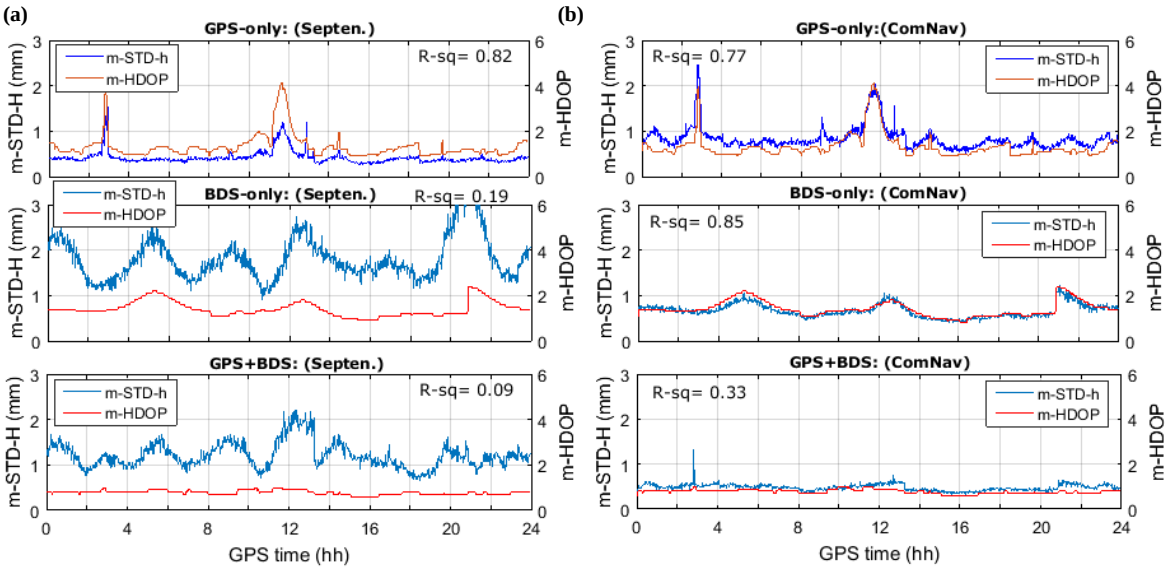


Fig. 4.38 Comparison between the linear correlation of moving HDOP values and moving standard deviation of the horizontal component of GPS-only, BDS-only and combined GPS/BDS for (a) Septentrio receivers and (b) ComNav receivers.

According to Fig. 4.38, the compared assessment between correlations of the two pairs of receivers indicates the correlation of GPS-only solution can evaluate with Septentrio or ComNav receivers (with priority for Septentrio). For the correlation of BeiDou records, the ComNav data related to better correlation as achieved uniform low noise (σ_H = 0.66 mm) correlated with geometry (μ_{HDOP} =1.40). Therefore, the correlation coefficient was 0.85.

Accordingly, the correlation of combined GPS+BeiDou was further reduced with ComNav receivers as a result of low noise level (σ_H = 0.49 mm) with improved geometry (μ_{HDOP} =0.76). Consequently, the correlation coefficient is 0.33. From these results, the correlation analysis is a useful tool to assess the relationship between the noise and the geometry of satellite.

4. 8 Spectral Analysis

In order to assess the contribution of the multi-GNSS solutions in the frequency domain and define the spectral characteristics of the noise, the GNSS time series were analysed using spectral analysis technique. Due to the gaps in some of the positional solution of the GPS/GNSS time series, the Lomb-Periodogram was used, which is based on the fitting of sinusoidal functions by using the least square method, and it can be used for non-equidistant data (Psimoulis et al., 2008). The daily GNSS time series were split into one-hour periods and were analysed. The spectra of descriptive cases are plotted in logarithmic scale to identify the characteristics in the low frequency-band (i.e. <0.1 Hz), which is characterised by characteristics GPS errors (i.e. multipath, etc. (Peppa et al., 2017)).

In the 24-hour GNSS time series, there are several time-intervals representative for the noise characteristics of the GNSS solutions. The following Figures present the spectra of the GNSS time series in the UK, for three representative cases.

The first representative case, when the GPS time series are characterised mainly by white noise (i.e. 04:00–05:00), the corresponding GLONASS time series are noisier than GPS (Fig. 4.39).

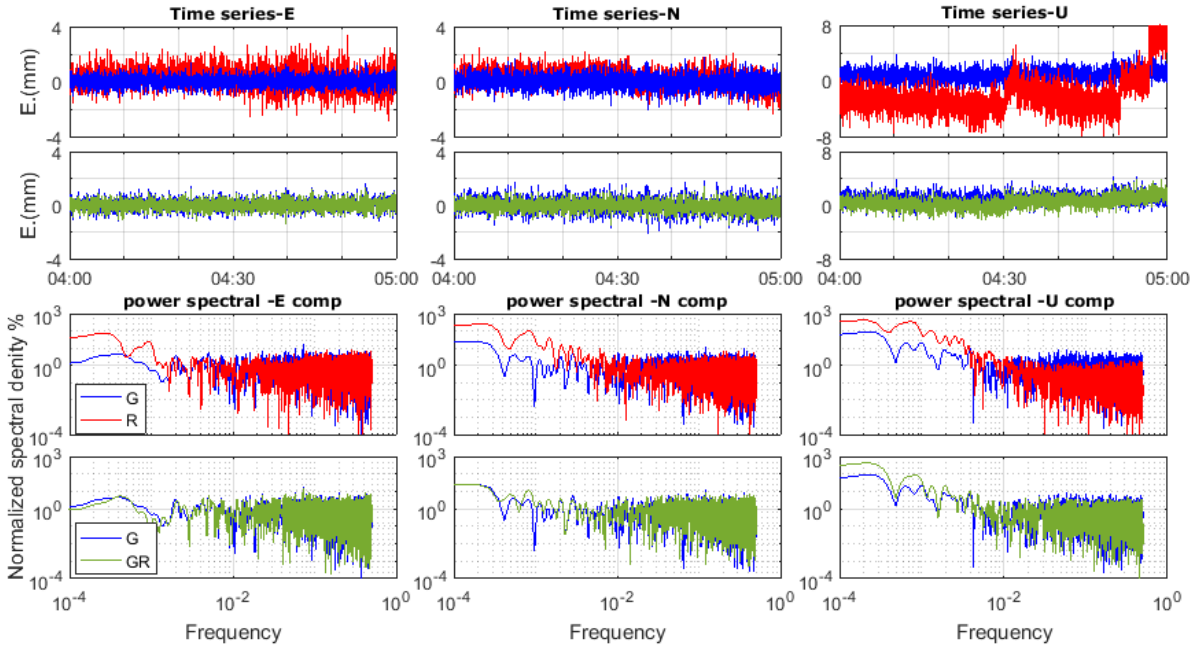


Fig. 4.39 Time series and corresponding spectra of the hourly interval (17:00-18:00) along E, N and U components for (G: GPS, R: GLONASS and combined G + R) solutions with Leica receivers in the UK site on 05/03/2015.

However, the GLONASS time series is noisier than GPS, its noise is characterised in the low frequency-band, while the noise level of GLONASS is lower than GPS in a high-frequency band, especially for N and U components. When applying a combined solution of GPS+GLONASS in this interval, there is no significant improvement relative to the GPS-only solution, as the corresponding spectra become noisier in the low frequencies (<0.05 Hz).

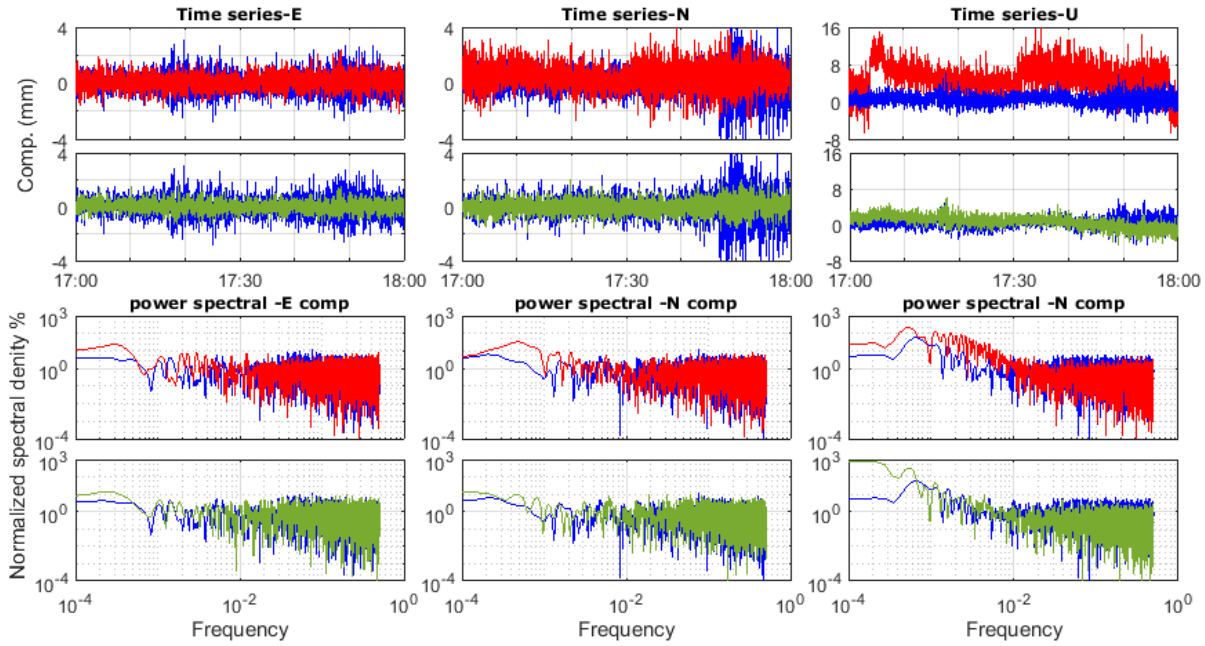


Fig. 4.40 Time series and corresponding spectra of the hourly interval (17:00-18:00) along E, N and U components for different GNSS solutions with Leica receivers in the UK site on 05/03/2015.

The second case, when GLONASS contributed to reducing the white noise level of GPS in combined solution for the interval (17:00 – 18:00) as shown in Fig. 4.40. It is clear that the noise level along the U component is reduced with a combined solution in a high-frequency band, as the peaks of the high-frequency bands (>0.25 Hz) become smaller.

On the contrary, when the GPS time series is biased or contains data gaps (i.e. 23:00–24:00), the corresponding spectrum is characterised by significant peaks in specific frequency bands and introduce more coloured noise in the low-frequency band (<0.05 Hz). For that case, the contribution of GLONASS may improve the spectrum, as the amplitude of the peaks become smaller and the coloured noise level is reduced, as it is expressed from the less significant peaks as shown in Fig. 4.41.

For the GPS time series in China, it is observed that the contribution of BeiDou can be beneficial for the cases where the GPS time series appear strong coloured noise for frequencies <0.05 Hz (Fig. 4.42). The contribution of BeiDou can reduce more significantly the characteristics of the GPS coloured noise, as the spectrum can become even flat (mainly for the horizontal components) in the low-frequency band, indicating that the characteristics of the noise are closer to white noise.

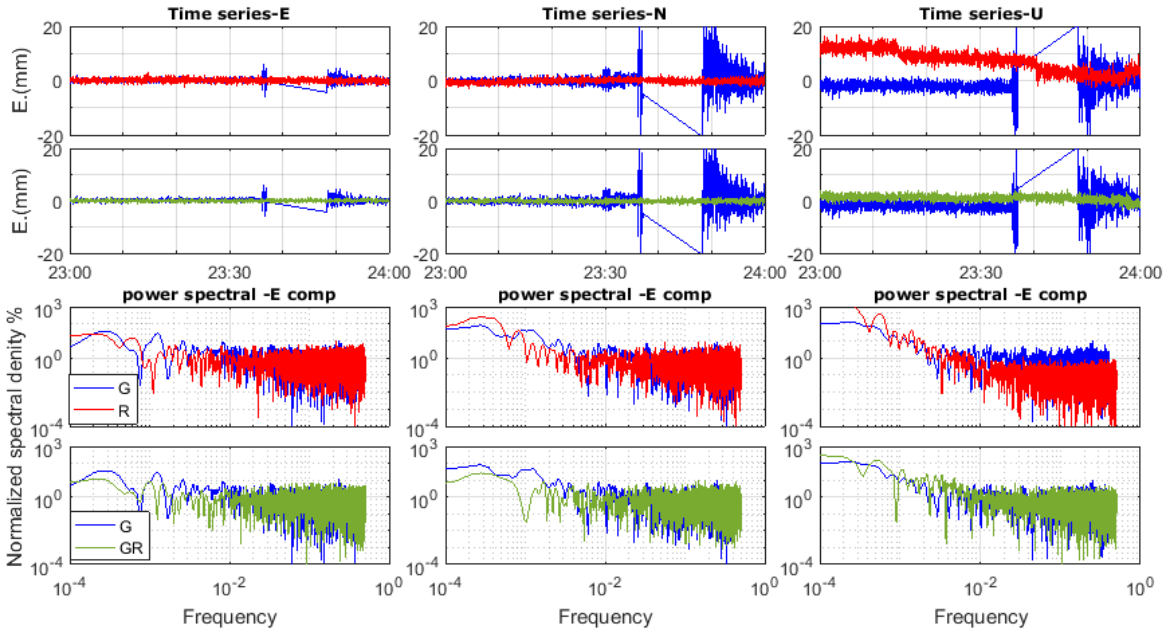


Fig. 4.41 Time series and corresponding spectra of the hourly interval with Leica receivers in the UK site on 05/03/2015.

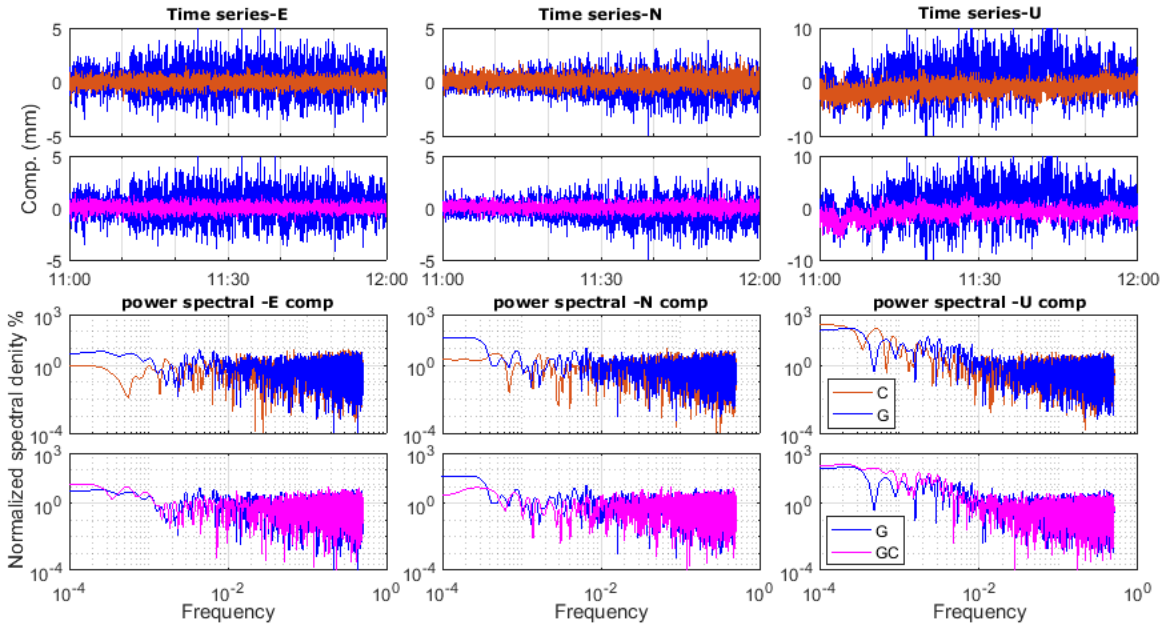


Fig. 4.42 Time series and corresponding spectra at China site for (G: GPS, C: BeiDou and GC combined GPS+BeiDou with ComNav receivers on 05/03/2015.

4. 9 Different Scenarios of Satellite Obstruction

In order to determine the position of points with any GNSS constellation, at least four satellites need to be observed. In some cases, the receiver antenna is located in a position that suffers from obstructions such as buildings or huge objects, especially for positioning in the urban environment. The obstructions lead to signal losses from a number of satellites either permanently or for a period of duration. In a bridge structural monitoring, for instance, when the antenna is located on the deck

and the pylon or tower blocks many satellite signals (Roberts et al., 2014), in this case, only high satellites can be observed.

Although the number of visible satellites becomes limited due to this blockage, the position solution may not be possible because the number of observed satellites will be less than four. As other available satellites from another GNSS constellation can be observed, the additional satellites will contribute to overcoming this limitation. Adding only one more satellite from another constellation system (except QZSS) will not contribute in change the positioning of the combined solution, due to the relative positioning with DD operation required one satellite selected as a reference satellite with another one from the same constellation system. There is no satellite-side generated between different constellations, such as between GPS and GLONASS (T. Takasu, 2013), due to different delays of receivers toward different systems which is known as a receiver ISB (inter-system bias (T. Takasu, 2013, Li et al., 2015a)). In this case, the additional two satellites are added to the observation equation, which means two satellites at least from other constellation required to have a combined solution.

To highlight the effect of obstruction, a number of scenarios are examined where the signals of observed satellites covering a specific part of the sky-plot, which blocked by a hypothetical obstruction. For this analysis, the observations of Leica receivers of duration (00:00 – 01:00) on 05/03/2015 have been used and the orientation of the obstruction will rotate by 60°. The results from these scenarios are shown in Fig. 4.43 and Table 4.8.

From the above Fig. 4.43 and Table 4.8, it is obvious that adopting GPS-only with limited available satellites leads to no solution in three cases (d, e and f) and reduced availability of fixed solutions in the rest. While combined GPS+GLONASS is showing the improved availability as well as the precision in the analysed data.

In order to have a clear idea of the final solution, the first two representative cases are discussed. According to Table 4.8 and Fig. 4.44. It can be noticed in the first case of scenario (a), the obstruction caused tracking signals from limited GPS satellites of no solution at the first 20 min (no of valid satellites < four), then the observed satellites become four, which results in a noisy solution, thereby the availability of GPS-Only solution was 46% (see Table 4.8). While observing GPS and GLONASS solution enables to achieve full availability of 100% with less noisy results as explained in Fig. 4.44 and Table 4.8. The improved geometry was performed as the mean GDOP of combined GPS/GLONASS was reduced to 4.8 from 12.1 at GPS-only.

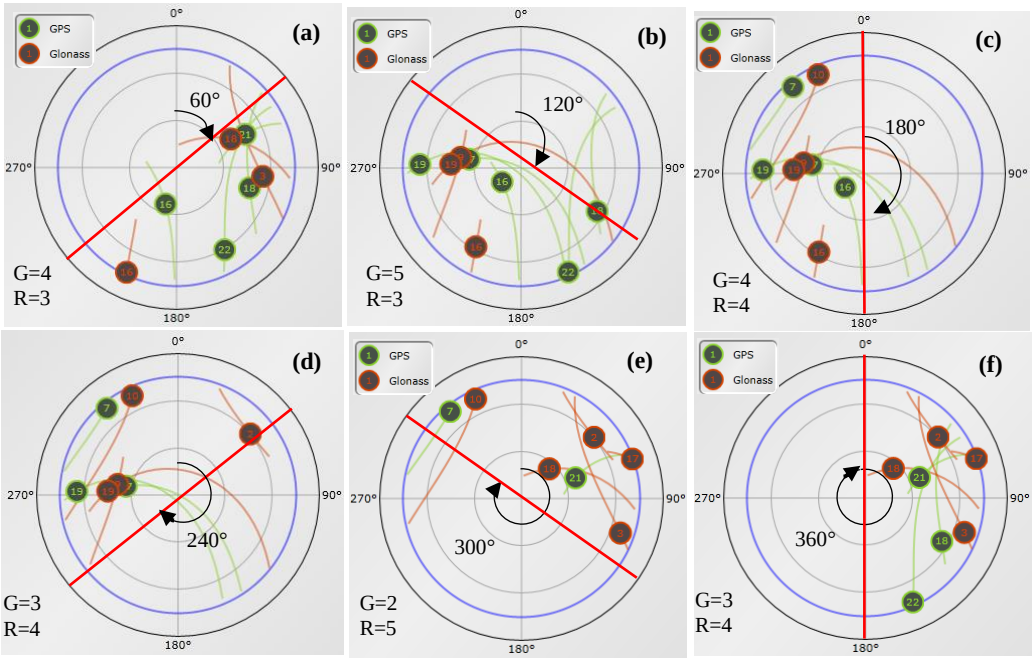


Fig. 4.43 Different scenarios of blockage according to the different orientation of the blockage axis.

Table 4.8 Compared results of different scenarios when adopting GPS-only and Combined GPS+GLONASS.

case	Solution	No. of satellites	Fixed %	STD mm			Mean DOP values			
				E	N	U	GDOP	PDOP	HDOP	VDOP
a	GPS-only	4G	46	2.2	1.8	4.9	12.1	9.4	5.1	7.9
	GPS+GLONASS	4G+3R	100	1.7	1.7	7.3	4.8	3.9	2.3	3.2
b	GPS-only	5G	53	2.7	3.7	2.2	13.1	12.1	11.0	5.2
	GPS+GLONASS	5G+3R	94	2.9	1.9	4.3	8.3	6.4	4.4	4.6
c	GPS-only	4G	53	1.9	1.4	2.7	10.1	7.9	5.4	5.7
	GPS+GLONASS	4G+4R	94	1.8	0.9	2.2	5.1	4.1	2.9	2.8
d	GPS-only	3G	0	-	-	-	-	-	-	-
	GPS+GLONASS	3G+4R	100	0.6	1.6	2.2	4.5	3.8	2.5	2.7
e	GPS-only	2G	0	-	-	-	-	-	-	-
	GPS+GLONASS	2G+5R	80	1.0	1.4	2.5	4.2	3.6	2.2	2.8
f	GPS-only	3G	0	-	-	-	-	-	-	-
	GPS+GLONASS	3G+4R	70	4.4	1.2	4.6	7.0	5.6	3.9	4.1

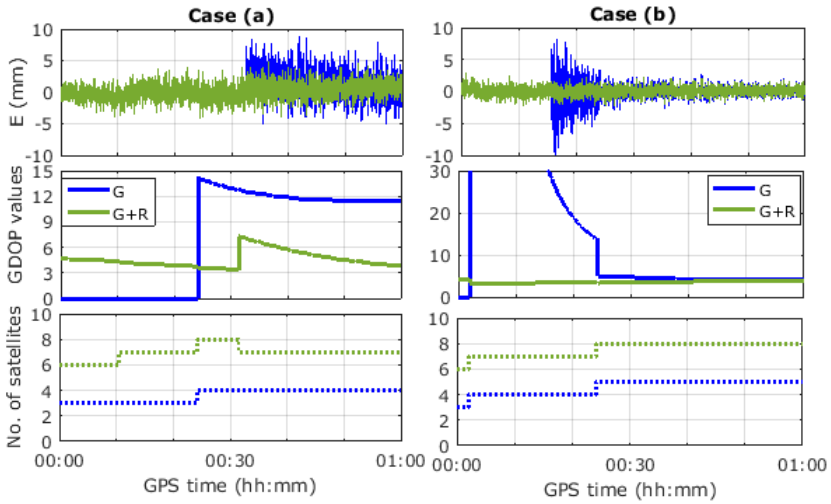


Fig. 4.44 GPS-only and combined GPS/GLONASS performance at scenarios (a) and (b).

In the second case of scenario-b, however, a sufficient number of GPS satellites was observed (four satellites), the distribution of these satellites leads to weak geometry, thereby the GDOP value was more than 30 at the first 15 min (no solution beyond the threshold of a solution configuration of RTKLIB). Then the geometry was enhanced as the DOP value reduced, but with a noisy solution. Then the positioning performance improved when observed five satellites. In contrast, the combined GPS/GLONASS achieved less noisy results with a more available fixed solution (see Fig. 4.44 and table 4.8).

4. 10 Chapter Summary

The GPS measurements are susceptible to a variety of errors that degrade the positioning quality and solution availability. The additional observations from other GNSS constellation can contribute to improving the positioning performance. Therefore, this chapter was investigated the positioning performance through different GNSS observations by zero baseline measurements in two locations (i.e. in the UK and China sites). The details of experimental measurements conducted simultaneously with different pairs of receivers in both locations over 12 consecutive days using different GNSS solutions were discussed in this chapter. As the relative positioning in zero baseline measurements eliminates most of the error sources except the random noise errors with the impact of satellite geometry. A preliminary analysis was performed to select the pair of available receivers in each location that had the most reliable performance and can be characterised by uncorrelated data, which also could be estimated by the autocorrelation technique.

This chapter then analysed the data quality through residual analysis of derived positions and discussed some of the represented cases of high noise level, which resulted from cycle slip of problematic satellites and low-quality observations with low SNR. In addition, the analysis of the outliers (i.e. spikes) and the occurrence of sudden jumps (resulted in time series) and how it can be resolved were also achieved.

The results of combined GNSS positioning showed an improvement in availability and precision compared to the GPS-only solution. The significant improvement at the UK site was achieved in Northing component when combined GPS/GLONASS data, while overall improvement was obtained from GPS/BDS solution in China site.

A new approach of correlating the noise level and satellite geometry has been proposed which based on moving standard deviation of derived noise and mean DOP values of related geometry. The results of the GPS-only solution showed a good correlation at the noisy interval, while weak correlation was achieved due to the reduced noise level in the combined solution.

Chapter 5: Performance Assessment of Static and Kinematic Short Baselines with Multi-GNSS Measurements

As discussed in Chapter 4, the results of 1 Hz static measurements demonstrate that the use of combined GNSS solution (i.e. GPS/GLONASS) provides a better solution than a GPS-only solution. The most significant improvement was achieved in Northing component. This chapter discusses the results of GNSS short baselines measurements, which conducted from stations in Ningbo, China. As part of an analysis, the results of 1-Hz static data will be discussed, as well as the kinematic observations of the high sampling rate (10-Hz and 20-Hz) that performed by moving rotating arm, to achieve the positioning precision and accuracy of different GNSS solutions. In kinematic analysis, the mathematical models of the best fitting with related issues are derived to identify the actual required parameters, which can be then compared with the measured values to conclude the achieved accuracy.

5. 1 Introduction

Chapter-4 is based on zero baseline measurements to investigate the noise level of different GNSS solutions, while the current chapter focuses on the short baselines (< 50m) experiments to assess the accuracy and precision of different GNSS solutions. In such short baselines, although the relative solution will eliminate most of the error sources, the presence of multipath effect and measurement noise can affect the estimated accuracy and precision of analysed data. The analysed GNSS data can be collected in static or kinematic mode; therefore, it is required to investigate the accuracy and precision of different GNSS datasets in static and kinematic observations. For kinematic applications, the GPS-only has been used to monitor the dynamic movements in suspension bridges and other large engineering structures (Yi et al., 2013b). In this study, when implementing multi-GNSS to improve the positioning performance in kinematic applications, it is essential to investigate the accuracy and precision of proposed solution.

To achieve this aim, the precision and accuracy of different GNSS solutions will be discussed with real data to simulate the kinematic movements as well as the static mode. Static experiments were conducted on predifiened stations of known coordinates, while the kinematic tests were performed using a rover rotating GNSS antenna attached on a moving arm. The recorded GNSS coordinates for the moving antenna were used as a simulated environment for detecting displacement in engineering structures under loading. Thus, the aim is to investigate the significant change in the positions of moving antenna to evaluate the achievable accuracy and also to examine the ability of multi GNSS to detect the correct frequency of any detected movements when compared with a GPS alone solution.

5. 2 Description of the Short Baselines Experiments

In order to create a short baseline in this analysis, two control stations (located on top of two pillars) A and B of known coordinates have been used, which are occupied by GNSS antennas (see Fig. 5.1). In addition to these fixed stations, a third moving station (Pi) was also used to collect the multi-GNSS data, which enables to determine its relative position at each epoch. All these stations are located on the roof of the Science and Engineering Building at the University of Nottingham-Ningbo, in China (UNNC). The pillar of first control station (A) was equipped with a Leica AR-20 (LEIAR20) choke ring antenna. A low noise cable was used to connect this antenna to a signal splitter (GEMS GS18), which was connected via cables into two GNSS receivers. These two receivers are a Leica GR-25 (able to track GPS, GLONASS and Galileo satellites) and a Javad-TRIUMPH VS receivers (has the ability to track all GNSS signals) as shown in Fig. 5.1. Both receivers are set to record GNSS data in a static mode.

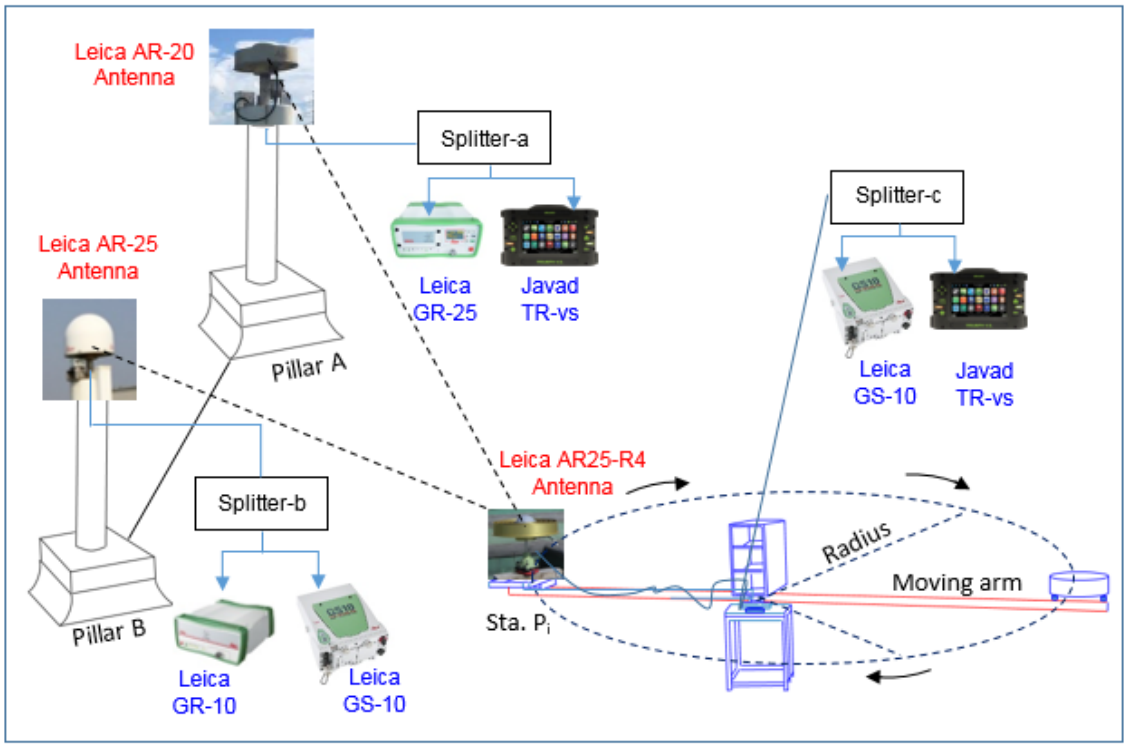


Fig. 5.1 The specification of the experiment of different short baselines.

The other Leica AR-25 (LEIAR25) choke ring antenna was mounted on the second pillar (B) and connected via a splitter and cables to two different receivers, which are Leica GR10 and Leica GS10 receivers (to be homogenous with others) that logging GNSS observations in static mode as well. The third group of collecting data was set up at a station (Pi) on the ending side of a moving arm that rotates in a horizontal circular trajectory. At this moving station, a Leica AR-25 (LEIAR25.R4) choke ring antenna was attached to a platform at the ending edge of the moving arm and connecting to a signal splitter (GEMS) to Javad-TRIUMPH VS receiver and a Leica GS10 receiver, which are

recording GNSS data in kinematic mode. From the above details, the experiment setup leasds to three short baselines includes receivers antennae collected data at an open sky environment. These baselines imply AB in static mode and other two baselines in kinematic mode, which are AP_i and BP_i as shown in Fig. 5.1 and summarised in Table 5.1.

Table 5.1 The details of the collected data by different GNSS receivers located on the two pillar stations and the platform of moving the arm on 15/06/2016.

Point	Antenna Type	Receiver Type	Record Sample	Record mode	starting Record	Ending Record	Durat.	GNSS Record
Pillar A	Leica AR-20	Leica GR-25 Javad TR-vs	1 Hz 10 Hz	Static Static	00:00:00 03:26:30	23:59:59 07:58:04	24-h ~4.5 h	G, R, E G,R,E,C,J
Pillar B	Leica AR-25	Leica GS-10 Leica GS-10	1 Hz 20 Hz	Static Static	00:00:00 03:26:30	23:59:59 07:58:04	24-h ~4.5 h	G, R, E G,R
Move Arm	Leica AR25-R4	Javad TR-vs Leica GS-10	10 Hz 20 Hz	Kinem. Kinem.	03:26:30 03:26:30	07:58:04 07:58:04	~4.5 h ~4.5 h	G,R,E,C,J G,R

The moving arm represents a simple monitoring system of 4m total length, which is designed to move in a circular trajectory. The centre of this arm is fixed and installed on the embedded pin that rotates the arm by an electric motor with constant angular velocity of 1 cycle/3.1847s (i.e. 3.94574 m/s for t=3.1847s and R=2.00m) to generate a uniform horizontal circular motion accompanied by slight vertical displacement, due to the equipment not being exactly level. Above the centre, there is a cabinet to house the GNSS receivers, which rotates with the arm's movement around the fixed centre. As the GNSS antenna at the end of the arm attached to a platform, there is a counterbalanced weight on the other end (Roberts and Tang, 2017), see Fig. 5.2.

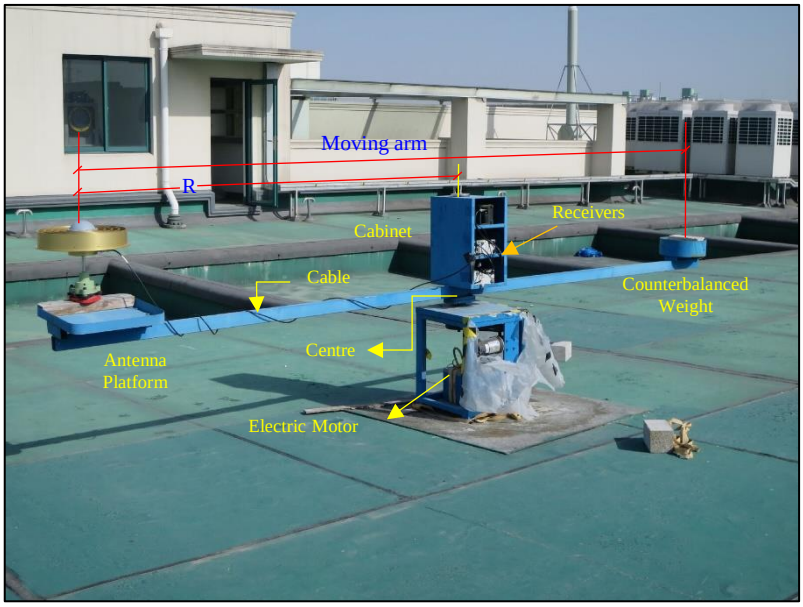


Fig. 5.2 The specification of the experiment of different short baselines.

5.2.1 Short Baseline in a Static Mode

A static test was carried out for 24-h on 15/06/2016 with a known short baseline of 10.484 m, between the two pillar stations A and B of known coordinates. Pillar A is selected as the reference base station, which was equipped with a fixed antenna connecting to a Leica GR-25 receiver, while the rover station was set on pillar B with Leica GR-10 receiver (as shown in Figure 5.1). Both receivers are operating for a continuous 24-h period and recording GNSS data with a sampling rate of 1-second (i.e. 1-Hz). These two receivers can track GPS, GLONASS and Galileo constellations with no capacity to track other constellations such as BeiDou. As the actual length of this short baseline is known from previously determined coordinates, the achievable accuracy and precision of different GNSS solutions can be assessed depending on the residuals in the computed coordinates at the rover station.

5.2.2 Short Baselines in a Kinematic Mode

The motive to create short kinematic baselines was to evaluate the quality of different GNSS solutions of collected data at a moving station. The detecting movement at this controlled station can simulate the real exciting of engineering structure under loading. For this purpose, a Leica AR-25 (LEIAR25.R4) choke ring antenna was attached on a platform at the ending part of the moving arm. The latter antenna was connected to two receivers (Javad-TRIUMPH-VS and Leica GS10) via splitter and cables. The set of receivers and splitter are housing in the in the cabinet that placed over the centre of the moving arm (Fig. 5.2). Each moving rover receiver was relative to a fixed base station that occupied by two receivers to be homogeneous with rover ones (as shown in Fig. 5.1). Therefore, two kinematic simultaneous datasets (baselines APi and BPi) have been collected on 15th June 2016 for a total period of around 4.5 hours from 03:26 to 08:00 GPS time.

The two Javad TRIUMPH-VS receivers were used to collect the GNSS data with a sampling rate of 10 Hz at the first baseline AP_i, While two Leica GS10 receivers were used to collect GNSS data of the second baseline BP_i with 20 Hz sampling rate. However, the Javad receivers have the ability to track all GNSS signals, the Leica receivers are restricted to track GPS, GLONASS and Galileo signals. The distance between the reference pillar A and the centre of the rotating trajectory was within 41.7 m, while it is 36.0 m length from pillar B.

During the experiment, while the continuous static measurements were recorded at the base stations, the kinematic data at location Pi was observed at four irregular intervals depending on the movement of the rotating arm. These observations were recorded for a period when the rover is forced to move followed by a duration of no movement and then two intervals of moves as explained in Table 5.2.

Table 5.2 The duration of the collected data at the rover station of a moving arm on 15/06/2016.

Case of movement	GPS time at Start of Recording	GPS time at the End of Recording	Trail Duration
Rotating movement-1	03:06:30	04:03:00	$00^{h}\,36^{m}\,30^{s}$
No movement	04:04:04	05:35:00	$01^{h}\,31^{m}\,00^{s}$
Rotating movement-2	05:36:00	06:37:40	$01^{h}\,01^{m}\,40^{s}$
Rotating movement-3	06:38:03	07:58:04	$01^{h}\,20^{m}\,01^{s}$

5. 3 Processing the Data

The RTKLIB software has been used to process the different GNSS data for either an individual solution of GPS, GLONASS, BDS, or combination between different constellations. Therefore, it is possible to investige the accuracy and precision of GNSS data that derived from short baseline measurements at each solution.

In Chapter 4 (which presenting the zero baseline results), the residuals of measurements have been defined as the measurement noise. In this chapter, the residuals of short baselines are comprised of the measurement noise and multipath (de Bakker et al., 2012). Both residuals of zero and short baselines are affected by the satellite geometry.

The processing of relative positioning is formed for one constellation system (i.e. GPS or GLONASS), by subtracting measurements of each observed satellite from the measurements of one reference satellite belonging to that system. The satellite with a maximum elevation angle at each epoch is selected by RTKLIB to be the reference satellite, which eleminats residual errors.

Due to different group delays in the receiver for various GNSS constellations, there is no single difference (SD) between satellites of different systems in RTKLIB. The group delay in receivers is known as a receiver ISB (Inter-System Bias, (T. Takasu, 2013, Odijk et al., 2017) as discussed in Section 3.2.4). However, the latter is applicable when tracking data of different constellations on the same frequencies (i.e. differencing between some GPS/Galileo or BDS/Galileo) and different receiver types (Odijk and Teunissen, 2013).

In addition, the data of the first baseline collected in a static mode at a 1-second interval along 24-h was processed in a kinematic manner with a cut-off elevation angle of 15° to evaluate the positioning performance epoch by epoch (single epoch). In parallel with this assessment, the comparisons have been made between different GNSS solutions with single and dual frequencies. Also, the processing was carried out for every hourly duration to evaluate the impact of satellite geometry on positioning quality.

For all static solutions, ambiguity fixing was in continuous mode for processing the individual constellation of GPS or GLONASS, while it was an instantaneous mode for processing combined

GPS+GLONASS systems. Consequently, the final positions are computed and the derived residuals have been achieved with their statistical results and represented as a time series of baseline components. Data processing was focused on datasets that were collected in a kinematic scenario. Therefore, the rover station of moving arm was set up to track and analyse all available GNSS signals. The collected GNSS measurements in each dataset were post-processed in a kinematic mode through RTKLIB with the following settings as summarised in Table 5.3.

Table 5.3 RTKLib setting for processing of moving arm experiment.

Setting	Details
Positioning mode	Kinematic relative positioning with the DD technique.
Base-point	Fixed position of station A for 1st baseline and station B for the 2nd one.
Rover point	Moving point (P_i)
Frequencies	Dual frequencies L1 and L2
Elevation Mask	15°
Satellite Ephemeris	Broadcast
Integer Ambiguity	Fix & Hold for individual constellations (short duration) and Instantaneous for combined solutions.
Processing Interval	10 Hz for the 1st dataset and 20 Hz for the 2nd one.

In resolving the ambiguity resolution, which represents the essential process, the three different strategies have been examined to apply the most appropriate mode for a kinematic solution. As the processing time was short for every session (i.e. maximum 1.25 h duration), the fix and hold can be used for the individual constellation, while the maximum rate of success ambiguity fixing was achieved with an instantaneous mode for the combined GNSS solution but more available satellites.

5. 4 Results of a Static Baseline

As two main GNSS constellations have been observed in this experiment (i.e. GPS and GLONASS), it is essential to investigate the positioning performance of every individual constellation as well as their combined solution. This investigation evaluates the precision and accuracy of the calculated results. After fixing the ambiguity and mitigating error sources by applying the DD method with dual frequency, the remaining residual represents the noise measurement including any effects from multipath. This means that the quality of the derived position is affected by these two factors.

Due to the known coordinates of the baseline, the true length can be applied as a constraint to calculate positioning residuals. In the same manner, it is possible to determine the positioning residuals by differencing the computed coordinates from the most probable values. Therefore, the components of positioning differences between known and computed coordinates at every epoch are identified over the 24-hours on 15/06/2016 for GPS-only, GLONASS-only and combined GPS+GLONASS. As described in section 4.6.2, the GLONASS-only solution showed numerous

intervals of noisy positioning solutions at China site, which is attributed to weak geometry with extream DOP values. Thus primary attention will be given to assess the quality of the GPS-only solution and investigate the impact of adding GLONASS observations to GPS to obtain a combined solution. The time series of derived positioning residuals of the GPS-only solution are compared with the corresponding residuals of the combined GPS+GLONASS as shown in Fig. 5.3. The results show that the positioning can achieve mm level accuracy for both solutions.

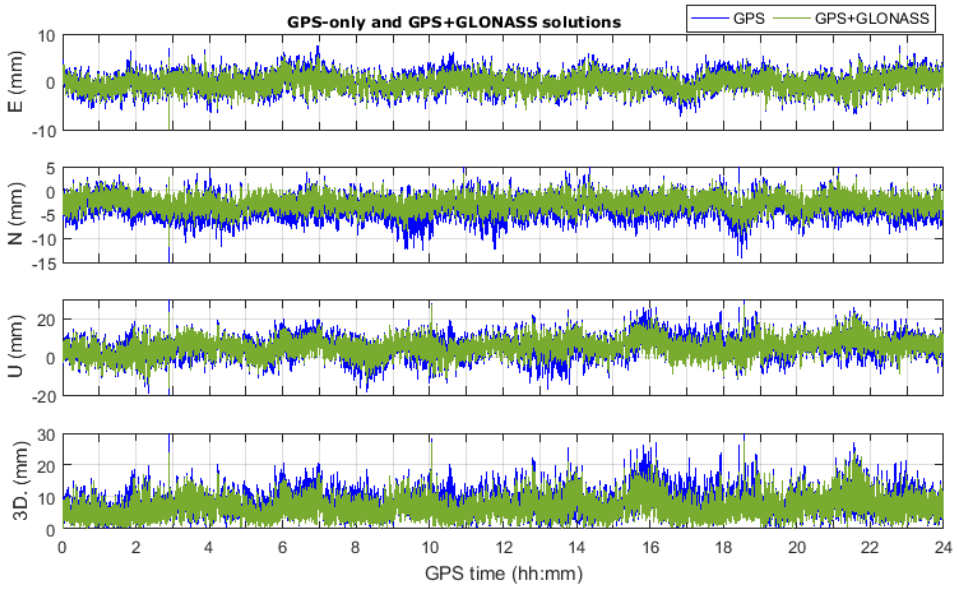


Fig. 5.3 Time series of positioning residuals showing a comparison between GPS-only and combined GPS+GLONASS on 15/06/2016.

The comparison through derived position revealed that significant improvement could be achieved when utilising combined GPS+GLONASS solution, especially at intervals of noisy positioning with a GPS-only solution. These intervals represent periods of increased DOP values that correlate with a reduced number of satellites as presented in Fig. 5.4.

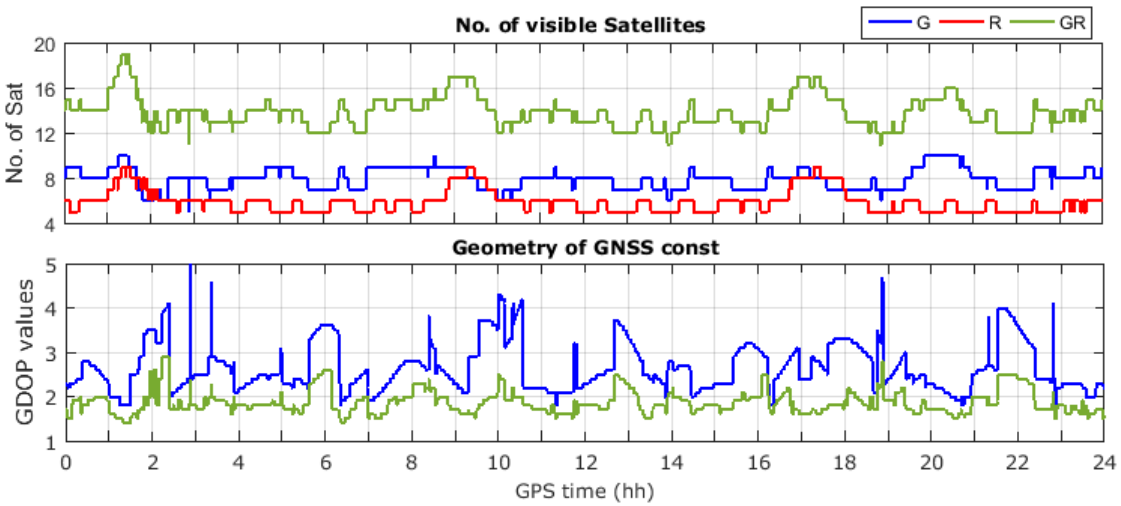


Fig. 5.4 The number of valid satellites for GPS-only, GLONASS-only and GPS+GLONASS (top) and the associated GDOP values (bottom) on 15/06/2016.

It is worth pointing out that the number of GLONASS satellites is usually fewer than the number of GPS satellites visible during the entire experimental period. However, the excellent availability of the GPS constellation with at least six observed satellites; the achieved position interspersed with some noisy intervals.

For overall assessment, the 24-h measurements are used to evaluate the positioning performance of every GNSS solutions. The evaluation involved assessing the availability of a fixed solution, the achieved precision and accuracy as well as the satellite geometry. The results of this analysis are summarised in Table 5.4.

Table 5.4 The statistical results of different GNSS solutions for 24-h on 15/06/2016.

Solution	Epochs	Avail.	Mean GDOP	STD (mm) E	N	U	2D	3D
GPS-only	86400	99.8	2.6	1.7	1.8	4.8	2.476	5.400
GLONASS-only	85269	98.3	4.6	3.2	2.0	20.7	3.774	21.041
GPS+GLONASS	86400	100	1.9	1.4	1.3	4.0	1.910	4.433
Improvement*	-	-	27%	18%	28%	17%	23%	18%

Solution	Mean PDOP	Mean VDOP	Mean HDOP	RMS (mm) E	N	U	2D	3D
GPS-only	2.3	2.0	1.1	1.7	4.0	6.8	4.346	8.070
GLONASS-only	4.0	3.7	1.6	3.3	2.2	20.9	3.966	21.273
GPS+GLONASS	1.6	1.4	0.8	1.4	2.9	6.4	3.220	7.164
Improvement*	30%	30%	27%	18%	28%	06%	26%	11%

As shown in the Table, all different solutions have a high percentage of the ambiguity fixed solutions (availability) with the optimum fixing shown to be when utilising the combined solution. The geometry of 24-h was calculated concerning the GDOP, PDOP, VDOP and HDOP for different combinations of satellite constellations. The mean GDOP and PDOP for GPS-only are 2.6 and 2.3 respectively, while the corresponding values are decreased to be 1.9 and 1.6 with a combined solution. This indicates that the combined solution can improve the geometry by 27% and 30% respectively relative to GPS-only solution.

The computed STD for every solution can be used to identify the positioning precision while positioning accuracies are determined through the differences between the calculated position and the actual (reference) coordinates. According to Table 5.4, it can be observed that there is a visible improvement of position precision when applying combined solution compared to the GPS-only solution. This improvement is a result of increasing the number of observations used in the solution beside the enhanced geometry with more available satellites. The enhancement was noticeable with N-component by reducing 28% of achieved STD, while the least improvement was made by 18% and 17% for E and U components, respectively. This improvement will reflect the achievable

precision of 2D and 3D. To figure out this improvement, Fig. 5.5 present the residual scatter graphs, which showing the distribution of residual errors along the positioning components.

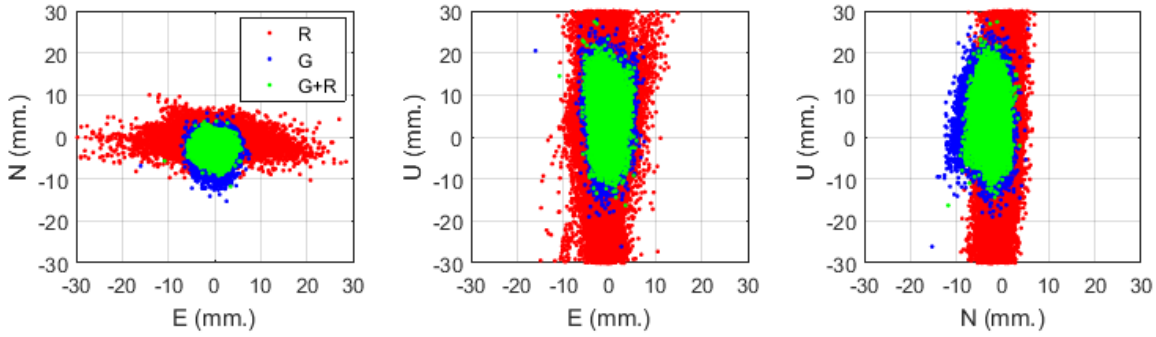


Fig. 5.5 The scatter graphs of distributed residuals with different GNSS positioning.

However, the noisy solution of the GLONASS-only positioning, the N-component has less elongation scatter compared with the other two components. Due to reducing the noise level in a combined solution, it is beneficial to examine the combined results with those obtained through the GPS-only solution when evaluating the accuracy. For a GPS-only solution, due to the distribution of satellites in each direction, the largest errors are expected with U-component, while the N-component seems to be noisier than E-component. However, a combining of the two systems in one positioning solution leads to enhance the positioning precision (Fig. 5.6). This figure also shows the distribution of residuals around the mean value (precision) which follow the normalised statistical distribution.

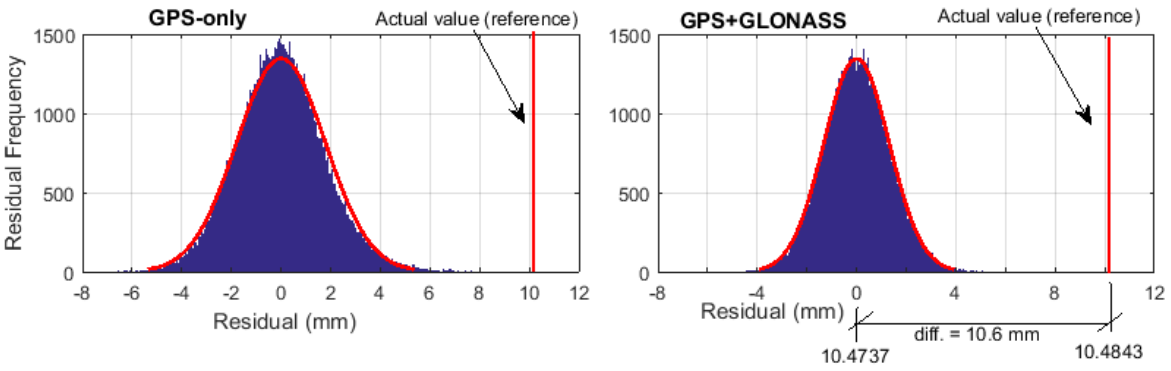


Fig. 5.6 Histogram of distributed residuals with GPS-only and combined GPS+GLONASS.

For accuracy, as the actual length of the analysed baseline is 10.484 m, which can be achieved with very accurate results along 24h of observing data in static mode. Therefore, it doesn't show a significant improvement in accuracy. Thus, when comparing the derived length of the baseline calculated using different GNSS solutions, the level of accuracy was approximately at the cm level as illustrated in Fig. 5.6 and 5.7 along the represented time series. In spite of that, this will not be true at the intervals of weak geometry as the apparent differences between actual and derived lengths within two solutions are evident (Fig. 5.7). The computed RMS of the GPS-only solution was 10.67mm, while it was 10.57mm for a combined solution along 24h.

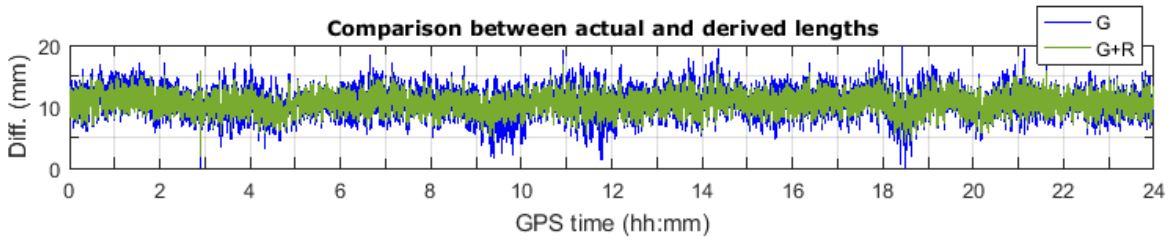


Fig. 5.7 Time series of differences between the actual and derived length of baseline for solutions of GPS-only and combined GPS+GLONASS.

To further investigate the positioning quality, the 24-h dataset was divided into hourly sessions. Each session is processed separately so that a total of 24 sets of results are obtained to derive comparable positioning results. In contrast to the GPS-only solution, the STD of the combined solution has been calculated for the 3D residual for every hourly session, and the mean GDOP values are computed for each session as presented in Fig. 5.8.

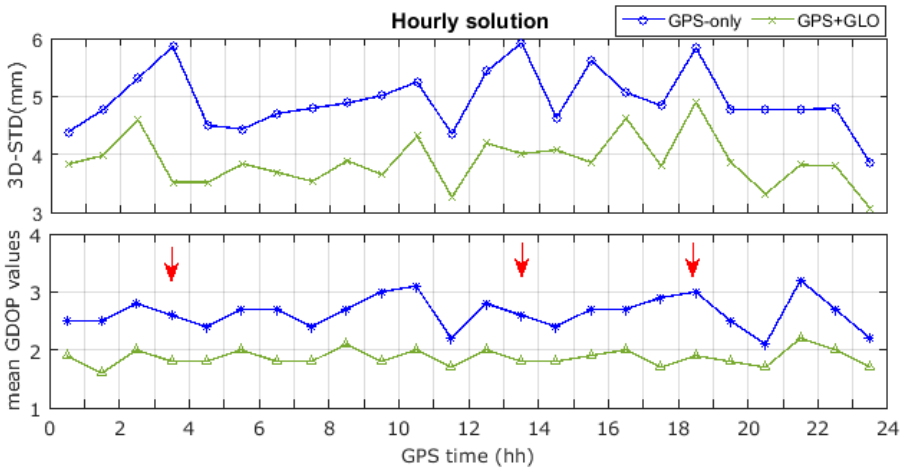


Fig. 5.8 Evaluation of hourly positioning of GPS-only and combined GPS+GLONASS.

It can be noticed from Fig 5.8 that the positioning improvement is correlated with the associated enhanced geometry for most sessions except some intervals (i.e. intervals identified by arrows in Fig 5.8). By analysing the latter intervals, it was found that the positioning in these sessions was contaminated by multipath effect, while in combined solution with increasing the number of valid satellites, the derived position is improved, which means reduce the influence of multipath indirectly without removing this effect (this will be discussed in the following).

Additionally, to assess if there any noticeable effect on the positioning results when processing the datasets with single frequency instead of applying dual frequency with similar techniques in processing. This implies using DD with single frequency observation from GPS L1 and GLONASS G1 signals under the same conditions in this analysis. However, applying dual frequency will contribute to reducing the effect of the ionosphere and accelerate fixing the ambiguity resolution (Cosser et al., 2003). Hence over the relative very short baseline, the ionospheric effect will remove,

but the fixing of ambiguity required verification. The same dataset was processed again, and the results are listed in Table 5.5.

Table 5.5 The statistical results of different GNSS solutions for 24-h on 15/06/2016.

Solution	Epochs	Frequency	Fixing the AR (%)		STD (mm)		
			Fix	float	E	N	U
GPS-only	86,400	Dual	99.8	0.2	1.7	1.8	4.8
GPS-only	86,400	Single	94.4	5.6	spike	spike	Spike
GPS+GLONASS	86,400	Dual	100	0	1.4	1.3	4.0
GPS+GLONASS	86,400	Single	99.6	0.4	1.9	1.8	5.8

From the Table, it can be seen that the positioning of GPS-only has degradation in the rate of ambiguity fixing compared to the rate with dual frequency. The float solution of less accurate results became 5.6%, which means a loss of 4838 epochs. The reasons behind this reduction are due to insufficient quality/number of observations to validate the successful fixing. Adding GLONASS observations will increase the observation equations, where the increased redundancy are introduced and leading to high rate of fixing 99.6% as given in Table 5.5 and exhibited in Fig. 5.9.

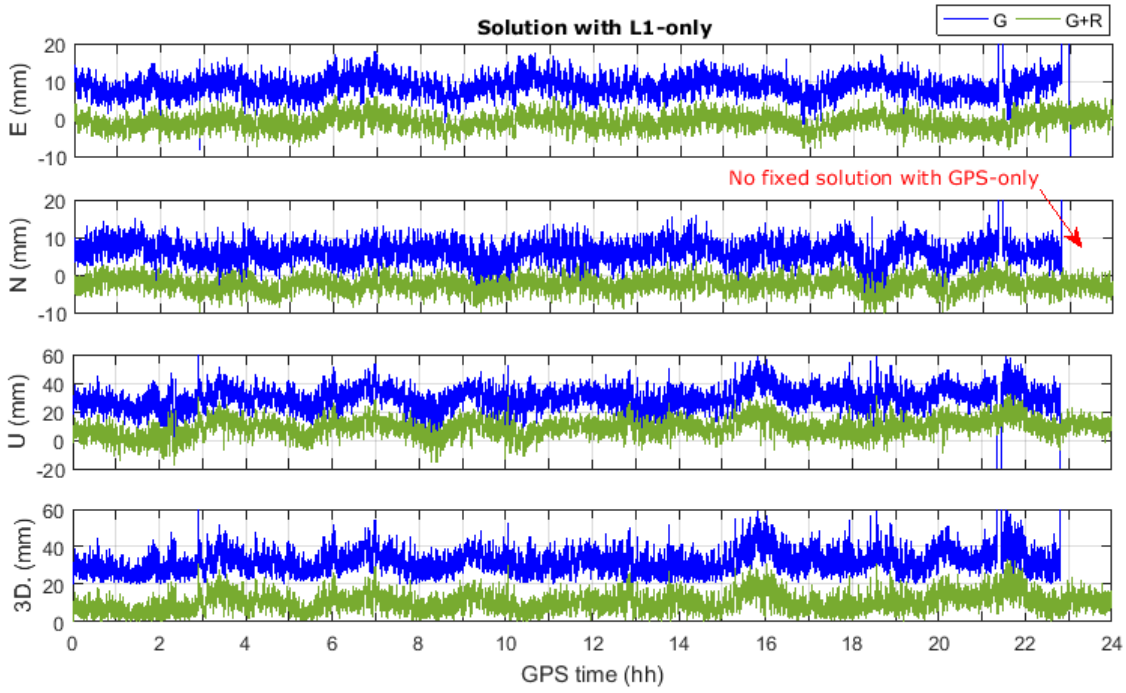


Fig. 5.9 Time series of GPS-only and combined GPS+GLONASS with a single frequency (L1).

For more specification, in Figure 5.9 the GPS time series exhibit abrupt changes at the interval between 21:00 -23:00 GPS time followed by no fixed solution. This period requires further analysis to identify the reasons behind achieved incorrect fixing. When analysing the identified period as illustrated in Fig. 5.10, the GPS positioning solution showing two spikes of incorrect ambiguity fixing. According to the achieved carrier-phase residual at this interval, it was found that these two

spikes (outliers) are related to two primary satellites, which are G12 and G24. In other words, these two satellites have carrier-phase residuals can reach a metre or more, which are outliers.

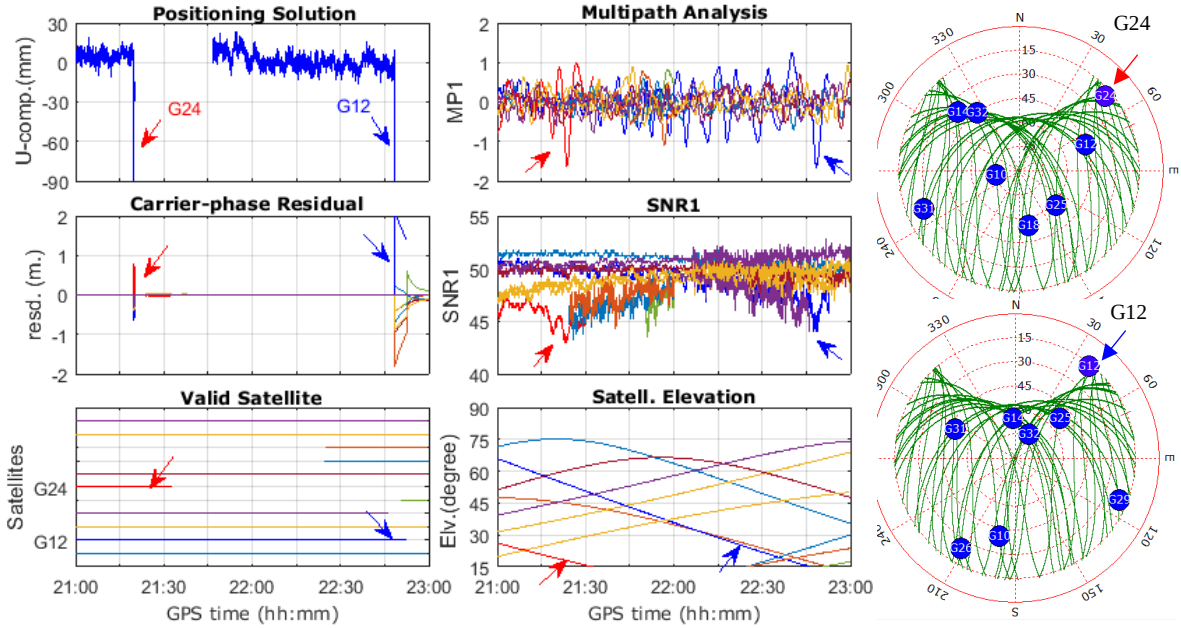


Fig. 5.10 Analysis of GPS-only with a single frequency (L1) at interval 21:00 – 23:00 GPS time.

By analysing the estimated multipath with satellite elevations, it was observed that the low elevation of these satellites could be susceptible to multipath effect. This was demonstrated by evaluating the estimated MP1 of all observed satellites as shown in Fig. 5.10 (It is worth mentioning that the estimated MP1 required dual frequency). However, these two satellites have low elevations, they observed in the same direction that caused multipath as shown in the sky-plots. As a consequence, the derived positions with carrier phase measurements are estimated and determined in float-solution, followed by another step to resolved the fixed integer values (Teunissen et al., 2014). On the other hand, the successful and reliable fixing of the ambiguity is dependant on the precise float solution (Deng et al., 2014), therefore, with measurements contaminated with multipath, this will affect the estimated positional accuracy. This leads to incorrect or failure to fix the ambiguity when a high rate of multipath is introduced (Lau et al., 2015).

For a combined solution with more redundant observations, the estimated position will be close to the final values, which means a more reliable ambiguity fix. Regarding the quality of derived positions when applying L1 only, the combined solution shows evidence of improved availability of fixed solution compared to GPS-only. Even though the achieved accuracy of the combined solution of a single frequency is comparable with a solution of GPS-only with dual frequency, This agrees with the conclusions drawn by Odolinski and Teunissen (2016). In particular, it can be indicated that the positioning performance of GPS-only with dual frequency is more precise than the corresponding solution of combined GPS+GLONASS solution as explained in Table 5.5.

5. 5 Results of the Kinematic Experiment

From the experiment using the rotating arm, the derived coordinates of the moving antenna (Pi) at every epoch are determined with different combinations of GNSS solutions. In this regard, the assessment of various kinematic GNSS positions can be utilised to investigate the performance of every solution. For this reason, the two main GNSS datasets of different recording rates have been processed. The 10Hz results of the first dataset relative to reference station A with Javad receivers comprise the GPS-only, GLONASS-only, BDS-only and combined solutions between these constellations. Whereas, the second dataset of 20Hz relative to station B including the GPS-Only, GLONASS-only and combined solution between them with Leica receivers.

Considering the recorded GNSS coordinates of the moving station and the corresponding coordinates derived from real elements of rotating movement, it can achieve the quality of positioning regarding estimated accuracy. This appropriate technique enables the assessment of the accuracy of kinematic positioning and simulates the potential of different GNSS to monitor the displacement of a moving object. From the derived displacement, the dominant frequency of the oscillating movement can also be calculated, which provides modelling analysis with a procedure similar for detecting and analysing deformations in structural health monitoring of engineering structures. During the whole time of experiment that is lasting for about 5-h (i.e. divided into four sessions) and for cut-off elevation angle of 15°, the derived GNSS positions calculated from GPS-only and BeiDou-only showing a good availability of fixed solution due to the sufficient available satellites. Whereas less available satellites were observed with GLONASS constellation as shown in Fig. 5.11, which also demonstrates the different GDOP values of each constellation over the periods of movements.

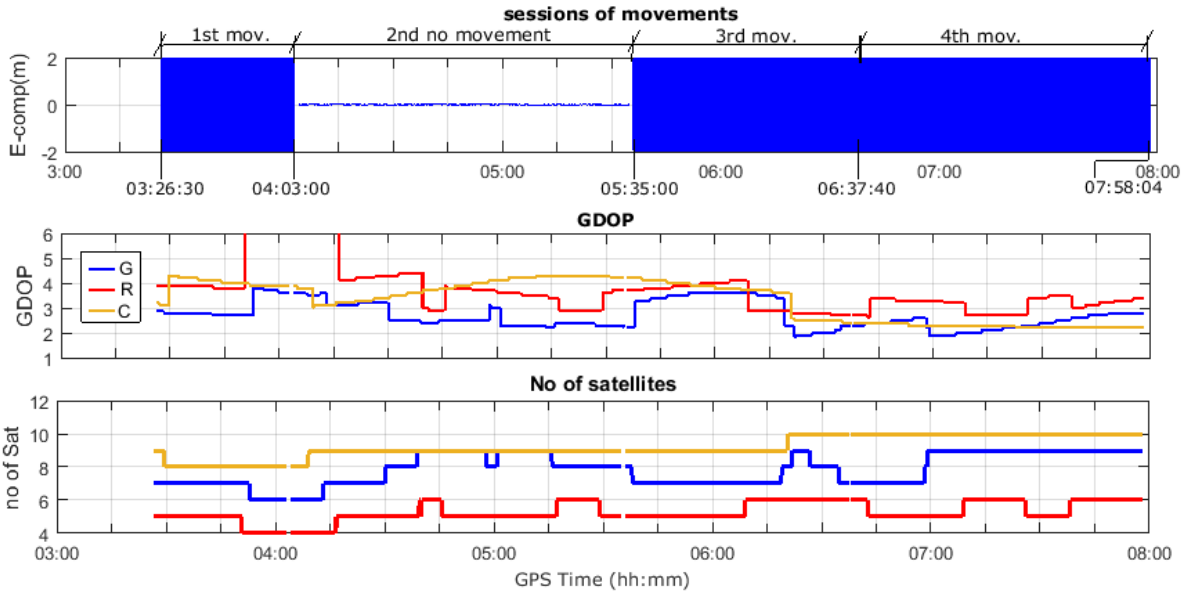


Fig. 5.11 The periods of movement (top), GDOP values of individual GNSS constellations (middle) and the number of valid satellites (bottom) in the experiment of moving arm.

It can be observed over the first and second sessions that the number of GLONASS satellites drops to four satellites, which affect the derived satellites geometry. Consequently, high GDOP values are evaluated, and no fixing of the ambiguity can be achieved at these intervals of limited satellites. This is evident in the demonstrated results from the first dataset, which are listed in Table 5.6.

Table 5.6 The summarised results of derived components of the baseline on the first data set according to different GNSS solutions on the experiment of moving rotating arm.(G: GPS, R: GLONASS and C: BeiDou).

1st: moving interval (03:26:30 – 04:03:00)						**2nd : no movement** (04:04:00 – 05:35:00)				
GNSS	epochs	% fix	Average (m) E	N	U	epochs	% fix	Average (m) E	N	U
G	21,910	100	25.4897	-34.2990	-1.2415	54,601	99.7	27.2236	-33.3932	-1.2479
R	19,219	88.0	25.4895	-34.2993	-1.2288	48,001	88.0	27.2236	-33.3933	-1.2483
C	21,910	99.7	25.4921	-34.2973	-1.2478	54,601	100	27.2257	-33.3923	-1.2452
G+R	21,910	100	25.4897	-34.2988	-1.2403	54,601	99.8	27.2238	-33.3931	-1.2487
G+ C	21,910	99.7	25.4899	-34.2980	-1.2429	54,601	99.8	27.2240	-33.3928	-1.2479
G+R+C	21,910	100	25.4902	-34.2986	-1.2421	54,601	99.8	27.2240	-33.3927	-1.2483

3rd : moving interval (05:35:00 – 06:37:40)						**4th : moving interval** (06:38:03 – 07:58:04)				
GNSS	epochs	% fix	Average (m) E	N	U	epochs	% fix	Average (m) E	N	U
G	37,001	99.9	25.4924	-34.2991	-1.2431	48,001	100	25.4903	-34.2960	-1.2419
R	37,001	99.9	25.4910	-34.2985	-1.2434	48,001	100	25.4906	-34.2964	-1.2461
C	37,001	100	25.4925	-34.2979	-1.2418	48,001	100	25.4915	-34.2958	-1.2435
G+R	37,001	99.8	25.4924	-34.2982	-1.2435	48,001	100	25.4907	-34.2962	-1.2429
G+ C	37,001	99.8	25.4931	-34.2986	-1.2426	48,001	100	25.4909	-34.2959	-1.2438
G+R+C	37,001	100	25.4923	-34.2981	-1.2428	48,001	100	25.4923	-34.2981	-1.2428

In Table 5.6, the derived components of the baseline connecting the fixed station A and the centre of the moving rotating arm. At every session, the coordinates of the centre are determined by the average values of the measured coordinates of the moving antenna (Pi) for each GNSS positioning. As the GPS positioning represents the primary focus of different GNSS solution, the combined solution of GPS with other constellation will be assessed to achieve the contribution of these constellations in improving the positioning performance. When applying the recoding coordinates of moving antenna of point Pi at the first dataset, the time series of the GPS-only solution showing the components of apparent relative position around the mean centre in E, N and U as illustrated in Fig. 5.12.

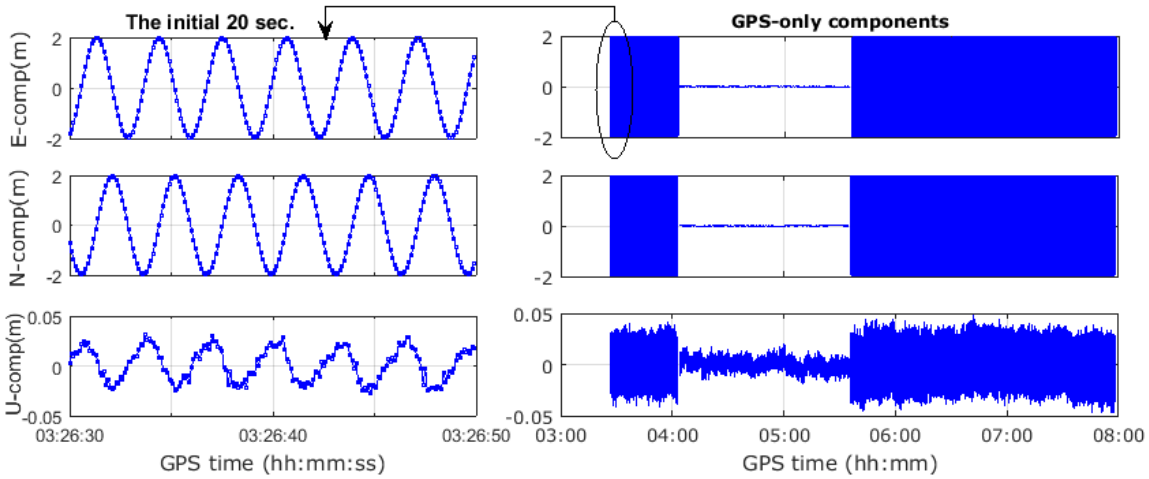


Fig. 5.12 The GPS-only time series represent the measured components of moving station Pi for the initial 20 sec of movement (left) and the whole period of the experiment (right).

Due to a large number of observations with the high sampling rate (e.g. 10Hz), the typical changes in positioning may not be evident along the time series of the whole dataset. Therefore, the initial 20 seconds of movement is presented in Figure 5.12. It is evident that the oscillating nature of the movement is represented with sinusoidal curves in all three components of E, N and U. Regarding the first session of movement, when the rotating arm is turning around the fixed centre, the traced trajectories of recording relative coordinates are displayed in Fig. 5.13.

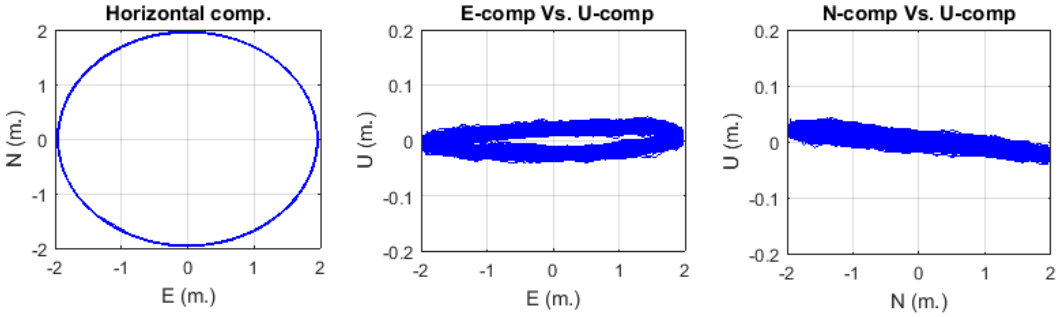


Fig. 5.13 The traced path of the GPS-only solution at the 1st session of movement.

It is evident that the recorded horizontal coordinates are changed in circular trajectory with small changes in the vertical direction as a result of the unleveled platform, which should be taken into account when analysing the quality of the positioning.

Since the analysis is focusing on evaluating the performance of different GNSS solutions, the comparison between GPS-only and another GNSS positioning may lead to small positioning differences due to the very short baseline. Therefore, the results of these differences are presented as a time series for different components. The compared results of the first session are used as examples to evaluate the performance of multi-GNSS as explained in Fig. 5.14 and their statistical evaluation is summarised in Table 5.7.

Table 5.7 The achieved STD of differences between GPS-only and other GNSS solutions

Diff.	**STD (mm) 1st sess.**			**STD (mm) 2nd sess.**			**STD (mm) 3rd sess.**			**STD (mm) 4th sess.**		
	E	N	U	E	N	U	E	N	U	E	N	U
G & R	7.37	4.50	18.71	-	-	-	3.53	3.17	8.64	4.12	3.45	10.96
G & C	4.25	4.16	12.38	3.54	3.69	10.13	3.30	3.07	9.25	6.20	3.39	17.95
G & GR	1.00	1.91	2.05	0.90	1.50	1.86	0.91	1.09	2.67	0.59	1.04	2.19
G & GC	1.73	2.95	2.67	1.67	2.30	2.73	1.71	1.69	3.85	1.32	1.95	3.13
G & GRC	1.78	2.99	3.20	1.70	2.32	2.93	1.79	1.76	4.23	1.40	2.00	3.30

*The difference between GPS and GLONASS not listed in the 2nd session due to characterised spikes of GLONASS solution

From Figure 5.14 and the Table 5.7, it can be seen that the maximum differences can detect between GPS and other individual solutions of GLONASS or even BeiDou, especially in vertical components. Whereas, the combined solutions are achieved with less level of differences.

In spite of the minimum STD have been achieved with the results of combined GPS+GLO along the four sessions, this will not represent the most accurate results because the minimum differences will not reflect the most definite improvement. Therefore, the positioning quality (i.e. accuracy and precision) of every solution are investigated.

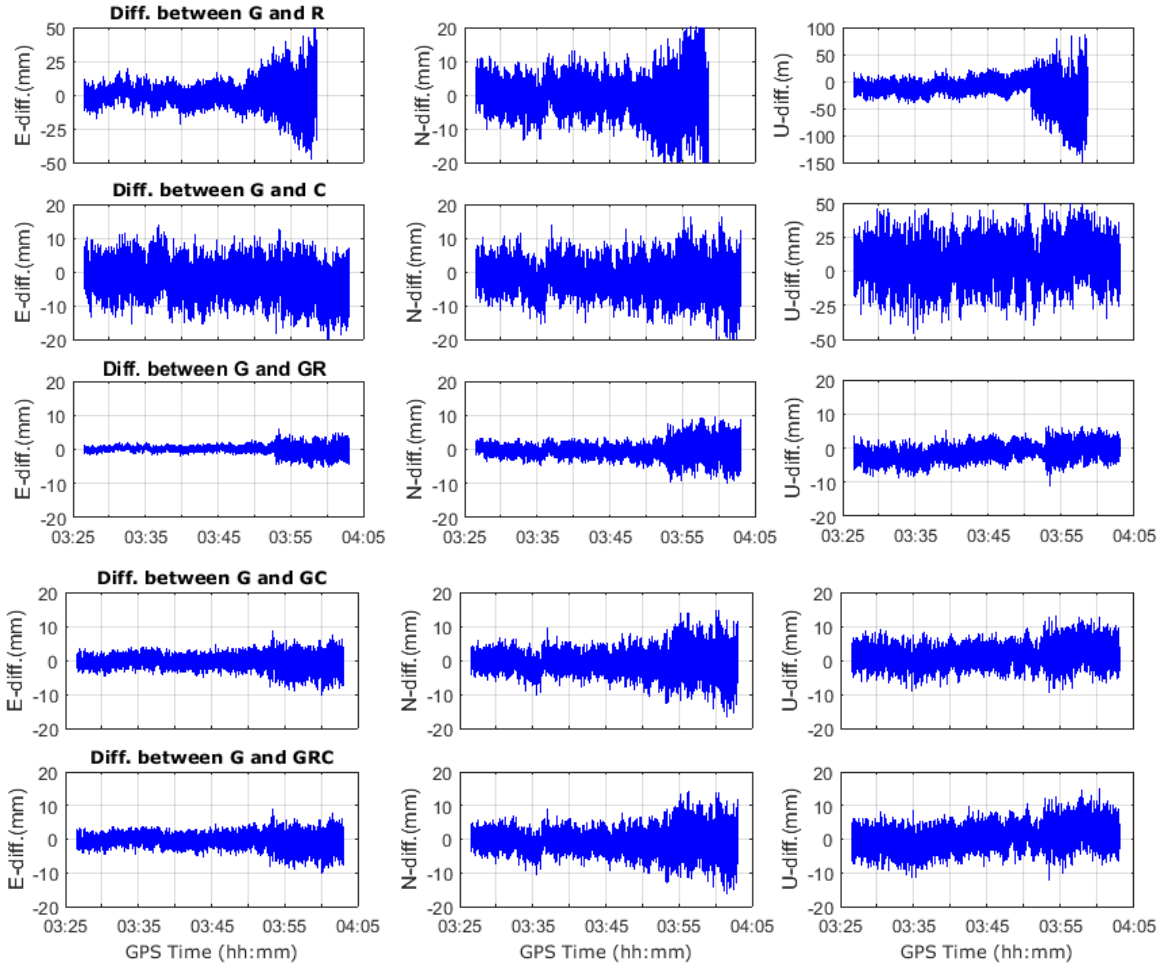


Fig. 5.14 The time series of differences between the GPS-only solution and another GNSS positioning at the 1st session of movement.

5.5.1 Accuracy and Precision of Kinematic GNSS Solutions

For different GNSS solutions, the positioning quality regarding precision and accuracy are analysed. The precision refers to the dispersion of measurements around the mean value (MPV, Most Probable Value), while the accuracy describes the closeness of the measures to the actual value (Hofmann-Wellenhof et al., 2012). It seems that the real value is the critical issue to assess the accuracy, which does not exist in the kinematic positioning due to the movement of the receiver's antenna. For this reason, it is possible to achieve the estimated accuracy of kinematic GNSS by comparing their results with the corresponding results obtained from one of the other approaches such as FEM analysis, accelerometer results or RTS results (Nickitopoulou et al., 2006). In addition, a comparison of the real true values of the predefined elements with their corresponding results from GNSS observations

to analyse the accuracy. Therefore, the various GNSS positioning results of the rotating arm will be compared with the real true derived elements (i.e. the coordinates of the centre of rotation and radius value) of a circular trajectory to estimate the accuracy.

When the rotating arm was moved around its fixed origin (Fig. 5.1), the observed GNSS measurements were recorded in three-dimensions. However, most of the similar previous studies considered only a two-dimensional assessment (e.g. (Breuer et al., 2002), (Nickitopoulou et al., 2006) and (Breuer et al., 2008)), in this analysis the real derived elements (centre and radius) will be defined in 3D. To accomplish this requirement, different mathematical techniques (Equations and computations are given in Appendix-A) can be applied using the Least Square (LS) fitting (Ghilani and Wolf, 2010).

Consequently, three different primitive forms of a 3D circle, cylinder and sphere can be investigated for the best fit of the measurements to estimate the radius length of the rotating arm as well as the 3D coordinates of the fixed centre. The most probable values of estimated elements will indicate the precision of the different conducted GNSS measurements of GPS, GLONASS, BeiDou and other combinations.

Further, the estimated arm's length is compared to the reference value, and a Root Mean Squared RMS is computed to assess the accuracy of the measurements using the individual solution of each GNSS constellation and investigate the potential of improvement with combined solutions.

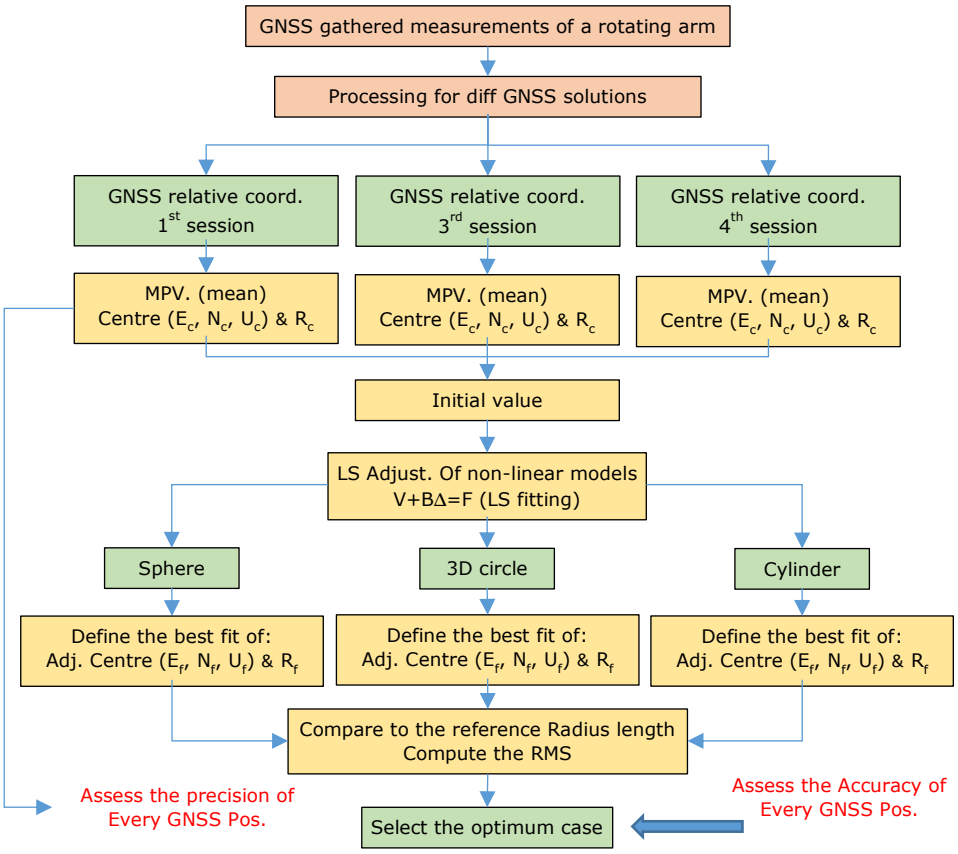


Fig. 5.15 Flowchart is summarising the workflow to assess the precision and accuracy of diff. GNSS solutions.

Fig. 5.15 illustrates the computations workflow to assess the precision and accuracy of the GNSS measurements as follows:

- After processing every dataset with different GNSS solutions, the corresponding relative coordinates are computed for each GNSS positioning at every session.
- An assessment of the precision of each solution at every session can be made by comparing the measured coordinates with the computed ones using the MPV of the radius and the centre.
- For the whole duration of movement, the mean values of measured coordinates and the derived radius will represent the initial values to apply LS adjustment of non-linear models.
- Apply the primitive surface of sphere, 3D circle and cylinder by LS fitting for every source of all measurements.
- Select the most accurate surface that achieves the most exact results of the derived radius concerning a reference length value and has the minimum RMS among other surfaces.
- Depending on the real elements of the best-fit surface, the accuracy of every GNSS solution can be evaluated by computing the RMS.

5.5.1.1 Fitting to Find the Optimum Surface

After processing the collected data, the implementation of the flowchart mentioned above depends on identifying the main elements of the circular path that produced by the movement of the rotating arm. For this purpose, the optimum 3D surface that would be fitting the circular recorded data can be one of three cases, which are a 3D circle, sphere or cylinder (Fig. 5.16). For every case, the computation of final elements is derived from the Least-squares fitting of non-linear models (the detailed calculations are given in (Forbes, 1991, Shakarji, 1998)). A MatLab script was developed to identify the main parameters. When analysing the derived elements of each fitting versus the correct reference length, it can define the most identical surface that consistency with the actual elements (i.e. centre and Radius).

In order to determine the optimum coordinates of the centre of the movement, the data of the three sessions of movement are implemented as one dataset (106,913 epochs), which contains the recorded coordinates that are expressed in relative positioning with components of E, N and U. The final adjusted results of radius length and the coordinates of the best-fitted centre are presented in Table 5.8 with various GNSS solutions for different cases. To achieve the accuracy at every solution, the RMS is computed concerning the best-fitted radius.

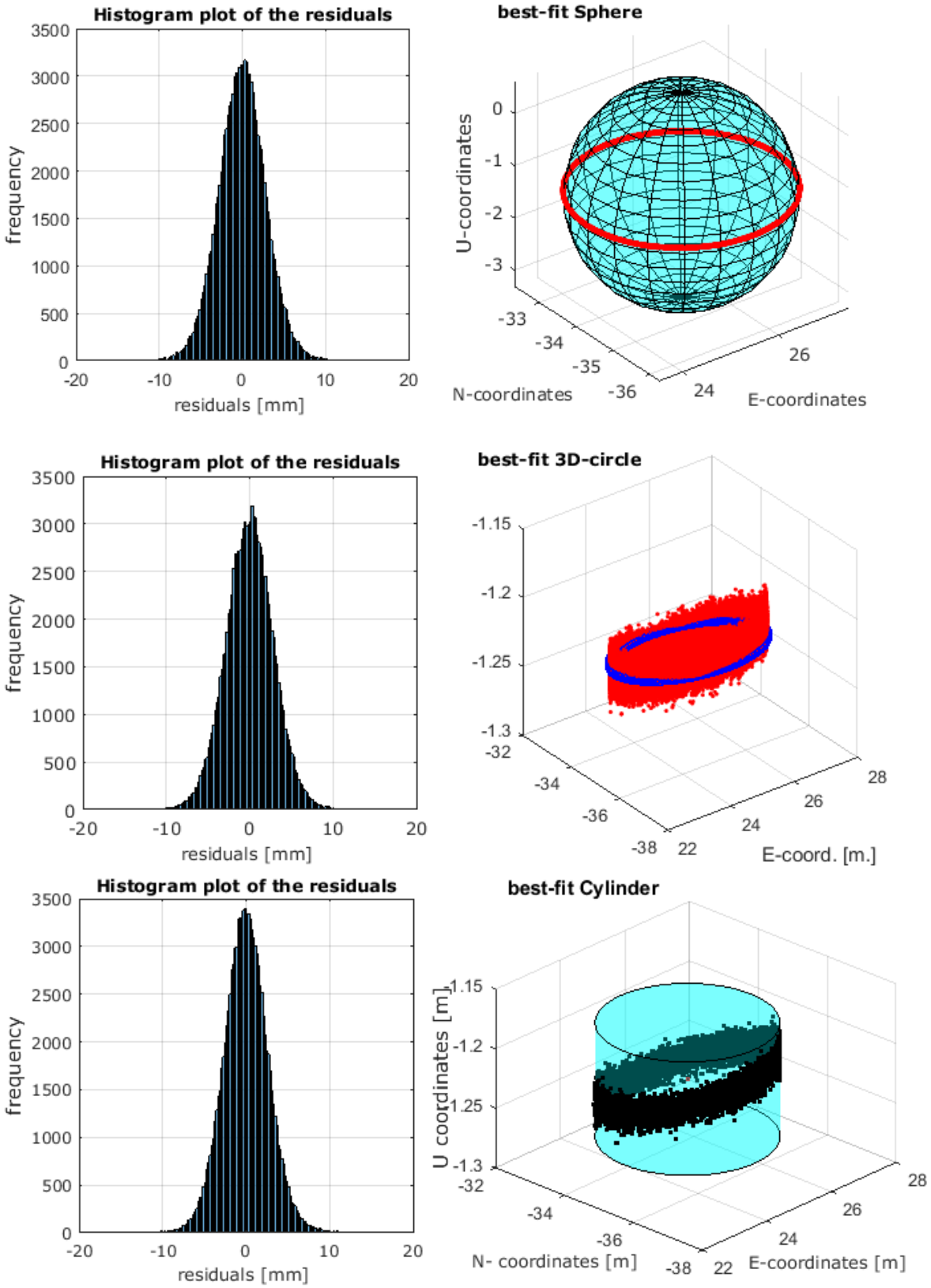


Fig. 5.16 Fitting the recorded GPS data of the moving arm with surfaces of a sphere, 3D circle and cylinder with histograms of derived residuals between measured and best-fit radius in each case.

Table 5.8 The adjusted elements to define the circular trajectory of the moving arm with three representative surfaces among different GNSS solutions of the first dataset.

1st case: Sphere						**2nd case: 3D circle**				
GNSS	**Adjust**	**Adjusted centre (m.)**			RMS	**Adjust**	**Adjusted centre (m.)**			RMS
	R (m.)	E_0	N_0	U_0	mm.	**R (m.)**	E_0	N_0	U_0	mm.
G	1.9642	25.4905	-34.2985	-1.3460	2.84	1.9612	25.4909	-34.2977	-1.2422	2.89
R	1.9614	25.4900	-34.2972	-1.2331	3.81	1.9612	25.4906	-34.2977	-1.2419	3.80
C	1.9619	25.4915	-34.2967	-1.2607	3.81	1.9616	25.4920	-34.2968	-1.2438	3.60
G+R	1.9644	25.4905	-34.2985	-1.3507	2.37	1.9612	25.4910	-34.2975	-1.2425	2.40
G+ C	1.9646	25.4908	-34.2982	-1.3521	1.99	1.9614	25.4912	-34.2972	-1.2432	2.04
G+R+C	1.9654	25.4907	-34.2984	-1.3657	1.89	1.9614	25.4913	-34.2973	-1.2433	1.94

3rd case: Cylinder

GNSS	**Adjust**	**Adjusted centre (m.)**			RMS
	R (m.)	E_0	N_0	U_0	mm.
G	1.9601	25.4903	-34.2972	-1.2422	2.69
R	1.9600	25.4900	-34.2972	-1.2419	3.67
C	1.9602	25.4915	-34.2964	-1.2438	3.32
G+R	1.9601	25.4902	-34.2972	-1.2425	2.20
G+ C	1.9603	25.4905	-34.2968	-1.2432	1.81
G+R+C	1.9603	25.4905	-34.2969	-1.2432	1.70

It can be recognised that the results of the sphere cannot be adopted due to significant differences in the vertical components, while the results of the vertical components of other two cases are consistency and performing closing results that can be represented as real elements. These derived accurate parameters can be used without any prior knowledge of the actual values. Overall, the accuracy was improved when additional constellations are added to GPS in a combined GNSS solution, which strongly agreed with the real values. Therefore, the results of combined GPS+GLO+BDS can be considered as actual values with even a 3D circle or cylinder fitting technique.

5.5.1.2 Mathematical Model and Assessment

As an accurate model has been applied for defining the elements of a circular trajectory (radius length and centre), it is possible now to assess the precision and accuracy of kinematic measurements. Since the measurements introduce errors into the actual coordinates, the measured trajectory will differ from the real best-fitted path by a shifted difference that changed from epoch to another.

For every epoch, due to the difference between the measured and computed radius, the components of this difference can be determined by assuming that the measured and the calculated points are falling on the same radial line as shown in Fig. 5.17. The detailed computations are given as follows:

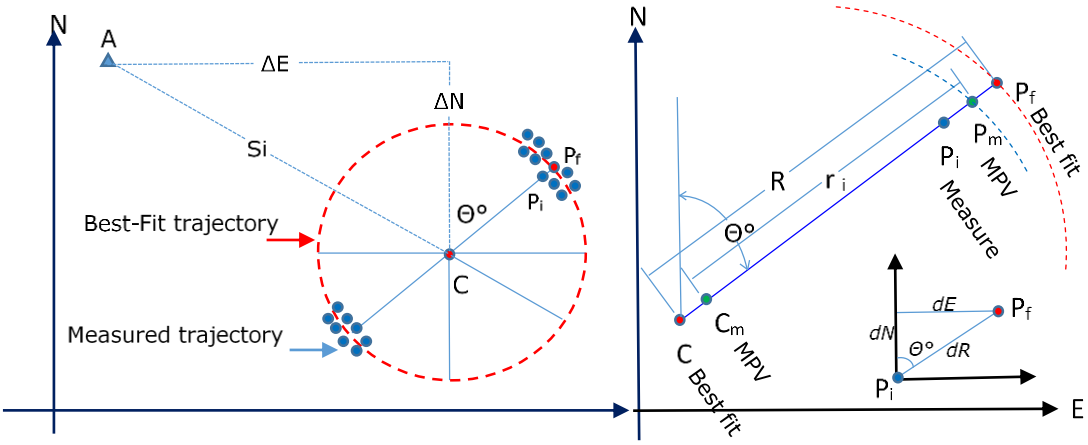


Fig. 5.17 The relationship between the measured and computed parameters.

For each session of circular movement, the set of measured coordinates of point P_i (i= 1,…,n) have been computed relative to station A, so that it is possible to determine the coordinates of the centre of rotation (C_m) as follows:

$$E_{C_m} = \frac{\sum E_{P_i}}{n} \quad , \quad E_{C_m} = \frac{\sum E_{P_i}}{n} \quad , \quad E_{C_m} = \frac{\sum E_{P_i}}{n} \tag{5.1}$$

The calculated coordinates of C_m represent the MPV of the centre, which of course differ from the actual coordinates. Therefore when achieving the precision, the required computation will be based on the MPV of evaluated elements (r_m and C_m). Thus, the coordinates of each computed point P_m can be found by the following equations:

$$\begin{aligned} \Delta E_m &= E_{P_i} - E_{C_m} \\ \Delta N_m &= N_{P_i} - N_{C_m} \\ \Delta U_m &= U_{P_i} - U_{C_m} \end{aligned} \tag{5.2}$$

$$r_i = \sqrt{\Delta E_m{}^2 + \Delta N_m{}^2 + \Delta U_m{}^2} \quad , \quad r_m = \frac{\sum r_i}{n} \tag{5.3}$$

$$\theta_i^\circ = \tan^{-1}\left|\frac{\Delta E_m}{\Delta N_m}\right| \quad , \quad \varphi_i^\circ = \sin^{-1}\left|\frac{r_i}{\Delta U_m}\right| \tag{5.4}$$

$$\begin{aligned} E_{P_{mi}} &= E_{C_m} + r_m * \sin\theta_i \\ N_{P_{mi}} &= N_{C_m} + r_m * \cos\theta_i \\ U_{P_{mi}} &= U_{C_m} + r_m * \sin\varphi_i \end{aligned} \tag{5.5}$$

$$dr_i = r_i - r_m \tag{5.6}$$

where ΔE_m, ΔN_m, ΔU_m are the differences between the measured and computed coordinates in a relative positioning system, r_i and r_m are the measured and MPV of the radius of rotation, respectively, computed for every GNSS solution. The horizontal direction is represented by θ_i°, while φ_i° reffers to the change in vertical direction that could be up or down the horizontal orbit of rotation, depending on the nature of movement at every epoch. Then the estimated relative coordinates of the computed point P_m are determined at a specific epoch i in terms of $E_{P_{mi}}$, $N_{P_{mi}}$, $U_{P_{mi}}$, therefore the difference between the measured and the computed radius (residual) is described by dr_i for evaluating the precision. On the other hand, the positioning accuracy can be achieved through the actual elements, which are defined by the best fitting procedure. Thus, the estimated coordinates of the actual position of each point P_{fi} can be computed at evry epoch as follows:

$$\begin{aligned} E_{P_{fi}} &= E_{C_f} + R_f * \sin\theta_i \\ N_{P_{fi}} &= N_{C_f} + R_f * \cos\theta_i \\ U_{P_{fi}} &= U_{C_f} + R_f * \sin\varphi_i \end{aligned} \tag{5.7}$$

$$dR_i = r_i - R_f \tag{5.8}$$

where $E_{P_{fi}}$, $N_{P_{fi}}$, $U_{P_{fi}}$ are described the coordinates of the point P_{fi} that reffers to the equivalent actual point at any epoch *i* based on the actual centre C_f and the true radius R_f for the whole duration.

The difference between the measured and the actual radius is provided by Equation 5.8. Then the positioning accuracy will be investigated by calculating the RMS at any interval of duration for each GNSS solution of kinematic positioning.

In order to assess the positioning quality regarding the precision and accuracy, the above procedure can be applied to the individual constellations as well as the combined solutions for recording data. However, the measured multi-GNSS datasets of 10 Hz have been carried out with another set of 20 Hz; the analysis can be applied to representative data, which holds true for the rest. Hence, the first session of 36 min duration (which corresponds to 21,900 samples of data) is analysed with GPS, GLONASS, BeiDou and the impact of combining GPS with other constellations is assessed. Due to a large number of measurements concerning the short length of moving arm, the differences between the results are relatively small, and small variations (residuals) can be detected between measured and computed (estimated) positions, especially in the vertical components. Therefore, the horizontal components of the residuals are presented as well as the 3D differences as illustrated in Fig. 5.18.

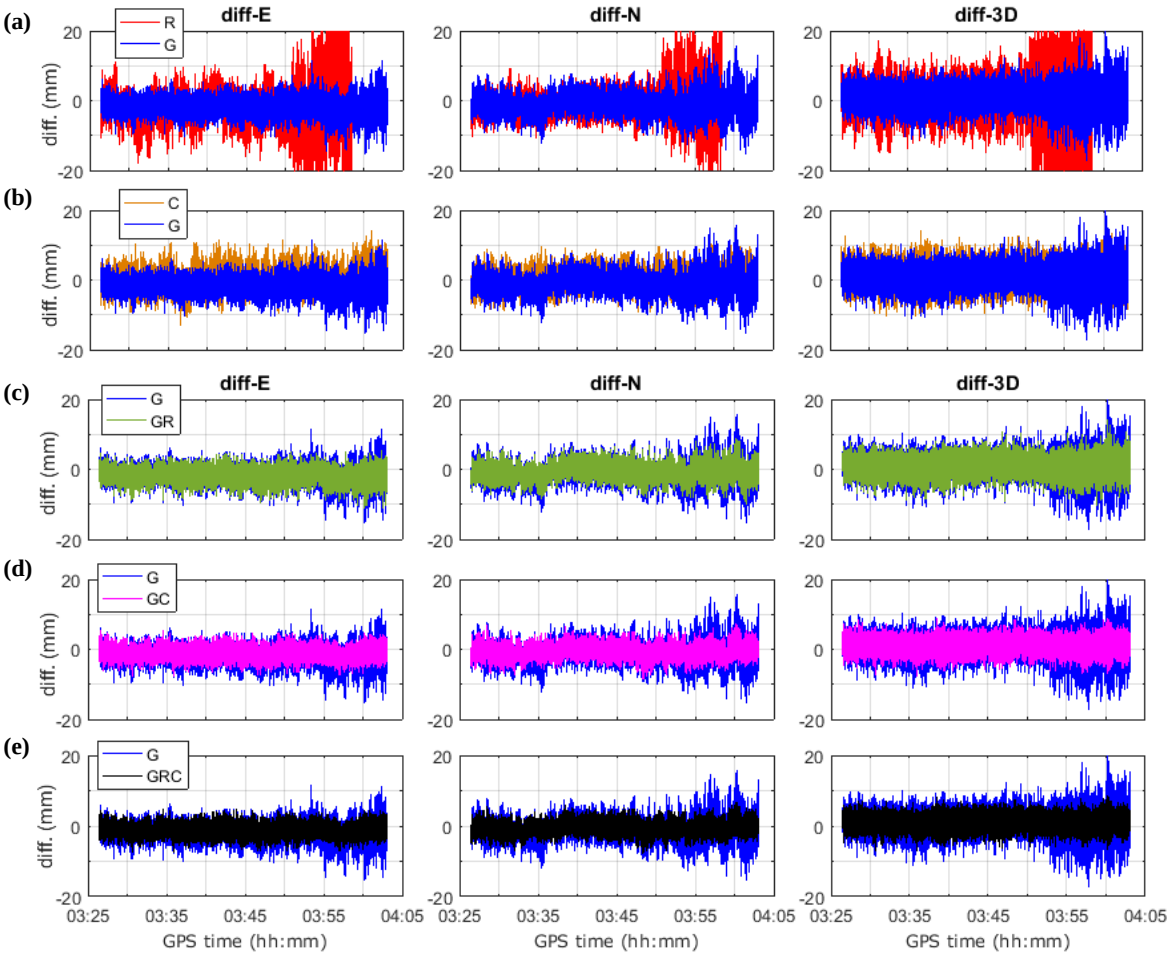


Fig. 5.18 Results of residuals between the measured and estimated fitted positions for recording data of moving arm during the first representative session of 36 min, expressing as compared time series of GPS-only and other GNSS solutions, resulting in E, N and 3D components.

The comparison between GPS and GLONASS confirms that the GPS results are more precise and accurate than GLONASS results and have a higher availability of fixed solutions as illustrated in Fig. 5.18a. When comparing the GPS and BeiDou positioning, the results of GPS show a slight improvement in positioning accuracy against BeiDou. Whereas the RMS values of GPS are 2.14mm, 2.40mm and 3.24mm in the E, N and 3D components respectively, while the corresponding RMS values of BeiDou are 2.43mm, 2.12mm and 3.30mm as summarised in Table 5.9 and illustrated in Fig. 5.18b.

Table 5.9 The achieved precision and accuracy of different GNSS solutions for 1st session.

Diff.	r_m	STD (mm) : Precision			R_f	RMS (mm) :Accuracy		
		E	N	3D		E	N	3D
G	1.9624	2.14	2.40	3.24	1.9614	2.81	2.83	3.40
R	1.9622	4.89	3.60	6.17	1.9614	5.34	3.81	6.23
C	1.9626	2.43	2.12	3.30	1.9614	2.63	2.34	3.53
GR	1.9625	1.70	1.75	2.50	1.9614	2.58	2.18	2.73
GC	1.9625	1.42	1.48	2.13	1.9614	2.00	1.84	2.39
GRC	1.9625	1.37	1.40	2.05	1.9614	2.00	1.76	2.33

As part of the assessment, the comparison between GPS-only and other combined solution of GPS with other constellation was evaluated. The positioning accuracy of the combined solution was expected to improve due to the improved of satellites geometry. However, the combined of GPS+BDS showing better improvement than GPS+GLO, the combination of GPS+GLO+BDS leads to the most accurate positioning results as presented in Fig 5.18e. From the above results, it can be concluded that the increase of a number of valid satellites will improve the satellite geometry (Fig. 5.19) and result in improving accuracy.

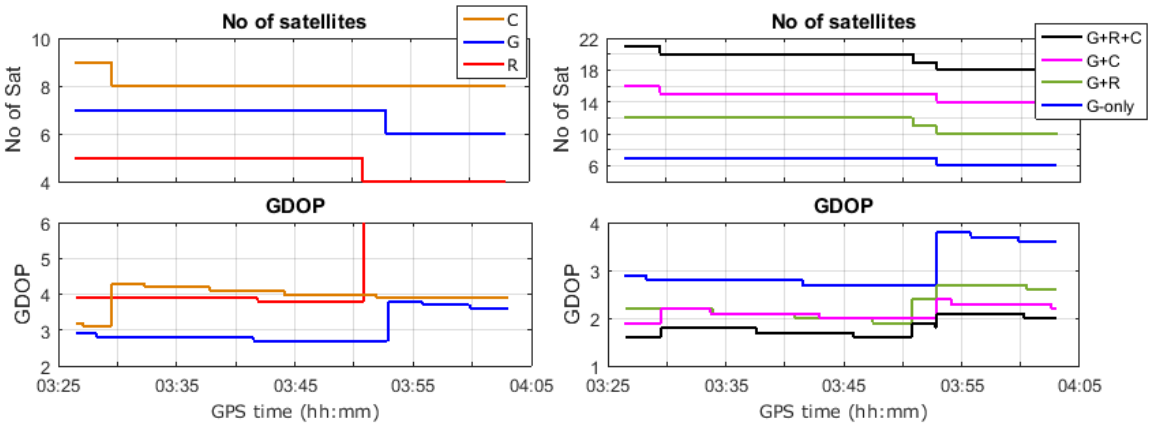


Fig. 5.19 The number of valid satellites and the corresponding GDOP values (left) individual constellations (right) combined GPS with other constellations compared to GPS-only at first subset.

As a result of this improvement, there is a tendency of a combined solution to enhance the positioning quality, especially for the positioning results at intervals that detected as noisy with GPS-only or other individual constellations. Therefore, when all the GNSS constellations are entirely in operation, this will be useful for GNSS applications, such as structural monitoring.

5.5.2 Frequency Identification

In order to define the dominant frequency of the oscillation movement using the GPS and other GNSS oscillating data, the Normperiod code has been applied to the time series of these solutions. Thus, it can detect oscillation frequency from different solutions regarding the same oscillation movement. Consequently, the derived frequencies from relative GNSS positioning are compared to confirm the real oscillation frequency, and also to assess if there any significant differences achieved between the derived frequencies from different solutions. In parallel with that, the derived frequencies can also be examined according to the represented time series of differences between the GPS-only solution and other constellations.

Since the first dataset has a sampling rate of 10 Hz, the frequencies of 5 Hz or less can be detected (Nyquist Theorem). For the subset of 36 min where movement occurred, by applying the Normperiod code on the time series of GPS-only positioning, the visible peaks of oscillating frequencies are detected as shown in the spectrum of Fig. 5.20 for all three positional components. From this Figure,

it is evident that the dominant frequency is identified at 0.314 Hz for all components. However, a single dominant frequency was detected with the horizontal components; the vertical one defines more than one dominant frequency, whereas other peak at 0.6278 Hz represents the second possible frequency.

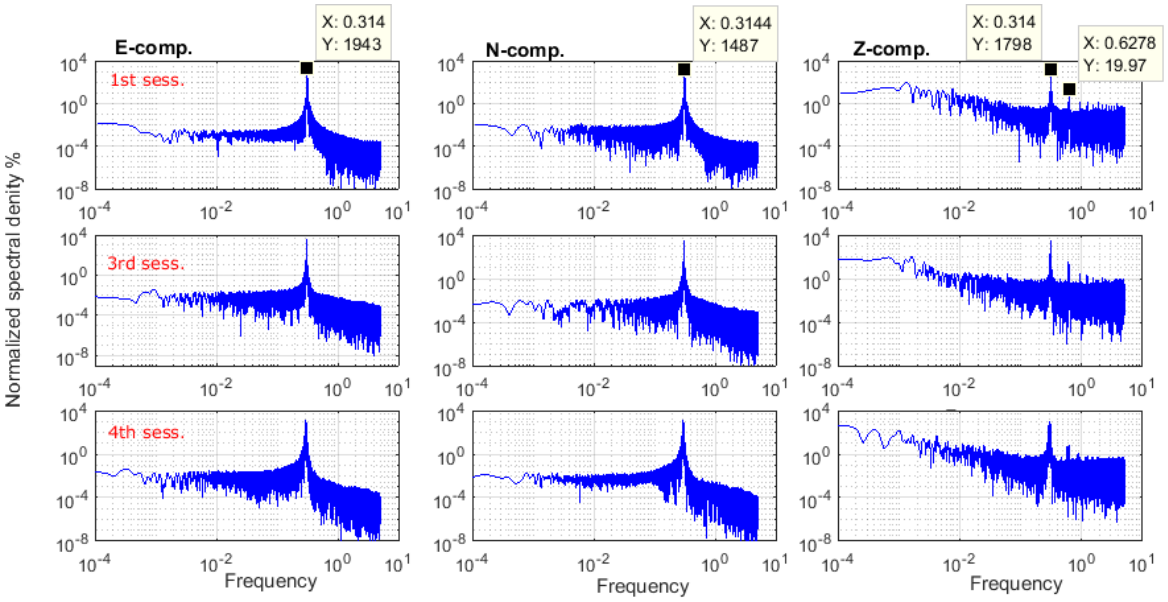


Fig. 5.20 Spectra of derived frequencies from the time series of the first dataset (10 Hz rate) with a GPS-only solution along E, N and U components.

When a Normperiod code was performed on the other GNSS data, similar results of detected frequencies were achieved. Moreover, the peak of 0.314 Hz has been highlighted in all different periods of movement with all other GNSS solutions. Thus, the results of derived frequencies from other GNSS are consistent, whether they are derived from the individual or combined GNSS solutions. This property will help to detect certain real frequencies when applying different GNSS solutions.

On the other hand, when adopting the deriving time series of differences results between GPS and other GNSS solutions (Fig. 5.14), the similar magnitude of derived frequencies was defined even they are derived from different position solutions. Regarding the second dataset of 20 Hz sampling rate, which permits to analyse their time series at the subset of 36 min, it was found that the identified dominant frequency was also 0.314 Hz as illustrated in Fig. 5.21.

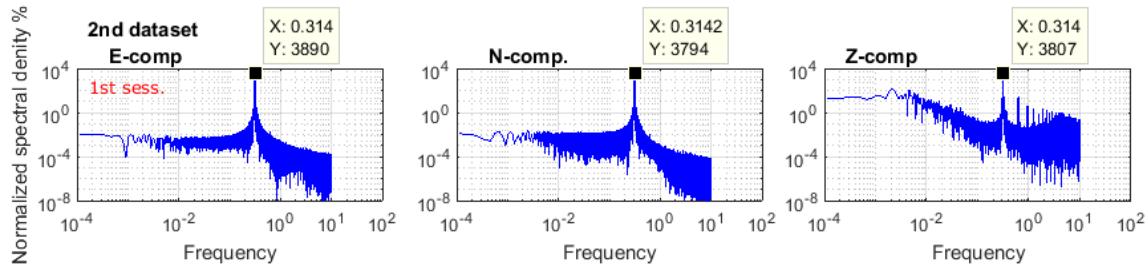


Fig. 5.21 Spectra of derived frequencies from the time series of second dataset (20 Hz rate)

However, the same magnitude of frequency was detected, they differ in the amplitude values. According to results of this analysis, it can be concluded that the most likely value of the dominant frequency is 0.314 Hz. This value was frequently appeared in all solutions due to the movement with constant velocity. It is interesting to note that the correct derived frequency is similar to the GPS-only and other GNSS solutions even though there are differences in the corresponding time series.

When this analysis is carried out for the derived differences of measured positioning from the estimated real ones, the normperiod spectra revealed that the dominant frequency is detected with the main peak of 0.314 Hz for all components of E, N and U.

5. 6 Summary and Conclusions

The short baseline tests were conducted to achieve the positioning precision and accuracy of different GNSS solutions through static and kinematic measurements. The collected static data of 1Hz along 24h at the first baseline were processed to evaluate the positioning performance with GPS-only, GLONASS-only and combined GPS/GLONASS solutions. The results showed that the positioning could achieve mm level of precision. However, the GLONASS-only solution was characterised by various noisy intervals (due to weak geometry). The combined GPS/GLONASS solution proved significant improvement against the GPS-only solution. The satellite geometry has also been evaluated with each solution, and the results indicated that the combined GPS/GLONASS solution could improve the geometry by 27% and 30% for GDOP and PDOP respectively, relative to GPS-only solution.

The comparisons between single and dual frequencies have been performed as a further investigation, which showed a reduction in fixing rate with single frequency compared to dual frequencies. It was demonstrated that with excluding multipath contaminated data, it is possible to increase the rate of fixing ambiguity.

This chapter has also presented the results of short kinematic baselines to evaluate the positioning quality of different GNSS solutions from measurements of moving antenna on a rotating arm relative to fixed two reference stations. The assigned true value of the evaluating elements represents a critical point in moving objects of kinematic measurements, which was investigated in this chapter. Thus, the estimated accuracy was determined by comparing the recorded GNSS data (the measured elements) and the actual values of these elements, which were identified by a new approach using a 3D best fitting. The new approach is based on non-linear least squares adjustment models to determine the actual values of circular movement elements (i.e. radius and centre).

Among the comparison of three surfaces, the 3D-circle fitting was chosen as the best fitting model. In addition, the mathematical models have been derived to estimate the positioning accuracy. The estimated accuracies for GPS-only, GLONASS-only and BeiDou-only were achieved as well as the

corresponding accuracy of combined solutions between these satellite systems. The results showed that GPS-only was more accurate than GLONASS and BeiDou. The analysed results revealed improvements when adding other observations to GPS data, while the combined solution of GPS/GLONASS/BDS achieved the most accurate solution, due to more redundant observations from three systems as well as improved geometry.

This appropriate technique enables to assess the accuracy of kinematic GNSS positioning and simulate their potential to monitor the significant changes in the positioning of a moving antenna. The outcomes of these experiments provide a modelling analysis that can be implemented to monitor real structures through deflection monitoring by GNSS measurements. This has been further studied in the following chapter.

Chapter 6: The Contribution of Multi-GNSS Applied in Real Cases of Bridge Deformation Monitoring

Part of this chapter has been published as:

MSAEWE, H. A., HANCOCK, C. M., PSIMOULIS, P. & ROBERTS, G. W. 2017b. Monitoring dynamic deflections at towers of Severn Suspension Bridge in the UK using GNSS technique.

In order to overcome the GPS-only limitations and improve the positioning performance for structural health monitoring system, this chapter discusses the use of a combined GNSS solution as a technique that is capable of enhancing the positioning quality and reducing the limitations, which substantially enhance the GPS system for Structural Health Monitoring. This technique can be implemented by adopting a developed suggested strategy (see the methodology in Section 6.2) aimed to achieve the best possible consistency of GNSS constellations for structural monitoring with more reliable and accurate positioning. A real monitoring data of two long-span suspension bridges in the UK, namely, the Severn Bridge and the Forth Road Bridge, which are used to validate the effectiveness of the proposed approach with multi-GNSS constellations.

6. 1 Introduction

GPS has been used at the last two decades as a technique to measure deflections and deformations, which could then possibly be used as part of structural health monitoring system to different infrastructures such as high-rise buildings, dams and bridges. Due to severe bridge environment, yet the GPS measurements still suffer from errors (i.e. noise, multipath, cycle slips, etc.) degrading the positioning quality and solution availability. Considerable studies have been carried out to overcome these limitations by integrating GPS with other complementary sensors (i.e. accelerometer, RTS, pseudolite, etc.) in order to achieve the accuracy requirements of the deformation and deflections determination for structural monitoring.

In this study, it has been proved that the combined GNSS solution contributes in improving the positioning performance by reducing the noise level as discussed in Chapter 4 and enhancing the achievable precision and accuracy for both static and kinematic positioning, which was investigated in Chapter 5. Based on the experimental GNSS measurements, a methodology was developed for the processing and analysis of the GNSS measurements of bridge monitoring, which can enhance the achieved accuracy and the availability of the GNSS solutions and improve the outcome of the bridge monitoring. The developed methodology was applied to two pilot studies of the abovementioned bridges.

6. 2 Proposed Methodology

For monitoring the long-span suspension bridges, the response of the top of the towers and other critical points of the main span (e.g. midspan, quarter-span, etc.) can be recorded from the GPS monitoring stations. Even though the response of the long-span suspension bridges is greater than cm-level, it can be detectable with GPS measurements. However, the GPS monitoring is still challenging due to multipath effects from towers, cables and passing vehicles on the bridge as well as obstructions causing cycle slips in measurements (Raziq and Collier, 2007). These effects resulting in additional coloured noise and biases errors (Moschas and Stiros, 2013), which may lead to outlier level including missed and false alarms (Brown et al., 1999, Nickitopoulou et al., 2006).

Even with the presence of these limitations, GPS can be still used in bridge monitoring by adopting methods and techniques to eliminate the GPS data errors and enhance the accuracy of GPS solution. In the current study, a new methodology was proposed and developed, where multiple GNSS constellations were used in order to reduce the noise level of the positioning solution and enhance the achieved accuracy relative to that of the GPS-only solution.

The flowchart shown in Fig. 6.1 can demonstrate the suggested approach, which implies several sequential steps to achieve GNSS structural monitoring in more reliable and accurate positioning results. Generally, the approach of this flowchart can be summarised by the following steps:

Step-1. Collecting GNSS data:

Use GNSS receivers at the reference base station and the monitoring points of the bridge, in order to record signals from the different GNSS constellation (i.e. GPS, GLONASS, Galileo, BDS). The base station could consist of two GNSS-receivers connected via a splitter to the base-station GNSS antenna, to assess the quality of the GPS/multi-GNSS solutions. The same type of GNSS receivers should be deployed at both base and rover stations.

Step-2. Pre-processing analysis:

The pre-processing procedure is performed to assess the quality of measurements and exclude the observables that may substantially degrade the positioning quality. This procedure is applied for the base and the rover station data, before estimating the final positions, aiming to detect and potentially repair cycle slips (see Section 3.5.2), multipath detection based on MP1 and MP2 (see Section 3.5.4) and identify the rising and setting satellites with low SNR values. The low-quality measurements, contaminated by noise etc., are excluded from further processing.

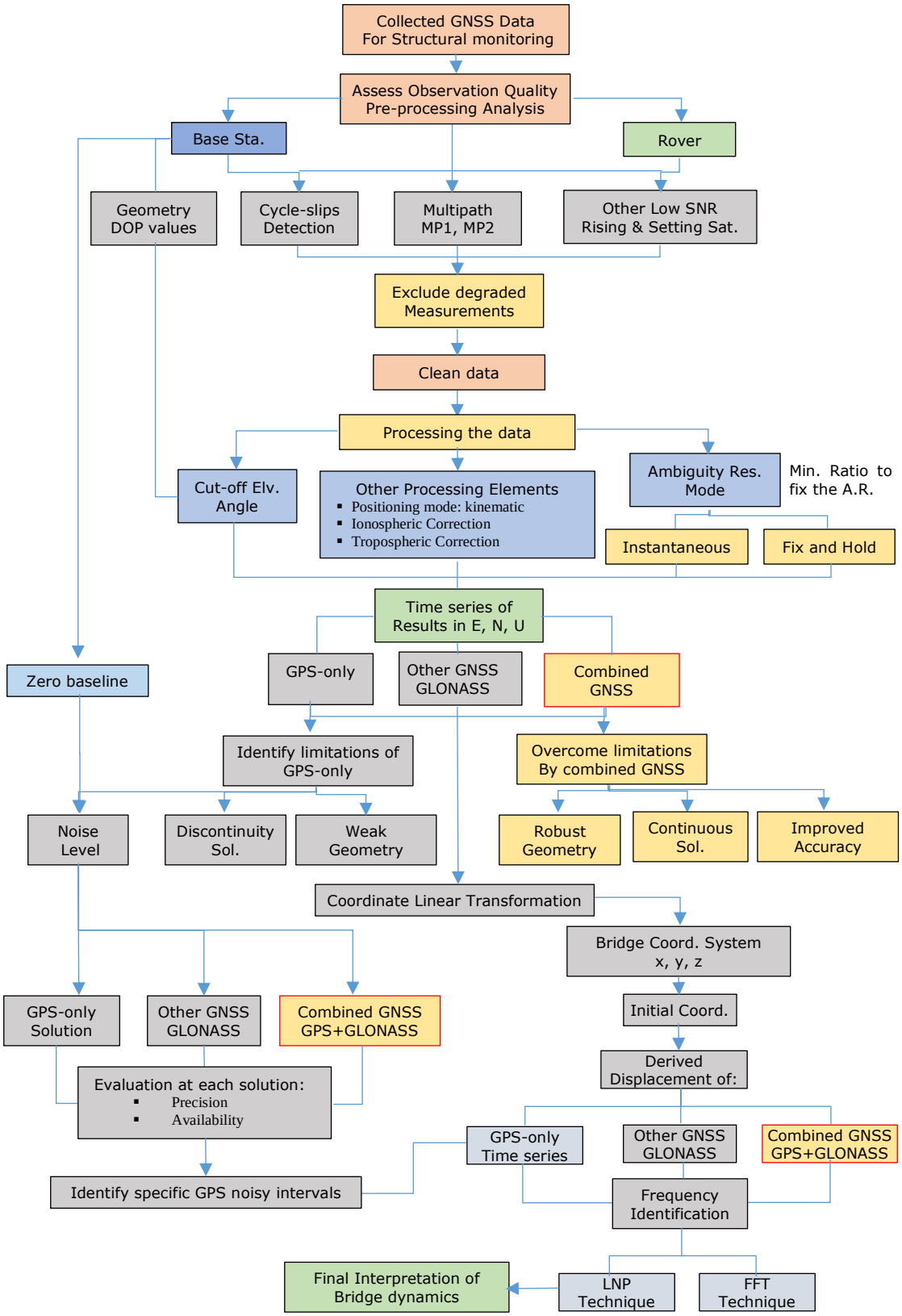


Fig. 6.1 Flowchart summarising the proposed monitoring procedure.

Step-3. Evaluate the satellite geometry (DOP values):

For the available GNSS constellations, it is assessed the geometry of each constellation, by analysing the dilution of precision (DOP) values at each epoch. The DOP values for each GNSS constellation represent the quality of the satellite geometry, which has an impact on the derived solution. It is expected that the increase of the observed satellite with proper distribution will improve the geometry.

Step-4. Noise assessment by multi-GNSS zero baseline:

Based on the experiments of Chapter 4, the noise level of the various GNSS solutions can be evaluated by using zero-baseline measurements. The zero-baseline measurements at the base station will provide the noise level, the solution availability and the positioning precision for the E, N and U components of different GNSS solutions. As proved in Section 4.7, the precision of noise level correlates with derived geometry; therefore, the improved geometry will reduce the noise level. Specific noisy GPS intervals due to weak geometry will be identified, and the option of using multi-GNSS constellations to reduce this noise level is analysed (Msaewe et al., 2017b)

Step-5. Processing GNSS data:

Applying the appropriate mode of fixing ambiguity resolution (e.g. see Section 3.5.1) and evaluate the alternative fixing. Consequently, the kinematic positions of monitored stations on the bridge are calculated

Step-6. Determination of the displacement:

The GNSS data in the geodetic coordinate system were converted to bridge coordinate system using the linear transformation of rotating data. In this way, the x-axis and y-axis are aligned with the lateral and longitudinal direction of the bridge, respectively, while the z-axis represents the vertical component of height variations. The derived displacements at each monitoring station are computed from the difference between the initially fixed coordinates and the corresponding measured values.

Step-7. Spectral analysis:

The displacement time-series were analysed by using spectral analysis to extract the information of the main modal frequencies of the bridge at each direction (x-lateral, y-longitudinal and z-vertical). For the spectral analysis was done by applying the LNP technique. The FFT technique was also applied for verification of the results, but could not generally be applied, as the displacement time-series were not always continuous.

Step-8. Analysis and final interpretation:

When achieve accurate and reliable results along with continuous monitoring data by implementing the suggested strategy with multi-GNSS, it is possible to evaluate the response of monitored structure (i.e. suspension bridge) with correct interpretation.

6. 3 Severn Bridge Monitoring

6.3.1 Severn Bridge Description

In this study, the Severn Suspension Bridge, which is one of the largest suspension bridges in the UK (Fig. 6.2), was monitored using GNSS receivers. The bridge was opened in September 1966, carries the 4-lanes of the M48 motorway as a dual carriageway over the Severn Estuary.



Fig. 6.2 The Severn Suspension Bridge.

It is located in south-west England and southeast Wales connecting the Bristol area to South Wales (Roberts et al., 2014). The bridge's deck is supported by two main cables and hangs between two steel towers. Its length is 1,600 m, consisting of a central suspended main span of 988 m in length, which is supported by the two towers, through the cables. Each tower has a height of 136 m above the mean level of water (Roberts et al., 2015).

6.3.2 Monitoring Points and Measurements

In order to monitor the response of the bridge, the measurements were conducted continuously at 11 locations, between 20th and 23rd July 2015. The GNSS antenna at each location was fixed on the bridge and connected via cables to the GNSS receiver, located in a secure place allowing easy access. Four GNSS receivers were installed on the top of two towers; two of them were Leica receivers established on two sides of the eastern tower (T1 and T2) and other two Trimble receivers on two sides of the western tower (T3 and T4). In addition, four GNSS receivers (of a different type) were installed on the suspension cables; three on the northern upstream side (Fig. 6.3, points A, B and D) and one on the southern downstream side (Fig. 6.3, point F). Both GNSS stations B and F were located at the midspan of the cables, in the opposite side of bridge width, while (A) and (D) where

on the same cable at the quarter-span from each tower. Moreover, three GNSS stations were installed on the handrail of the bridge (B1, D1 and G).

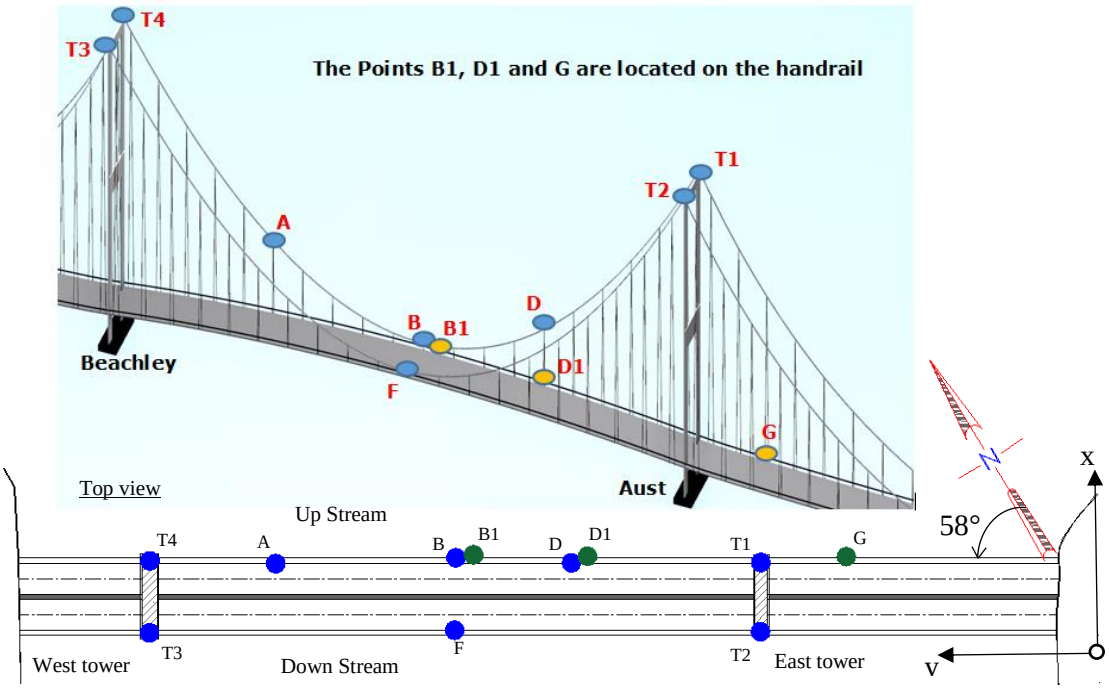


Fig. 6.3 Locations of monitoring points upon the Severn Bridge.

A GNSS station was installed on the roof of the toll building, ~1 km away from the eastern tower of the bridge, which was used as a reference station, expected to be a fixed location, not affected by the bridge movement. The GNSS receivers, which were used, are dual frequency, consist of Leica GR10, Leica GS10, Leica 1200, Trimble-NET9 and Javad, while most of the antennae used were Leica AT504 choke ring antennas. The latter help to mitigate the multipath effects (see Fig. 6.4).



Fig. 6.4 The Leica AT504 choke ring antenna located on the main suspension cable.

All the GNSS receivers recorded pseudorange and carrier phase observations with a sampling rate of 10 Hz. Due to an insufficient number of receivers, some receivers were moved from one location to another for different durations. The details of the operation for each GNSS station is listed in Table 6.1.

Table 6.1 Specifications of monitoring points upon the bridge.

Group	Points	Antenna Type	Receiver Type	Duration of collecting GNSS data			
				20/07	21/07	22/07	23/07
Base	Ref.	Leica AR10	Leica GR10	12 h	24 h	24 h	9 h
	R-b		Leica GS10	12 h	24 h	8 h	x
Tower points	T1	Leica AS10	Leica GS10	10 h	24 h	24 h	9 h
	T2	Leica AS10	Leica GS10	10 h	24 h	24 h	9 h
	T3	Leica choke ring	Trimble Net-R9	12 h	24 h	24 h	9 h
	T4	Leica choke ring	Trimble Net-R9	12 h	24 h	24 h	9 h
points on cables	A	Leica choke ring	Javad -Leica1200	11 h	8 h	21 h	9 h
	B	Leica choke ring	GS10 -Leica1200	x	6 h	24 h	9 h
	D	Leica choke ring	Javad	x	12 h	6 h	9 h
	F	Leica choke ring	Leica GS10	12 h	24 h	24 h	9 h
Handrail points	B1	Leica AS10	GS10 -Leica1200	x	15 h	x	x
	D1	Leica AS10	Leica GS10	9 h	3 h	x	x
	G	Leica AR10	Leica GS10	x	x	15 h	9 h

At the base station two GNSS receivers, a Leica GR10 and an updated Leica GS10 were connected via a splitter to a single Leica AR-10 dome antenna to form a zero baseline. The GNSS measurements of zero baseline were conducted for 44 consecutive hours, starting at 12:00 am on 20/07/2015 until 09:00 am on 22/07/2015 to study the noise level of different GNSS constellations. Then, the base station was restricted on Leica GR10 after moving GS10 to a handrail location on the bridge.

6.3.3 Tracking Multi-GNSS Constellations

To overcome the limitations of GPS-only for bridge deformation monitoring and to investigate the potential improvement of using the multi-GNSS positioning, all receivers used in the Severn Bridge monitoring are set to collect observations from different GNSS constellations. More specifically, all receivers can record both GPS and GLONASS data, while two of the Leica GS-10 receivers have the potential to collect all GNSS data, including also observations from BeiDou and Galileo. Therefore, one of two receivers was installed at the second base station (R_f), while the other one was operated at the handrail station of D1, then moved to station B1 followed by collecting GNSS data at station B as illustrated in Fig. 6.5, which shows all the observed stations and their durations.

Thus, it is possible to evaluate the impact of multi-GNSS constellations on the derived positions when comparing the results of GPS-only with the corresponding combined solution of GPS with other GNSS constellations.

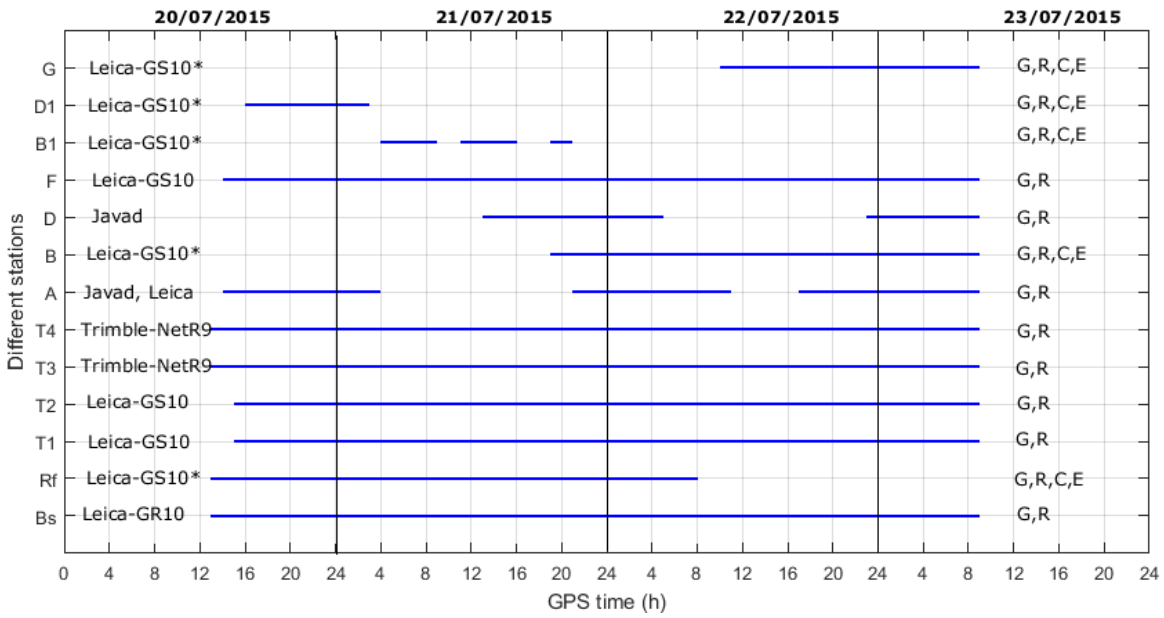


Fig. 6.5 All observed stations of monitoring Severn Bridge with operated receivers' types and their operating durations over the four days of monitoring.

However, BeiDou and Galileo are under development, both GPS and GLONASS are full operational satellite systems with global coverage. By implementing the observations from these two systems, the performance of multi-GNSS solutions can be evaluated. However, we have more than one type of receivers; the performance evaluation will be restricted to the use of Leica receivers. The reason behind this selection is due to the ambiguity of GLONASS correct fixing, which requires receivers of the same type in the differential solution because of the Inter-Frequency Bias (IFB) (Al-Shaery et al., 2013). Therefore, the combined GPS/GLONASS solution is applicable when the base and rover receivers are homogeneous. In addition to the GNSS data, other meteorological data, including air temperature and bridge's steel temperature, relative humidity, wind speed and wind directions, were all gathered during the survey in specific locations.

6. 4 Pre-Processing Analysis of the Severn Bridge Measurements

In order to attain high precision positioning for structural monitoring with GNSS measurements, the factors that degrade the quality of the satellite signals must be analysed. Some of these factors can be detected before processing, while others are eliminated in the processing procedure by implementing the DD technique with a short baseline in differential positioning. One of these factors is the acquisition of a new rising satellite of low elevation with relatively low SNR or sudden signal loss (i.e. cycle slips) that occurs on either the receiver of the base station or the rover receiver. Since the base station is located in an open sky environment, it does not suffer from any cycle slips or severe multipath, while the GNSS antennae of the monitoring stations on the bridge are susceptible to the multipath effect from the surrounding environment of cables, towers or passing vehicles.

Therefore, all these factors should be taken into account as part of the investigation when assessing the time series of detected displacement of bridge movements.

6.4.1 Cycle Slip Detection

As it was pointed out in Section 3.8, the occurrence of cycle slips can add biases to carrier phase observations, which affect achieving precise positioning (Bisnath and Langley, 2000). Therefore, detecting these biases in the preliminary investigation and subsequently repairing them in the processing stage, will remove these biases. However, if to correct the cycle slips is not possible then the integer ambiguity must be re-estimated (Huang et al., 2015).

The detection of the cycle slips was made in the processing stage, using the software of GNSS data processing (i.e. RTKLIB). Since the observed data are in dual frequency, it is possible to implement the "LG jump" technique to monitor jumps of the geometry-free linear combination, which oriented to use the data from a single receiver (T. Takasu, 2013). This technique indicates the occurrence of cycle slip on single GNSS station (base or rover receiver) and identifies at which satellite the cycle slip occurred and at which epoch of the GNSS record.

To clarify that, when applying the RINEX observation data as input measurements in RTKLIB, the detected cycle slips are presented in the satellite visibility plot. For instance, for the GNSS record of the tower station T2 on 21/07 for the time interval between 08:00-09:00, the plot indicates that many cycle slips (the vertical red ticks) have occurred with a particular satellite G15 as depicted in Fig. 6.6. Whereas, the simultaneous counterpart measurements at the base station are free from cycle slips specifically for G15.

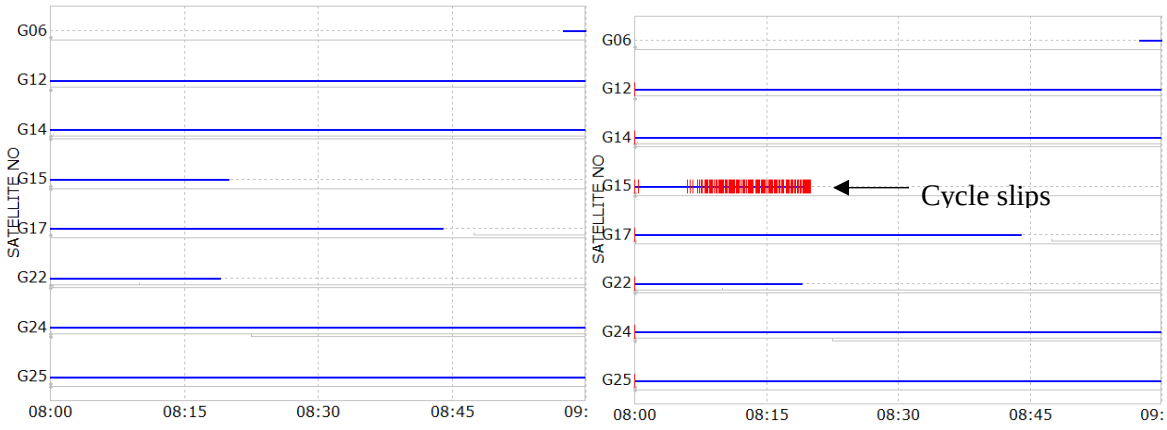


Fig. 6.6 Detecting cycle slips with visible satellites plot for base station (left) and monitoring tower station T3 (right) on 21 July 2015.

Furthermore, using the corresponding signal to noise ratio (SNR) for every satellite at each frequency (L1 and L2), it was found that the cycle slips on satellite G15 were related with low SNR on L2 signals, which means the receiver has lost track of the cycle count to this specific satellite (G15).

Based on that, the cycle slips must be correctly repaired to guarantee correct ambiguity at the data processing stage.

Accordingly, to verify the effects of detected cycle slips on fixing the ambiguity and derived results, the same datasets of Fig. 6.6 are implemented. By using the instantaneous mode for the GNSS data processing, the ambiguity of each epoch is fixed independently. The derived solution of GPS-only with this approach resulted in a time series with 71% success-rate of ambiguity fixing, which represents the positioning availability. This degradation in availability may be attributed to the existence of cycle slips. However, Teunissen et al. (2014) demonstrated that the instantaneous approach has an added advantage that the derived solution will be insensitive to the occurrence of the carrier-phase cycle slip. On the other hand, the limited number of valid satellites, high observation noise and multipath may hinder successful single-epoch resolution (Verhagen and Teunissen, 2014).

That means that there is another effect along with the detected cycle slip which can reduce the availability of the dataset. The potential cause might be a bias induced by the multipath and/or the low quality of SNR for one or more available satellites. This will be investigated in the following section. Anyway, to verify the fixing of ambiguity with another mode, Fix-and-hold has been used, and the percentage of the correct fixed solution was 67% as illustrated in Fig. 6.7.

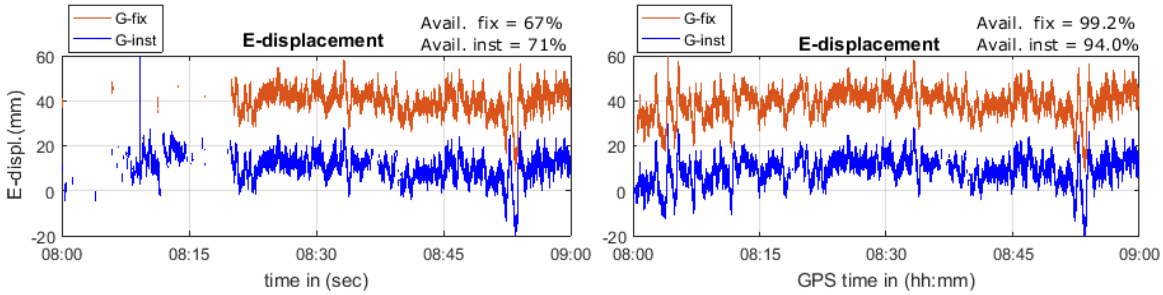


Fig. 6.7 Time series of GPS-only for a dataset of station T2 in Fig. 6.6 (left) apparent solution (right) solution with clean data after excluding G15 on 21 July 2015.

Along the problematic interval (i.e. 08:06 - 08:20), the comparison between fixed solutions of two techniques showing that an instantaneous mode yielded fixing solution even the cycle slips occur, while there is no fixing achieved with fix-and-hold technique.

This results reinforced the above observation. However, the option of the instantaneous processing-mode requires a sufficient number of visible satellites with good quality of observations (generally with good SNR's). Otherwise, it can apply the Fix-and-hold as an alternative technique in cases of reduced availability with instantaneous fixing for the individual constellation.

However, even if the satellite geometry is affected when satellites are excluded, to remove a problematic satellite might improve the positioning solution. Therefore, it is possible to examine the positioning performance when excluding the satellite G15 from the above dataset. This will lead to

clean data with the remaining observations that solved with the availability of 94% with instantaneous fixing, while 99.2% was obtained when employed the fix-and-hold method. Apparently, the higher availability with the fix-and-hold method is due to the fact that the integer number of cycles are hold constantly between the receiver and every satellite in view after success fixing. Although the improved availability was achieved with this procedure of excluding satellite, the derived position still suffers from noise, which will discuss in the next section, in addition to the influence of multipath effect.

6.4.2 Multipath Detection

As the cycle slips were detected in the initial investigation, another limitation that needs to identify is the multipath, which degrades the GPS performance for bridge monitoring. The multipath represent the major error source that may substantially reduce the positioning quality and affects the correct interpretation of bridge deformation (Roberts et al., 2002).

In order to minimise the impact of multipath, one of the particular pre-observation strategies is to use choke-ring antennas (Momoh, 2013). Although, the choke-ring antennas success to suppress multipath arrivals from the ground, or low-elevation scatters (Kaplan and Hegarty, 2005); the reflected signals above the antenna, which in the case of bridge monitoring might be due to the cables, towers, etc., still affects the GNSS observations (Hofmann-Wellenhof et al., 2008). Therefore, in spite of using choke-ring antennae at most of the monitoring stations on Severn Bridge, the multipath signature was detected in observations of many satellites. This was recognised when employing the RTKLIB for the Rinex observations of the individual monitoring station and using the values of MP1 and MP2, which are indicators of the multipath conditions based on linear combination of dual frequency measurements of L1 and L2 (de Bakker et al., 2012) as discussed in Section 3.5.4. This quality check is essential to identify the multipath contaminated satellites of low-quality observations in the initial assessment, which can be used when analysing the accuracy of the achieved positions. Therefore, this investigation will be useful especially for intervals that suffer from lower ambiguity success rate (fixing), which may attribute to the existence of multipath effect at these intervals (Lau et al., 2015).

When applying the approach of the linear combination on the collected data of Severn Bridge, the observations of different satellites were characterised by multipath. The identification and visualisation of the specific satellite affected by multipath for a specified duration were made by using a Matlab script developed during this study, where the evaluated multipath (MP) is compared with the SNR for each satellite in view. For example, when analysing the above hourly dataset in Fig. 6.6, it is clear that the satellite G15 exhibited high variation in estimated multipath, specifically with MP2 as illustrated in Fig. 6.8.

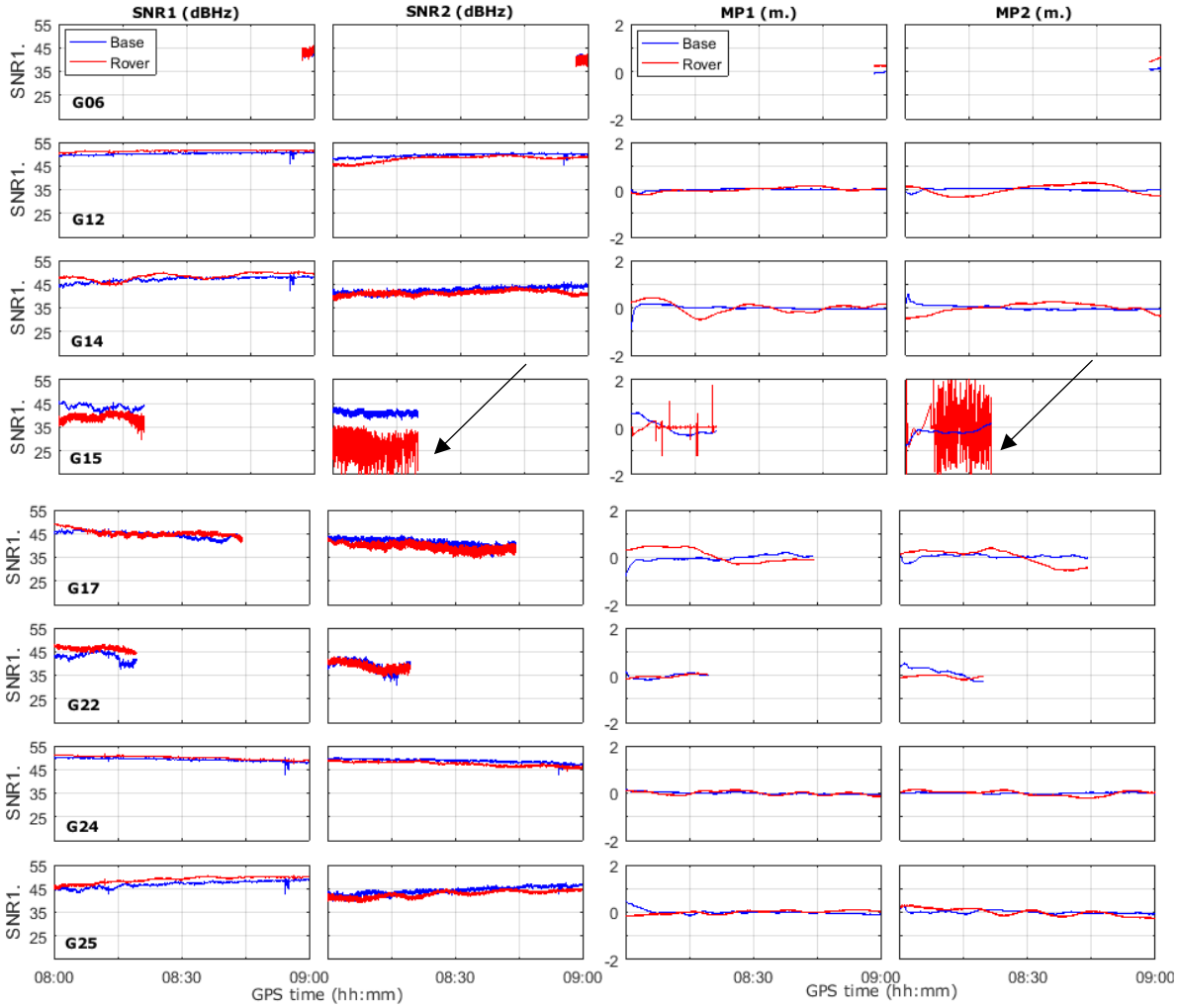


Fig. 6.8 The results of detected multipath MP1 and MP2 and the corresponding SNR1 and SNR2 of GPS-only for a dataset of station T2 in Fig. 6.7 on 21 July 2015.

It can be seen from Fig. 6.8 that the values of SNR on L2 is less than that on L1 for the same satellite, which indicates that the L2 frequency of the GPS signals is more susceptible to multipath. This could introduce gaps in the derived time series as a result of unfixing ambiguity. Furthermore, it is evident that among all observed satellites, G15 has high variations of SNR2 values within time associated with MP2.

In GNSS data processing, the option to exclude multipath contaminated satellites may improve the estimated position and achieve highly accurate measurements (Lepadatu and Tiberius, 2014), which however is possible only if a sufficient number of redundant visible satellites have been observed; otherwise, this could result in no solution. This justifies the need to add other satellites from other GNSS constellation, to exclude the low-quality ones and improve the performance positioning.

6. 5 Processing the Severn Bridge Data

The GNSS records were downloaded on a periodic basis while gathering measurements and they were processed using RTKLIB v2.4.2. In order to analyse the response of the bridge, the data have been post-processed in a kinematic mode using the Double Differencing (DD) technique with dual frequencies. For the processing of the GNSS records were used the broadcast ephemeris and 15° cut-off elevation angle, which are typical options in GNSS processing for monitoring application (Psimoulis and Stiros, 2012). Furthermore, the atmospheric effect is minimised with DD; a Saastamoinen model was also applied to ensure more efficient modelling of the tropospheric effect. Thus, the derived kinematic positions at each monitoring point are computed relative to the fixed position of the reference station on the toll building.

Accordingly, to have efficient monitoring, it is essential to achieve accurate positioning with high availability of continuous precise GPS/GNSS solution. The precise positioning is based on precise carrier-phase measurements, which depends on the successfulness of fixing the Ambiguity Resolution (AR). As discussed in Section 6.4.1, the suitable strategy for a kinematic solution is the instantaneous mode, which fixes the ambiguity epoch-by-epoch. In some cases, it can be adopted fix-and-hold as an alternative technique to increase the availability of a fixed solution. Even though, to compare the positioning performance achieved with different GNSS solutions, it is preferable to use the same mode of fixing the ambiguity. This will lead to comparable results with the same specifications to process the corresponding data.

Due to a large amount of the collected measurements of the four days of monitoring (i.e. 20th-23rd July), the GPS/GNSS data were split into hourly intervals, which processed sequentially. The GNSS records of the monitoring stations were processed with respect to the reference base station in order to derive the relative position with the same origin (i.e. the reference base station). Therefore, the position of the base station was determined based on the static measurements of zero baseline along 44h. Afterwards, the relative GPS/GNSS positions of different monitoring stations were calculated relative to the reference station along the whole duration of processing.

Eventually, the output of processing will be datasets of geodetic coordinates of 10 Hz, which they were transformed to E, N and U coordinates of the local system. The ‘mean’ coordinates of the fixed base station were then subtracted from the coordinates of the monitoring stations, resulting to the E, N and U relative coordinates which represent the components of baseline (i.e. connecting the base station with the rover monitoring station). Therefore, the final output will be GPS/GNSS time-series in the NEU coordinate system of 10 Hz sampling rate. To assess the displacement at each monitoring station, there is a need to specify the initial coordinates of that station. Following that approach, the initial positions are derived from the mean values of the first 10 min of the fixed solution as presents in Table 6.2.

Moreover, to evaluate the displacement at these stations oriented with the bridge axes, the 3D GNSS coordinates (E, N and U) were transformed into the local bridge coordinate system (x, y and z), by using a linear transformation, as applied in the following equations:

$$x = E * \cos(\varphi) + N * \sin(\varphi) \quad (6.1)$$

$$y = N * cos(\varphi) - E * sin(\varphi) \quad (6.2)$$

$$z = U \quad (6.3)$$

where (φ) represents the anticlockwise rotation angle.

For this purpose, the positions of handrail points were used, as they were located along a path parallel to the main axes of the bridge, which represents its longitudinal orientation. Thus, the computed bearing was N 58° W as shown in Fig. 6.9.

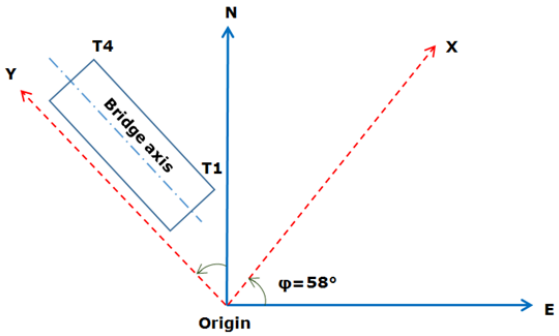


Fig. 6.9 Coordinate transformation in the local horizontal system (BCS).

Therefore, the x-axis and y-axis express the lateral and longitudinal axis, respectively, while the z-axis represents the vertical axis of the bridge. In this way, the initial coordinates of all stations are computed relative the origin at the reference station as listed in Table 6.2.

Table 6.2 The initial coordinates of monitoring stations in two systems

Group	Sta.	**Components of short baseline (m.)**			**Local Bridge Coordinates (m.)**		
		E	N	U	x	y	z
Tower stations	T1	- 759.6546	522.3896	106.4076	40.4559	921.0479	106.4076
	T2	- 771.6844	504.8446	106.4835	19.2020	921.9523	106.4835
	T3	- 1616.0926	1021.2312	106.3497	09.6546	1911.6943	106.3497
	T4	- 1605.1588	1039.1407	106.5644	30.6367	1911.9125	106.5644
Cable stations	A	- 1291.3370	847.7767	29.8564	34.6511	1544.3691	29.8564
	B	- 1166.6067	771.5535	24.7486	36.1071	1398.1996	24.7486
	D	- 1073.0672	714.3146	29.9879	37.1342	1288.5417	29.9879
	F	- 1178.0211	752.8426	24.7233	14.1906	1397.9643	24.7233
Handrail stations	B1	- 1164.0327	775.5221	20.7802	40.8366	1398.1198	20.7802
	D1	- 1070.4064	718.2798	20.5766	41.9068	1288.3864	20.5766
	G	- 632.8522	450.5270	13.4858	46.7080	775.4320	13.4858

6. 6 Noise Assessment

The most commonly used method to identify the noise level is applying zero baseline measurements as discussed in Section 4.2. Therefore, a zero baseline was established at the base station to investigate the noise level of different GNSS solutions, and to assess at the same time the positioning precision of those different GNSS solutions. By processing the GNSS data using Double-Difference (DD) technique, both receivers theoretically have the same errors caused by multipath, satellite orbits and clocks and atmospheric delay; thereby double differencing between receivers cancels these errors. Thus, the only error sources remaining in the solution are caused by independent receiver noise with the effect of the geometry of satellite constellations (Dróżdż and Szpunar, 2012, Msaewe et al., 2017b).

In order to define the noise level of the GNSS solutions for a 24-hour period, and to assess their precision, the data on 21/07/2015 was used. Subsequently, the daily data was split into 24h sub-sessions, to estimate the noise level at each hour duration. Also, the DOP values were evaluated at these hourly intervals to analyse how the derived noise was related to the geometry of the corresponding GNSS constellations. As GPS and GLONASS observations represent the common GNSS data at the two receivers in the base station, the possible positioning solutions will be GPS-only, GLONASS-only and combined GPS/GLONASS. The resulting GNSS positions were computed and their precision evaluated by calculating the RMS along each component of different hourly GNSS solutions.

To verify the noise level for each GNSS solution within time, the time series of the deviation of computed position from the initial position was analysed (Fig. 6.10). The results show that the precision is within mm level, which indicates the stability of this point as well as reflecting the noise level for the solution of each point.

As expected, the noise level of the height component is larger than that of the plane components for all GNSS solutions, due to the geometry of GNSS constellations. The comparison between individual solutions showing that the GLONASS-only solution is noisier than GPS-only, especially in the vertical component, while significant improvement can be achieved in N component of the GLONASS-only solution at several intervals. Even though the N component of GLONASS at some other intervals is nosier than the corresponding GPS component, this can be attributed to the weak geometry of GLONASS-only at these intervals. On the other hand, the combined GPS/GLONASS solution showing improvement in reducing the noise level when compared to the GPS-only solution along each component. The significant improvement of combined GPS/GLONASS was observed with N component. After rotating the derived positional coordinate to local bridge coordinate system, the expected impact of improving N component will reflect on enhancing the magnitude of the

derived lateral component, in addition, to enhance other components. Owing to an improved geometry of increasing the valid satellites as expressed in DOP values (Fig. 6.10).

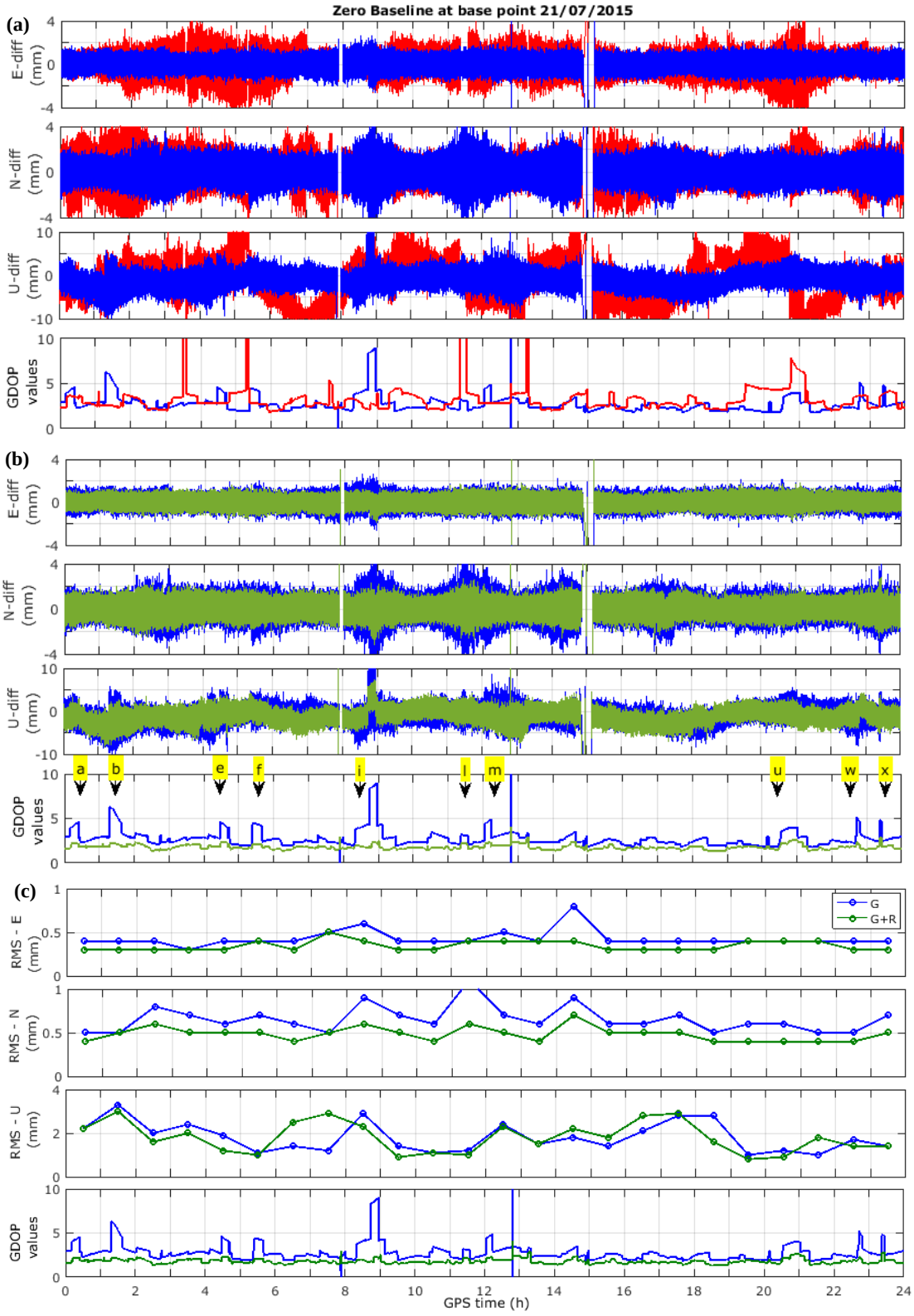


Fig. 6.10 E, N and U noise levels and associated GDOP values obtained from the zero baseline measurements at the base station showing comparison between different GNSS solutions (a) GPS (blue) & GLONASS (red), (b) GPS & combined GPS/GLONASS (green) and (c) their achieved precision on 21/07/2015.

6. 7 Analysis

The collected GNSS datasets of Severn Bridge consist of measurements from GPS, GLONASS, BeiDou and Galileo. Using GPS as the main satellite system, by adding supplementary observations from other constellations (i.e. GLONASS, BeiDou, etc.) will contribute in improving the performance of GNSS positioning (Odijk et al., 2015, Chen et al., 2015a). To show the improvement which can be achieved in positioning performance by using additional satellite systems, the analysis of processed data will be investigated for the GPS-only solution and compared to the combined GNSS solutions for deformation monitoring.

Regarding the combined solution of GPS with either BeiDou or Galileo constellations, their contribution will be assessed briefly in another section due to the limited visibility of satellites of these systems at that period in the UK. Therefore, the analysis results will focus on the contribution of GLONASS constellation when added to GPS observations, having as criteria: a) the availability of the solution, the b) accuracy of the displacement and c) the identified frequencies which derive from the spectral analysis of the monitoring stations data.

6.7.1 Availability Analysis

When analysing the availability of apparent GPS-only solution for each hourly interval along the whole day, the results revealed some intervals characterised by gaps. These gaps are the result of the weak geometry of the GPS constellation and other limitations (i.e. high noise, multipath) that affects fixing the ambiguity and reducing the solution availability at these intervals (Msaewe et al., 2017a).

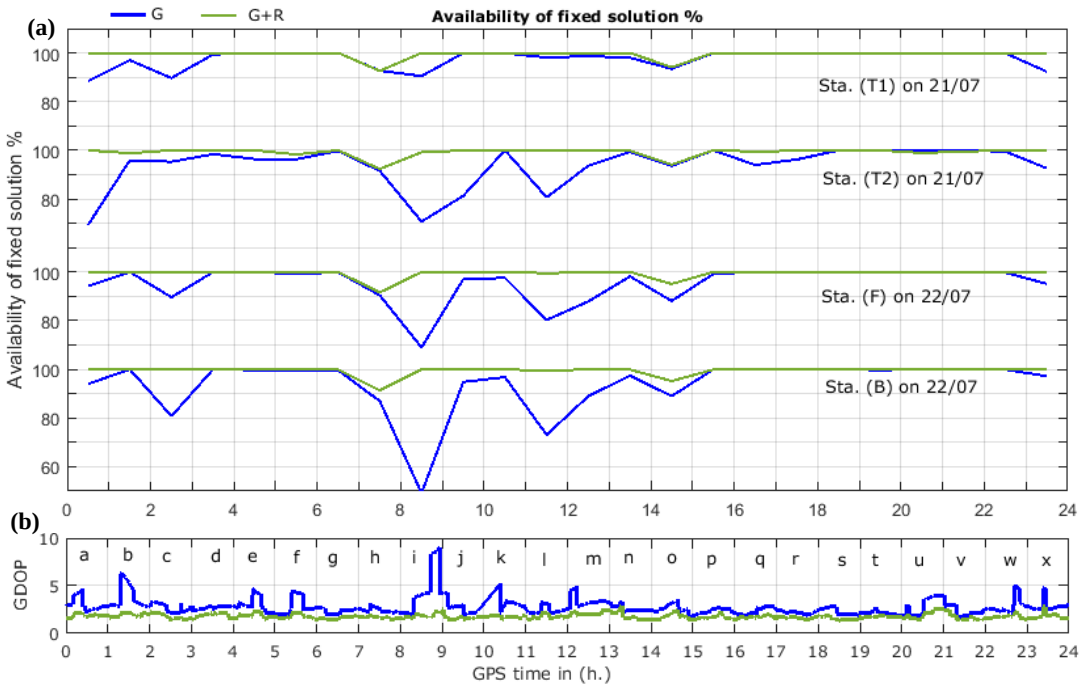


Fig. 6.11 The availability of fixed solution for GPS-only and combined GPS/GLONASS from different bridge stations and (b) the corresponding GDOP values.

According to Fig. 6.11b, it can be noticed that the weak geometry is concentrated at specific intervals with peaks of high GDOP values (e.g. a, b, i, etc. intervals), but also to intervals with relatively good geometry (e.g. d, e and q to w). This proved that satellite geometry is the main but not the only factor with an impact on the availability of the solution and that the combined solution improved the availability of the solution. To identify the causes of these defects, we analyse the first hourly duration (a) [00:00-01:00] as an example, and their results are listed in Table 6.3.

Table 6.3 The availability of fixing rate solution for the first hourly duration for tower points T1, T2 and on 21/07 and cable points at mid-span B, F on 22/07.

Sta.	**Avail. Of apparent sol. %**		**Avail. Of improved sol. %**		The caused satellite /remarks
	GPS-only	GPS+GLO	GPS-only	GPS+GLO	
T1	88.4	99.7	90.7	99.9	G03 : Descending satellite
T2	69.3	95.9	98.9	100	G30: Rising satellite
B	94.0	100	94.0	100	Weak geometry
F	94.2	100	94.2	100	Weak geometry

For the availability of GPS-only solution, it is evident that both tower points T1 and T2 are affected by noise and the analysis of the SNR values showed high variations within a short time. More specifically, the point T1 was affected by a signal received from descending satellite G03, while rising satellite G30 was introduced a high carrier-phase residual. Apparently, this effect can cause biases that affect the success rate of the instantaneous fixing ambiguity at the intervals of limited satellites (Verhagen and Teunissen, 2013). In contrast, the combined GPS/GLONASS with redundant available satellites can achieve high availability. However, it is possible to increase the availability of GPS-only solution by excluding the weak satellite (G03, G30 in Table 6.3); noise still contaminates the introduced GPS solution compared to the improved solution of combined GPS/GLONASS as illustrated in Fig. 6.12.

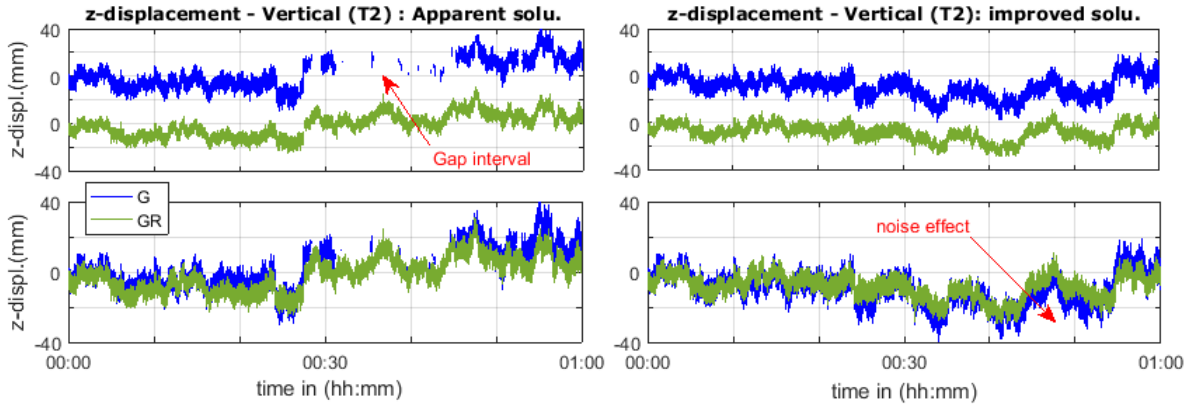


Fig. 6.12 Time series of derived vertical displacement at station T2 (left) the apparent solution and (right) the improved solution after excluding G30.

As inferred from Fig. 6.12, the comparison between the two apparent solutions (as they are without any excluding) shows that the time series of GPS-only affected by rising satellite G30 and provide a solution with the availability of 69.3% versus 90.9% for combined solution. In addition, the derived vertical displacement can reach 4cm for GPS solution. When the problematic satellite G30 is excluded, there is an improvement in the availability as it becomes 98.9% for GPS-only and 100% for combined GPS/GLONASS solutions (Table 6.3). However, the derived vertical displacement becomes within 2cm for GPS-only, the time series is still affected by noise in comparison with the improved combined GPS/GLONASS solution (Fig. 6.12 right).

For the availability of GPS-only solution of stations B and F at the mid-span as listed in Table 6.3, the dominant cause of reducing availability is related to weak geometry at this duration.

6.7.2 Derived Displacement of the Severn Bridge Monitoring

6.7.2.1 Derived Displacement at Tower Stations

When applying the GPS-only solution at tower stations T1 and T2 during subsequent 24h sessions on 21/07/2015 and comparing with the corresponding solution of combined GPS/GLONASS, differences in derived displacements along different durations can be observed between two solutions as illustrated in Fig. 6.13.

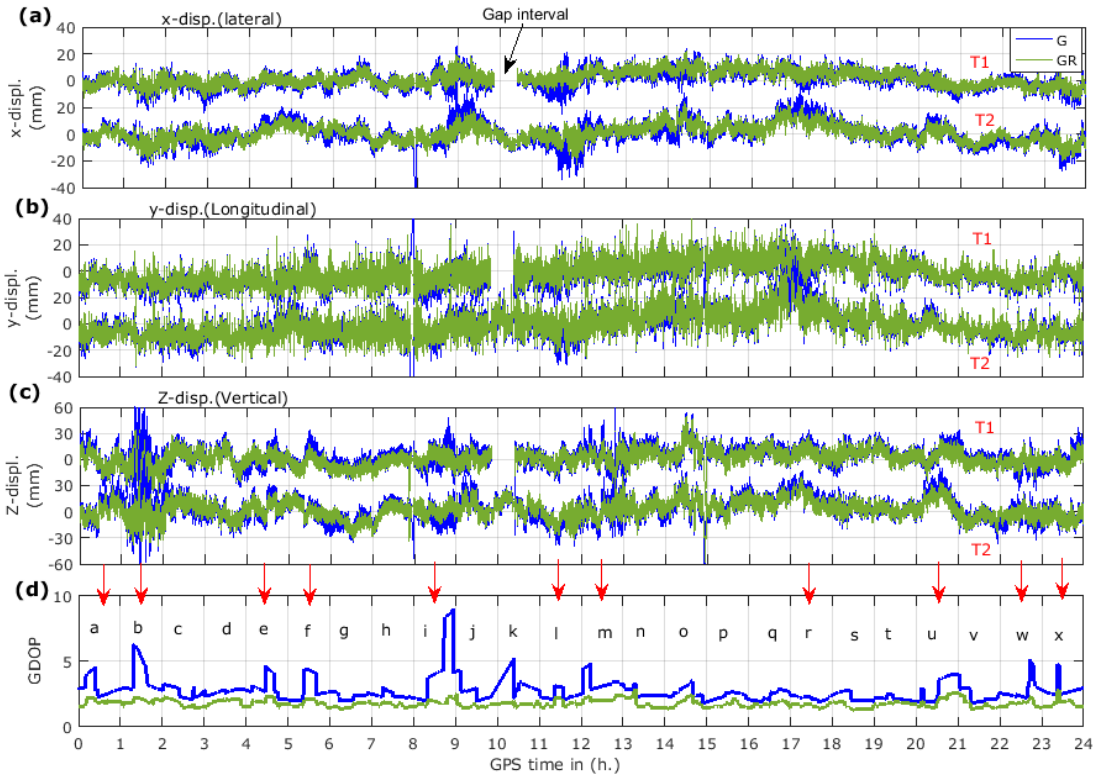


Fig. 6.13 Comparison of derived displacement between GPS-only and combined GPS/GLO solutions during 24h (a-c) at tower points T1 and T2 and (d) the corresponding GDOP values on 21/07/2015.

Regarding the movement at these tower stations, as expected the deflections in the longitudinal direction will be higher than in lateral direction (Raziq and Collier, 2007), as the tower is mainly affected longitudinally by the tension of the cables. Thus, the latter effect will also cause particular vertical movement for the upper part of the tower. The longitudinal movement demonstrates an increase from 11:00 until 17:00, while for the time interval from 17:00 to 20:00 a decrease is observed in the longitudinal movement.

According to Fig. 6.13, the results of derived displacement demonstrated that the solution through GPS-only is larger (noisier) than the corresponding GPS/GLONASS solution, especially at the periods that are identified as noisy intervals in the zero baseline assessment (i.e. duration of a, b, e, f, i… in Fig.6.13). These intervals require further investigation in details to evaluate the positioning performance of each solution as well as to define the main problems faced GPS-only solution.

The noise level at these intervals is the result of a weak geometry of distributed satellites, which is one of the main problems, occurred with a GPS-only solution. When depending on the results of these noisy durations, this will lead to incorrect interpretation of bridge deflections. For example, the analysis of the movement at station T1 in the interval (b) between 01:00 – 02:00 revealed significant variations, mainly in the vertical component, between the displacement time-series of GPS-only and combined GPS/GLONASS (Fig. 6.14).

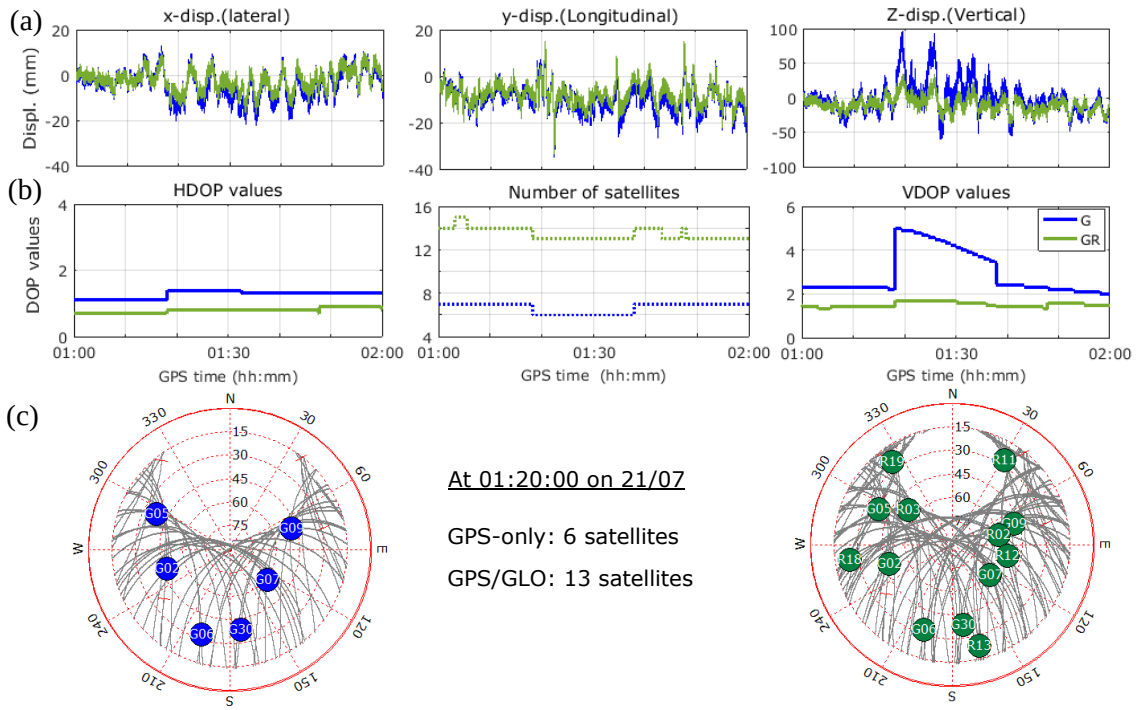


Fig. 6.14 Analysis of derived positioning at a tower station T1 during hourly period-b at 01-02h for (a) apparent deflection (b) corresponding geometry and a number of satellites and (c) the sky plot.

The results show that the detected vertical displacement can reach (10cm) with the GPS-only solution, while it was about (3cm) with the combined GPS/GLONASS solution (Figure 6.14a). The

analysis of the geometry at this interval indicates a high VDOP value for the GPS that is reduced with the combined approach; VDOP value of 5 for a constellation of 6 GPS satellites, while it was 1.3 with 13 combined satellites (Fig. 6.14b).

The high VDOP value of GPS was caused by a weak distribution of their valid satellites, which was reduced with a combined solution as exhibited in the sky plot of Fig. 6.14c. In addition, the GLONASS adding satellites offer good coverage in Northern area that has a useful role to strengthen the geometry. The discontinuity in the derived time-series due to gaps represents one of the limitations to evaluate the correct response of structural monitoring. The gap interval can occur when the receiver stops recording data, like what happened with the receiver at T1 along duration between 09:51 to 10:24. As well, the gap could be introduced when tracking insufficient satellites, due to the obstacles (i.e. a number of satellites <4 or high DOP values>30), or existence of a specific problematic satellite of weak signal, in addition to presence satellite affected by severe multipath from surrounding objects.

At the tower stations T1 and T2, the same Leica receivers and antennae occupy both stations. However, the time series from station T2 was characterised by more gaps than the corresponding one at T1, which can be attributed to the different surrounding environment at these two locations, which affected the availability of fixed solution (Table 6.4).

Table 6.4 Comparison between rates of fixed solution achieved with GPS-only and combined GPS/GLONASS in different periods at tower stations T1 and T2 on 21/07/2015

Interval	Availability sol. % at T1		Availability sol. % at T2		Problematic
	GPS-only	GPS/GLO	GPS-only	GPS/GLO	Satellite at T2
(i) 08:00 -09:00	90.5	100	70.7	92.0	G15
(l) 11:00 -12:00	98.1	100	80.7	100	G21
(q) 16:00 -17:00	100	100	94.0	99.5	G26

It is clear from Table 6.4 that gaps intervals characterise the concerned results of station T2, which decrease the availability of a fixed solution as shown in Fig. 6.15a. The cause of these gaps is related to the existence of low elevated satellite, whose signal is affected multipath at each interval. This was observed when the signal of the distributed GPS satellites was analysed at the sky plot for each interval, which shows that the low elevated satellites are affected by multipath when passing at a specific azimuth and elevation, shown in Fig. 6.15b.

For further investigation and following what discussed in Section 6.4.2, the analyses of MP1 and MP2 values for all observed satellites confirm that these low elevated satellites were susceptible to multipath as illustrated in Fig. 6.16. As expected, the occurrence of multipath associated with low SNR, especially on L2, affects the fix of the ambiguity.

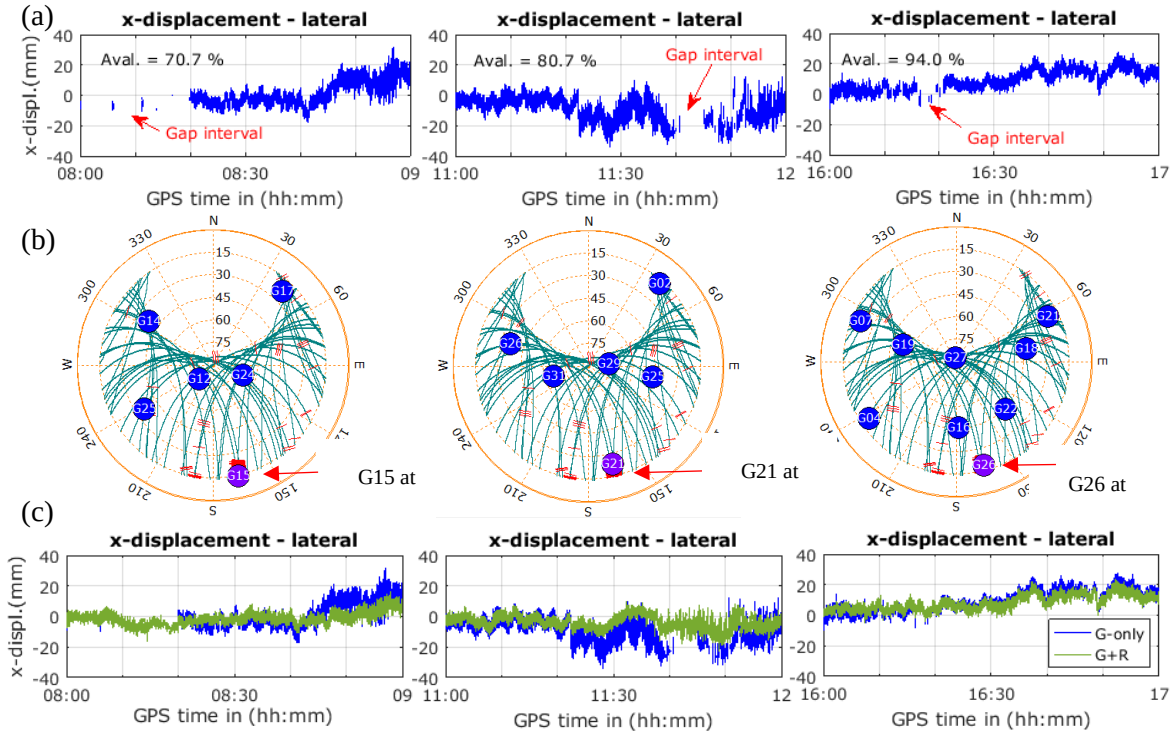


Fig. 6.15 (a) Different periods with discontinuity solution of GPS-only positioning (b) corresponding sky-plot and (c) improved time series of the combined solution compared to GPS-only at station T2.

On the other hand, the solution of the combined constellations increases the number of valid satellites and improves the possibility of achieving an estimated position with more reliability. Therefore, the validation of ambiguity will achieve success and provide a fixed solution of combined systems that compensates the gap intervals by reducing the noise level with improved quality as shown in Fig. 6.15c.

However, most of the detected cycle slips are corrected as earlier described in Section 6.4.1, some of them are not accurately corrected, which resulting in wrong ambiguity estimates. In this way, the incorrect fixing yields positioning with outliers (spikes) appears along the single epoch when using instantaneous fixing. This was detected along different durations of the GPS-only solution. For example the data of station T2 in Fig. 6.15 was contained these spikes as shown in Fig. 6.16, which are caused by the same problematic satellites.

In contrast, the combined GPS/GLONASS solution of instantaneous fixing strategy exceeds this limitation as demonstrated in Fig.6.17, because it is insensitive to the occurrence of carrier-phase cycle slip (Verhagen and Teunissen, 2014). If these outliers not dressed in derived solution, that will influence the correct achieving the derived displacement and frequency as will discuss in details in the following section. Therefore, it was recommended to exclude these problematic satellites in pre-processing stage and applying the combined GNSS solution.

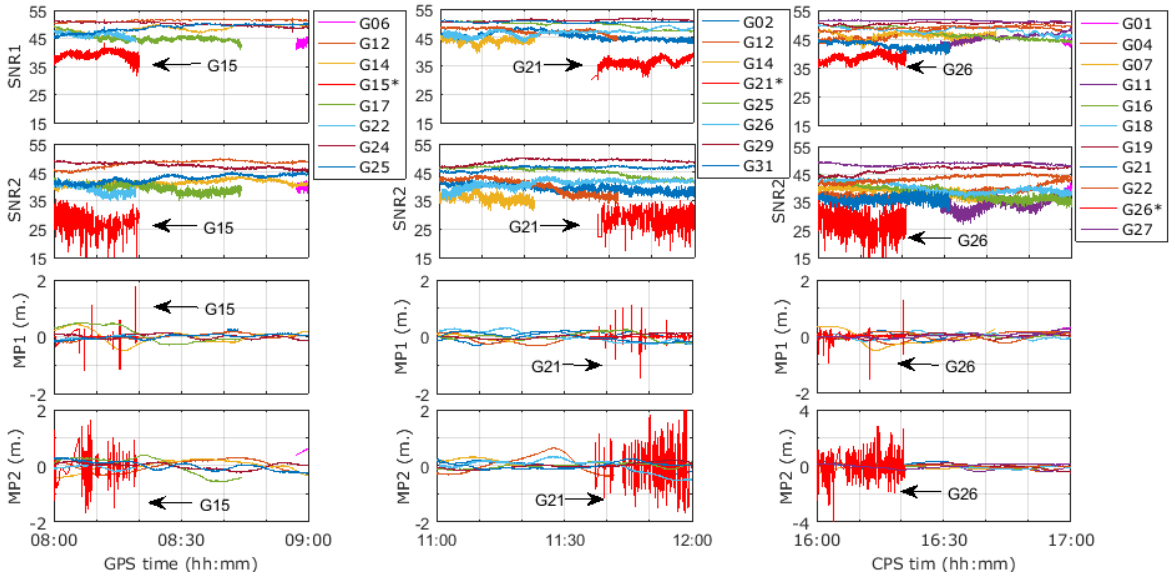


Fig. 6.16 Analysis of SNR and MP of GPS-only for three sessions in Fig. 6.16 at station T2 on 21/07/2015.

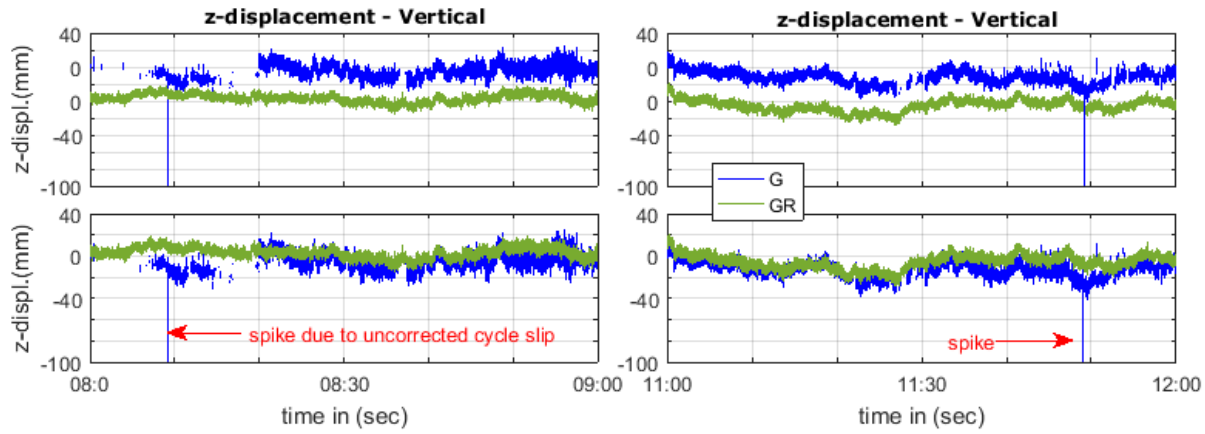


Fig. 6.17 Appearance of uncorrected cycle slips in the time series of station T2 on 21/07.

Thus, the combined solution reduces the noise level and tackle the gap intervals, in addition, eliminate the impact of multipath contaminated satellites and achieve a high rate of success fixing of the ambiguity. This will lead to overcoming the GPS-only limitations in problematic periods and proves considerable contribution of other GNSS constellations by enhancing the positioning performance for structural monitoring. Also, to improve the results for the combined solution, we can filter the problematic and low-quality satellites and introduce observations with clean data when an adequate number of satellites are available (Tokura et al., 2014).

6.7.2.2 Derived Displacement at Mid-Span Stations

To assess the movement of the suspension cables, the analysis is focused on the mid-span, where the largest motion is expected. Therefore, the results of the two mid-span opposite stations B and F were analysed, and a summary of all other results are given in Appendix-B (see Fig. B.1). The comparison

between the deflections at these stations for 24h showed a similar trend for each component as shown in Fig. 6.18.

The lateral deflection (x) occurs as a result of wind loading, while the resulting of extensive vertical deflections (z) that can reach more than 30 cm are due to temperature changes and traffic loading as shown in Fig. 6.19.

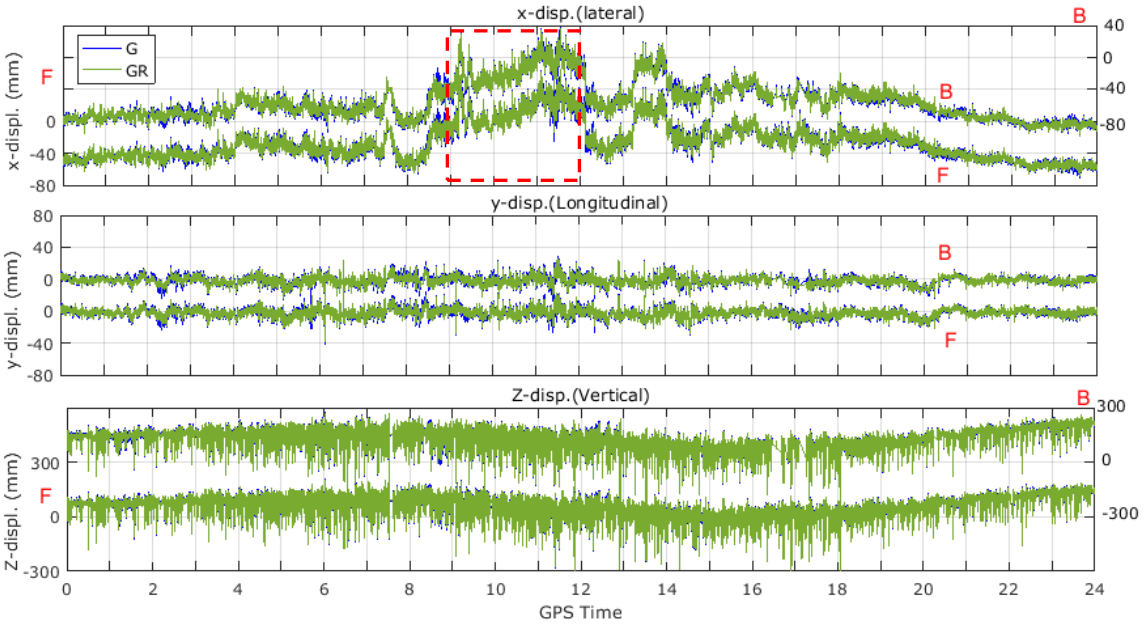


Fig. 6.18 The daily time series of derived displacement obtained from GPS-only and combined GPS/GLO solutions at mid-span stations B and F on 22/07/2015.

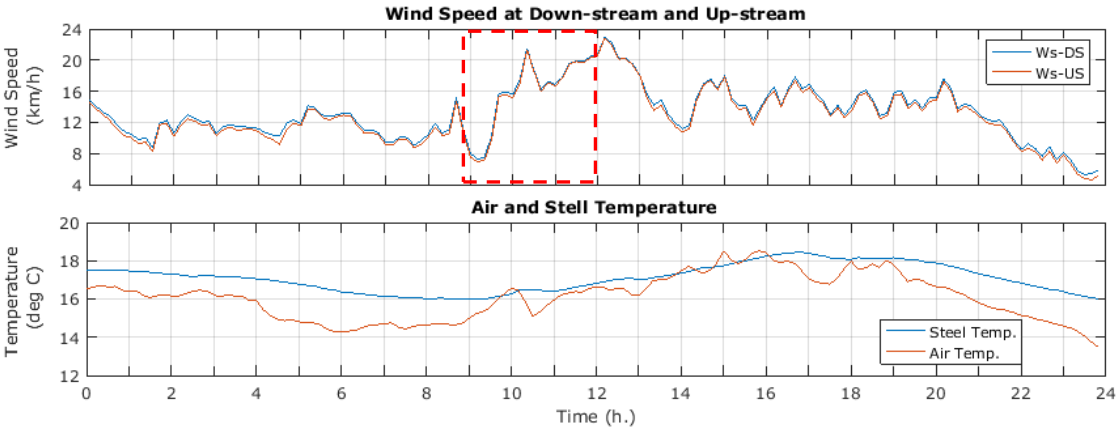


Fig. 6.19 The recorded daily data of wind loading and temperature changes at Severn Bridge on 22/07/2015

As can be seen from Fig. 6.18 and Fig 6.19, there is a correlation between lateral deflection (x) and the wind speed. For example, at maximum wind speed occurred between 9hr and 12hr, the lateral displacement (x) showed a maximum deflection. In addition, the vertical deflections (z) can also be correlated with the temperature variation of the steel (a blue curve in Fig 6.20) (Roberts et al., 2016). It is clear that when the temperature increases the vertical displacement (z) decreases due to the steel

expansion; this can be seen for example at the period of 10hr to 17hr. In addition to the above, it should be mentioned that in the time interval between 10 hr and 17hr, the traffic load is expected to reach its peak.

According to the derived displacement shown in Fig. 6.18, it can be seen from different periods that the combined solution improved positioning results, which might be small but it is still evident. More specifically, there is an improvement in the displacement time-series of lateral (x-axis) and longitudinal (y-axis) for the periods 02:00-03:00 and others, which are illustrated in Fig. 6.20.

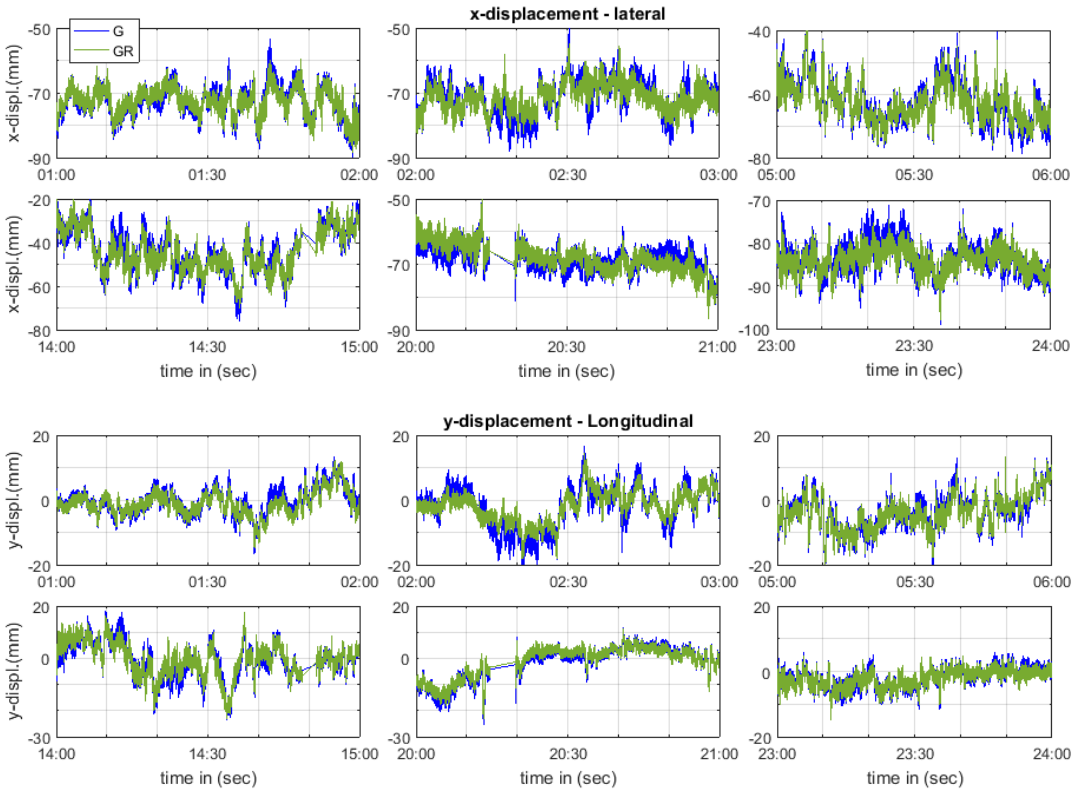


Fig. 6.20 Samples of derived displacements along the lateral and longitudinal direction of bridge deformations detected on mid-span station B on 22nd July 2015.

It is seen from Fig. 6.20 that the noise levels have been reduced when combined GPS/GLO was used. A similar improvement is also observed in the vertical displacement (z-axis), which however it is not clear graphically due to the considerable variation in the z-direction in comparison with that in x and y-direction (this is also clear from Fig 6.18).

Furthermore, as discussed in Section 6.3.2, three monitoring stations were fixed at the handrail of bridge deck (B1, D1 and G, in Fig.6.2) to detect the deflection in x, y and z-direction. It was found that the displacement obtained from the handrail stations were similar to that detected from the cable stations in x (lateral), y (longitudinal) and z (vertical) direction. For example, the oscillation of the movement at the cable station F (at the mid-span, see Fig. 6.3) was synchronised with the movement along the handrail station B1 (adjacent to cable point B at the mid-span) as shown in Fig. 6.21.

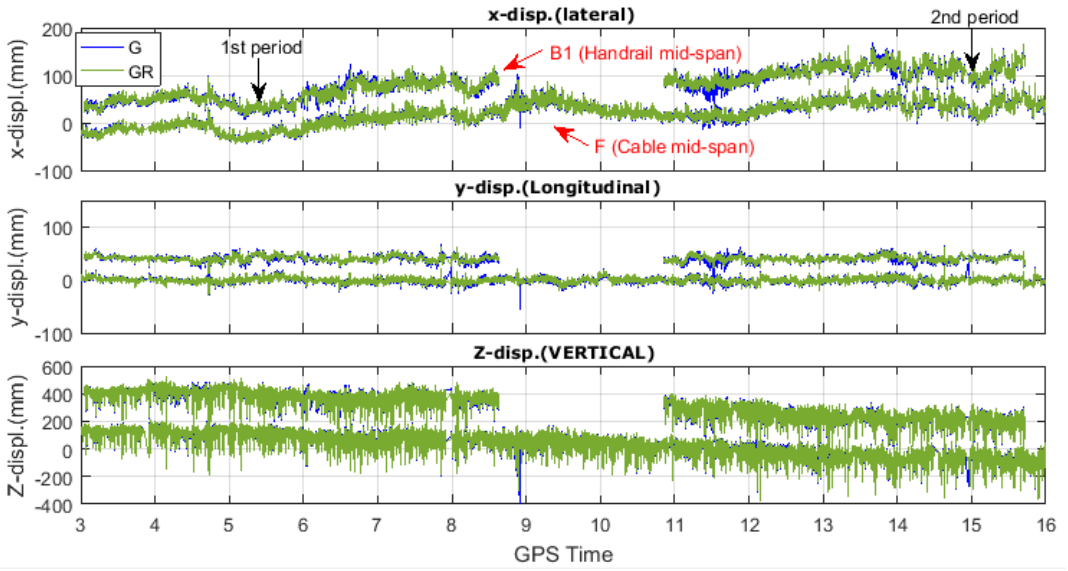


Fig. 6.21 The derived time series of displacements along x, y and directions of bridge deformations at mid-span stations B1 and F on 21st July 2015.

Therefore, it is expected that the magnitude and the frequency of the movement at these two stations would be similar for the same constellations. It should be noted that, three different periods of continuous collecting data were gathered at station B1 (only two of them are shown in Fig.6.21, named as '1st period' and '2nd period') in which the recording data was stopped after each set of data while the time series of station F was recording continuously for the whole 24 hours. To show the effect of adding the GLONASS on improving the positioning, x, y and z displacement during the most obvious noisy time interval period (11 hr to 12hr) are plotted in Fig. 6.22. As can be seen, the combined GPS/GLONASS reduces the detected deflection of the GPS-only solution particularly for horizontal displacement (x and y components).

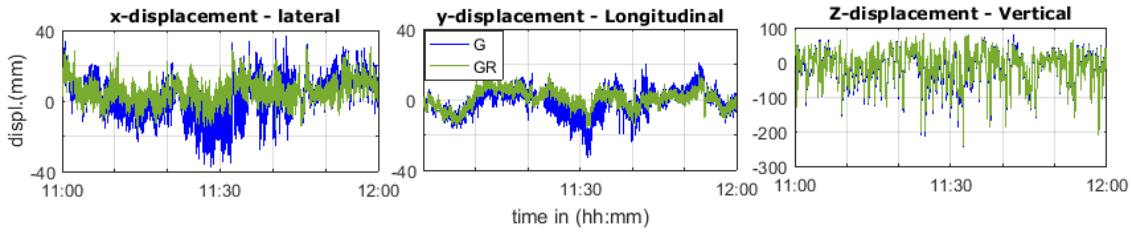


Fig. 6.22 Comparison between time series of GPS-only and combined GPS/GLONASS of station B1 at period 11:00 – 12:00 on 21/07/2015.

6.7.3 Frequency Response at the Severn Bridge

After analysing the bridge movement at monitoring stations (see Sections 6.7.2) in linear time series along lateral, longitudinal and vertical displacements, the natural frequencies of a bridge can be identified and analysed by spectral analysis of these movements. As the derived time series had an acquisition rate of 10 Hz for the GNSS observations, it is possible to detect the frequencies up to 5 Hz based on the Nyquist theorem (Meng et al., 2007). Apparently, most of the analysed time series

in this monitoring is discontinuity with gaps. Therefore the most suitable technique for such analysis is the Lomb Normalized Periodogram (LNP) using Norm-Period code (Pytharouli et al., 2006, Psimoulis et al., 2008). Subsequently, the Norm-Periodogram was applied to the time series of every component of movement at all stations of towers, cables and handrails to derive the frequencies of the movement with both GPS-only and combined GPS/GLONASS solutions.

In addition, the Fast Fourier Transform (FFT) technique was also used (using FFT Matlab code) to check the derived frequencies when applying continuous data. It should be mentioned that, due to the discontinuity in the time series data of the displacement, FFT was only applied to the selected period where there is no gap in the time series.

As discussed in the above section (see section 6.7), the noise has an impact on the derived displacement in the time series of the GPS-only solution along with some limitations, which was improved by adding GLONASS in combined GPS/GLONASS solution. Consequently, it is possible to assess how that noise and constraints will effect on the derived frequencies by analysing the detected peaks and dominant frequency of spectrum in every solution.

It is worthwhile to analyse the frequency where the maximum availability is 100% to make sure that the GPS; (i) has a good geometry with a sufficient number of valid satellites which achieved an optimum performance and (ii) has a continuous time series which enables to apply FFT in frequency analysis. The optimum time intervals were selected to be from 16:00 to 17:00 and from 17:00 until 18:00, presented in Fig. 6.14. Dominant frequencies of the displacement time series for x-lateral, y-longitudinal and z-vertical (of both GPS-only and combined solutions) using LNP and FFT are compared and summarised in Table 6.5.

Table 6.5 The derived dominant natural frequencies by FFT and LNP at tower station T1.

Component		Freq. at interval (16:00 – 17:00)				Freq. at interval (17:00 – 18:00)			
		GPS-only		GPS/GLONASS		GPS-only		GPS/GLONASS	
		FFT (Hz)	LNP (Hz)	FFT (Hz)	LNP (Hz)	FFT (Hz)	LNP (Hz)	FFT (Hz)	LNP (Hz)
x-lateral	1st	0.153	0.153	-	0.153	0.150	0.152	-	0.152
	2nd*	0.336	0.336	-	0.336				
y-longitudinal		0.145	0.145	-	0.145	0.145	0.143	-	0.143
z-vertical		0.153	0.153	-	0.153	0.150	0.152	-	0.152

2nd *: This is the dominant frequency with the highest amplitude

As can be seen from the above Table, the frequency data obtained from LNP is well agreed with that obtained from FFT. Due to the presence of gaps in limited epochs of the combined solution, FFT technique was only applied for GPS-only. It is seen that although there are different levels of noise in the derived displacement between two solutions (GPS-only and combined), the dominant frequency in two solutions showed similar values in x, y and z directions. It was also observed that the dominant peak in longitudinal and vertical direction was clear (i.e. one distinctive peak) while

for the lateral direction there was more than one (low amplitude) peak, as it is presented in Table 6.5 (i.e. 1st and 2nd for x-component). Roberts et al. (2015) reported that the dominant frequency of four tower stations in the Severn Bridge is approximately 0.146 Hz in the longitudinal direction, which is agreed with the data shown in Table 6.5.

Spectral diagram of GPS-only solution using FFT at time interval 17:00-18:00 in Table 6.5 is plotted in Fig.6.23. It is important to notice that the analysis of linear spectrums solely represented up to 1 Hz (not the whole spectrum of 5Hz) as the main frequencies are concentrated in regions below 1 Hz.

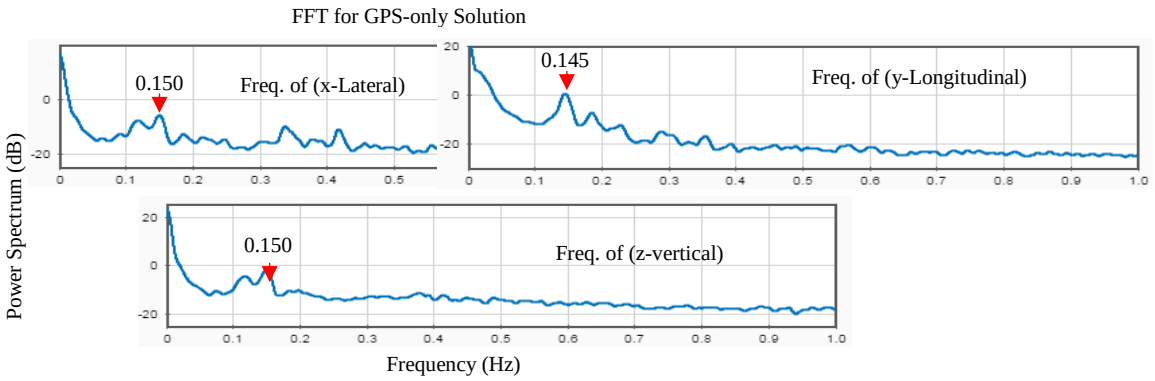


Fig. 6.23 FFT spectra of GPS data on tower station T1 at the period 17:00 – 18:00.

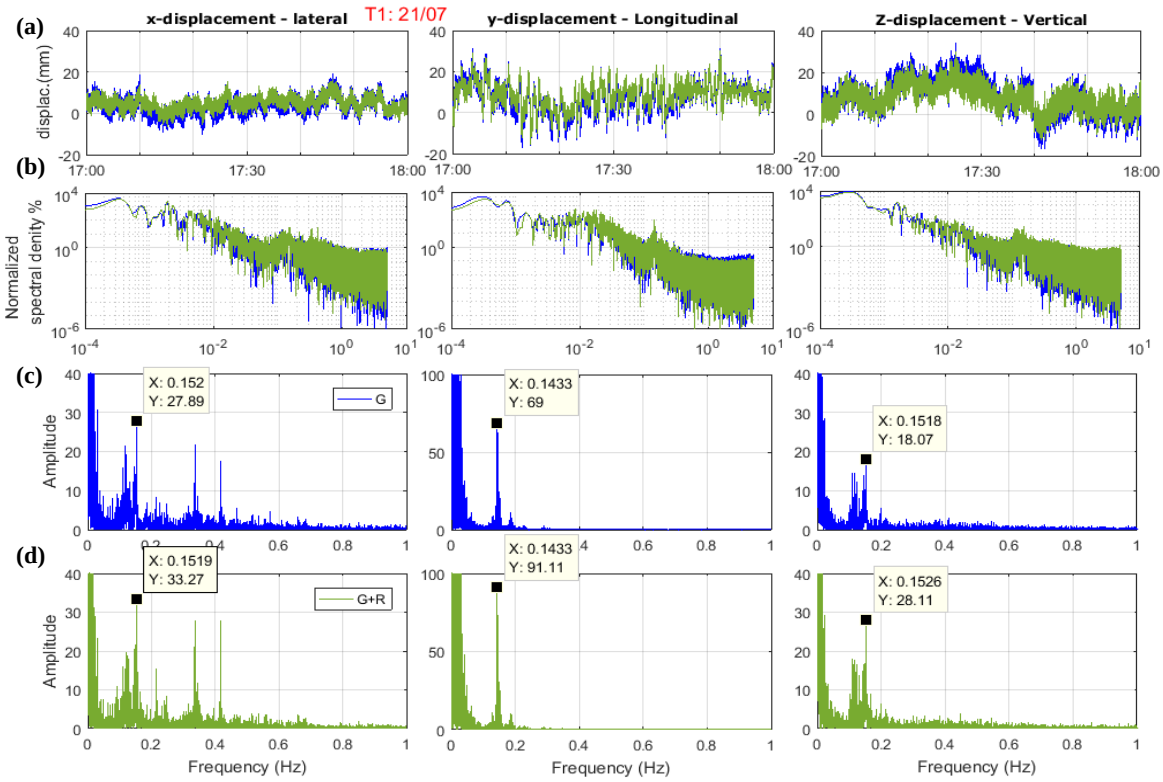


Fig. 6.24 Analysis of movement at tower station T1 (a) displacement time series (b) logarithmic spectra of movement (c) linear spectra of the GPS-only solution and (d) linear spectra of combined GPS/GLO solution.

For analysis with LNP technique, Fig. 6.24a presents the comparison between detected displacements obtained through a GPS-only positioning (blue colour) with the corresponding time series derived from combined GPS/GLONASS solution (green colour).

Due to a reduction in noise level, a slight improvement can be considered in components of the combined solution against the solution of GPS-only. The evidence of this reduction can be seen in the LNP spectrum of Fig. 6.24b, especially in the longitudinal component.

As mentioned earlier (in Table 6.5), the detected peaks in the linear LNP spectrums are similar to the detected frequencies from GPS-only and combined solution as presented in Figures 6.24c and 6.24d. This indicates that the dominant frequency from GPS-only will not be affected by low noise level when GPS solution derived from clean observed data with proper geometry. On the other hand, when the GPS-only solution has an issue of any problem along with the noise, (i.e. weak geometry, the existence of problematic satellite affected by multipath or multiple cycle slips), these issues have an impact on the identified frequency.

It has been already shown that the uncorrected cycle slips affect the derived displacement (see Section 6.7.2), which prevents identifying the correct frequencies. In addition, when the multipath occurred in bridge monitoring, it will be considered as a very low-frequency fluctuation (Ogaja and Satirapod, 2007) and it is characterised by frequencies <0.05 Hz (Moschas and Stiros, 2014a). This was detected in the analysis of movement at tower stations at different periods of measurements.

For example, when analysing the movement of tower points at period 08:00 – 09:00 on 21st July, it was observed that some peaks of detected frequencies were lost from the spectrum of the GPS-only, while they appeared in the spectrum of a combined solution as shown in Fig. 6.25. This might be due to the high noise level exist in GPS-only solution.

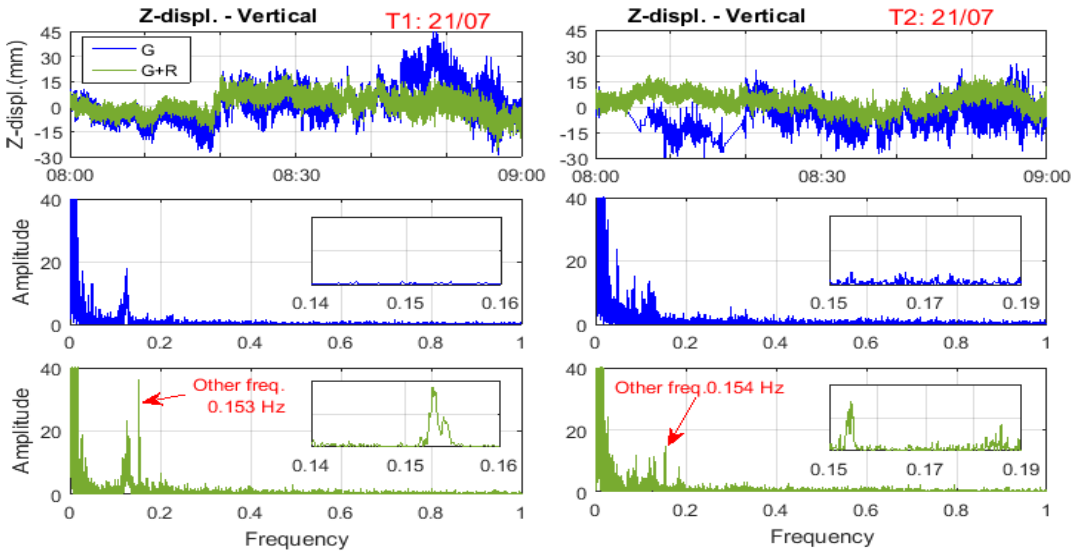


Fig. 6.25 Analysis of vertical movement at tower stations T1 and T2 at period 08:00 – 09:00 on 21st July.

For the station T1 (Fig. 6.25 left), it is clear that the peak of frequency 0.153 Hz was not detected in the GPS-only spectrum due to weak geometry with a limited number of satellites. This undetected peak was identified with a combined solution. This dominant frequency (0.153 Hz) was already detected in a good GPS geometry interval of (17:00 -18:00) as already shown in Table-6.5, indicating that this peak corresponds to the actual frequency of the signal and not the noise.
Similarly in Fig. 6.25 right, the time series of station T2 displacement has a problem with satellite G15 affected by multipath (assessed in Fig. 6.16), Which caused gap interval beside weak geometry. Therefore, two peaks of 0.154 and 0.186 Hz are not detected in a lateral component as well as the vertical component when spectrum derived at an interval of weak geometry.
To identify the natural frequencies of movements for sequential hours, a Matlab script was written in this study to analyse these subsequent periods. Therefore, the natural frequencies of the bridge tower were identified for the separate sequential 24h or more. The results indicate that a stable value of noticeable natural frequencies can be achieved along the longitudinal movement of tower station within 0.143 - 0.148 Hz, while variable values of frequencies were identified along the lateral and longitudinal direction of movement. The results are listed in Appendix-B (Fig. B.5).

In the same procedure, the frequency of movement at mid-span stations can be identified. Two time periods were chosen at 03:00 – 04:00 hr and 18:00 – 19:00 hr on 22nd July, in which the maximum availability of fixed solution was achieved. Table 6.6 summarises the identified frequencies at mid-span station B according to FFT and LNP techniques, while Fig. 6.26 illustrates the derived peaks of identified frequencies at this station.

Table 6.6 The derived natural frequencies by FFT and LNP at cable mid-span station B.

Component		Interval (03:00 – 04:00)				Interval (18:00 – 19:00)			
		GPS-only		GPS/GLONASS		GPS-only		GPS/GLONASS	
		FFT (Hz)	LNP (Hz)	FFT (Hz)	LNP (Hz)	FFT (Hz)	LNP (Hz)	FFT (Hz)	LNP (Hz)
x-lateral		0.093	0.093	0.093	0.093	0.096	0.096	-	0.096
y-longitudinal	1st	0.187	0.187	0.187	0.187	0.189	0.189	-	0.189
	2nd *	0.292	0.292	0.292	0.292	0.289	0.289	-	0.289
z-vertical		0.144	0.144	0.144	0.144	0.145	0.145	-	0.145

2nd* is the dominant frequency, when there is no FFT value that means discontinuity time series.

Comparing Table 6.6 and Table 6.5, one can see that the dominant frequency of the vertical component at cable mid-span station B (in Table 6.6) is almost similar to that of the longitudinal component (in Table 6.5), which is approximately 0.145 Hz. This finding proves that the longitudinal movement of the top of the bridge tower agrees with the vertical movement of the mid-span stations, which coincides with the finding reported by Brown et al. (2007).

It is also seen from Table 6.6 that the frequency obtained from the time series of the displacement for the GPS-only is close to that for the combined (GPS/GLONASS) solution, indicating that the dominant frequency is quite independent on the noise associated with the GPS-only solution (this noise was due to satellite geometry, as already discussed in section 6.6).

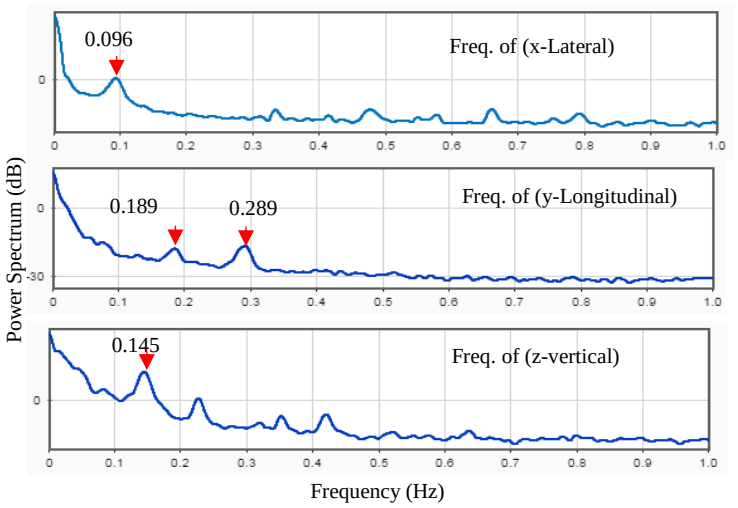


Fig. 6.26 FFT spectra of GPS data on mid-span station B at the period 17:00 – 18:00.

In contrast, for cable station B at the noisy interval (08:00-9:00, also refer to Fig 6.18), the derived frequency showed the appearance of frequency peaks at the spectrum of combined GPS/GLONASS solution, while losing these peaks from the spectrum of the GPS-only solution as illustrated obviously in Fig. 6.27. This is due to the high level of noise and multipath effect.

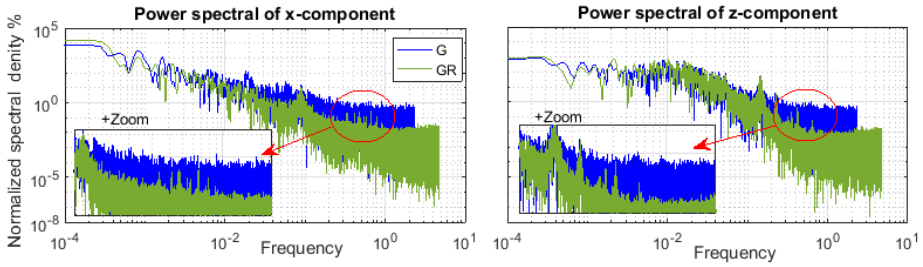


Fig. 6.27 The spectra of GPS-only and the combined GPS/GLONASS at mid-span station B.

To demonstrate the derived frequencies at all bridge-monitoring stations for the same observed duration, the period 03:00 – 04:00 on 22nd July was chosen to summarise an overall depiction of identified frequencies, for most of the monitored stations as listed in Table 6.7.

Table 6.7 The derived natural frequencies by LNP at period 03:00 – 04:00 on 22nd July 2015

Bridge element	Station	Freq.	Freq. at x-lateral		Freq. at y-longitudinal		Freq. at z-vertical	
			GPS-only (Hz)	GPS/GLO (Hz)	GPS-only (Hz)	GPS/GLO (Hz)	GPS-only (Hz)	GPS/GLO (Hz)
Towers	T1		0.155	0.155	0.144	0.144	0.155	0.155
	T2		0.159	0.159	0.144	0.144	0.159	0.159
	T3		0.160	-	0.143	-	0.160	-
	T4		0.159	-	0.144	-	0.158	-
Cable Mid-span	B	1st	0.093	0.093	0.187	0.187	0.144	0.144
		2nd *			0.292	0.292		
	F	1st *	0.093	0.093	0.187	0.187	0.144	0.144
		2nd			0.292	0.292		
Cable	A	1st	0.093	0.093	0.187	0.187	0.144	0.144
		2nd *			0.292	0.292		
	D	1st *	0.093	-	0.187	-	0.144	-
		2nd			0.292	-		

6. 8 BeiDou/Galileo Satellites in the Severn Bridge monitoring

As stated in Section 6.3.3 that during conducting GNSS data at Severn Bridge site, a number of BeiDou and Galileo satellites were observed by the receivers at the second base station R_f and other individual rover stations (D1, B1, B and G). From the current BeiDou operational constellation, although, MEO and IGSO satellites appear at the sky of Severn Bridge site, most of them can be observed with low elevation angles. Therefore, a few satellites will be visible with 15° cut-off elevation angle. This leads to tracking limited BeiDou satellites during collecting data (i.e. mostly just one or two visible satellites appear) as shown in Fig. 6.28.

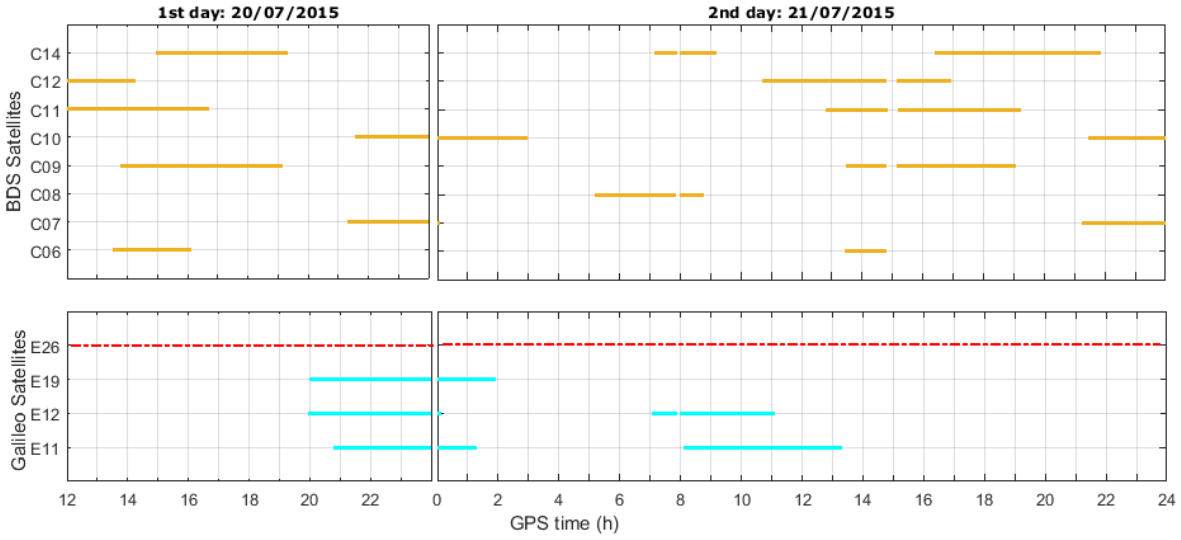


Fig. 6.28 The BeiDou and Galileo visible satellites observed at a base station (Rf) of monitoring the Severn Suspension Bridge.

In addition, limited operating Galileo satellites were also observed during measurements time (July 2015). As depicted in Fig.6.28 that only three satellites were operated (E11, E12 and E19) with another unhealthy one (E26), which has problems in the navigation data. Therefore, when two or more BDS or Galileo satellites are available, it can be added to GPS observations to investigate their contribution to the positioning performance.

As analysed in Chapter 5, when a number of satellites from other GNSS constellations integrated with GPS observations, some of the limiting factors that degrade the GPS-only solution are expected to be overcome. For instance, the reduced availability of fixed solution is expected to be improved for a combined solution of GPS with other added GNSS satellites. In addition, the positioning precision can also be improved with a reduction in noise level. Thus, different GNSS solutions were implemented, and their results were compared with a GPS-only solution to reveal the expected improvement. As shown in Fig. 6.28, the maximum available BDS/Galileo satellites can be observed at the base station on 20th July, while the counterpart of rover observations was at the handrail station

D1 (adjacent to station D on the cable, see Fig. 6.4). The visibility results of different highlighted GNSS solutions are listed in Table 6.8.

Table 6.8 The visible BDS and Galileo satellites with different GNSS solutions at handrail station D1 on 20th July.

	Intervals	BDS (C)	Galileo (E)	Availability of fixed solution (%)			
				GPS-only	GPS+BDS	GPS+Galileo	GPS+C+E
q	16:00 – 17:00	C09, C14	-	99.0	99.4	--	--
r	17:00 – 18:00	C09, C14	-	96.1	97.4	--	--
s	18:00 - 19:00	C09, C14	-	99.8	100.0	--	--
v	21:00 – 22:00	C07, C10	E11, E12, E19	100.0	100.0	100.0	100.0
w	22:00 – 23:00	C07, C10	E11, E12, E19	92.8	97.1	100.0	100.0
x	23:00 – 24:00	C07, C10	E11, E12, E19	90.9	97.3	100.0	100.0

It is seen from the table that when the availability of the GPS-only is already at optimum level, the effect of adding Galileo and BDS is not that significant, while when the availability of the GPS-only is low (due to, for example, a weak geometry or limited number of satellite), the improvement effect of adding Galileo and BDS is noticeable, as can be seen at intervals w and x. At w-interval, the improvement of adding BDS reduced the gap from 7.2% to 2.9% while adding Galileo to achieve optimum availability with no gap. In addition, for x-intervale, it is clear that the gap limitation reduced from 9.1% (GPS-only) to 2.7% (GPS+BDS), where adding the Galileo (i.e. GPS+ Galileo) eliminated the gap limitation completely.

As analysed in Section 4.6, that one of the limitations of GPS-only in relative to the high latitude is the distribution of GPS satellites due to the inclination of GPS orbits, which has a significant effect on achieving precise northing. Furthermore, in some cases, the distribution of GPS satellites required other GNSS satellites to have a geometry that is more robust and enhanced the positioning solution. Therefore, adding BDS and/or Galileo to GPS-only can also improve the limited geometry of distributed satellite associated by the GPS-only solution. To show the effect of adding other constellation (BDS/Galileo) on the derived positioning, Fig. 6.29 illustrates the analysed results for the period from 22:00 -23:00.

A slight improvement on the lateral (x) displacement can be achieved when adding either BDS or Galileo to the GPS-only, as shown in Fig 6.29a while adding both consultations to GPS showed a significant improvement as shown in Fig 6.29 (right graphs). Fig 6.29 (c), a sky plot is shown which clearly indicates that adding both constellations improved the geometry-distribution. The mean of computed DOP values at this period(22:00-23:00) are demonstrated in Table 6.9. It can be seen that the DOP values were improved after adding either or both consultations to GPS. For example, the GDOP of GPS-only was 2.8 while adding both BDS and Galileo reduced the GDOP value to 2. From the above results of adding BDS/Galileo satellites, it is evident that the future of Galileo and BeiDou constellations to improve the GNSS positioning is promising and needs further investigation.

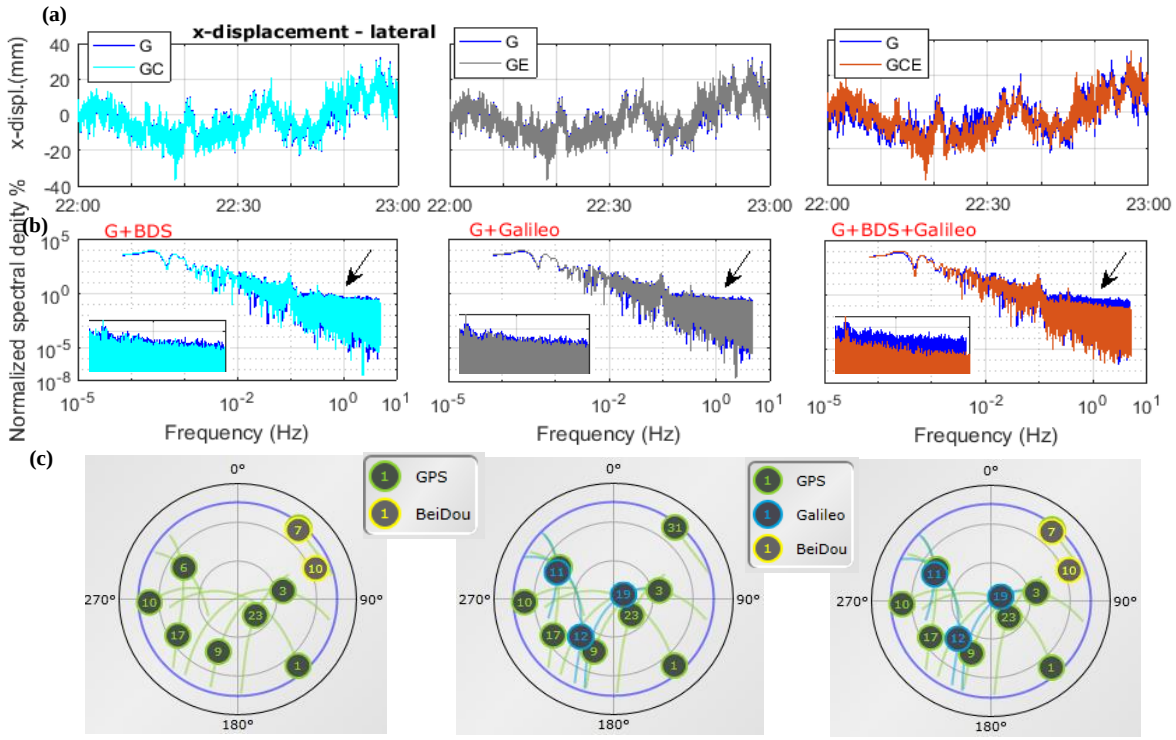


Fig. 6.29 The contribution of BeiDou and Galileo observed satellites at handrail station D1 (at a period of 22:00 to 23:00.

Table 6.9 The geometry of different GNSS solution represented by mean DOP values at period 22:00-23:00 on 20th July**.**

GNSS solution	Mean DOP values at 22:00-23:00			
	GDOP	PDOP	HDOP	VDOP
GPS-only	2.8	2.4	1.2	2.1
GPS+BDS	2.4	2.1	1.1	1.8
GPS+Galileo	2.4	2.0	1.0	1.8
GPS+BDS+Galileo	2.0	1.8	0.9	1.5

6. 9 Forth Road Bridge Monitoring

The conducted GNSS observations at the Forth Road Bridge represent the second case study that used in the current research to investigate and validate the implementing of the suggested methodology (see Section 6.2), which is used to overcome the limitations of GPS observations and improve the positioning performance for structural health monitoring. The location of this bridge, in comparison with Severn bridge (discussed previously), is relatively higher (by 4.5°) which gives the opportunity to investigate the GPS results at the relatively higher latitude and evaluate the contribution of GLONASS to enhance the monitoring procedure in the combined solution. In addition, the possibility of using GLONASS alone and its effect on the positioning as an alternative solution in structural monitoring was also investigated and analysed.

6.9.1 Forth Road Bridge Description

The Forth Road Bridge as shown in Figure 6.30 is a long span suspension bridge that located in east central Scotland and crosses the Firth of Forth. It was inaugurated in 1964 to connect the north of Scotland with Edinburgh in the south at Queensferry. The centre of bridge is located at (lat. 56° 00' 05" N, long. 03° 24' 15" W) and the main span of the bridge is oriented at bearing of N 03° E. The bridge is carrying the A90 road of the UK, and has an overall length of 2.5 Km (Roberts et al., 2012, Han et al., 2016), while the central suspended main span is 1006m long between two steel towers that have height of 156 m above water level. Currently, the bridge has permanent structural health monitoring established as part of a GeoSHM project that sponsored by ESA (Meng et al., 2016).



Fig. 6.30 The Forth Road Bridge.

6.9.2 Monitoring Stations on the Forth Road Bridge

To investigate the dynamic oscillations of the bridge by using multi-GNSS observations, three monitoring stations were installed at specific locations on the bridge's structure, in addition to the forth stable station that set up to be the reference base station. Each station was equipped with

LEIAR10 antenna, which fixed and connected to GNSS GR10 Leica Geosystem receiver. That means all receivers at the base and rover stations are similar/homogeneous receivers. Two of them were installed at the mid-span of the bridge deck and to reduce the multipath effect; they fixed on 4m tall masts at P2 and P3 stations on opposite side as illustrated in Fig. 6.31. While the third one was located on the top of the southern bridge tower on the west side at station P4 to record the response of movement at this tower. The reference station P1 was installed in a location within 1 km away south from the southern tower (Psimoulis et al., 2017).

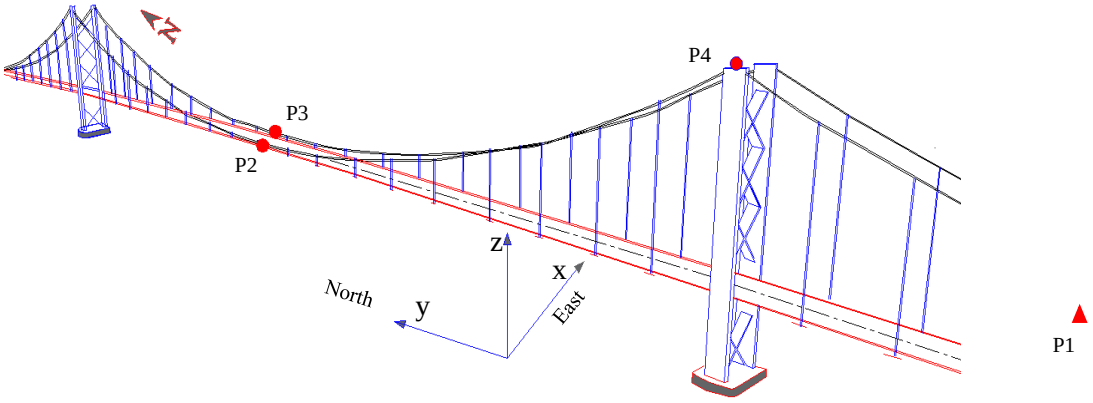


Fig. 6.31 Locations of monitoring stations upon the Forth Road Bridge.

All receivers are recording GNSS data from GPS and GLONASS with a sampling rate of 10 Hz. The conducted GNSS measurements were gathered for two continuous days of 48 hours on 9th and 10th January 2016. The coordinates of the reference station (obtained from P1) were supplied from well-previous data/records, while the initial coordinates of other monitoring stations (under the current investigation) are computed and defined from the mean values measured at the first 10 min of the fixed solution. To minimise the values of relative coordinates to the same origin at the base station, the derived coordinates are listed in Table 6.10.

Table 6.10 The initial coordinates of monitoring stations of Forth Bridge.

Location	Stations	**Components of short baseline (m.)**		
		E(x)	N(y)	U(z)
Base station	P1	00.000	00.000	00.000
mid-span station	P2	-10.606	1528.704	18.586
mid-span station	P3	25.775	1527.646	18.660
tower station	P4	-17.767	1026.585	109.544

6. 10 Pre-Processing Analysis at the Forth Road Bridge

As described in methodology (see Section 6.2), an initial step is to assist first the observation quality (Section 6.4). This can be achieved by detecting cycle slips and define the measurements that

contaminated by multipath effect from specific satellites, in addition to analysing the satellite geometry. Therefore, the pre-processing procedures will reveal the identified weak observations that should be taken into consideration when investigating the derived results. Although the selection of the cut-off elevation angle at 15° enables to exclude all received data below this elevation, the observed satellites within 15° (i.e. low elevated rising and setting satellites) are still subjected to cycle slips and multipath.

In the pre-processing analysis, it was observed different low elevated satellites, which are vulnerable to cycle slips and multipath. However, the base station was set up in an open sky environment, which ideally considered being free from multipath effect; the observations at some periods reviled that P1 could be detected as contaminated data with multipath and cycle slips for both GPS and GLONASS as shown in Fig. 6.32.

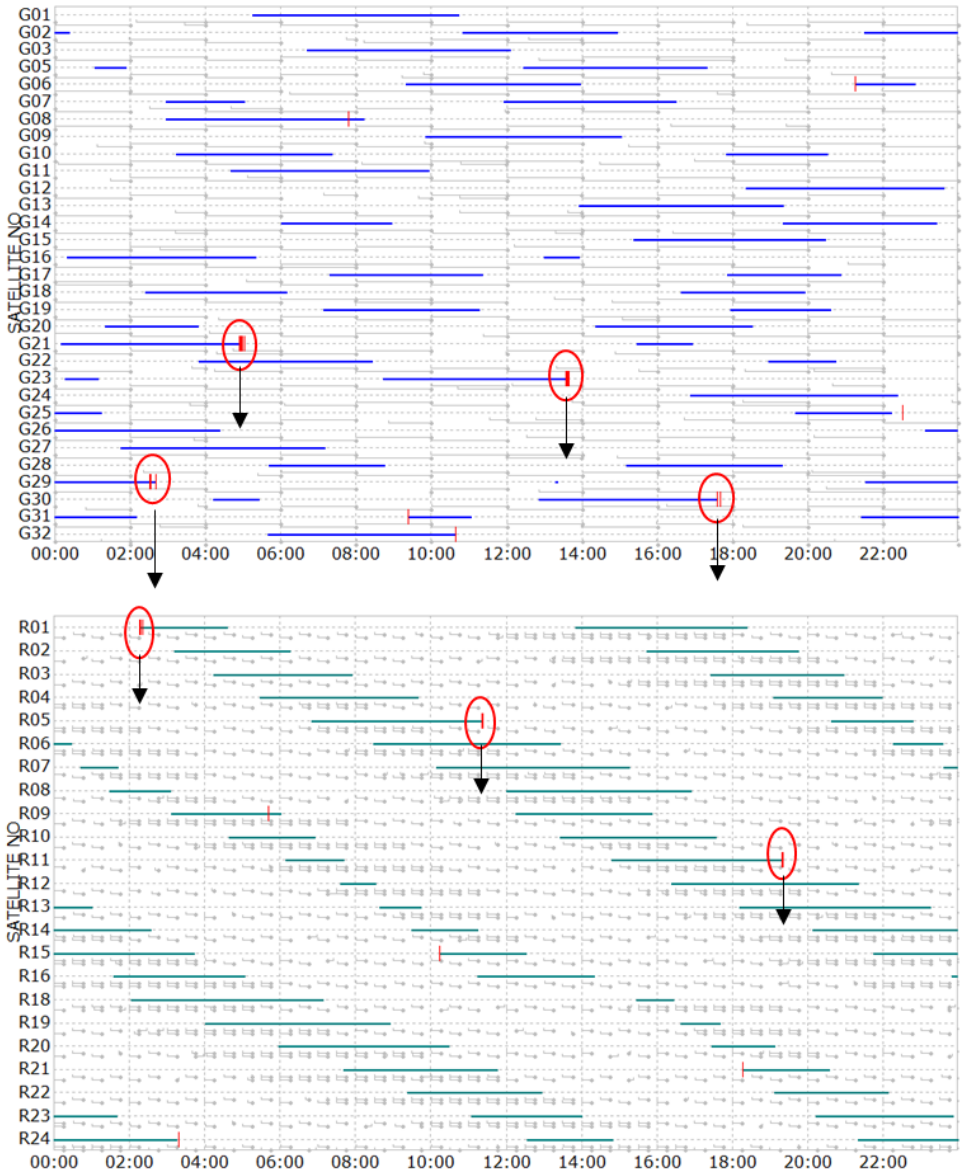


Fig. 6.32 Detected cycle slips on visible satellites of GPS (top) and GLONASS (bottom) at the base station on 09th Jan.

As shown in Fig. 6.32 (top), among the visible observed GPS satellites during the 24h, some satellites at specific periods are detected as affected satellites by cycle slips (red circles in the figure). The more prominent satellites are G21, G23, G25, G29, G30 and G32. At the same time, several of the GLONASS observed satellites are featured with cycle slips as shown in Fig. 6.32 (bottom); these are R01, R05 and R11, in addition to other satellites with single cycle slip.

To clarify the above in more details, a period (c) at 02:00 -03:00 was chosen to analyse the quality of GNSS observations at the base station as shown in Fig. 6.33.

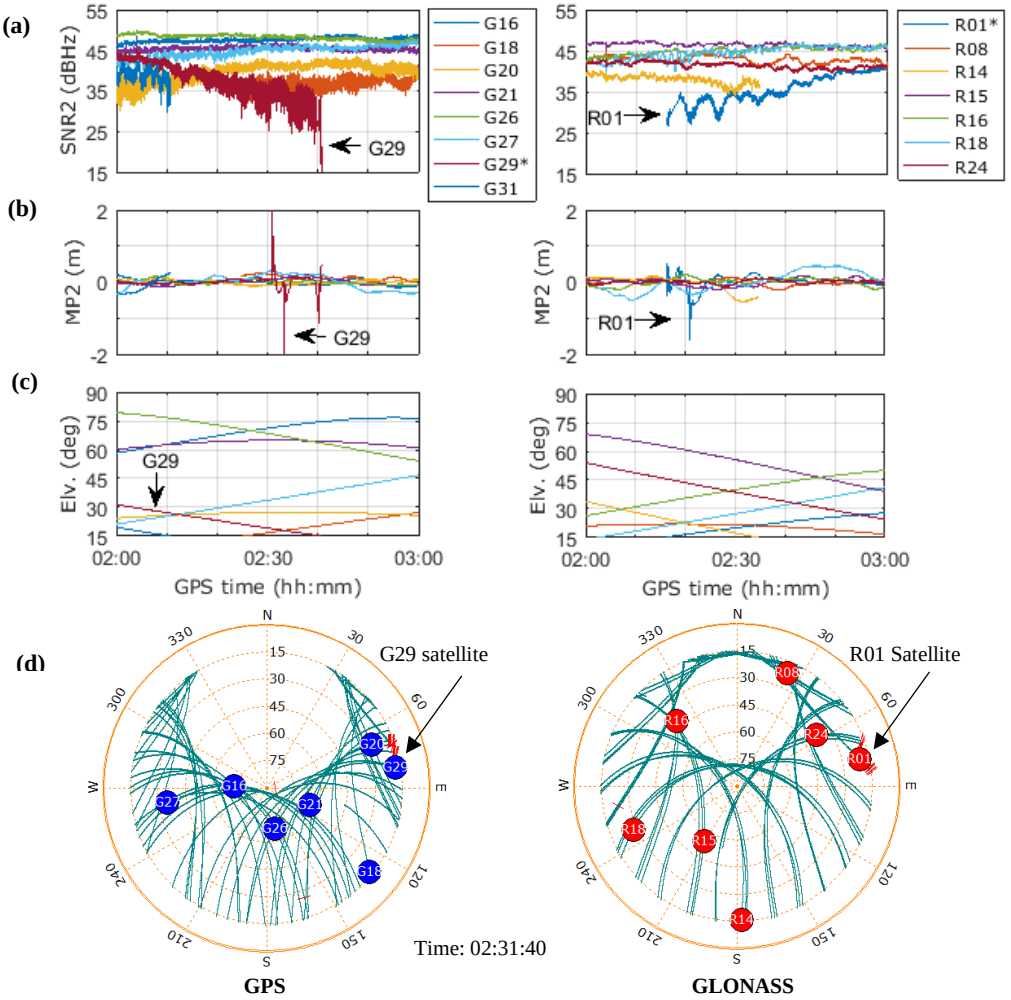


Fig. 6.33 The analysis of observed GPS and GLONASS satellites at the base station P1 on 9th Jan.

In Fig.6.33 (left), it is clear that the GPS setting satellite G29 has a low SNR2 that shows a significant fluctuation in their values, which was susceptible to multipath as detected with MP2. Whereas Fig.6.33 (right) shows the GLONASS satellite R01 raised with 15° elevation angle with low SNR2, which was changed rapidly with the occurrence of multipath. It should be noted that for the sake of brevity, the represented data is shown with frequency L2 only.

For more evidence on the effect of cycle slips and multipath at the base station, the sky-plot is illustrated as shown in Fig. 6.33d. It was found that the multipath or the cycle slip occurred when the low elevated satellites tracked at azimuth between 60° and 80°.

It should be mentioned that, at this azimuth range, the satellite signals might be either blocked or degraded. This is owing to discontinuity measurements recorded from these low elevated satellites, in addition to the presence of cycle slips at short durations. This could be attributed to the existence of any possible obstacle object near the base station during the receiving GNSS signals at this range of azimuth.

In the same manner, when applying the pre-processing analysis to the GNSS data of each monitoring station, various satellites with low-quality observations were identified along different periods. It is worth mentioning that, the observations quality at the mid-span stations P2 and P3 are better than that collected at the tower station P4. This means that the site environment at the mid-span stations is less susceptible to multipath and cycle slips, which will confirm more specifically when process the GNSS collecting data. The results of detected cycle slips on GNSS satellites are given in Appendix-C (Fig. C.1).

6. 11 Fixed Solution Availability at the Forth Road Bridge

As mentioned above in Section 6.10, the evaluation of GNSS measurements, which correspond to weak observations (i.e. contaminated by errors, etc.) at some intervals, should be taken into consideration. Consequently, the contaminated observations from low elevated satellites could prevent resolving the ambiguity resolution (especially for limited satellites of the individual constellation), which increase the failure rate of fixing the ambiguity and in turn will reduce the availability of fixed solution (Verhagen and Teunissen, 2013, Teunissen et al., 2014).

In order to investigate the impact of contaminated observation on the fixing rate availability, the collected GNSS data at each monitoring stations (P2, P3 and P4) have been post-processed using RTKLIB v2.4.2. Thus, the DD kinematic positions were generated for every hour of the full day with 15° cut-off elevation angle for GPS-only and combined GPS/GLONASS solutions. In order to fix the ambiguity and based on the instantaneous mode, the fixing rate of availability was assessed at each period for GPS-only and combined GPS/GLONASS. The use of instantaneous fixing mode helps to identify the low-quality positioning obtained by low quality or contaminated observations (Verhagen and Teunissen, 2014). Therefore, the periods with a specific degradation in fixing rate availability can be quantified.

Fig. 6.34 shows the fixing rate availability for an apparent GPS-only solution at monitoring stations (P2, P3 and P4), which are defined for every hour of the full day of 9th Jan. It is clear that the occurrence of reduced availability at mid-span stations (P2 and P3) is less than that at the tower

station (P4). The high level of contaminated observation occurred at station P4 might be due to the site environment, which reduces the quality of observed signals, as discussed in Section 6.10.

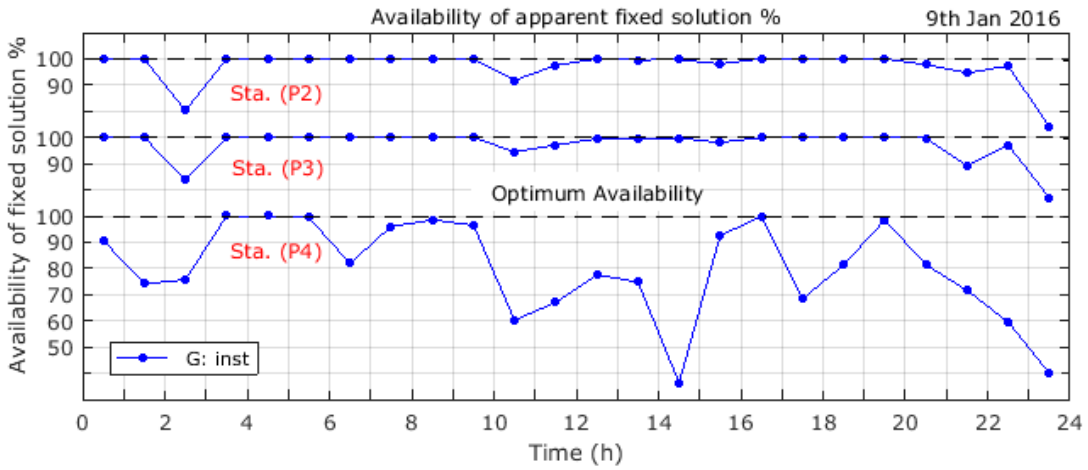


Fig. 6.34 The fixing rate availability of apparent GPS-only solutions at monitoring stations (P2, P3 and P4) of Forth Road Bridge on 9th Jan.

To obtain a clean data and improve the fixing rate of ambiguity, the corresponding contaminated observations were removed during the data processing. However, most of the detected cycle slips can be corrected in the processing stage, while the multipath effect can be effectively removed by excluding the contaminated data from the specific observed satellite. For example, since the observations of tower station P4 contain the most contaminated data, the fixing rate of availability would be improved by excluding the contaminated observations in each period, as explained in Table 6.11.

Table 6.11 Availability of fixing the rate at tower station P4 for every hour of a full day on 9th Jan.

Hourly periods		Availability % of Apparent solution		Satellites featured with Multipath, cycle slips		Availability % of Improved solution		
		G	GR	GPS	GLONASS	G: inst.	G: fix	GR: inst.
a	00:00 – 01:00	90.7	99.9	--	--	90.7	99.6	99.9
b	01:00 – 02:00	74.1	99.1	G31	--	78.1	99.7	100
c	02:00 – 03:00	75.7	91.7	G29 G31	R01	92.3	99.9	100
d	03:00 – 04:00	100	92.5	--	R15	100	--	100
e	04:00 – 05:00	100	100	--	--	100	--	100
f	05:00 – 06:00	99.4	99.8	--	--	99.4	--	99.8
g	06:00 – 07:00	81.9	70.5	G03	R05 R09	100	--	99.8
h	07:00 – 08:00	96.0	70.2	G03 G19	--	100	--	100
i	08:00 – 09:00	98.5	83.7	G23	R06 -R13	100	--	100
j	09:00 – 10:00	96.5	96.6	--	--	96.5	--	96.6
k	10:00 – 11:00	60.2	50.8	G09 G32	R07 R15 R20	70.9	99.1	99.2
l	11:00 – 12:00	67.0	67.6	G17 G19	R21	89.3	99.2	100
m	12:00 – 13:00	77.6	99.9	G30	--	80.0	99.9	100
n	13:00 – 14:00	74.8	87.6	G06 G23 G30	--	74.8	98.9	100
o	14:00 – 15:00	36.3	85.6	G02	R11	81.3	100	100
p	15:00 – 16:00	92.6	99.7	G09	R09 R11	92.6	95.1	100
q	16:00 – 17:00	99.8	89.9	G24	R12 R19	99.8	--	99.6
r	17:00 – 18:00	68.4	95.3	G05 G20	R10 R19	89.4	99.7	100
s	18:00 – 19:00	81.3	55.8	G12 G20	R01 R21	100	--	100
t	19:00 – 20:00	98.5	82.8	G18 G25	R02 R11	98.6	--	99.5
u	20:00 – 21:00	81.4	99.0	G15 G17 G19	--	81.7	100	100
v	21:00 – 22:00	71.6	96.6	G29	--	73.1	99.7	100
w	22:00 – 23:00	59.5	94.0	G06 G14	--	59.5	98.3	100
x	23:00 – 24:00	39.9	96.8	G14	R07	41.1	67.0	97.6

However, excluding the contaminated observations increases the fixing rate in most periods; an optimum availability is still unachieved in some periods. This can be attributed to noisy data or low-quality measurements (i.e. limited number of satellites or low SNR), which might prevent fixing the ambiguity with the instantaneous mode. It is clear from Table 6.11 that using the instantaneous mode cannot achieve a high rate of availability (e.g. at b, k and other periods). Therefore, an alternative technique of fix and hold mode (which relied upon the Kalman filter) can be used to improve the rate of availability at these specific periods, Fig. 6.35.

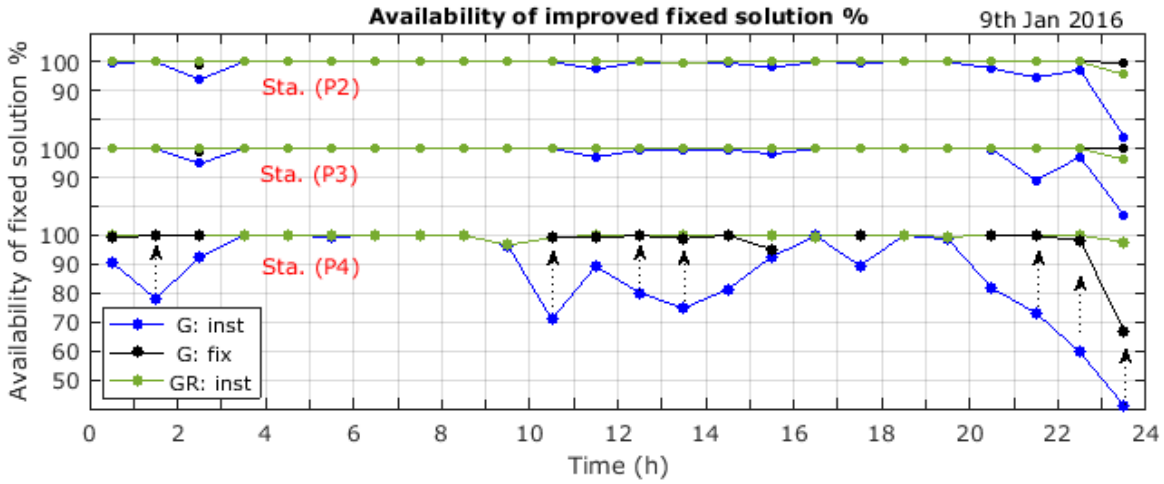


Fig. 6.35 The fixing rate availability of improved GPS-only and the corresponding combined GPS/GLONASS solutions at monitoring stations (P2, P3 and P4) of Forth Road Bridge on 9th Jan.

It is also seen in Fig. 6.35 that the improved GPS-only solution using either instantaneous or fixed and hold techniques success to achieve an optimum availability at the majority of periods, except a period x (23:00 – 24:00), which suffered from a limited number of satellites (i.e. four satellites with low geometry).

On the other hand, the combined GPS and GLONASS solutions achieved an optimum availability of fixing the rate of ambiguity at all periods. This leads to comparable results between GPS-only and combined GPS/GLONASS solutions with equivalent availability, which allows investigating the contribution of combined GNSS against GPS-only positioning in the assessment of derived displacement and frequency response for dynamic monitoring of Forth Road Bridge.

6. 12 Derived Displacement at the Forth Road Bridge

To investigate the deflection of the Forth Road Bridge, the relative displacements have been calculated at each monitoring station by using different GNSS measurements. The computed GNSS displacements at each epoch were estimated from the difference between the pre-defined initial coordinates and the measured coordinates at the monitoring stations (obtained from each receiver) of the bridge to produce the time series of the derived displacement along 3D components of bridge

movement. Due to the location of the bridge site at high latitude areas (φ=56°N), the computed GNSS positions are affected by the satellite geometry, which has an impact on the derived displacement.

When employing the GPS-only positioning at high latitudes, it is expected that the number of visible observed satellites in E-W direction would be greater than that in the N-S direction. This is due to the fact that the design of the GPS constellation includes an inclination angle of 55° (Meng et al., 2004). This variation of distributed satellites affects, in turn, the achieved accuracy of the horizontal components in the E-W and N-S directions. In addition, the vertical component is already less accurate than the horizontal component. Therefore, the GPS-only positioning has a disparity of achieved accuracy along the three components, which influences the accuracy of derived displacement. Thus, to strengthen the positioning performance with more accurate results, the combined GPS/GLONASS has been proposed to obtain more precise structural deformation data and overcome the GPS-only limitations.

In order to identify the periods of weak geometry during the bridge monitoring, the 24h measurements of the first day were used. Thus, the DOP values are computed for the GPS-only constellation as well as for combined GPS/GLONASS to investigate the improved geometry as illustrated in Fig. 6.36a. It is clear from Fig. 6.36a that the periods of a limited number of satellites has a weak geometry, especially at the periods of a sharp decreasing in the number of satellites, which might accompany with spikes of high magnitude of DOP values as observed in hourly periods of a, p, u, v and x (Fig. 6.36a.). For these periods, a definite improvement was attained with the increasing of observed satellites when adding GLONASS to GPS observations in combined positioning; in addition, all the spikes of the weak geometry of GPS-only are removed in the combined GPS/GLONASS geometry. These events indicate that a more robust and reliable solution can be achieved with combined GPS/GLONASS solution.

From the linear correlation as discussed in Section 4.7, it has been proved that there is a correlation between the geometry and the noise of measurements, thereby it is expected that the periods of weak geometry with high DOP values introduce noisy results of computed positions that have an impact on the derived displacements.

Thus, to quantify any improvement in the relative displacement due to the applying of combined GPS/GLONASS solution, the results of derived displacements are compared between two datasets; the first was the time series using the observations of GPS-only satellites and the second when using the data of combined GPS/GLONASS. This comparison was applied to the resulting displacement at all monitoring stations (P2, P3 and P4) for 24h of the first day of monitoring as shown in Figs. 6.36b and 6.36c.

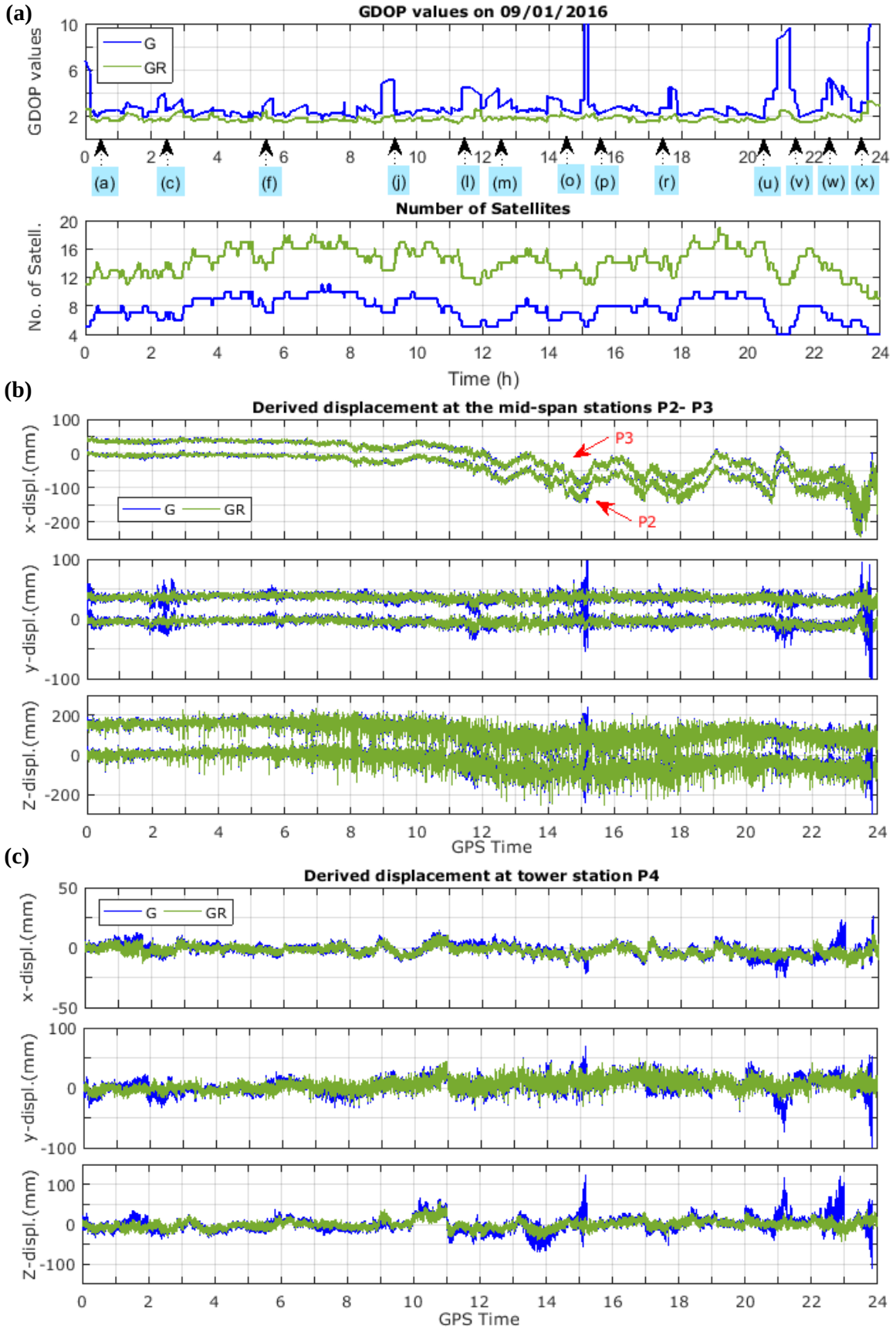


Fig. 6.36 Comparison between derived results from GPS-only and the corresponding combined GPS/GLONASS solutions for (a) GDOP values with the number of satellites, (b) and (c) the derived relative displacement at monitoring stations (P2, P3 and P4) of Forth Road Bridge on 9th Jan 2016.

It can be shown in Figs. 6.36b and 6.36c that different periods were considered to demonstrate the impact of the combined solution on the detected displacement, where significant differences can be achieved between the derived displacement from GPS-only results, and that computed from combined GPS/GLONASS solutions. Therefore, the positioning performance at these intervals needs further investigation. In addition, Figs. 6.36b and 6.36c are showing the overall response of bridge deflection during the 24 hours on 09/01/2016. It can be seen from Fig. 6.36b that both mid-span stations P2 and P3 showed a similar trend of movement along the three components.

The smallest movement at these mid-span stations was observed along the y (longitudinal) component compared with the z (vertical) and x (lateral) movements. As the main axis of the Forth Road Bridge is oriented to the North direction, the expected improvements of combined GPS/GLONASS solution can be evaluated along the longitudinal component.

However, a limited movement was observed in the lateral component at the first 8 hours, followed then by a gradual increase of the lateral deflection (x) to reach 25 cm in relative to the initial value. The most significant movement at the mid-span stations occurred at vertical component as shown in Fig. 6.36b, which can reach 30 cm. in contrast, the vibrated movement at tower station as shown in Fig. 6.36c exhibits a somewhat similar trend among the three components of movement. Regarding the positioning performance, in order to examine the GPS-only solution and what improvement can be achieved when implementing a combined GPS/GLONASS solution, various hourly periods have been extracted from the time series (shown in Fig. 6.36) to analyse the positioning performance in more details. Analysing the results at monitoring stations (P2, P3 and P4) at the period (c) in Fig.6.37 during (02- 03h) showed a considerable improvement in derived displacement when adding GLONASS to GPS observations.

Figs. 6.37 (a-c) reveals that although improvements on the x-lateral displacement were relatively small, significant improvements were observed on the y-longitudinal and z-vertical deflections. The slight improvement in x-lateral deflection is related to a stable geometry of GPS-only in E-W direction, due to the sufficient distributed GPS satellites in that direction, while limited GPS satellites being in the N-S direction as shown in the sky-plot of Fig. 6.37e. Thus, the weak geometry of GPS-only solution affects the N-component, which leads to degradation in N positioning that appears as a noisy solution at this interval.

Conversely, the combined GPS/GLONASS solution strengthen the satellite geometry by adding GLONASS observations, which indicates well-distributed satellites with more robust geometry, leading to more accurate and reliable results. To evaluate the improved geometry mathematically, the mean values of different DOPs in the period (c) at (02– 03h) were computed for GPS-only and combined GPS/GLONASS, and the results are listed in Table 6.12. The comparable results showed

that the geometry of the combined solution resulted in a 50% improvement in HDOP values that appeared on enhanced N components.

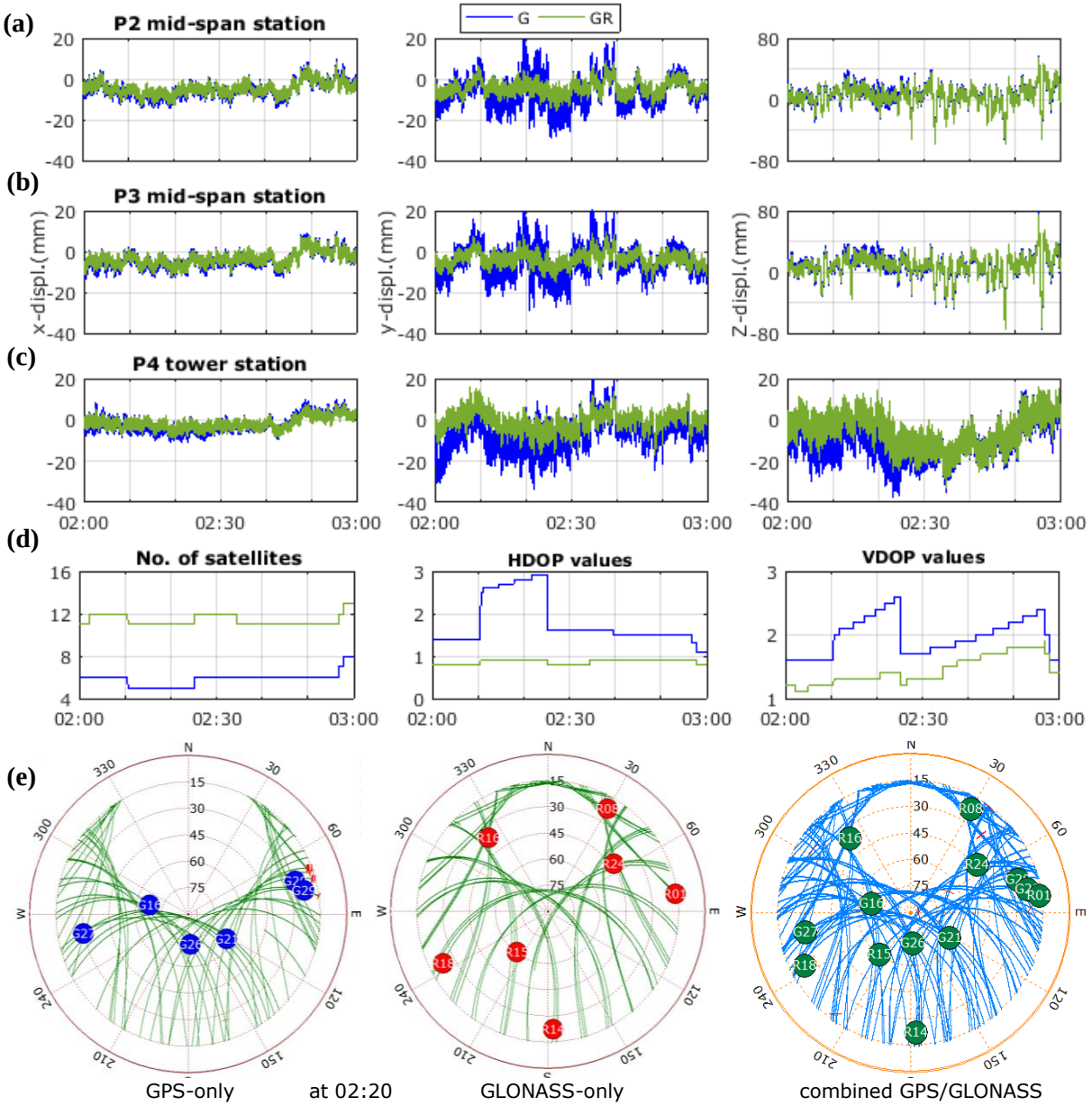


Fig. 6.37 Analysis of derived displacement in period c at (02:00 – 03:00) for GPS-only and the corresponding combined GPS/GLONASS solutions (a-c) at monitoring stations, (d) the computed geometry and (e) the sky-plot of distributed satellites at this interval on 9th Jan 2016.

Table 6.12 Availability of fixing rate ambiguity at a monitoring station in period c at (02:00 – 03:00).

Solution	Availability of fixing rate %			Mean	Mean	Mean	Mean
	P2	P3	P4	GDOP	PDOP	HDOP	VDOP
GPS-only	99.9	99.9	99.9	3.1	2.7	1.8	2.0
GLONASS-only	99.7	99.5	97.1	3.9	3.44	1.3	3.1
GPS+GLONASS	100	100	100	1.9	1.7	0.9	1.4
Improvement*				29%	27%	50%	30%

To examine the positioning performance at another interval, period P (see Table 6.11) was selected and analysed. The GPS-only solution in the period P at (15:00-16:00) exhibited noisy behaviour, which was detected in all monitoring stations (P2, P3 and P4) as shown in Fig. 6.38a-c.

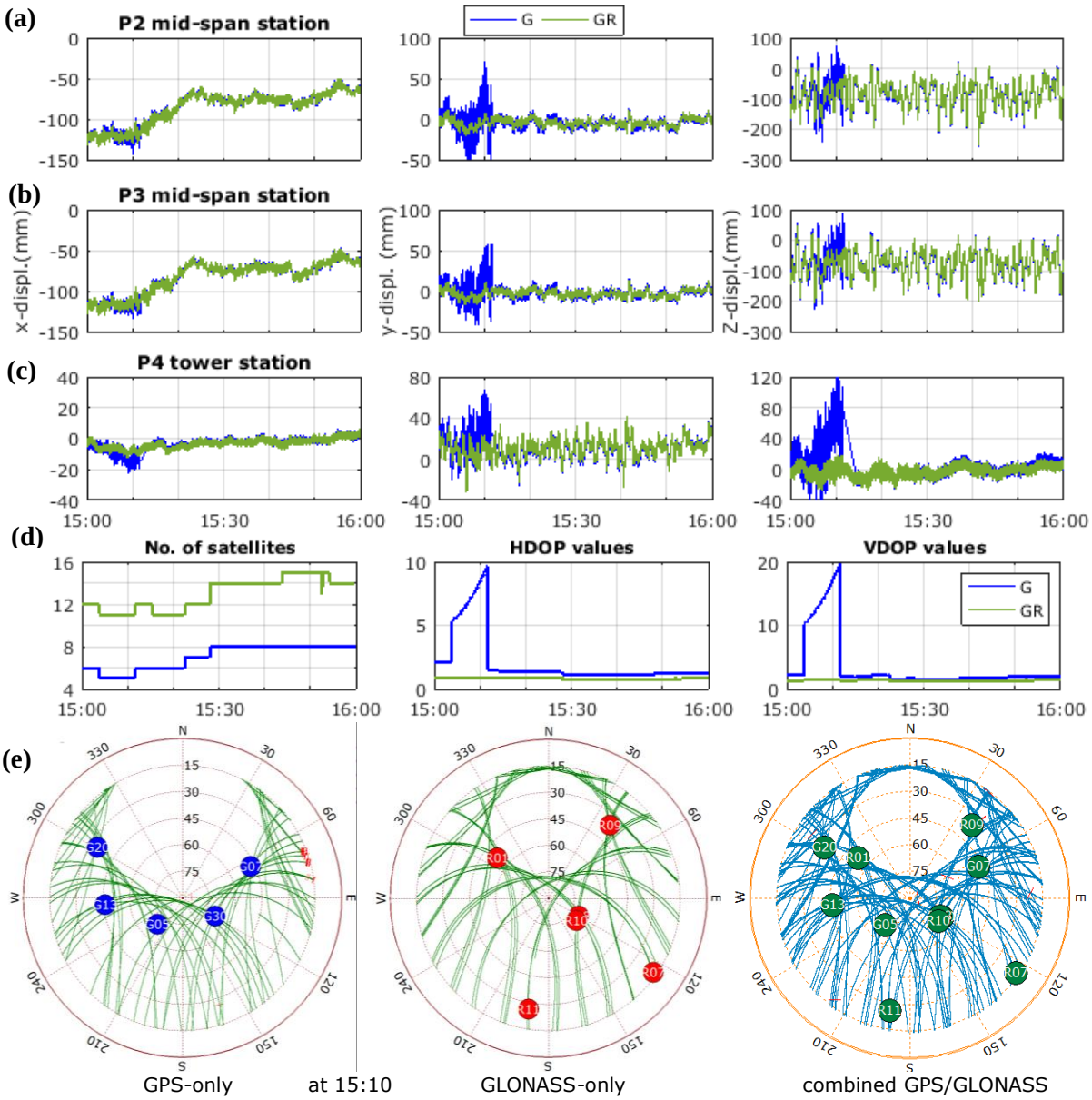


Fig. 6.38 Analysis of derived displacement at p-period (15:00 – 16:00) for GPS-only and the corresponding combined GPS/GLONASS solutions (similar to Fig. 6.37).

Table 6.13 Availability of fixing rate ambiguity at the monitoring station at p-period (15:00 – 16:00).

Solution	Availability of fixing rate %			Mean	Mean	Mean	Mean
	P2	P3	P4	GDOP	PDOP	HDOP	VDOP
GPS-only	98.1	98.1	95.5	4.8	4.0	2.1	3.4
GLONASS-only	100	100	69.0	3.0	2.6	1.5	2.1
GPS+GLONASS	100	100	99.8	1.9	1.6	0.9	1.3
Improvement*				60%	60%	57%	62%

This noise is associated with the weak geometry that induced by a limited number of GPS satellites as displays in Fig. 6.38d, which also shows a spike in high DOP values for both HDOP and VDOP factors. Therefore, in the GPS-only solution, the longitudinal and vertical components of derived displacement at monitoring stations contains a high level of noise particularly at the first ten minutes which gives a false indication of the actual (real) displacement due to the magnification caused by such noise.

The combined GPS/GLONASS solution shows substantial improvements on derived displacements with added GLONASS observations. Apparently from Fig. 6.38, an enhanced satellite geometry of combined solution was achieved with no spikes that lead to improving overall positioning performance. As demonstrated in Table 6.13, the percentage of improvement in the geometry of the combined solution compared with GPS-only was 57% and 62% for HDOP and VDOP respectively.

The impact of this improvement will appear on the derived displacements in which the longitudinal displacement extracted from GPS-only solution can reach 7cm, while this was reduced in combined solution to be within 1cm (Figs. 6.38a-c). In addition, the derived vertical displacement of the combined solution at tower point P4 was within 1cm instead of 12cm with GPS-only. According to Wang et al. (2010), the accuracy of a kinematic positioning by using DD in GPS-only is quantified as 1-2 cm + 1ppm of baseline length. It should be noticed that in the current study, the maximum length of the baseline was about 2.5 km. Therefore, the acceptable uncertainty in position (according to (Wang et al., 2010) should be within 1 cm, while the current GPS-only data exceeds this acceptable limit.

One of the prominent example of improved positioning performance when implementing combined GPS/GLONASS solution can also be seen in a period x at (23-24h). In this period the deficiency of GPS-only solution is related to limited visible satellites in which observing limited satellites with weak geometry introduced noisy solution as shown in Fig. 6.39a-c.

It is clear from Fig. 6.39a-c that both y and z components of derived displacements with GPS-only solution have noisy results appeared as sharp fluctuations in resulted deflection. This can be attributed to increased DOP values as illustrated in Fig. 6.39d, which shows a rapid increase in DOP values associated with increasing of derived displacement. Thus, the derived displacement of GPS-only (which already includes a high level of noise) at mid-span stations P2 and P3 varies from +5cm to -17cm for y-longitudinal (N-component), and within -30cm for z-vertical displacements, while the results of corresponding combined GPS/GLONASS would be ±2cm for y-component and -12cm for z-vertical component, respectively (Fig. 6.39a-b). It should be mentioned that the DOP values below 10 indicate reasonably an accurate solution. The DOP value after 30 showed no solution which creates obvious gap intervals (leading to discontinuity) in the time series.

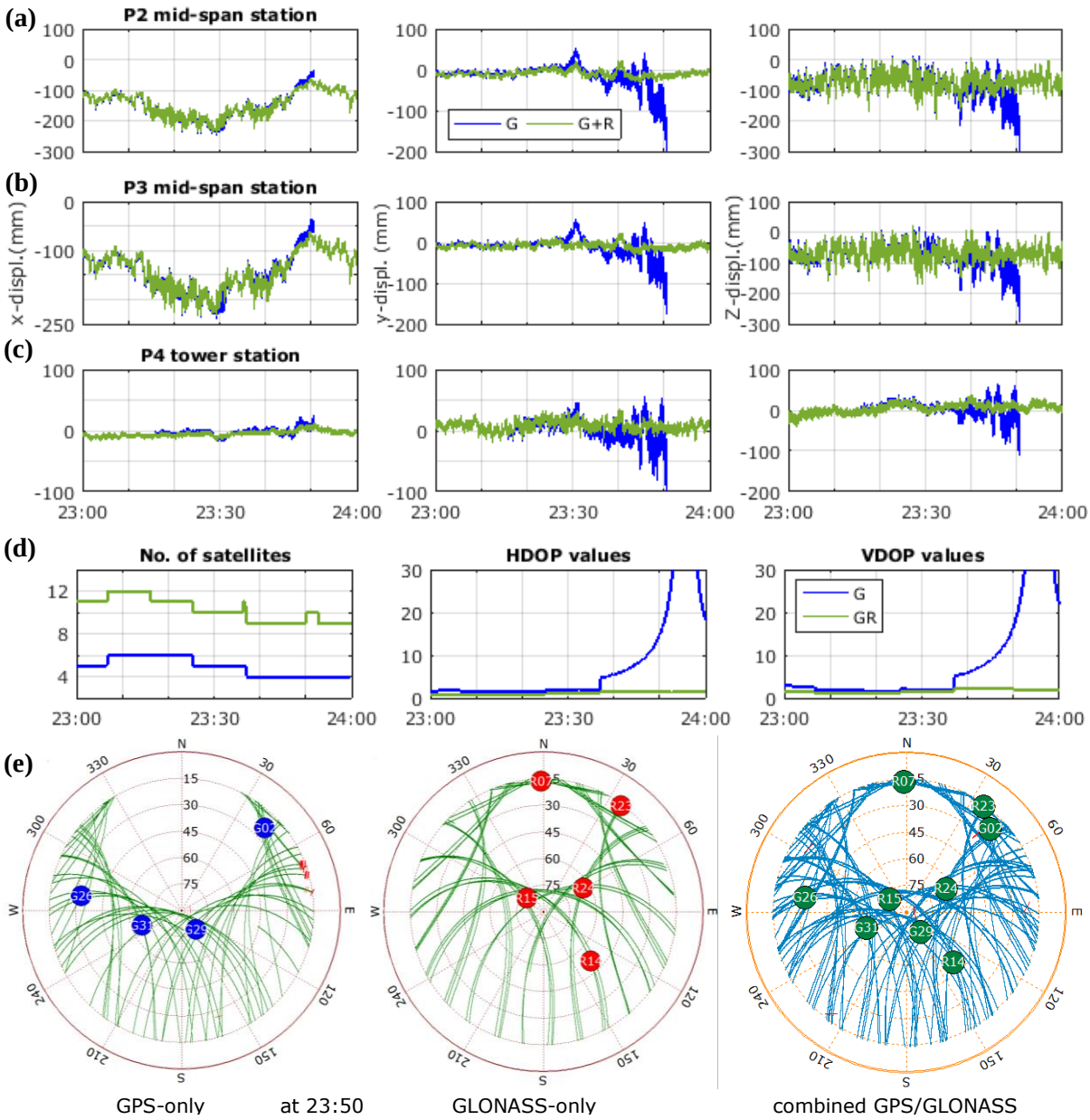


Fig. 6.39 Analysis of derived displacement at x-period (23:00 – 24:00) for GPS-only and the corresponding combined GPS/GLONASS solutions (similar to Fig. 6.37).

To quantify the apparent discontinuity in GPS-only solution, Table 6.14 summarises the availability rate of fixed GPS-only solution. The availability of fixing rate positioning was 84.5% at mid-span stations P2 and P3, while it was 58% at tower station P4 even with the use of fix and hold technique.

Table 6.14 Availability of fixing rate ambiguity at the monitoring station at x-period (23:00 – 24:00).

Solution	Availability of fixing rate %			Mean GDOP	Mean PDOP	Mean HDOP	Mean VDOP
	P2	P3	P4				
GPS-only	84.5	84.5	58.0	5.9	5.6	4.7	5.0
GLONASS-only	100	100	100	4.4	3.6	2.3	2.8
GPS+GLONASS	99.8	99.1	97.7	2.3	2.0	1.2	1.6
Improvement*				61%	64%	74%	68%

This variation in availability rate related to the different quality of observations from various environment sites, which has an impact on positioning performance. While, excellent quality of combined GPS/GLONASS with enhanced geometry enables to achieve a high rate of success fixing availability, which was within 99% at mid-span stations and about 98% at tower station.

Also, a noticeable improvement was achieved in the derived geometry of combined GPS/GLONASS, where the HDOP and VDOP values improved by 74% and 68%, respectively as shown in Table 6.14. It is obvious that the combined GPS/GLONASS solution is capable to sustains enough continuous observations to overcome the effect of discontinuity in the derived solution of the GPS-only and enhance the positioning performance as well as the reliability of the combined GNSS solutions.

6. 13 Comparison of GLONASS-Only and GPS-Only Positioning at the Forth Road Bridge

As the Forth Road Bridge locates at higher latitudes area (φ=56° N), GLONASS geometry would be expected to give better geometry; it would be of interest to investigate the positioning performance of the GLONASS-only solution and compare it with GPS-only. Most of the structural monitoring studies reported in the literature focus on applying GPS-only measurements to evaluate the dynamic response of engineering structure, unlike GLONASS-only, which received less attention. Thus, in this Section, the derived results of GLONASS-only are investigated and compared with GPS-only positioning. Therefore, the idea in this section is to show whether the GLONASS-only could achieve better performance than that obtained by GPS-only or not.

According to 24h measurements of each independent constellation of GPS and GLONASS on 9th Jan, the assessment of the derived geometry (that achieved by GDOP values from visible satellites at cut-off elevation angle 15°) was performed. The comparison between the two constellations showed that the number of observed GPS satellites was more than that of GLONASS in most periods as depicted in Fig. 6.40a. Even though, the good distribution of GLONASS satellites enables to achieve better geometry than GPS in some periods, such as j, l, m, p and others (Fig. 6.40a), which are explained in sky-plot representation at Appendix-C (see Fig. C-3). For the positioning results at mid-span stations P2 and P3, the derived displacements demonstrate a noticeable improvement when applying GLONASS-only solution as shown in Fig. 6.40b.

This improvement emerges in the y-component (N) of periods that identified as noisy periods with a GPS-only solution (see Section 6.13), such as c, p, x and other periods. It is clear from Fig. 6.40c that the GLONASS performance at tower station is less accurate than that at mid-span station (Fig. 6.40b) due to noisy measurements affected by site environment (see Section 6.12). Therefore, a number of periods were characterised by gap intervals at tower station, such as i, k, p and other periods (see Fig. 6.40c).

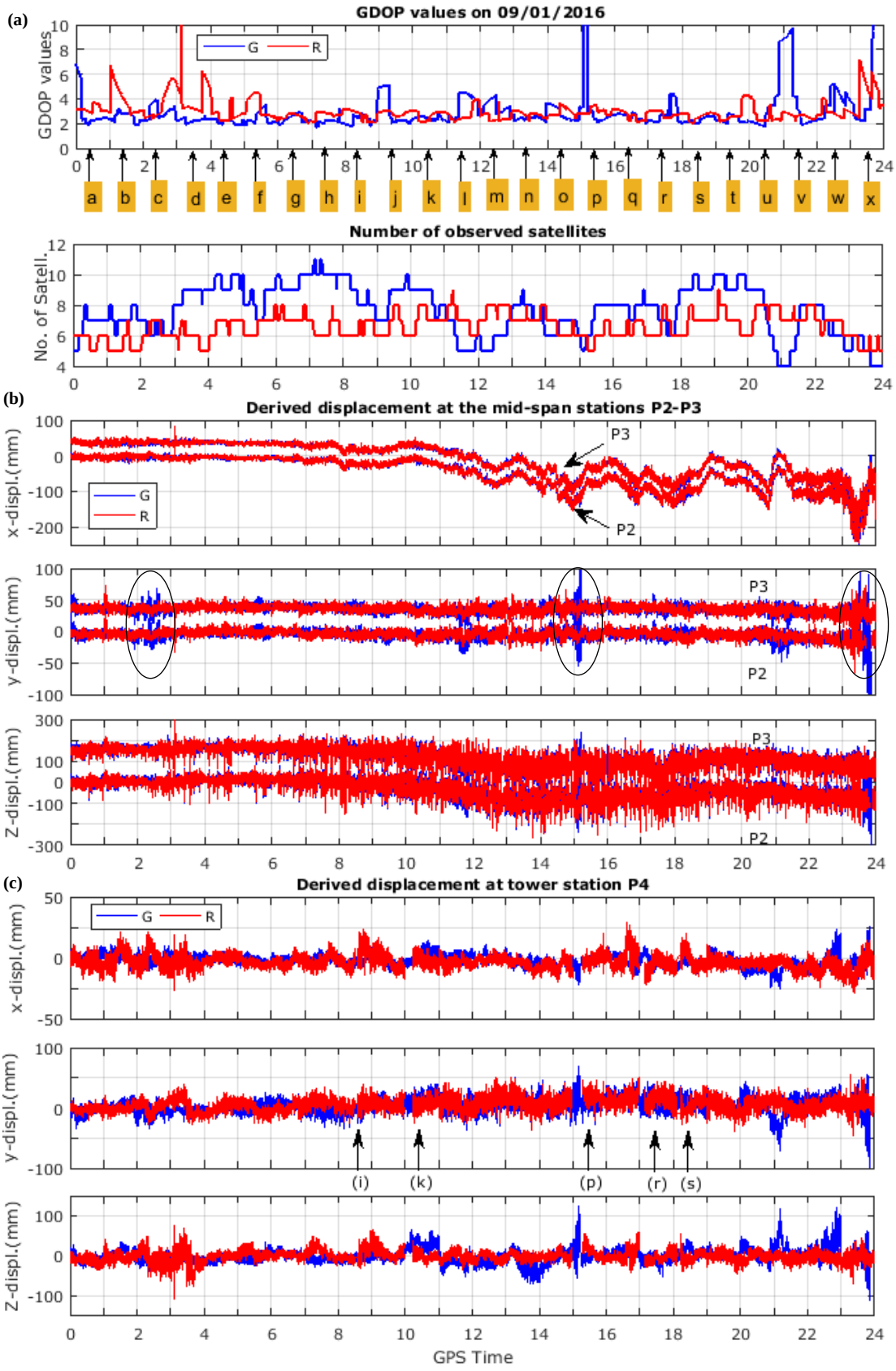


Fig. 6.40 Comparison between derived results from GPS-only and the corresponding GLONASS-only solutions for (a) GDOP values with the number of satellites, (b) and (c) the derived relative displacement at monitoring stations (P2, P3 and P4) of Forth Road Bridge on 9th Jan 2016.

It is also evident from Fig. 6.40c that noisy GLONASS solution observed at the various interval, such as the time series of the periods at the first four hours solutions can be attributed to limited GLONASS satellites at these intervals. While other periods are showing improved GLONASS results compared to the GPS-only solutions. For example, the magnitude of derived displacement in period u at (21-22h) reveals improved results in y and z components of movement as shown in Fig. 6.41a.

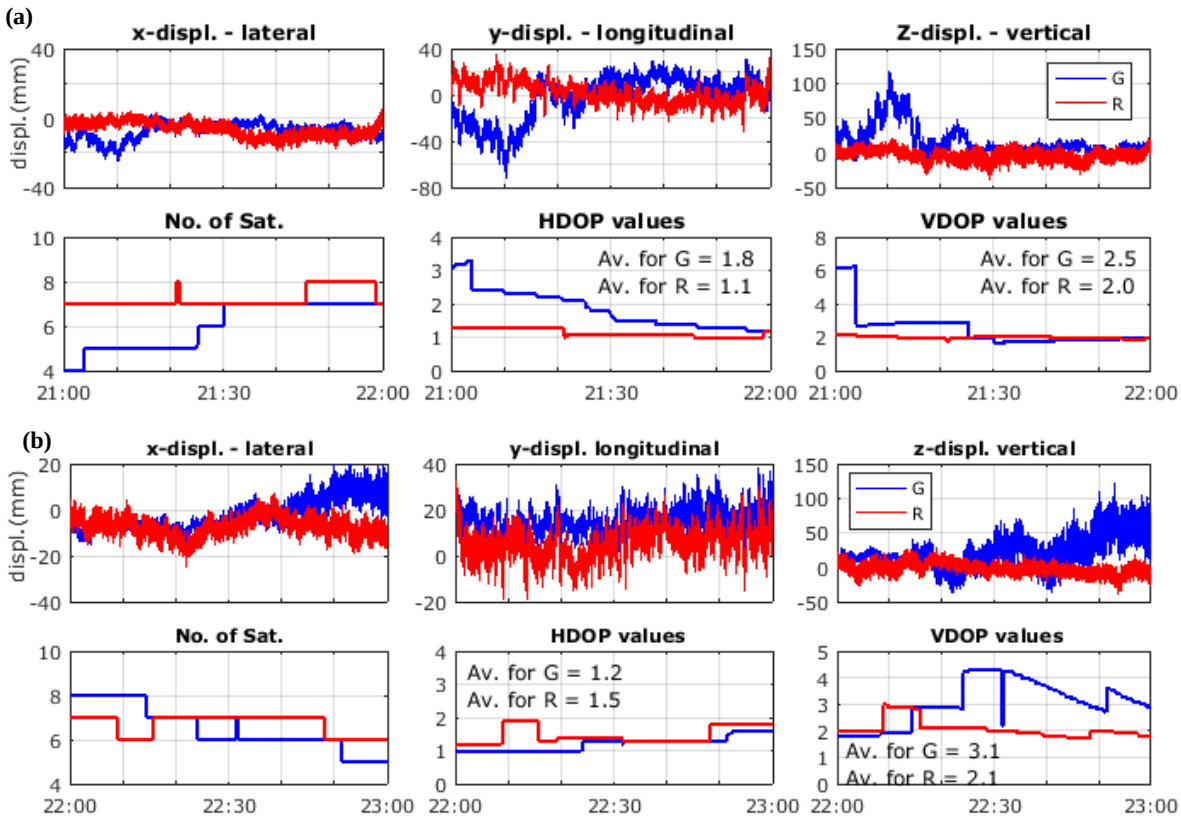


Fig. 6.41 Comparison between dynamic displacements derived from GPS-only and GLONASS-only at tower station P4 with the corresponding DOP values and a number of satellites in (a) period u at (21-22h) and (b) period v at (22-23h) on 09th Jan 2016.

The enhanced performance of GLONASS positioning is related to improved geometry by reduced both HDOP and VDOP values, which indicates well-distributed (adequate) satellites (Fig. 6.41a). Nevertheless, for the same above reason, the significant improvement of GLONASS positioning was achieved in the z-component. For instance, the vertical component of derived displacement in period v at (22-23h) has a significant improvement as shown in Fig. 6.41b, whereas the horizontal components of GPS positioning showed better performance.

From the above discussion, one can conclude that it is quite hard to generalise the observation between GLONASS-only and GPS-only as the resulting positioning gave a good performance for GLONASS-only at certain periods and showed better performance for GPS-only at other periods. This might occur due to the variation in derived geometry. However, generally speaking,

GLONASS-only, at mid-span station, showed less noise compared to GPS-only. In contrast, at the tower station, GPS-only showed less discontinuity features compared to GLONASS-only.

As a result, it is important to mention that, to overcome noise and discontinuity problems associated with a single constellation (GPS-only or GLONASS only), the combined GPS/GLONASS was proposed and implemented in this study which already showed significant improvements.

6. 14 The Frequency Response of the Forth Road Bridge

Following the proposed methodology summarised in the flowchart shown in Fig. 6.1, and in order to identify the natural frequencies of the Forth Road Bridge at a 10 Hz sampling rate, the same approach used in analysing frequency response for Severn Bridge (Section 6.7.3) was applied to quantify the dominant frequencies of dynamic movements at Forth Bridge. Thereby, to analyse the frequency response by using a Fast Fourier Transform (FFT) technique, a continuous time series of derived displacement was first extracted from the whole time series of 24h. Therefore, the data of hourly period ('e' at 04:00-05:00, see Fig. 6.40) that achieves continuous time series with the GPS-only solution was selected to apply FFT technique. In addition, the results obtained from FFT was compared with that obtained by the Lomb Normalized Periodogram (LNP) for the same continuous period as demonstrated in Table 6.15.

Table 6.15 Extracted frequencies provided by FFT and LNP techniques.

Monitoring station	Frequency Technique	Extracted frequencies (Hz)		
		x-lateral comp.	y-longitudinal comp.	z-vertical component
P2 mid-span	FFT	**0.074**, 0.269	0.083, 0.132, 0.153	0.035, 0.104, 0.203, 0.269
	LNP	**0.074**, 0.269	0.071, 0.133, 0.153	0.033, 0.104, 0.204, 0.269
P3 mid-span	FFT	0.074, 0.269	0.080, 0.133, 0.153	0.035, 0.104, 0.203, 0.269
	LNP	0.074, 0.269	0.080, 0.133, 0.153	0.035, 0.104, 0.204, 0.269
P4 tower sta.	FFT	0.081, 0.152	0.104, 0.123, 0.153	0.080, 0.125, 0.190, 0.202
	LNP	0.085, 0.153	0.104, 0.122, 0.153	0.076, 0.125, 0.190, 0.202

Bold values are related to the dominant (distinct) frequency with maximum amplitude.

As can be seen from the above table that most peaks of frequencies (obtained from FFT and LNP) are well agreed. It is also obvious that, for P2, the first peak (using FFT) showed the dominant frequency (i.e. 0.035 Hz), while the dominant frequency identified by LNP corresponds to the second peak (i.e. 0.104 Hz). From the results shown in Table 6.15, it is found that the longitudinal frequency of P4 obtained from both FFT and LNP was similar (0.104 Hz). This value of frequency is also agreed with the vertical frequency of P2 & P3 (which is consistent with the finding reported by Brown et al. (2007). Therefore the actual dominate frequency of vertical component at mid-span station is 0.104 Hz.

To visualise the identified frequencies in Table 6.15, Fig. 6.42 illustrates the peak-picking frequencies from the spectrum of LNP approach for the data of three monitoring stations. For mid-span stations P2 and P3, it is evident that for mid-span stations P2 and P3, a single dominant frequency can be clearly seen in x and z-direction. At y-component, multiple peaks of frequency were observed. This was also observed with an x-lateral component of tower station P4. The appearance of multiple peaks might be due to the noise level, which makes the identification of the true dominant frequency quite hard.

To show the effect of this noise in y-component, the time series of the displacement at period p (15:00-16:00) is illustrated in Fig. 6.43. It is clear that y-component (using GPS only) showed a significant level of the noise. The dominant frequency values in y-component of GPS is quite far away from the data shown in Table 6.15, while for GLONASS and Combined solution these values are approximately similar to that shown in Table 6.15.

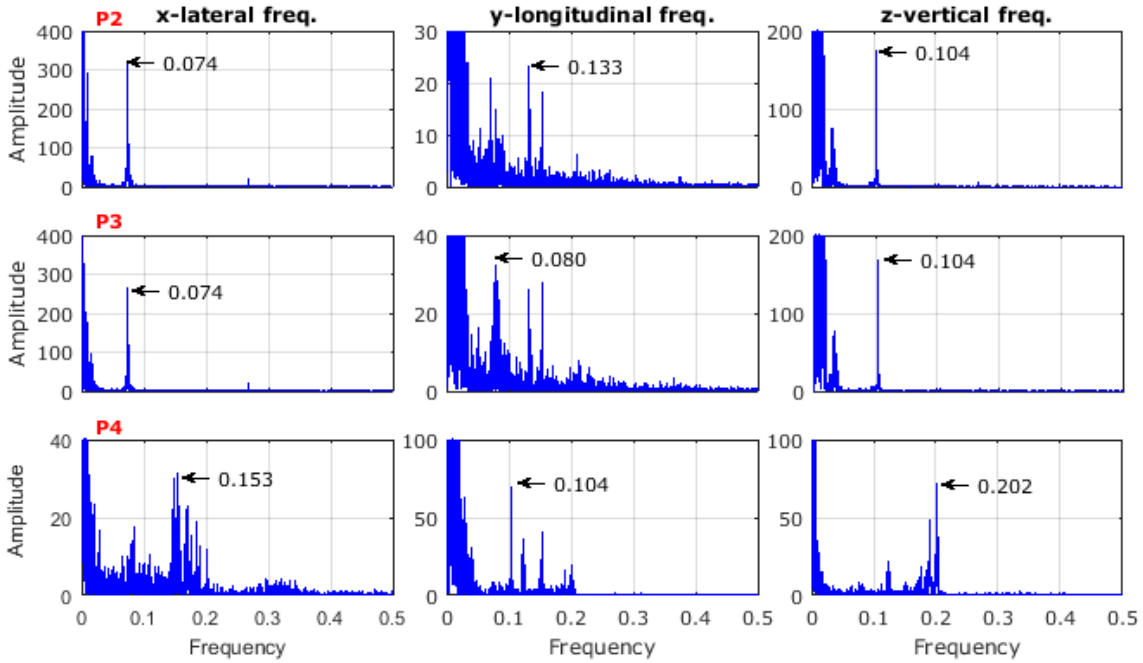


Fig. 6.42 Identified dominant frequencies at monitoring stations extracted from the time series of derived displacement in the interval (e) at (04:00 -05:00).

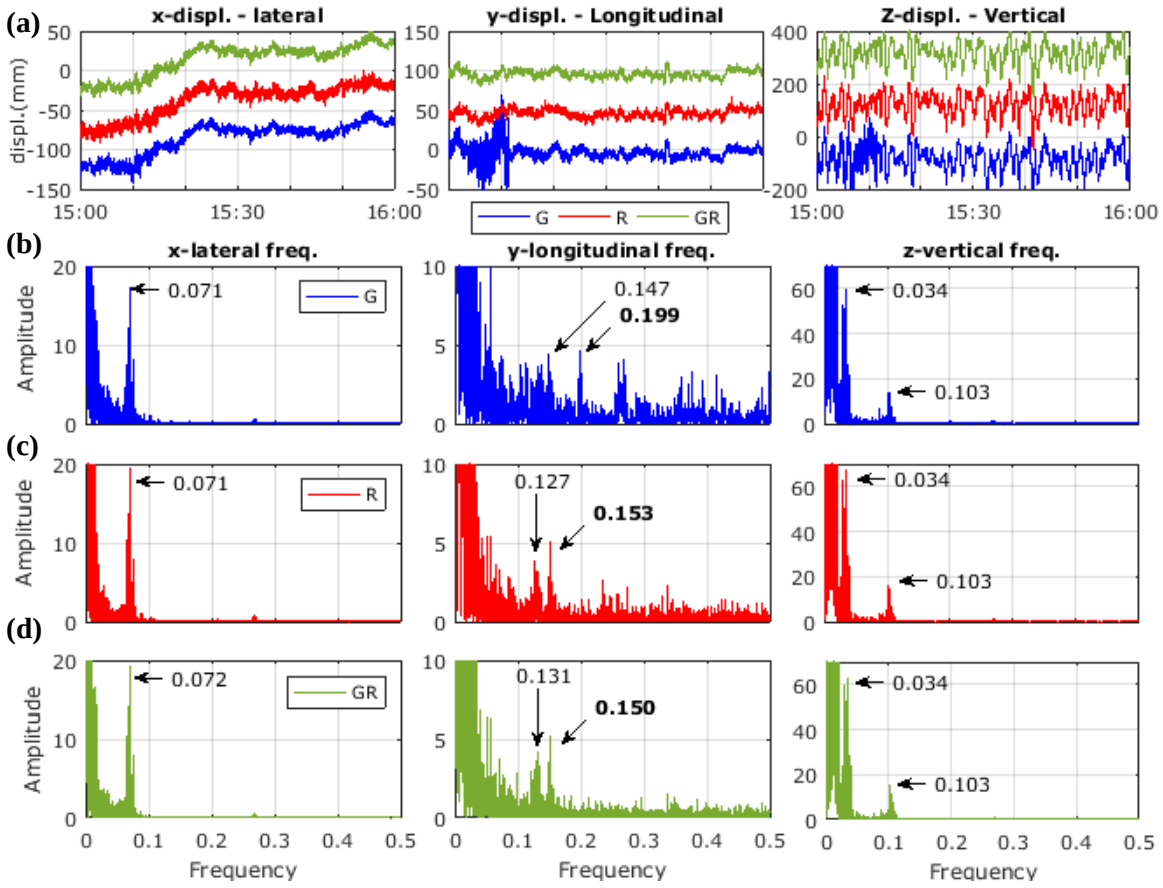


Fig. 6.43 (a) Comparison between time series of derived displacement of different GNSS solutions, (b-d) the corresponding defined frequencies by LNP technique.

6. 15 Chapter Summary

A new proposed methodology has been employed in this chapter to investigate the positioning performance of the combined GNSS solution compared to the GPS-only solution for structural health monitoring. Real monitoring tests were carried out in two long-span suspension bridges in the UK (Severn Bridge and Forth Road Bridge) to evaluate the effectiveness of the proposed approach and to verify the improved performance. These bridges represent a challenging environment to GPS-only measurements. Therefore, the initial step of this approach was based on pre-processing analysis to evaluate the quality of the measurements and to identify the observations, which cause a potential reduction in the solution precision. In this step, the cycle slip, as well as the multipath detections, were discussed to mitigate/remove contaminated data. These low-quality data should be taken into consideration to identify the clean data that represent the real deflections in the followed steps. Furthermore, a noise assessment was presented by static zero baseline measurements at the base station along with analysing the satellite geometry of different GNSS solutions to figure out the weak intervals. The processing of GPS-only data was performed first to identify its limitations, then the combined GPS/GLONASS solutions were used to evaluate the contribution of adding GNSS observations in structural monitoring. The instantaneous mode was chosen as the most suitable

technique to fix the ambiguity resolution for every epoch. Consequently, the kinematic positions of monitored stations on the bridge were calculated.

The GNSS recorded coordinates in the geodetic system were converted to bridge coordinate system; then the resulted displacements were determined by taking the difference between the calculated coordinates and the initial coordinates of every monitoring station. A spectral analysis technique to analyse the displacement time series for every component at each station was implemented. For this purpose, the FFT was used for several intervals of continuous data, and the results were compared with the LNP technique for different GNSS results.

A new assessment at each bridge was analysed. In Severn Bridge structural monitoring, in addition to applying a combined GPS/GLONASS solution, a possibility of using BeiDou and/or Galileo available constellations were also investigated (at the time of measurements, July 2015). However, limited BDS and Galileo satellites were observed, they improved the geometry and contributed to increased the rate of fixing solution availability (see Section 6.8). On the other hand, the possibility of using the GLONASS-only solution at the higher latitude areas as the alternative solution was also studied in Forth Road Bridge monitoring and compared to the GPS-only solution. It was observed that the derived displacements at mid-span stations showed noticeable improvements when the GLONASS-only solution was applied at several intervals, especially in N-component.

Finally, it is important to mention that the noise errors and discontinuity problems associated with a single constellation (GPS-only or GLONASS only) were reduced by implementing the proposed combined GNSS solution in the current study and demonstrated significant improvements.

Chapter 7: Conclusions and Recommendations

7. 1 Conclusions

The research work conducted in this study focused on investigating the contribution of the recently developed or modernised GNSS constellations (i.e. GLONASS, BeiDou, etc.) to improve the quality of positioning solution, and to achieve a high rate of fixed solution availability throughout the combined solution of GPS with another GNSS system. The motivations behind this investigation are due to limitations in the GPS-only measurements that degrade its performance to obtain highly accurate positioning and continuous fixed solution. These limitations include; the multipath effect, random noise, cycle slips as well as the need of the proper geometry of sufficient available satellites. Therefore, the main aim was to identify an effective positioning technique of a combined GNSS solution that capable to overcome the positioning limitations and achieve more precise positioning. Thus, the identified combined solution can be implemented in structural health monitoring to detect the structural deformations precisely and surpass the positioning limitations in a challenging environment of the monitored structures such as long-span bridges. To achieve the research aim, the potential improvement of a combined GNSS solution compared to the GPS-only was investigated. For this purpose, different experiments were conducted to assess the noise level by applying zero baseline measurements. In addition, short baseline experiments of static and kinematic measurements were carried out and examined to achieve the positioning precision and accuracy of different GNSS solutions. The knowledge gained from these experiments was then applied to a real structure bridge monitoring.

This chapter presents the main conclusions drawn from the research findings which reflect the aim and objectives of the current study, in which implementing a combined GNSS solution led to significant improvements in the accuracy, reliability and the quality of the positioning solution. Recommendations for future work are also highlighted.

7.1.1 The Noise Level in Multi-GNSS Measurements

The presence of noise in GPS measurements represents one of the main limitations that degrade the positioning quality and solution availability by affecting the ambiguity fixing. Thus, the need to overcome these limitations in terms of improving the positioning performance was assessed in this study by adopting a combined GNSS technique. The evaluation of noise level was analysed through the results of zero baseline experiments with different types of pairs of receivers over 12 consecutive days at the UK ($\varphi \approx 53°$ N) and China ($\varphi \approx 30°$ N) simultaneously, and the results revealed the following conclusions with 15° of cut-off elevation angle:

- For the availability of fixed solution, the daily results of zero baseline at the UK site showed gap intervals characterised the time series of the GPS-only solution, while fewer gap intervals achieved with the corresponding GLONASS-only solution. However, in a combined GPS/GLONASS solution, there were no gaps appeared in their time series, which leads to the full availability of 100% fixing rate of ambiguity resolution. This proved that the combined GNSS solution could overcome problematic periods and achieved the highest availability. For the dataset in China, both GPS and BeiDou daily data have an optimum availability of full fixed solution, while GLONASS-only solution suffered from weak geometry at several periods, which leads to less availability, mainly when the reference GLONASS satellite was lower than 50°.
- The evaluated positioning precision with different GNSS solutions at two locations (the UK and China) indicates that the N-component of the GPS-only solution at the relatively high latitudes areas (e.g. the UK) was less accurate than E-component, due to fewer GPS satellites that are distributed in an N-S direction against more satellites in E-W direction, which attributed to GPS orbit design. However, the GPS/GLONASS combination provides a more accurate solution for all components. Furthermore, the combined GPS/BeiDou at China site was better than the individual solution of either GPS or BeiDou system alone. This improvement is related to the increasing number of available satellites.
- Regarding the outlier results introduced in GPS-only solution as a result of weak geometry or existence of problematic satellites, the combined GNSS solution was beneficial in removing most of these outliers, due to the improved geometry. In more specific, the individual solution of any GNSS system influenced by the existence of rising or setting low elevated satellites, which has an impact on estimated position. On the other hand, the combined GNSS solution limited the effects of these problematic satellites and improved the positioning precision. Consequently, the combined GNSS solution can reduce the noise relative to the GPS-only or GLONASS-only solution.
- At the current stage, as the BeiDou system is still under development, its contribution in a combined GNSS solution is less than GLONASS in the UK site, due to limited MEO satellites. Similarly for the Galileo system with limited satellites during experiments time.
- The new approach in this study was based on correlating the satellite geometry with the noise level, which showed that the mean DOP values of the GPS-only solution were well correlated with the noise precision derived from moving standard deviation at intervals of mean DOP values higher than the corresponding daily values. The low correlated intervals were recognised when the moving standard deviation of the derived noise was lower than the limit of daily standard deviation, which means the precision is practically independent of the satellite system. In contrast, the correlation of combined GNSS results was weaker than the

GPS-only solution, which revealed that the added observations from another GNSS constellation reduce the effect of noise measurements significantly.

- The availability of more redundant satellites in a combined GNSS solution gives the opportunity to deal with clean data by excluding the problematic or contaminated satellites, which will have a significant contribution for applications that required high precision.

7.1.2 Achievable Accuracy of Multi-GNSS Measurements

To assess the GNSS positioning precision and accuracy, static and kinematic experiments of short baselines were conducted. The outcomes of these experiments were then applied to real structural monitoring systems. In the kinematic trial of rotating GNSS antenna, the recorded coordinates of moving object were compared with the real ones that identified by a proposed new approach which based on 3D best fitting of non-linear least squares adjustment models. From these experiments the following conclusions can be drawn:

- It was observed that different GNSS solutions could achieve mm level of accuracy when clean data with a good geometry are applied. However, the precision of GPS-only was reduced in periods of weak geometry or presence of problematic satellites. Therefore, the combined GNSS proved significant improvement in comparison to the GPS-only solution. In addition, the geometry of the combined GPS/GLONASS solution was improved by 27% and 30% for GDOP and PDOP, respectively.
- The results of GPS-only was more accurate than the corresponding results of GLONASS or BeiDou. It was observed that the solution precision was improved when adding other observation to GPS data and a significant improvement was achieved when using the GPS/GLONASS/BeiDou solution, due to more redundant observations.

7.1.3 Bridge Deflection Monitoring with Multi-GNSS

The structural monitoring of long-span suspension bridges by multi-GNSS observations has been investigated in this study. The proposed methodology of workflow was tested using real GNSS measurements conducted in two bridges in the UK (the Severn Bridge and Forth Road Bridge). The methodology focused on improving the positioning performance to have more accurate and reliable results that lead to a correct interpretation of bridge deflections and deformations. Therefore, the feasibility of combined GNSS positioning was investigated to show the positioning improvements in comparison with the GPS-only solutions. The implementation of the proposed methodology resulted in the following conclusions:

- At bridge monitoring stations, due to the multipath effect of towers, cables and passing vehicles, as well as obstructions, caused additional noise and biases errors. Therefore, the initial step in the methodology was based on detecting the cycle slips and multipath effects

in collected measurements. This enables to exclude any contaminated measurement data. Although this procedure in dealing with clean data was more efficient, with GPS-only, this might lead to characterised gaps. Therefore, this was surpassed by combined GNSS observations with more redundant data.

- At the base station of Severn Bridge monitoring, the GNSS results showed that the GLONASS-only solution has more noise compared to the GPS-only in E and U components, while the N-component of GLONASS was less noisy. In contrast, the GPS/GLONASS solution reduced the noise level at all components, which leads to more accurate results. This was observed significantly along intervals of the weak geometry of GPS-only data.
- It was found that gaps characterised the time series of derived displacement of the GPS-only solution in various sessions due to insufficient valid satellites or weak geometry that prevent fixing the ambiguity. Consequently, the combined GNSS solution augments the geometry leading to a continuous solution without gaps.
- In terms of spectral analysis, the detected frequencies, in most intervals, from GPS-only solution agreed with the corresponding frequencies extracted from combined GPS/GLONASS solution, some peaks of detected frequency were lost from a spectrum of GPS-only. This could attribute to noisy intervals or undetected multiple cycle slips.
- In Severn Bridge structural monitoring, a possibility of using BeiDou and/or Galileo available satellites were investigated. However, limited satellites were observed at the time of conducting the experiments/measurements. It was found that using such configurations improved the geometry, which in turns increased the availability of fixed solution.
- Since the Forth Road Bridge locates in high latitude areas (φ= 56°N), the possibility of using GLONASS-only solution was investigated. It was inferred from the experimental data that the derived displacements at mid-span station demonstrated noticeable improvements against GPS-only solution at several intervals, especially in N-component.

Finally, it can be concluded that the noise errors and discontinuity problems, as well as other limitations of the GPS-only solution, were reduced by implementing the proposed combined GNSS solution in this study, which proved significant improvements in positioning performance. These findings are promising for many real structural monitoring applications. Therefore, applying the combined GNSS solution for such applications needs further work and investigation. Recommendations for future work are discussed and highlighted in the following section.

7. 2 Recommendations for Future Work

The findings presented in this thesis revealed that implementing a multi-GNSS technique in structural health monitoring showed a significant improvement in positioning performance and proved the ability of such a technique to overcome the limitations of GPS-only. Therefore, it is essential this

research to continue and carry out further investigation, aiming to make even more efficient the application of multi-GNSS approach for the cases where the GPS-only solution appears weaknesses and problems. The recommendations for further work are summarised below:

- As demonstrated in Chapter 4, the correlation was implemented between HDOP and the precision of the GPS-only/multi-GNSS solution for the horizontal component. It would be even more beneficial to apply the same approach for the Easting and Northing components to assess the corresponding correlation. For locations of high latitude, the performance in Northing component is expected to be even more challenging.
- For kinematic measurements, addressed in Chapter 5, it is necessary to conduct field test with the higher sampling rate (i.e. 100 Hz) to investigate the performance of the multi-GNSS solution for very high sampling-rate and examine the noise level for that data. In addition, it should be also identified the limitations of high-rate multi-GNSS measurements for extended period and extended length of assessed baseline.
- The suggested workflow methodology in Chapter 6 can be developed by the coding algorithm to be used by non-professional users that have limited GNSS knowledge. Developing this algorithm with the capability of applying multi-GNSS would be highly recommended, as it would be a very useful tool for decision making whether to apply specific constellation or combined GNSS solutions for different durations. Additionally, it should be included also the decision making process for the combination of the satellites which would give the most precise and available solution with fixed the ambiguities resolution.
- Investigating the noise level and assessing the different GNSS solutions by collecting short baseline connecting two zero baselines in the base and rover stations are recommended in the future work. In this approach, different receivers can occupy each station. In addition, it can assess the relative positioning by considering these points as rover stations to reference ones of network measurements. The type of GNSS receivers taking into consideration when evaluating GLONASS measurements. Furthermore, this approach can be extended to investigate the network RTK positioning, which will contribute in providing a comprehensive picture of different GNSS solutions that can be used for future structural monitoring applications.
- The future of multi-GNSS is broad and offers a variety of research opportunities. The modernisation of new signals in existing full operation systems (GPS and GLONASS) and the rapid development in other constellations (Galileo and BeiDou) could increase the availability of visible satellites with improved signals. The new signals have the properties of less noise, and they can eliminate multipath compared to the previous signals. In addition, the triple-frequency GNSS allows additional observations with the ability to detect cycle

slips for more refined measurements. This would make GNSS positioning more reliable for different applications, which needs further investigation to be used precisely for structural health monitoring.

- It is recommended to apply SBAS observations and their corrections to assess their impact on derived positions.
- Although the Precise Point Positioning (PPP) has limitations of a convergence time to fix the ambiguity, it is worthwhile to use and test the PPP in kinematic applications within a certain level of accuracy. In addition, employing the developed multi-GNSS in such applications needs further investigation.

References

ABD RABBOU, M., EL-SHAZLY, A. & AHMED, K. 2017. Comparative analysis of multi-constellation GNSS single-frequency precise point positioning. *Survey Review***,** 1-10.

AFIFI, A. & EL-RABBANY, A. 2015. Performance Analysis of Several GPS/Galileo Precise Point Positioning Models. *Sensors,* 15**,** 14701-14726.

AL-SHAERY, A., ZHANG, S. & RIZOS, C. 2013. An enhanced calibration method of GLONASS inter-channel bias for GNSS RTK. *GPS Solutions,* 17**,** 165-173.

ALKAN, R. M., ILCI, V., OZULU, I. M. & SAKA, M. H. 2015. A comparative study for accuracy assessment of PPP technique using GPS and GLONASS in urban areas. *Measurement,* 69**,** 1-8.

AMIRI-SIMKOOEI, A. & TIBERIUS, C. 2004. Testing of high-end GNSS receivers. *in 2nd ESA/Estec Workshop on Satellite NavigationUser Equipment Technologies NaviTec'2004, edited by G. S. Granados,WPP-239, Noordwijk, Netherlands, 8 – 10 Dec.*

AMIRI-SIMKOOEI, A. R. & TIBERIUS, C. C. J. M. 2007. Assessing receiver noise using GPS short baseline time series. *GPS Solutions,* 11**,** 21-35.

ANQUELA, A. B., MARTIN, A., BERNE, J. L. & PADIN, J. 2013. GPS and GLONASS Static and Kinematic PPP Results. *Journal of Surveying Engineering-Asce,* 139**,** 47-58.

AQUINO, M., MONICO, J. F. G., DODSON, A. H., MARQUES, H., DE FRANCESCHI, G., ALFONSI, L., ROMANO, V. & ANDREOTTI, M. 2009. Improving the GNSS positioning stochastic model in the presence of ionospheric scintillation. *Journal of Geodesy,* 83**,** 953-966.

ASHKENAZI, V. & ROBERTS, G. 1997. Experimental monitoring of the Humber Bridge using GPS. *Proceedings of the ICE-Civil Engineering,* 120**,** 177-182.

BANVILLE, S. & LANGLEY, R. B. 2010. Instantaneous Cycle-Slip Correction for Real-Time PPP Applications. *Navigation,* 57**,** 325-334.

BARNES, J., RIZOS, C., WANG, J., MENG, X., COSSER, E., DODSON, A. H. & ROBERTS, G. W. 2003. The monitoring of bridge movements using GPS and pseudolites. *Proceedings, 11th FIG Symposium on Deformation Measurements, Santorini, Greece.*

BEHR, J., HUDNUT, K. & KING, N. 1998. Monitoring structural deformation at Pacoima dam, California using continuous GPS. *PROCEEDINGS OF ION GPS,* 11**,** 59-68.

BHATTA, B. 2011. *Global Navigation Satellite Systems: Insights into GPS, GLONASS, Galileo, Compass, and others*, BS Publications, India.

BHUIYAN, M. Z., SODERHOLM, S., THOMBRE, S., RUOTSALAINEN, L. & KUUSNIEMI, H. 2014. Overcoming the challenges of BeiDou receiver implementation. *Sensors (Basel),* 14**,** 22082-98.

BISBY, L. A., ENG, P., BANTHIA, N., BISBY, L., BRITTON, R., CHENG, R., MUFTI, A., NEALE, K., NEWHOOK, J. & SOUDKI, K. 2006. An introduction to structural health monitoring. *ISIS Educational Module.*

BISCHOF, C. & SCHÖN, S. 2016. Vibration detection with 100Hz GPS PVAT during a dynamic flight. *Advances in Space Research*.

BISNATH, S. B. & LANGLEY, R. B. 2000. Efficient, automated cycle-slip correction of dual-frequency kinematic GPS data. *proceedings of 47th Conference of CASI, ION GPS.* Ottawa, Canada.

BONA, P. 2000. Precision, Cross Correlation, and Time Correlation of GPS Phase and Code Observations. *GPS Solutions,* 4**,** 3-13.

BONENBERG, L., ROBERTS, G. & HANCOCK, C. 2011. Using Locata to augment GNSS in a kinematic urban environment. *Archiwum Fotogrametrii, Kartografii i Teledetekcji,* 22.

BORIO, D. May 2017. Robust signal processing for GNSS. *Proc. of the European Navigation Conference (ENC), 2017 European.* Lausanne, Switzerland: May 2017, pp. 150–158, doi: 10.1109/EURONAV.2017.7954204. IEEE.

BREUER, P., CHMIELEWSKI, T., GORSKI, P. & KONOPKA, E. 2002. Application of GPS technology to measurements of displacements of high-rise structures due to weak winds. *Journal of Wind Engineering and Industrial Aerodynamics,* 90**,** 223-230.

BREUER, P., CHMIELEWSKI, T., GORSKI, P., KONOPKA, E. & TARCZYNSKI, L. 2008. The Stuttgart TV Tower - displacement of the top caused by the effects of sun and wind. *Engineering Structures,* 30**,** 2771-2781.

BROWN, C., ROBERTS, G., ATKINS, C., MENG, X. & COLFORD, B. 2007. Deflections and Frequency Responses of the Forth Road Bridge Measured by GPS. *5th International Conference on Current and Future Trends in Bridge Design, Construction and Maintenance. Beijing on 17–18 September 2007. Pub. Thomas Telford Publishing London, UK, pp. 479–486. ISBN 978-07277-3593-5.*

BROWN, C. J., KARUNA, R., ASHKENAZI, V., ROBERTS, G. W. & EVANS, R. A. 1999. Monitoring of structures using the global positioning system. *Proceedings of the Institution of Civil Engineers-Structures and Buildings,* 134**,** 97-105.

BROWNJOHN, J. 2005. Long-term monitoring of dynamic response of a tall building for performance evaluation and loading characterisation. *In: Proc. of the 1st international operational modal analysis conference, Copenhagen, Denmark, April, pp 143–154.*

BROWNJOHN, J., STRINGER, M., TAN, G., POH, Y., GE, L. & PAN, T. 2005. Experience with RTK-GPS system for monitoring wind and seismic effects on a tall building. *Structural Health Monitoring of Intelligent Infrastructure (SHMII-2), Shenzhen***,** 265-275.

CAI, C. & GAO, Y. 2007. Precise Point Positioning Using Combined GPS and GLONASS Observations. *Journal of Global Positioning Systems,* 6**,** 13-22.

CAI, C. S. & GAO, Y. 2013. Modeling and assessment of combined GPS/GLONASS precise point positioning. *Gps Solutions,* 17**,** 223-236.

CAI, C. S., GAO, Y., PAN, L. & ZHU, J. J. 2015. Precise point positioning with quad-constellations: GPS, BeiDou, GLONASS and Galileo. *Advances in Space Research,* 56**,** 133-143.

CASCIATI, F. & FUGGINI, C. 2009. Engineering vibration monitoring by GPS: long duration records. *Earthquake Engineering and Engineering Vibration,* 8**,** 459-467.

CELEBI, M. 2000. GPS in dynamic monitoring of long-period structures. *Soil Dynamics and Earthquake Engineering,* 20**,** 477-483.

CELEBI, M. & SANLI, A. 2002. GPS in pioneering dynamic monitoring of long-period structures. *Earthquake Spectra,* 18**,** 47-61.

CHAN, W., XU, Y., DING, X. & DAI, W. 2005. Calibration of GPS for dynamic displacement measurement of long span cable-supported bridges in vertical direction. *Advanced Sensor Technologies for Nondestructive Evaluation and Structural Health Monitoring, Proceedings of SPIE.* International Society for Optics and Photonics. No. 5770, 168-179. Doi: 10.1117/12.600358.

CHANG, X. W., YANG, X. & ZHOU, T. 2005. MLAMBDA: a modified LAMBDA method for integer least-squares estimation. *Journal of Geodesy,* 79**,** 552-565.

CHEN, D., YE, S., ZHOU, W., LIU, Y., JIANG, P., TANG, W., YUAN, B. & ZHAO, L. 2015a. A double-differenced cycle slip detection and repair method for GNSS CORS network. *GPS Solutions,* 20**,** 439-450.

CHEN, J. P., ZHANG, Y. Z., WANG, J. G., YANG, S. N., DONG, D. A., WANG, J. X., QU, W. J. & WU, B. 2015b. A simplified and unified model of multi-GNSS precise point positioning. *Advances in Space Research,* 55**,** 125-134.

CHEN, Q., JIANG, W., MENG, X., JIANG, P., WANG, K., XIE, Y. & YE, J. 2018. Vertical deformation monitoring of the suspension bridge tower using GNSS: a case study of the Forth Road Bridge in the UK. *Remote Sensing,* 10**,** 364.

COSSER, E., ROBERTS, G. W., MENG, X. & DODSON, A. H. 2003. The Comparison of Single Frequency and Dual Frequency GPS for Bridge Deflection and Vibration Monitoring. *Proc. of the Deformation Measurements and Analysis, 11th International Symposium on Deformation Measurements, International Federation of Surveyors (FIG), Commission 6 - Engineering Surveys, Working Group 6.1, 25-28 May, Santorini, Greece.*

COSSER, E., ROBERTS, G. W., MENG, X. & DODSON, A. H. 2004. Single frequency GPS for bridge deflection monitoring: Progress and results. *Proc. of 1st FIG International Symposium on Engineering Surveys for Construction Works and Structural Engineering.* Nottingham, United Kingdom, 28 June-1 July 2004.

CRAYMER, M. R. 1999. *The least squares spectrum, its inverse transform and autocorrelation function, theory and some applications in geodesy.* National Library of Canada= Bibliothèque nationale du Canada.

CSNO 2013a. BeiDou Navigation Satellite System Signal in Space interface control document (open service signal B1I). China Satellite Navigation Office, Beijing,Version 1.0.

CSNO 2013b. BeiDou Navigation Satellite System Signal in Space Interface Control Document (Open Service Signal). China Satellite Navigation Office, Beijing,Version 2.0, December 26, 2013.

DACH, R., HUGENTOBLER, U., FRIDEZ, P. & MEINDL, M. 2007. Bernese GPS software version 5.0. *Astronomical Institute, University of Bern,* 640**,** 114.

DAI, L., WANG, J., RIZOS, C. & HAN, S. 2002. Pseudo-satellite applications in deformation monitoring. *GPS Solutions,* 5**,** 80-87.

DE BAKKER, P. F., TIBERIUS, C. C., VAN DER MAREL, H. & VAN BREE, R. J. 2012. Short and zero baseline analysis of GPS L1 C/A, L5Q, GIOVE E1B, and E5aQ signals. *GPS Solutions,* 16**,** 53-64.

DE LACY, M. C., REGUZZONI, M. & SANSÒ, F. 2011. Real-time cycle slip detection in triple-frequency GNSS. *GPS Solutions,* 16**,** 353-362.

DE PONTE MÜLLER, F., STEINGASS, A. & STRANG, T. 2013. Zero-Baseline Measurements for Relative Positioning in Vehicular Environments. *Proceedings of the 6th European Workshop on GNSS Signals and Signal Processing.*

DELOACH, S. R. 1989. Continuous deformation monitoring with GPS. *Journal of Surveying Engineering,* 115**,** 93-110.

DENG, C. L., TANG, W. M., LIU, J. N. & SHI, C. 2014. Reliable single-epoch ambiguity resolution for short baselines using combined GPS/BeiDou system. *GPS Solutions,* 18**,** 375-386.

DILSSNER, F., SPRINGER, T., GIENGER, G. & DOW, J. 2011. The GLONASS-M satellite yaw-attitude model. *Advances in Space Research,* 47**,** 160-171.

DODSON, A., MENG, X. & ROBERTS, G. 2001. Adaptive method for multipath mitigation and its applications for structural deflection monitoring. *International Symposium on Kinematic Systems in Geodesy, Geomatics and Navigation (KIS 2001), pp 5-8.*

DONG, D., WANG, M., CHEN, W., ZENG, Z., SONG, L., ZHANG, Q., CAI, M., CHENG, Y. & LV, J. 2016. Mitigation of multipath effect in GNSS short baseline positioning by the multipath hemispherical map. *Journal of Geodesy,* 90**,** 255-262.

DONG, Y., SONG, R. & LIU, H. 2010. Bridges structural health monitoring and deterioration detection synthesis of knowledge and technology. Department of Civil & Environmental Engineering-University of Alaska Fairbanks.

DOW, J. M., NEILAN, R. E. & RIZOS, C. 2009. The international GNSS service in a changing landscape of global navigation satellite systems. *Journal of Geodesy,* 83**,** 191-198.

DRÓŻDŻ, M. & SZPUNAR, R. 2012. GNSS receiver zero baseline test using GPS signal generator. *Artificial Satellites,* 47**,** 13-22.

DU, S. & GAO, Y. 2012. Inertial Aided Cycle Slip Detection and Identification for Integrated PPP GPS and INS. *Sensors,* 12**,** 14344-14362.

ESTEY, L. H. & MEERTENS, C. M. 1999. TEQC: The Multi-Purpose Toolkit for GPS/GLONASS Data. *GPS Solutions,* 3**,** 42-49.

FORBES, A. B. 1991. Least squares best fit geometric elements. *NPL Report.* DITC 140/89 ed. United Kingdom: National Physical Laboratory.

GALILEO-ICD 2010. European GNSS (Galileo) Open Service Signal In Space Interface Control Document (OS SIS ICD). *European Space Agency/European GNSS Supervisory Authority, Issue 1.1, September 2010.*

GAO, G. X., HENG, L., DE LORENZO, D., LO, S., AKOS, D., CHEN, A., WALTER, T., ENGE, P. & PARKINSON, B. 2009. Modernization Milestone–Observing the First GPS Satellite with an L5 Payload. *Inside GNSS,* 7**,** 30-36.

GAO, X., DAI, W., SONG, Z. & CAI, C. 2016. Reference satellite selection method for GNSS high-precision relative positioning. *Geodesy and Geodynamics*.

GE, M., GENDT, G., ROTHACHER, M., SHI, C. & LIU, J. 2008. Resolution of GPS carrier-phase ambiguities in Precise Point Positioning (PPP) with daily observations. *Journal of Geodesy,* 82**,** 389-399.

GENG, J. & BOCK, Y. 2016. GLONASS fractional-cycle bias estimation across inhomogeneous receivers for PPP ambiguity resolution. *Journal of Geodesy,* 90**,** 379-396.

GENG, J. & LI, X. Undifferenced GLONASS ambiguity resolution over inhomogeneous stations: introducing ionosphere corrections or resolving ionosphere-free ambiguities. Proceedings of ION GNSS+ 29th international technical meeting of the satellite division, Portland, OR, 2016.

GHILANI, C. D. & WOLF, P. R. 2010. *Adjustment computations: spatial data analysis,* Hoboken, New Jersey, the United States of America, John Wiley & Sons.

GRELIER, T., GHION, A., DANTEPAL, J., RIES, L., DELATOUR, A., ISSLER, J., AVILA-RODRIGUEZ, J., WALLNER, S. & HEIN, G. 2007. Compass Signal Structure and First Measurements. *The Institute of Navigation Global Navigation Satellite System ION GNSS, 3015 Fort Worth, Texas, 3015-3024.*

GRIGGS, E., KURSINSKI, E. & AKOS, D. 2015. Short-term GNSS satellite clock stability. *Radio Science,* 50**,** 813-826.

GROVES, P. D. 2013. *Principles of GNSS, inertial, and multisensor integrated navigation systems (GNSS Technology and Applications)*, Artech House Publishers, London.

GROVES, P. D., JIANG, Z., RUDI, M. & STRODE, P. 2013. A portfolio approach to NLOS and multipath mitigation in dense urban areas. In: Proceedings of ION-GNSS-2013, Institute of Navigation Nashville, TN, September, pp 3231–3247. The Institute of Navigation.

GUO, F., LI, X. X., ZHANG, X. H. & WANG, J. L. 2017. The contribution of Multi-GNSS Experiment (MGEX) to precise point positioning. *Advances in Space Research,* 59**,** 2714-2725.

GUO, J. J., XU, L., DAI, L. J., MCDONALD, M., WU, J. P. & LI, Y. Y. 2005. Application of the Real-Time Kinematic Global Positioning System in Bridge Safety Monitoring. *Journal of Bridge Engineering,* 10**,** 163-168.

GURTNER, W. & ESTEY, U. 2013. The Receiver Independent Exchange Format .Version 3.02. RINEX, Version 3.02.

HABERLING, S., ROTHACHER, M., ZHANG, Y., CLINTON, J. F. & GEIGER, A. 2015. Assessment of high-rate GPS using a single-axis shake table. *Journal of Geodesy,* 89**,** 697-709.

HADAS, T. & BOSY, J. 2015. IGS RTS precise orbits and clocks verification and quality degradation over time. *GPS Solutions,* 19**,** 93-105.

HAKANSSON, M., JENSEN, A. B. O., HOREMUZ, M. & HEDLING, G. 2017. Review of code and phase biases in multi-GNSS positioning. *GPS Solutions,* 21**,** 849-860.

HAN, H. Z., WANG, J., MENG, X. L. & LIU, H. 2016. Analysis of the dynamic response of a long span bridge using GPS/accelerometer/anemometer under typhoon loading. *Engineering Structures,* 122**,** 238-250.

HANCOCK, C., ZHANG, P., LAU, L., ROBERTS, G. & LIGT, H. D. 2016. Satellite mapping in cities and below cities: how good is it now? *Proceedings of the Institution of Civil Engineers ICE, 170 Februrary 2017 issue CE1, pp33-38.* Thomas Telford Ltd.

HE, H. B., LI, J. L., YANG, Y. X., XU, J. Y., GUO, H. R. & WANG, A. B. 2014. Performance assessment of single- and dual-frequency BeiDou/GPS single-epoch kinematic positioning. *GPS Solutions,* 18**,** 393-403.

HE, X. F., GUANG, Y., DING, X. L. & CHEN, Y. Q. 2004. Application and evaluation of a GPS multi-antenna system for dam deformation monitoring. *Earth Planets and Space,* 56**,** 1035-1039.

HENKEL, P. & KIAM, J. J. 2013. Maximum a posteriori probability estimation of integer ambiguities and baseline. *Proc. of 55-th IEEE Symp. ELMAR, pp. 353-356, Zadar, Croatia, Sep. 2013.*

HOFMANN-WELLENHOF, B., LICHTENEGGER, H. & COLLINS, J. 2012. *Global positioning system: theory and practice*, Springer Science & Business Media.

HOFMANN-WELLENHOF, B., LICHTENEGGER, H. & WASLE, E. 2008. *GNSS–global navigation satellite systems: GPS, GLONASS, Galileo, and more,* Springer Wien NewYork, Springer Science & Business Media.

HOQUE, M. M. & JAKOWSKI, N. 2008. Mitigation of higher order ionospheric effects on GNSS users in Europe. *GPS Solutions,* 12**,** 87-97.

HRISTOPULOS, D. T., MERTIKAS, S. P., ARHONTAKIS, I. & BROWNJOHN, J. M. W. 2007. Using GPS for monitoring tall-building response to wind loading: filtering of abrupt changes and low-frequency noise, variography and spectral analysis of displacements. *GPS Solutions,* 11**,** 85-95.

HUANG, L., LU, Z., ZHAI, G., OUYANG, Y., HUANG, M., LU, X., WU, T. & LI, K. 2015. A new triple-frequency cycle slip detecting algorithm validated with BDS data. *GPS Solutions***,** 1-9.

IGS, R.-S. 2015. RINEX-The Receiver Independent Exchange Format (Version 3.03).

IM, S. B., HURLEBAUS, S. & KANG, Y. J. 2013. Summary Review of GPS Technology for Structural Health Monitoring. *Journal of Structural Engineering,* 139**,** 1653-1664.

IRSIGLER, M. 2010. Characterization of multipath phase rates in different multipath environments. *GPS Solutions,* 14**,** 305-317.

KALOOP, M. R., ELBELTAGI, E., HU, J. W. & ELREFAI, A. 2017. Recent Advances of Structures Monitoring and Evaluation Using GPS-Time Series Monitoring Systems: A Review. *Isprs International Journal of Geo-Information,* 6**,** 382.

KALOOP, M. R. & KIM, D. 2016. De-noising of GPS structural monitoring observation error using wavelet analysis. *Geomatics Natural Hazards & Risk,* 7**,** 804-825.

KALOOP, M. R. & LI, H. 2011. Sensitivity and analysis GPS signals based bridge damage using GPS observations and wavelet transform. *Measurement,* 44**,** 927-937.

KAPLAN, E. & HEGARTY, C. 2005. *Understanding GPS: principles and applications*, Artech house.

KAROUMI, R., WIBERG, J. & LILJENCRANTZ, A. 2005. Monitoring traffic loads and dynamic effects using an instrumented railway bridge. *Engineering Structures,* 27**,** 1813-1819.

KEDAR, S., HAJJ, G. A., WILSON, B. D. & HEFLIN, M. B. 2003. The effect of the second order GPS ionospheric correction on receiver positions. *Geophysical Research Letters,* 30.

KIJEWSKI-CORREA, T. & KAREEM, A. 2003. Application Challenge-The Height of Precision-Monitoring Buildings-GPS sensors track wind-driven displacements of Chicago skyscrapers and provide the first full-scale insight into structural. *GPS World,* 14**,** 20-35.

KIJEWSKI-CORREA, T., KAREEM, A. & KOCHLY, M. 2006. Experimental verification and full-scale deployment of global positioning systems to monitor the dynamic response of tall buildings. *Journal of Structural Engineering-Asce,* 132**,** 1242-1253.

KIJEWSKI-CORREA, T. & KOCHLY, M. 2007. Monitoring the wind-induced response of tall buildings: GPS performance and the issue of multipath effects. *Journal of Wind Engineering and Industrial Aerodynamics,* 95**,** 1176-1198.

KIM, D. & LANGLEY, R. B. Instantaneous real-time cycle-slip correction of dual frequency GPS data. In: Proceedings of the international symposium on kinematic systems in geodesy, geomatics and navigation, pp 255-264, 2001. Banff Alberta, 255-264.

KLOBUCHAR, J. A. 1987. Ionospheric Time-Delay Algorithm for Single-Frequency Gps Users. *Ieee Transactions on Aerospace and Electronic Systems,* 23**,** 325-331.

LANGLEY, R. B. 1997. GPS receiver system noise. *GPS World,* 8**,** 40-45.

LAU, L., TATESHITA, H. & SATO, K. 2015. Impact of Multi-GNSS on Positioning Accuracy and Multipath Errors in High-Precision Single-Epoch Solutions - A Case Study in Ningbo China. *Journal of Navigation,* 68**,** 999-1017.

LEICK, A. 1998. GLONASS satellite surveying. *Journal of Surveying Engineering,* 124**,** 91-99.

LEPADATU, A. & TIBERIUS, C. 2014. GPS for structural health monitoring–case study on the Basarab overpass cable-stayed bridge. *Journal of Applied Geodesy,* 8**,** 65-86.

LEWANDOWSKI, W. & ARIAS, E. F. 2011. GNSS times and UTC. *Metrologia,* 48**,** S219-S224.

LI, M., QU, L., ZHAO, Q., GUO, J., SU, X. & LI, X. 2014. Precise point positioning with the BeiDou navigation satellite system. *Sensors (Basel),* 14**,** 927-43.

LI, X. 2004. The advantage of an integrated RTK-GPS system in monitoring structural deformation. *Positioning,* 1**,** 0.

LI, X., ZHANG, X., REN, X., FRITSCHE, M., WICKERT, J. & SCHUH, H. 2015a. Precise positioning with current multi-constellation Global Navigation Satellite Systems: GPS, GLONASS, Galileo and BeiDou. *Sci Rep,* 5**,** 8328.

LI, X. J., GE, L. L., AMBIKAIRAJAH, E., RIZOS, C., TAMURA, Y. & YOSHIDA, A. 2006. Full-scale structural monitoring using an integrated GPS and accelerometer system. *GPS Solutions,* 10**,** 233-247.

LI, X. X., GE, M. R., DAI, X. L., REN, X. D., FRITSCHE, M., WICKERT, J. & SCHUH, H. 2015b. Accuracy and reliability of multi-GNSS real-time precise positioning: GPS, GLONASS, BeiDou, and Galileo. *Journal of Geodesy,* 89**,** 607-635.

LIU, Y. Y., YE, S. R., JIANG, P., SONG, W. W. & LOU, Y. D. 2016. Combining GPS plus GLONASS observations to improve the fixing percentage and precision of long baselines with limited data. *Advances in Space Research,* 57**,** 1258-1267.

LIU, Z. Z. 2011. A new automated cycle slip detection and repair method for a single dual-frequency GPS receiver. *Journal of Geodesy,* 85**,** 171-183.

LOVSE, J. W., TESKEY, W. F., LACHAPELLE, G. & CANNON, M. E. 1995. Dynamic Deformation Monitoring of Tall Structure Using Gps Technology. *Journal of Surveying Engineering-Asce,* 121**,** 35-40.

MENG, X. 2002. *Real-time deformation monitoring of bridges using GPS/accelerometers.* PhD thesis, University of Nottingham.

MENG, X., DODSON, A. H. & ROBERTS, G. W. 2007. Detecting bridge dynamics with GPS and triaxial accelerometers. *Engineering Structures,* 29**,** 3178-3184.

MENG, X., ROBERTS, G. W., COSSER, E., DODSON, A. H., BARNES, J. & RIZOS, C. 2003. Real-time bridge deflection and vibration monitoring using an integrated GPS/Accelerometer/Pseudolite System. *Proc., 11th FIG Symp. on Deformation Measurements, Santorini, Greece, pp 25-28.*

MENG, X., ROBERTS, G. W., DODSON, A. H., COSSER, E., BARNES, J. & RIZOS, C. 2004. Impact of GPS satellite and pseudolite geometry on structural deformation monitoring: analytical and empirical studies. *Journal of Geodesy,* 77**,** 809-822.

MENG, X., XIE, Y., BHATIA, P., SOWTER, A., PSIMOULIS, P., COLFORD, B., YE, J., SKICKO, M., DIMAURO, M. & GE, M. 2016. Research and development of a pilot project using GNSS and Earth observation (GeoSHM) for structural health monitoring of the Forth Road Bridge in Scotland.

MIAOYAN, Z., JUN, Z. & YONG, Q. 2008. Satellite selection for multi-constellation. *in Proceedings of the IEEE/ION Position, Location and Navigation Symposium, pp. 1053–1059, May 2008.*: IEEE.

MISRA, P. & ENGE, P. 2006. *Global Positioning System: Signals, Measurements, and Performance,* United State of America, Ganga-Jamuna Press.

MOMOH, J. A. 2013. *Robust GNSS Point Positioning in the Presence of Cycle Slips and Observation Gaps.* UCL (University College London).

MONTASSAR, S., BEN MEKKI, O. & VAIRO, G. 2015. On the effects of uniform temperature variations on stay cables. *Journal of Civil Structural Health Monitoring,* 5**,** 735-742.

MONTENBRUCK, O., HAUSCHILD, A., STEIGENBERGER, P., HUGENTOBLER, U., TEUNISSEN, P. & NAKAMURA, S. 2013. Initial assessment of the COMPASS/BeiDou-2 regional navigation satellite system. *GPS Solutions,* 17**,** 211-222.

MONTENBRUCK, O., STEIGENBERGER, P. & HAUSCHILD, A. 2015. Broadcast versus precise ephemerides: a multi-GNSS perspective. *GPS Solutions,* 19**,** 321-333.

MONTENBRUCK, O., STEIGENBERGER, P., PRANGE, L., DENG, Z., ZHAO, Q., PEROSANZ, F., ROMERO, I., NOLL, C., STÜRZE, A. & WEBER, G. 2017. The Multi-GNSS Experiment (MGEX) of the International GNSS Service (IGS)–achievements, prospects and challenges. *Advances in Space Research,* 59**,** 1671-1697.

MONTILLET, J. P., ROBERTS, G. W., HANCOCK, C., MENG, X., OGUNDIPE, O. & BARNES, J. 2009. Deploying a Locata network to enable precise positioning in urban canyons. *Journal of Geodesy,* 83**,** 91-103.

MOSAVI, M. R. & EMAMGHOLIPOUR, I. 2013. De-noising of GPS Receivers Positioning Data Using Wavelet Transform and Bilateral Filtering. *Wireless Personal Communications,* 71**,** 2295-2312.

MOSCHAS, F., PSIMOULIS, P. A. & STIROS, S. C. 2013. GPS/RTS data fusion to overcome signal deficiencies in certain bridge dynamic monitoring projects. *Smart Structures and Systems,* 12**,** 251-269.

MOSCHAS, F. & STIROS, S. 2011. Measurement of the dynamic displacements and of the modal frequencies of a short-span pedestrian bridge using GPS and an accelerometer. *Engineering Structures,* 33**,** 10-17.

MOSCHAS, F. & STIROS, S. 2013. Noise characteristics of high-frequency, short-duration GPS records from analysis of identical, collocated instruments. *Measurement,* 46**,** 1488-1506.

MOSCHAS, F. & STIROS, S. 2014a. Dynamic multipath in structural bridge monitoring: an experimental approach. *GPS Solutions,* 18**,** 209-218.

MOSCHAS, F. & STIROS, S. 2014b. PLL bandwidth and noise in 100 Hz GPS measurements. *GPS Solutions***,** 1-13.

MOSCHAS, F. & STIROS, S. 2015. Dynamic Deflections of a Stiff Footbridge Using 100-Hz GNSS and Accelerometer Data. *Journal of Surveying Engineering,* 141**,** 04015003.

MOSCHAS, F. & STIROS, S. C. 2014c. Three-dimensional dynamic deflections and natural frequencies of a stiff footbridge based on measurements of collocated sensors. *Structural Control and Health Monitoring,* 21**,** 23-42.

MOSCHASA, F. & STIROS, S. 2012. Noise characteristics of short-duration, high frequency GPS-records. *Advanced Mathematical and Computational Tools in Metrology and Testing, Series on Advances in Mathematics for Applied Sciences,* 84**,** 284-291.

MSAEWE, H., HANCOCK, C., PSIMOULIS, P., ROBERTS, G. & BONENBERG, L. 2017a. Assessment of the Effects of Combining Multi-GNSS Constellations on the Solution Accuracy and Availability. *FIG Working Week 2017.* Helsinki, Finland, May 29–June 2, 2017.

MSAEWE, H. A., HANCOCK, C. M., PSIMOULIS, P. A., ROBERTS, G. W., BONENBERG, L. & DE LIGHT, H. 2017b. Investigating multi-GNSS performance in the UK and China based on a zero-baseline measurement approach. *Measurement,* 102**,** 186-199.

NADARAJAH, N., TEUNISSEN, P. J. & RAZIQ, N. 2013. BeiDou inter-satellite-type bias evaluation and calibration for mixed receiver attitude determination. *Sensors (Basel),* 13**,** 9435-63.

NAKAMURA, S. 2000. GPS measurement of wind-induced suspension bridge girder displacements. *Journal of Structural Engineering-Asce,* 126**,** 1413-1419.

NICKITOPOULOU, A., PROTOPSALTI, K. & STIROS, S. 2006. Monitoring dynamic and quasi-static deformations of large flexible engineering structures with GPS: Accuracy, limitations and promises. *Engineering Structures,* 28**,** 1471-1482.

NICOLINI, L. & CAPORALI, A. 2018. Investigation on Reference Frames and Time Systems in Multi-GNSS. *Remote Sensing,* 10**,** 80.

ODIJK, D., NADARAJAH, N., ZAMINPARDAZ, S. & TEUNISSEN, P. J. G. 2017. GPS, Galileo, QZSS and IRNSS differential ISBs: estimation and application. *GPS Solutions,* 21**,** 439-450.

ODIJK, D. & TEUNISSEN, P. J. G. 2013. Characterization of between-receiver GPS-Galileo inter-system biases and their effect on mixed ambiguity resolution. *GPS Solutions,* 17**,** 521-533.

ODIJK, D., ZHANG, B. & TEUNISSEN, P. J. 2015. Multi-GNSS PPP and PPP-RTK: Some GPS+ BDS Results in Australia. *China Satellite Navigation Conference (CSNC) 2015 Proceedings: Volume II.* Springer, 613-623.

ODOLINSKI, R. & TEUNISSEN, P. J. G. 2016. Single-frequency, dual-GNSS versus dual-frequency, single-GNSS: a low-cost and high-grade receivers GPS-BDS RTK analysis. *Journal of Geodesy,* 90**,** 1255-1278.

ODOLINSKI, R., TEUNISSEN, P. J. G. & ODIJK, D. 2015. Combined GPS plus BDS for short to long baseline RTK positioning. *Measurement Science and Technology,* 26**,** 045801.

OGAJA, C., LI, X. & RIZOS, C. 2007. Advances in structural monitoring with Global Positioning System technology: 1997–2006. *Journal of Applied Geodesy jag,* 1**,** 171-179.

OGAJA, C. & SATIRAPOD, C. 2007. Analysis of high-frequency multipath in 1-Hz GPS kinematic solutions. *GPS Solutions,* 11**,** 269-280.

OGAJA, C., WANG, J. L. & RIZOS, C. 2003. Detection of wind-induced response by wavelet transformed GPS solutions. *Journal of Surveying Engineering-Asce,* 129**,** 99-104.

ÖNEN, Y. H., DİNDAR, A. A., GÜLAL, E., GÜRKAN, G., GÜRKAN, K. & AKPINAR, B. 2014. Use of High-Frequency GNSS Sensors in Dynamic Motions. *2nd European Conference on Earthquake Engineering and Seismology (2ECEES), Istanbul, 2014.*

ONG, R. 2010. *Reliability of combined GPS/GLONASS ambiguity resolution.* PhD Thesis, University of Calgary.

ONG, R. B., PETOVELLO, M. G. & LACHAPELLE, G. 2009. Assessment of GPS/GLONASS RTK under various operational conditions. *in Proc. 22nd Int. Tech. Meet. Satellite Div. ION GNSS, Savannah, GA, USA, 2009, pp. 3297–3308.*

PAZIEWSKI, J. & SIERADZKI, R. 2017. Integrated GPS plus BDS instantaneous medium baseline RTK positioning: Signal analysis, methodology and performance assessment. *Advances in Space Research,* 60**,** 2561-2573.

PAZIEWSKI, J., SIERADZKI, R. & BARYLA, R. 2018. Multi-GNSS high-rate RTK, PPP and novel direct phase observation processing method: application to precise dynamic displacement detection. *Measurement Science and Technology,* 29**,** 035002.

PAZIEWSKI, J. & WIELGOSZ, P. 2014. Assessment of GPS plus Galileo and multi-frequency Galileo single-epoch precise positioning with network corrections. *GPS Solutions,* 18**,** 571-579.

PAZIEWSKI, J. & WIELGOSZ, P. 2015. Accounting for Galileo–GPS inter-system biases in precise satellite positioning. *Journal of Geodesy,* 89**,** 81-93.

PAZIEWSKI, J., WIELGOSZ, P. & KRUKOWSKA, M. 2013. Application of Sbas Pseudorange and Carrier Phase Signals to Precise Instantaneous Single-Frequency Positioning. *Acta Geodynamica Et Geomaterialia,* 10**,** 421-430.

PEPPA, I., PSIMOULIS, P. & MENG, X. 2017. Potential of Detecting Dynamic Motion by Analysing SNR of GPS Satellite Signal. *FIG Working Week 2017.*

PEPPA, I., PSIMOULIS, P. & MENG, X. 2018. Using the signal-to-noise ratio of GPS records to detect motion of structures. *Structural Control and Health Monitoring,* 25**,** e2080.

PERA, D. & FERRANDO, I. 2017. An integrated monitoring system through 3d laser scanner and traditional instruments for load test on arch bridge. *The International Archives of Photogrammetry, Remote Sensing and Spatial Information Sciences,* 42**,** 321.

PETOVELLO, M. 2009. GLONASS inter-frequency biases and ambiguity resolution. *Inside GNSS***,** 24-28.

PIANOSI, F. & WAGENER, T. 2015. A simple and efficient method for global sensitivity analysis based on cumulative distribution functions. *Environmental Modelling & Software,* 67**,** 1-11.

PSIMOULIS, P., HOULIE, N., MEINDL, M. & ROTHACHER, M. 2015. Consistency of PPP GPS and strong-motion records: case study of Mw9.0 Tohoku-Oki 2011 earthquake. *Smart Structures and Systems,* 16**,** 347-366.

PSIMOULIS, P., MENG, X., OWEN, J., XIE, Y., NGUYEN, D. T. & YE, J. 2017. GNSS and Earth Observation for Structural Health Monitoring (GeoSHM) of the Forth Road Bridge. *In Pro. of the Conference on Smart Monitoring Assessment and Rehabilitation of Civil Structures (SMAR 2017), Zurich, Switzerland, 13–15 September 2017.*

PSIMOULIS, P., PYTHAROULI, S., KARAMBALIS, D. & STIROS, S. 2008. Potential of Global Positioning System (GPS) to measure frequencies of oscillations of engineering structures. *Journal of Sound and Vibration,* 318**,** 606-623.

PSIMOULIS, P. A. & STIROS, S. C. 2008. Experimental assessment of the accuracy of GPS and RTS for the determination of the parameters of oscillation of major structures. *Computer-Aided Civil and Infrastructure Engineering,* 23**,** 389-403.

PSIMOULIS, P. A. & STIROS, S. C. 2012. A supervised learning computer-based algorithm to derive the amplitude of oscillations of structures using noisy GPS and Robotic Theodolites (RTS) records. *Computers & Structures,* 92-93**,** 337-348.

PSIMOULIS, P. A. & STIROS, S. C. 2013. Measuring Deflections of a Short-Span Railway Bridge Using a Robotic Total Station. *Journal of Bridge Engineering,* 18**,** 182-185.

PYTHAROULI, P., MENG, X., STIROS, S. & ROBERTS, G. 2006. Analysis of the GPS monitoring record of the Forth Road Bridge in Scotland. *Proceedings of the 12th FIG international symposium on deformation measurements. Baden, Austria; 22–24 May 2006.*

QING, Y., LOU, Y. D., DAI, X. L. & LIU, Y. 2017. Benefits of satellite clock modeling in BDS and Galileo orbit determination. *Advances in Space Research,* 60**,** 2550-2560.

QUAN, Y. M., LAU, L., ROBERTS, G. W. & MENG, X. L. 2016. Measurement Signal Quality Assessment on All Available and New Signals of Multi-GNSS (GPS, GLONASS, Galileo, BDS, and QZSS) with Real Data. *Journal of Navigation,* 69**,** 313-334.

RABBOU, M. A. & EL-RABBANY, A. 2015. Precise Point Positioning using Multi-Constellation GNSS Observations for Kinematic Applications. *Journal of Applied Geodesy,* 9**,** 15-26.

RAY, J. K., CANNON, M. E. & FENTON, P. C. 1999. Mitigation of Static Carrier-Phase Multipath Effects Using Multiple Closely Spaced Antennas. *Navigation,* 46**,** 193-201.

RAZIQ, N. & COLLIER, P. 2007. GPS deflection monitoring of the West Gate Bridge. *Journal of Applied Geodesy jag,* 1**,** 35-44.

REN, W. X., PENG, X. L. & LIN, Y. Q. 2005. Experimental and analytical studies on dynamic characteristics of a large span cable-stayed bridge. *Engineering Structures,* 27**,** 535-548.

REUSSNER, N. & WANNINGER, L. 2011. GLONASS inter-frequency biases and their effects on RTK and PPP carrier-phase ambiguity resolution. *Proc. of the Int. Tech. Meeting of the Satellite Division of the Institute of Navigation, 712–716.*

ROBERTS, G. & BROWN, C. 2010. Monitoring the deflections of bridges in the UK by GPS. *In: Proc. of the International Conference on Computing in Civil and Building Engineering (icccbe), Nottingham, UK, 30 June-2 July.*

ROBERTS, G., MENG, X. & BROWN, C. 2004a. From St Paul's to the Tate Modern; Overcoming problems in monitoring bridge deflections using GPS. *In: Proc. of 1st FIG International Symposium on Engineering Surveys for Construction Works and Structural Engineering, Nottingham, United Kingdom ,June 2004*

ROBERTS, G., MENG, X., BROWN, C. & DALLARD, P. 2006. GPS measurements on the London Millennium Bridge. *Proceedings of Institution of Civil Engineers, Bridge Engineering, 159(4), 153–161.*

ROBERTS, G., MENG, X., DODSON, A. & COSSER, E. 2002. Multipath mitigation for bridge deformation monitoring. *Journal of Global Positioning Systems,* Vol. 1, No. 1: 25-33.

ROBERTS, G. W., BROWN, C. & MENG, X. 2005. Deflection monitoring of the Forth Road Bridge by GPS. *In Proc., 18th Int. Technical Meeting of the Satellite Division of the Institute of Navigation, ION GNSS 2005, Long Beach, Calif., 1016–1021.*

ROBERTS, G. W., BROWN, C. J., MENG, X., OGUNDIPE, O., ATKINS, C. & COLFORD, B. 2012. Deflection and frequency monitoring of the Forth Road Bridge, Scotland, by GPS. *Proceedings Institution of Civil Engineers Bridge Engineering. pp.105–123.*

ROBERTS, G. W., BROWN, C. J., TANG, X., MENG, X. & OGUNDIPE, O. 2014. A Tale of Five Bridges; the use of GNSS for Monitoring the Deflections of Bridges. *Journal of Applied Geodesy,* Vol. 8**,** 241-264.

ROBERTS, G. W., BROWN, C. J., TANG, X. & OGUNDIPE, O. 2015. Using satellites to monitor Severn Bridge structure, UK. *Proceedings of the Institution of Civil Engineers - Bridge Engineering,* 168**,** 330-339.

ROBERTS, G. W., DODSON, A. H., BROWN, C. J., KARUNAR, R. & EVANS, A. 2000. Monitoring the height deflections of the Humber Bridge by GPS, GLONASS, and finite element modelling. *In Proc. of Association of Geodesy (IAG) Symposia 2000, Edited by: Schwarz. 355–360. Berlin: Springer-Verlag. .*

ROBERTS, G. W., DODSON, A. H., AND ASHKENAZI, V. 1999. Twist and deflection: Monitoring motion of Humber Bridge. *GPS World,* 10**,** 24-34.

ROBERTS, G. W., MENG, X. L. & DODSON, A. H. 2004b. Integrating a global positioning system and accelerometers to monitor the deflection of bridges. *Journal of Surveying Engineering-Asce,* 130**,** 65-72.

ROBERTS, G. W. & TANG, X. 2017. The use of PSD analysis on BeiDou and GPS 10Hz dynamic data for change detection. *Advances in Space Research,* 59**,** 2794-2808.

ROBERTS, G. W., TANG, X. & BROWN, C. J. 2016. Temperature effects on the vertical movements of the Severn Suspension Bridge's suspension cables measured by GNSS. *FIG 2016.*

ROHM, W., ZHANG, K. & BOSY, J. 2014. Limited constraint, robust Kalman filtering for GNSS troposphere tomography. *Atmospheric Measurement Techniques,* 7**,** 1475-1486.

SAKA, M. H. 2008. Optimal positioning of pseudolites augmented with GPS. *Sea Technology,* 49**,** 39-42.

SALÓS, D., MARTINEAU, A., MACABIAU, C., KUBRAK, D. & BONHOURE, B. 2010. Groundwork for GNSS integrity monitoring in urban road applications. The road user charging case. *ION GNSS 2010, 23rd International Technical Meeting of The Satellite Division of the Institute of Navigation.* In Proc. of the 23rd International Technical Meeting of The Satellite Division of the Institute of Navigation, 21-24 September, Portland, OR, pp. 1130-1144.

SATIRAPOD, C. & RIZOS, C. 2005. Multipath mitigation by wavelet analysis for GPS base station applications. *Survey Review,* 38**,** 2-10.

SECO, A., TIRAPU, F., RAMIREZ, F., GARCIA, B. & CABREJAS, J. 2007. Assessing building displacement with GPS. *Building and Environment,* 42**,** 393-399.

SHAKARJI, C. M. 1998. Least-Squares Fitting Algorithms of the NIST Algorithm Testing System. *J Res Natl Inst Stand Technol,* 103**,** 633-641.

SHAN, Z. Y., HAN, H. Z. & JIANG, K. 2013. Optimization model of GNSS/pseudolites structure design for open-pit mine positioning. *Transactions of Nonferrous Metals Society of China,* 23**,** 2201-2208.

SHI, C., ZHAO, Q. L., HU, Z. G. & LIU, J. N. 2013. Precise relative positioning using real tracking data from COMPASS GEO and IGSO satellites. *GPS Solutions,* 17**,** 103-119.

SLEEWAGEN, J., SIMSKY, A., WILDE, W., BOON, F. & WILLEMS, T. 2012. Demystifying GLONASS inter-frequency carrier phase biases. *Inside GNSS,* 7**,** 57-61.

SOUZA, E. M. D., MONICO, J. F. G. & PAGAMISSE, A. 2009. GPS satellite kinematic relative positioning: analyzing and improving the functional mathematical model using wavelets. *Mathematical Problems in Engineering,* 2009.

STIROS, S., PSIMOULIS, P. & KOKKINOU, E. 2008. Errors introduced by fluctuations in the sampling rate of automatically recording instruments: Experimental and theoretical approach. *Journal of Surveying Engineering-Asce,* 134**,** 89-93.

SU, M. K., ZHENG, J. S., YANG, Y. X. & WU, Q. 2018. A new multipath mitigation method based on adaptive thresholding wavelet denoising and double reference shift strategy. *GPS Solutions,* 22**,** 40.

SUBIRANA, J. S., ZORNOZA, J. J. & HERNÁNDEZ-PAJARES, M. 2013. *GNSS Data processing. Volume 1: Fundamentals and Algorithms*.

T. TAKASU 2013. "Rtklib ver. 2.4.2 manual. *http://www.rtklib.com/prog/manual 2.4.2.pdf," Tech*.

TAKASU, T. & YASUDA, A. 2009. Development of the low-cost RTK-GPS receiver with an open source program package RTKLIB. *International symposium on GPS/GNSS, Seogwipo-si Jungmun-dong, Korea, 4–6 November.* International Convention Center Jeju Korea.

TAMURA, Y., MATSUI, M., PAGNINI, L.-C., ISHIBASHI, R. & YOSHIDA, A. 2002. Measurement of wind-induced response of buildings using RTK-GPS. *Journal of Wind Engineering and Industrial Aerodynamics,* 90**,** 1783-1793.

TEUNISSEN, P. 2003. Towards a unified theory of GNSS ambiguity resolution. *Journal of Global Positioning Systems,* 2**,** 1-12.

TEUNISSEN, P. J. 1998. Quality control and GPS. *GPS for Geodesy.* Chapter 7 in GPS for Geodesy, 2nd Edition, P. J. G. Teunissen and A. Kleusberg, editors, Springer, New York, NY, 1998.

TEUNISSEN, P. J. G. 1995. The least-squares ambiguity decorrelation adjustment: A method for fast GPS integer ambiguity estimation. *Journal of Geodesy,* 70**,** 65-82.

TEUNISSEN, P. J. G. 2000. The success rate and precision of GPS ambiguities. *Journal of Geodesy,* 74**,** 321-326.

TEUNISSEN, P. J. G., ODOLINSKI, R. & ODIJK, D. 2014. Instantaneous BeiDou plus GPS RTK positioning with high cut-off elevation angles. *Journal of Geodesy,* 88**,** 335-350.

TOKURA, H., YAMADA, H., KUBO, N. & PULLEN, S. 2014. Using multiple GNSS constellations with strict quality constraints for more accurate positioning in urban environments. *Positioning,* 5**,** 85.

TRAN, V. T., SHIVARAMAIAH, N. C., NGUYEN, T. D., GLENNON, E. P. & DEMPSTER, A. G. 2018. GNSS receiver implementations to mitigate the effects of commensurate sampling frequencies on DLL code tracking. *GPS Solutions,* 22**,** 24.

TRUONG, D. M. & TA, T. H. 2013. Development of real multi-GNSS positioning solutions and performance analyses. *In Proc. of the International Conference on Advanced Technologies for Communications (ATC '13), pp. 158–163, Ho Chi Minh, Vietnam, October 2013.*

VAGNOLI, M., REMENYTE-PRESCOTT, R. & ANDREWS, J. 2017. Railway bridge structural health monitoring and fault detection: State-of-the-art methods and future challenges. *Structural Health Monitoring*.

VERHAGEN, S. 2004. Integer ambiguity validation: An open problem? *GPS Solutions,* 8**,** 36-43.

VERHAGEN, S. 2005. On the reliability of integer ambiguity resolution. *Navigation,* 52**,** 99-110.

VERHAGEN, S. & TEUNISSEN, P. J. G. 2013. The ratio test for future GNSS ambiguity resolution. *GPS Solutions,* 17**,** 535-548.

VERHAGEN, S. & TEUNISSEN, P. J. G. 2014. Ambiguity resolution performance with GPS and BeiDou for LEO formation flying. *Advances in Space Research,* 54**,** 830-839.

WANG, C., FENG, Y., HIGGINS, M. & COWIE, B. 2010. Assessment of commercial network RTK user positioning performance over long inter-station distances. *Journal of Global Positioning Systems,* 9**,** 78-89.

WANG, F., CHEN, X. & GUO, F. 2015a. GPS/GLONASS Combined Precise Point Positioning with Receiver Clock Modeling. *Sensors (Basel),* 15**,** 15478-93.

WANG, J., MENG, X., QIN, C. & YI, J. 2015b. Vibration frequencies extraction of the forth road bridge using high sampling GPS data. *Shock and Vibration,* 2016.

WANG, M., CHAI, H. Z., LIU, J. & ZENG, A. M. 2016. BDS relative static positioning over long baseline improved by GEO multipath mitigation. *Advances in Space Research,* 57**,** 782-793.

WANG, W. & HUANG, B. 2014. Research on properties of DOP in multi-constellation. *In Proc. of the 2014 IEEE Seventh International Conference on Computational Intelligence and Design, China, pp. 445-448, 2014.*

WANNINGER, L. 2012. Carrier-phase inter-frequency biases of GLONASS receivers. *Journal of Geodesy,* 86**,** 139-148.

WATSON, C., WATSON, T. & COLEMAN, R. 2007. Structural monitoring of cable-stayed bridge: Analysis of GPS versus modeled deflections. *Journal of Surveying Engineering-Asce,* 133**,** 23-28.

WINIT, R. 2013. *Four-constellation GNSS reliability and the estimation of inter-system time-offsets for improved performance in challenging signal environments.* PhD Thesis, University of Calgary.

WU, Z., BIAN, S., JI, B., XIANG, C. & JIANG, D. 2015. Short baseline GPS multi-frequency single-epoch precise positioning: utilizing a new carrier phase combination method. *GPS Solutions,* 20**,** 373-384.

XIA, P., CAI, C. & LIU, Z. 2013. GNSS troposphere tomography based on two-step reconstructions using GPS observations and COSMIC profiles. *Annales Geophysicae,* 31**,** 1805-1815.

XU, G. & XU, Y. 2007. *GPS: Theory, Algorithms and applications*, Springer, Berlin, Germany.

YAMADA, H., TAKASU, T., KUBO, N. & YASUDA, A. 2010. Evaluation and calibration of receiver inter-channel biases for RTK-GPS/GLONASS. *In Proc. of ION GNSS-2010. Institute of Navigation, Portland, 21–24 Sept, pp 1580–1587.*

YANG, Y., YUE, X. K. & DEMPSTER, A. G. 2016. GPS-Based Onboard Real-Time Orbit Determination for LEO Satellites Using Consider Kalman Filter. *Ieee Transactions on Aerospace and Electronic Systems,* 52**,** 769-777.

YANG, Y. X. 2009. Chinese geodetic coordinate system 2000. *Chinese Science Bulletin,* 54**,** 2714-2721.

YANG, Y. X., LI, J. L., XU, J. Y., TANG, J., GUO, H. R. & HE, H. B. 2011. Contribution of the Compass satellite navigation system to global PNT users. *Chinese Science Bulletin,* 56**,** 2813-2819.

YI, T. H., LI, H. N. & GU, M. 2013a. Experimental assessment of high-rate GPS receivers for deformation monitoring of bridge. *Measurement,* 46**,** 420-432.

YI, T. H., LI, H. N. & GU, M. 2013b. Recent research and applications of GPS-based monitoring technology for high-rise structures. *Structural Control and Health Monitoring,* 20**,** 649-670.

YU, C., ZHANG, G., LIU, X., FAN, L. & HAI, H. 2018. Monitoring Bridge Dynamic Deformation in Vibration by Digital Photography. *IOP Conference Series: Earth and Environmental Science 108.* IOP Publishing.

YU, J., MENG, X., SHAO, X., YAN, B. & YANG, L. 2014. Identification of dynamic displacements and modal frequencies of a medium-span suspension bridge using multimode GNSS processing. *Engineering Structures,* 81**,** 432-443.

YU, M., GUO, H. & CHENGWU, Z. 2006. Application of wavelet analysis to GPS deformation monitoring. *Proc. of IEEE/ION PLANS 2006, San Diego, California, pp. 670-676.*

YU, X. D. & GAO, J. X. 2017. Kinematic Precise Point Positioning Using Multi-Constellation Global Navigation Satellite System (GNSS) Observations. *ISPRS International Journal of Geo-Information,* 6**,** 6.

ZHANG, B. & TEUNISSEN, P. 2016. Zero-baseline Analysis of GPS/BeiDou/Galileo Between-Receiver Differential Code Biases (BR-DCBs): Time-wise Retrieval and Preliminary Characterization. *Navigation 63(2): 181–191*.

ZHANG, X. H., ZHU, F., TAO, X. L. & DUAN, R. 2017. New optimal smoothing scheme for improving relative and absolute accuracy of tightly coupled GNSS/SINS integration. *GPS Solutions,* 21**,** 861-872.

ZHAO, S., CUI, X., GUAN, F. & LU, M. 2014. A Kalman filter-based short baseline RTK algorithm for single-frequency combination of GPS and BDS. *Sensors (Basel),* 14**,** 15415-33.

ZHENG, F., LOU, Y., GU, S., GONG, X. & SHI, C. 2018. Modeling tropospheric wet delays with national GNSS reference network in China for BeiDou precise point positioning. *Journal of Geodesy,* 92**,** 545-560.

Appendix-A: Least Squares (LS) Adjustments for Fitting a 3D Surface

As stated in Chapter 5, Section 5.5.1.1 that the optimum 3D surface can be identified from the best fitting of collected data. These data recorded by GNSS receiver when its antenna fixed on the end of a rotating arm to form a circular path.

Thus, the computation of final elements of circular movement is derived from the Least-squares fitting of non-linear models of one of three cases. The LS observation equation is given as the following (Ghilani and Wolf, 2010):

$$v + B\Delta = F \tag{A-1}$$

where

B: The matrix of partial derivatives of the function with respect to unknowns.

v: The vector of residuals.

Δ: The vector of unknowns (corrections when used initial values).

F: The vector of function evaluation

A.1 Fitting a Sphere

For specific datasets in a 3D circular path, the non-linear LS solution for the best fitting of the sphere can be identified from the coordinates of observed data. The computations required four parameters, which are three for centre coordinates (Ec, Nc, Uc) and the radius (R). Therefore, the minimum number of observation is four points, and the sphere equation can be given as:

$$(E - E_c^o)^2 + (N - N_c^o)^2 + (U - U_c^o)^2 - R^2 = 0 \tag{A-2}$$

The adjustment observation model (Eq. A-1) can be formed and the partial derivative values defined as the following:

$$\underset{(n*1)}{\begin{bmatrix} v_{E1} \\ v_{N1} \\ v_{U1} \\ \vdots \\ v_{En} \\ v_{Nn} \\ v_{Un} \end{bmatrix}} + \underset{(n*4)}{\begin{bmatrix} \frac{\partial F_1}{\partial E_c} & \frac{\partial F_1}{\partial N_c} & \frac{\partial F_1}{\partial U_c} & \frac{\partial F_1}{\partial R} \\ \vdots & \vdots & \vdots & \vdots \\ \vdots & \vdots & \vdots & \vdots \\ \vdots & \vdots & \vdots & \vdots \\ \frac{\partial F_n}{\partial E_c} & \frac{\partial F_n}{\partial N_c} & \frac{\partial F_n}{\partial E_c} & \frac{\partial F_n}{\partial R} \end{bmatrix}} \underset{(4*1)}{\begin{bmatrix} \delta_{Ec} \\ \delta_{Nc} \\ \delta_{Uc} \\ \delta_R \end{bmatrix}} = \begin{bmatrix} (E - E_c^o)^2 + (N - N_c^o)^2 + (U - U_c^o)^2 - R^2 \\ \vdots \\ \vdots \\ (E - E_c^o)^2 + (N - N_c^o)^2 + (U - U_c^o)^2 - R^2 \end{bmatrix}_{(n*1)} \tag{A-3}$$

$$\frac{\partial F_1}{\partial E_c} = -2(E - E_c^o)$$
$$\frac{\partial F_1}{\partial N_c} = -2(N - N_c^o) \tag{A-4}$$

$$\frac{\partial F_1}{\partial E_c} = -2(U - U_c^o)$$
$$\frac{\partial F_1}{\partial R} = -2R$$

Where (E, N, U) : The observed coordinates recorded by GNSS receiver.

(E_c^o, N_c^o, U_c^o) : The initial coordinates of the centre.

R : The initial value of the sphere radius.

$(\delta_{Ec}, \delta_{Nc}, \delta_{Uc}, \delta_R)$: Corrections to the initial values of centre and radius.

n : number of observations

A.2 Fitting a 3D Circle

The procedure for fitting a circle in 3D space (Fig. A.1) required sequential steps to identify the final parameters of the best-fitted surface, which are summarised in the following (Shakarji, 1998):

1. Based on observed points, the least squares plane can be determined.
2. Compute the rotation angle between the generated plane and the E-N plane.
3. Project each point in the generate plane onto the E-N plane.
4. Determine the elements of the best fit 2D circle in the E-N plane.
5. Applying the rotation angle, the best 2D circle will back rotate to its original orientation.

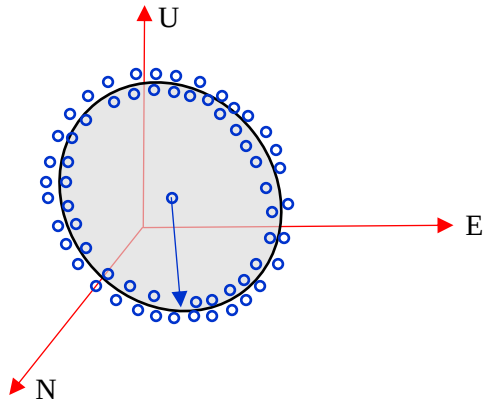


Fig. A.1 3D-circle with measured points.

- **Fitting a 2D Circle**

$$(E - E_c^o)^2 + (N - N_c^o)^2 - R^2 = 0 \quad \text{(A-5)}$$

$$\underset{(n*1)}{\begin{bmatrix} v_{E1} \\ v_{N1} \\ \vdots \\ \vdots \\ v_{En} \\ v_{Nn} \end{bmatrix}} + \underset{(n*4)}{\begin{bmatrix} \frac{\partial F_1}{\partial E_c} & \frac{\partial F_1}{\partial N_c} & \frac{\partial F_1}{\partial R} \\ \vdots & \vdots & \vdots \\ \vdots & \vdots & \vdots \\ \vdots & \vdots & \vdots \\ \frac{\partial F_n}{\partial E_c} & \frac{\partial F_n}{\partial N_c} & \frac{\partial F_n}{\partial R} \end{bmatrix}} \underset{(4*1)}{\begin{bmatrix} \delta_{Ec} \\ \delta_{Nc} \\ \delta_R \end{bmatrix}} = \underset{(n*1)}{\begin{bmatrix} (E - E_c^o)^2 + (N - N_c^o)^2 - R^2 \\ \vdots \\ (E - E_c^o)^2 + (N - N_c^o)^2 - R^2 \end{bmatrix}} \quad \text{(A-6)}$$

$$\frac{\partial F_1}{\partial E_c} = -2(E - E_c^o)$$
$$\frac{\partial F_1}{\partial N_c} = -2(N - N_c^o) \quad \text{(A-7)}$$
$$\frac{\partial F_1}{\partial R} = -2R$$

- **Rodrigues Rotation Formula**

To determine the required rotation angle between the inclined plane and a horizontal one, the Rodrigues rotation formula can be utilised. It applied to rotate the 3D points and get their E-N coordinates in the projected plane. It can be explained as a rotation from normal vector $n1$ of fthe irst plane to normal $n2$ for the second plane as illustrated in Fig. A.2

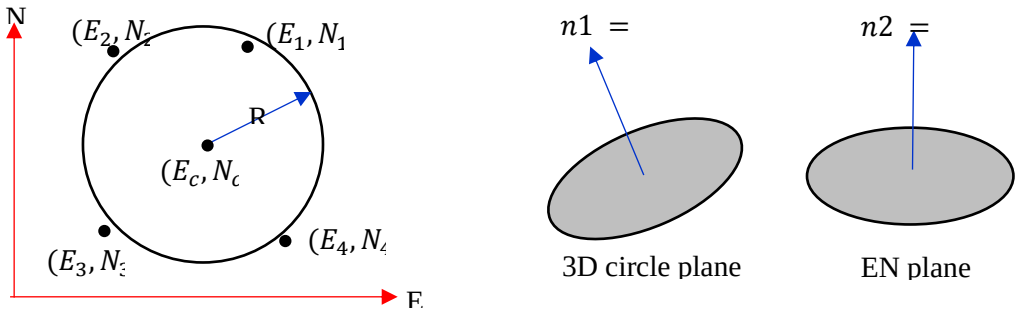


Fig. A.2 (left) 2D fitting circle in E-N plane and (right) rotation between two normal.

To determine the rotation matrix, the two steps should be followed:

a) Find axis and angle using both cross and dot product. The axis of rotation *k* is a cross product (x) between normal of first plane $n1$ and the normal $n2$ of the new EN coordinates as given:

$$n2 = (0,0,1)^t \ \ and \ \ k = n1 \times n2 \quad \text{(A-8)}$$

$$\theta = cos^{-1}\left(\frac{\overrightarrow{n1}.\overrightarrow{n2}}{\left\|\overrightarrow{n1}\right\| . \left\|\overrightarrow{n2}\right\|}\right) \quad \text{(A-9)}$$

b) Find the rotation matrix

$$M = I_{3*3} + \hat{k}\, sin(\theta) + \hat{k}^2(1 - cos\,\theta) \quad \text{(A-10)}$$

$$\textit{Skew- symmetric matrix } \hat{k} = \begin{bmatrix} 0 & k(3) & k(2) \\ k(3) & 0 & k(1) \\ k(2) & k(1) & 0 \end{bmatrix} \quad \text{(A-11)}$$

$$k = (n1 \times n2), \ \textit{then normalised}$$

The next step after rotating points is to find the best fit circle C_{points} with parameters $(E_c, N_c\ , R)$. Finally, rotate back to 3D space by taking $n2$ as the plane normal and $n1 = (0,0,1)^t$

$$C = C_{points} - [E_c, N_c, 0] \quad \text{(A-12)}$$

$$C = C * M' + points\ mean \quad \text{(A-13)}$$

A.3 Fitting a Cylinder

The observation Equation (A-1) can be formed as follows (Shakarji, 1998):

$$\underset{(n*1)}{\begin{bmatrix} v_{E1} \\ v_{N1} \\ v_{U1} \\ \vdots \\ v_{En} \\ v_{Nn} \\ v_{Un} \end{bmatrix}} + \underset{(n*7)}{\begin{bmatrix} \frac{\partial F_1}{\partial a} & \frac{\partial F_1}{\partial b} & \frac{\partial F_1}{\partial c} & \frac{\partial F_1}{\partial R} & \frac{\partial F_1}{\partial E_o} & \frac{\partial F_1}{\partial N_O} & \frac{\partial F_1}{\partial U_o} \\ \vdots & \vdots & \vdots & \vdots & \vdots & \vdots & \vdots \\ \frac{\partial F_n}{\partial a} & \frac{\partial F_n}{\partial b} & \frac{\partial F_n}{\partial c} & \frac{\partial F_n}{\partial R} & \frac{\partial F_n}{\partial E_o} & \frac{\partial F_n}{\partial N_O} & \frac{\partial F_n}{\partial U_o} \end{bmatrix}} \underset{(7*1)}{\begin{bmatrix} \delta_a \\ \delta_b \\ \delta_c \\ \delta_R \\ \delta_{E_o} \\ \delta_{N_o} \\ \delta_{U_o} \end{bmatrix}} = \underset{(n*1)}{\begin{bmatrix} F_a \\ F_b \\ \vdots \\ F_n \end{bmatrix}} \tag{A-14}$$

The least squares objective function is:

$$F = min \sum_{i=1}^{n} (f_i - R)^2 \qquad for\ n\ points \tag{A-15}$$

$$Where\ w_i = b(E_i - E_o) - a(N_i - N_o)$$

$$v_i = a(U_i - U_o) - c(E_i - E_o)$$

$$u_i = c(N_i - N_o) - b(U_i - U_o) \tag{A-16}$$

$$f_i = \sqrt{(w_i^2 + v_i^2 + u_i^2)}$$

$$d_i = f_i - R$$

$$\begin{aligned} \frac{\partial F_i}{\partial E_o} &= 2 \sum (f_i - R) \frac{\partial d_i}{\partial E_o} \\ \frac{\partial F_i}{\partial N_o} &= 2 \sum (f_i - R) \frac{\partial d_i}{\partial N_o} \\ \frac{\partial F_i}{\partial U_o} &= 2 \sum (f_i - R) \frac{\partial d_i}{\partial U_o} \\ \frac{\partial F_i}{\partial a} &= 2 \sum (f_i - R) \frac{\partial d_i}{\partial a} \\ \frac{\partial F_i}{\partial b} &= 2 \sum (f_i - R) \frac{\partial d_i}{\partial b} \\ \frac{\partial F_i}{\partial c} &= 2 \sum (f_i - R) \frac{\partial d_i}{\partial c} \\ \frac{\partial F_i}{\partial R} &= -2 \sum (f_i - R) \end{aligned} \tag{A-17}$$

Then the normal equations system is solved iteratively for the unknowns as follows:

$$\Delta = (B^t B)^{-1} (B^t F) \tag{A-18}$$

Appendix-B: Other Results of Severn Bridge monitoring

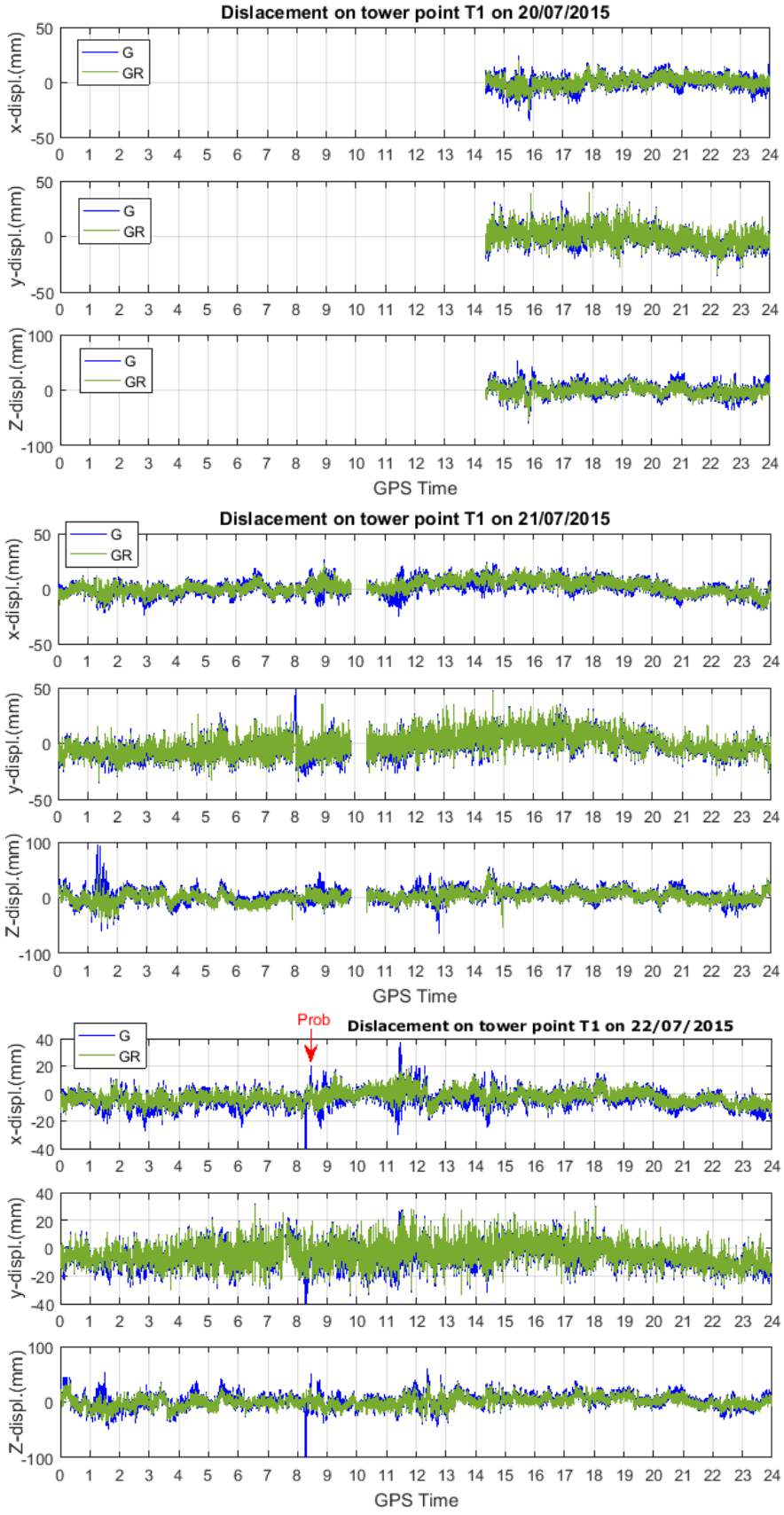


Fig. B.1 Comparison between displacement detected by GPS-only and combined GPS/GLONASS at T1.

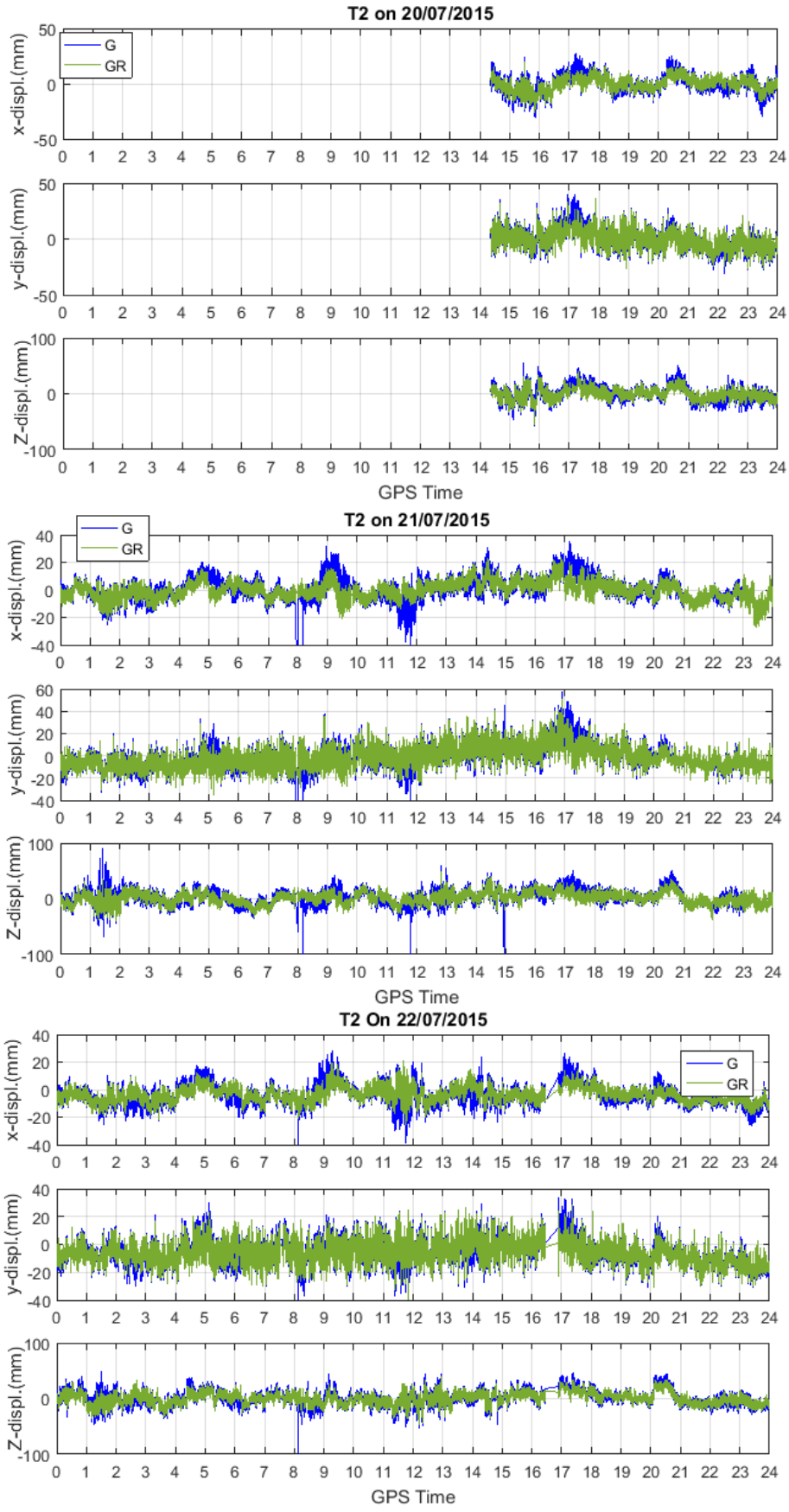


Fig. B.2 Comparison between displacement detected by GPS-only and combined GPS/GLONASS at T2.

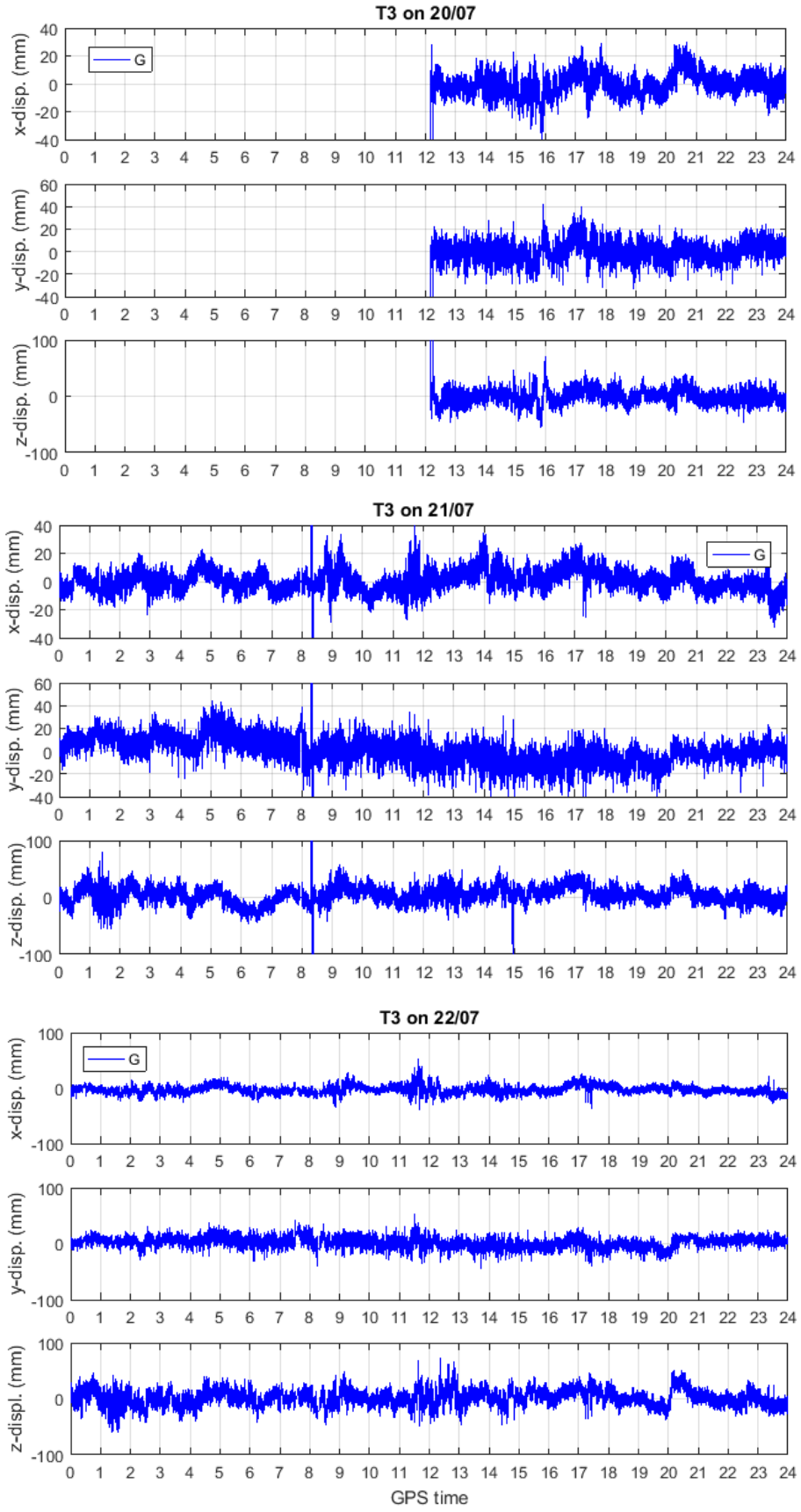


Fig. B.3 Displacement detected by GPS-only at T3.

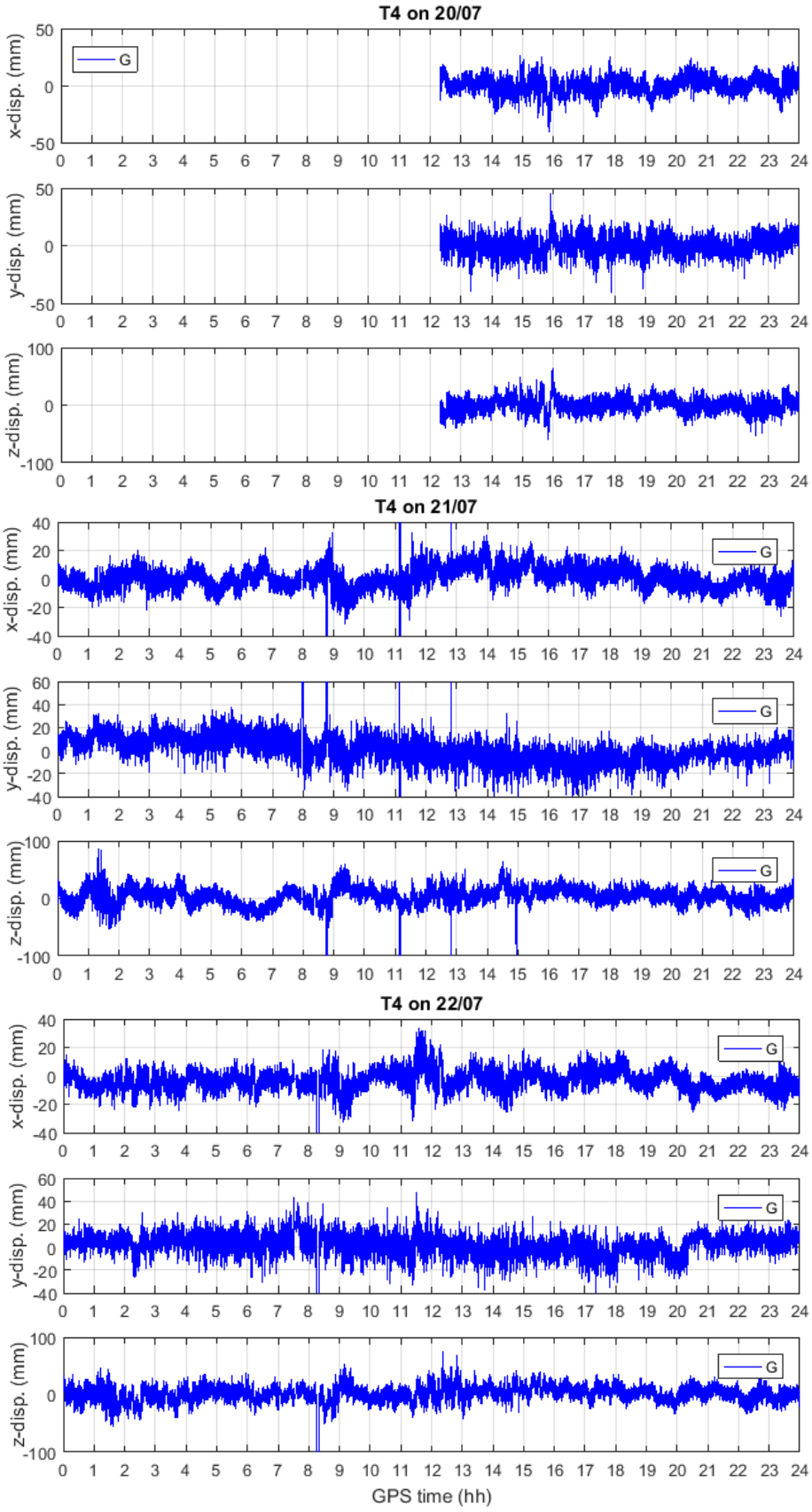


Fig. B. 4 Displacement detected by GPS-only at T4.

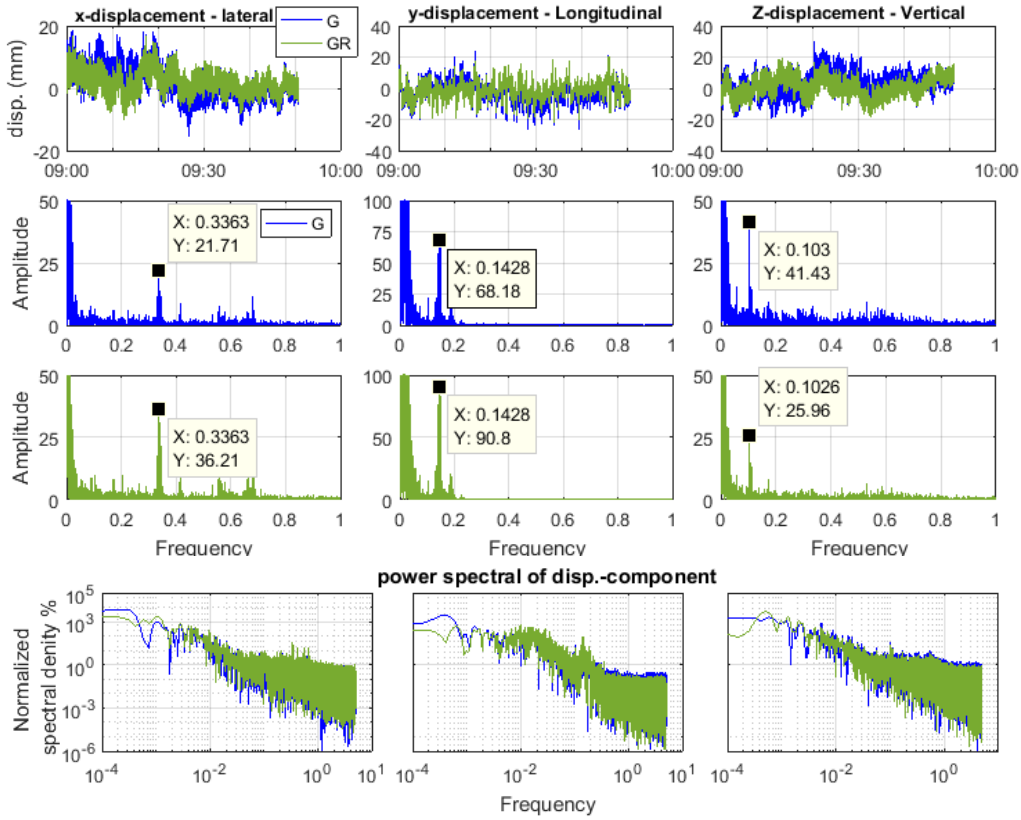


Fig. B. 5 Analysis of movement at tower station T1 for GPS-only compared to a combined GPS/GLO solution.

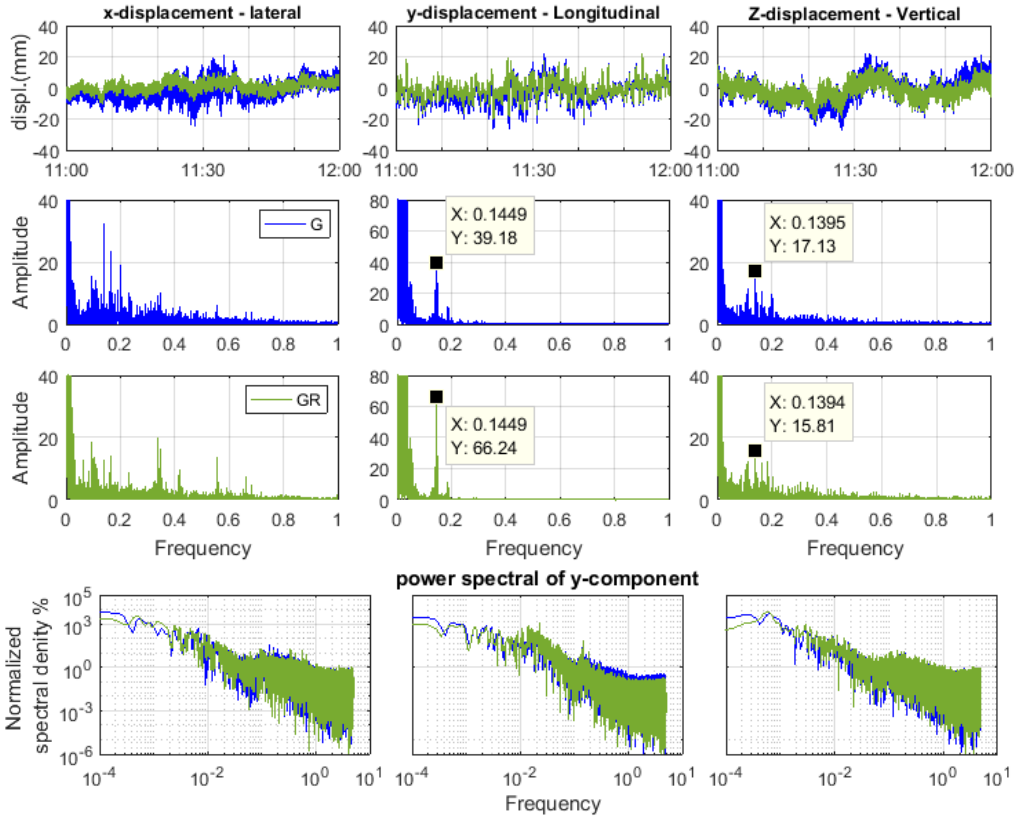


Fig. B. 6 Another interval at tower station T1 for GPS-only compared to a combined GPS/GLO solution.

Appendix-C: Other Results of the Forth Road Bridge.

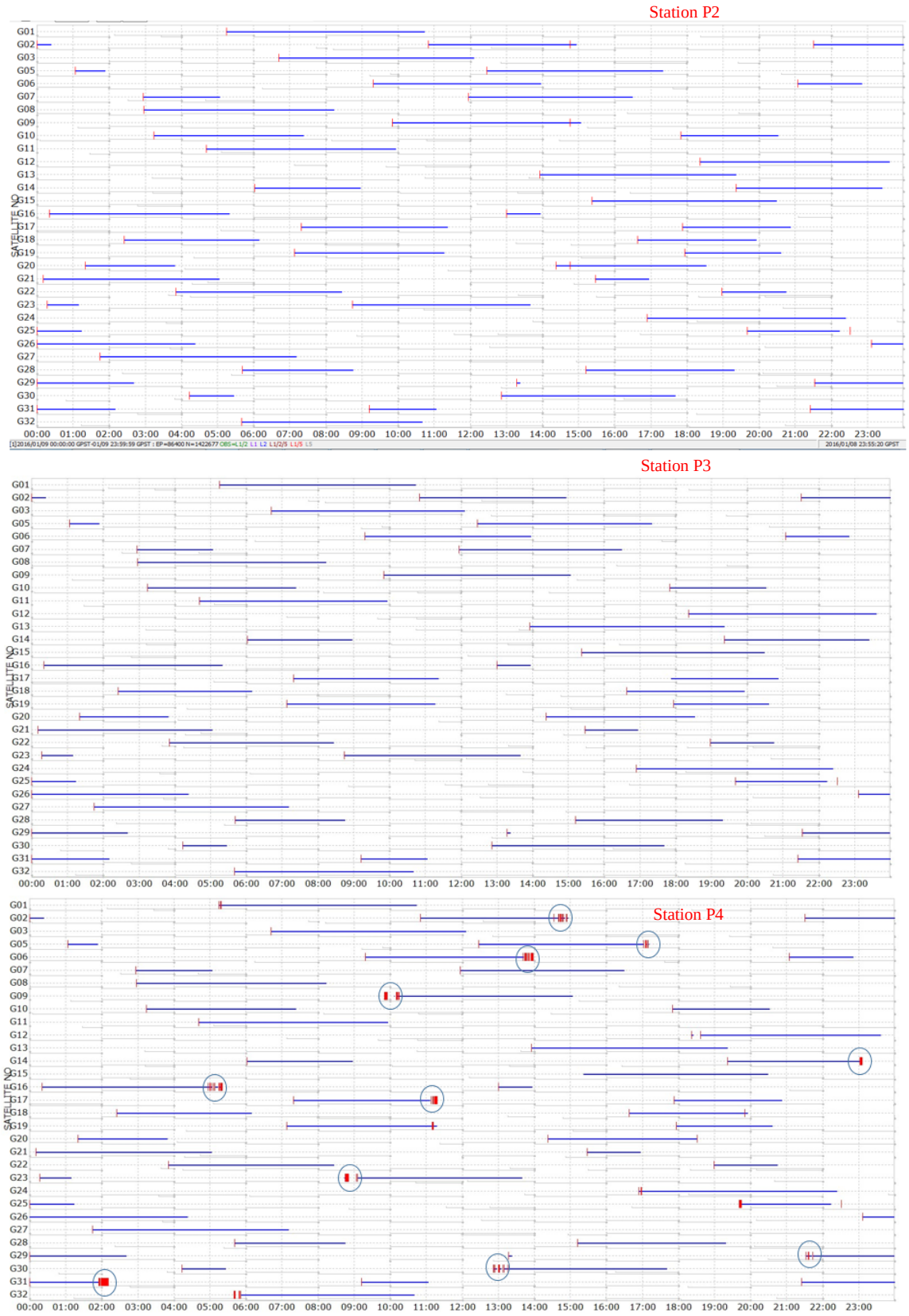


Fig. C. 1 Cycle slip detection at monitoring stations of Forth Road Bridge with GPS-only on 09/01/2016.

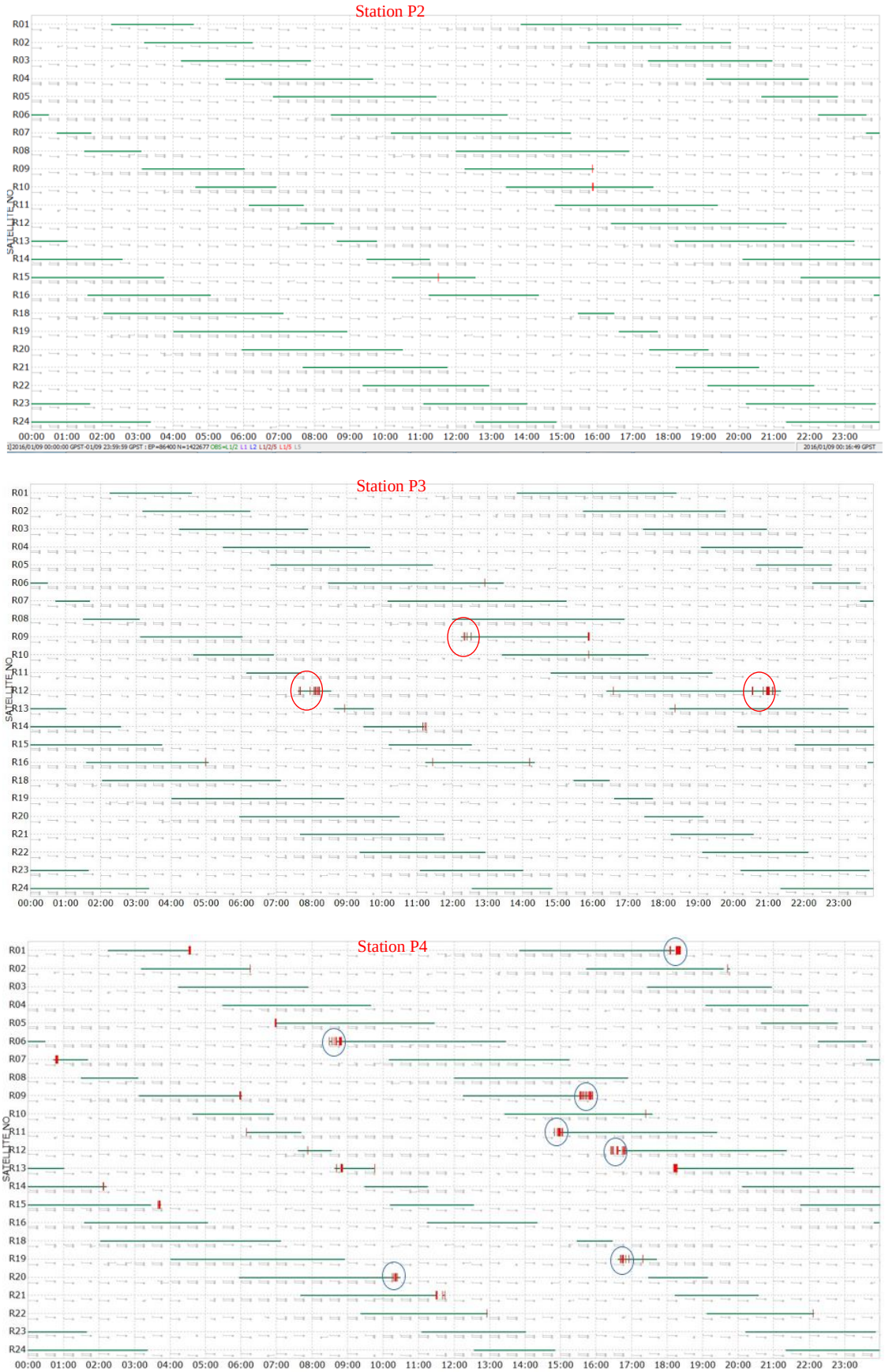


Fig. C.2 Cycle slip detection at monitoring stations of Forth Road Bridge with GLONASS-only on 09/01/2016.

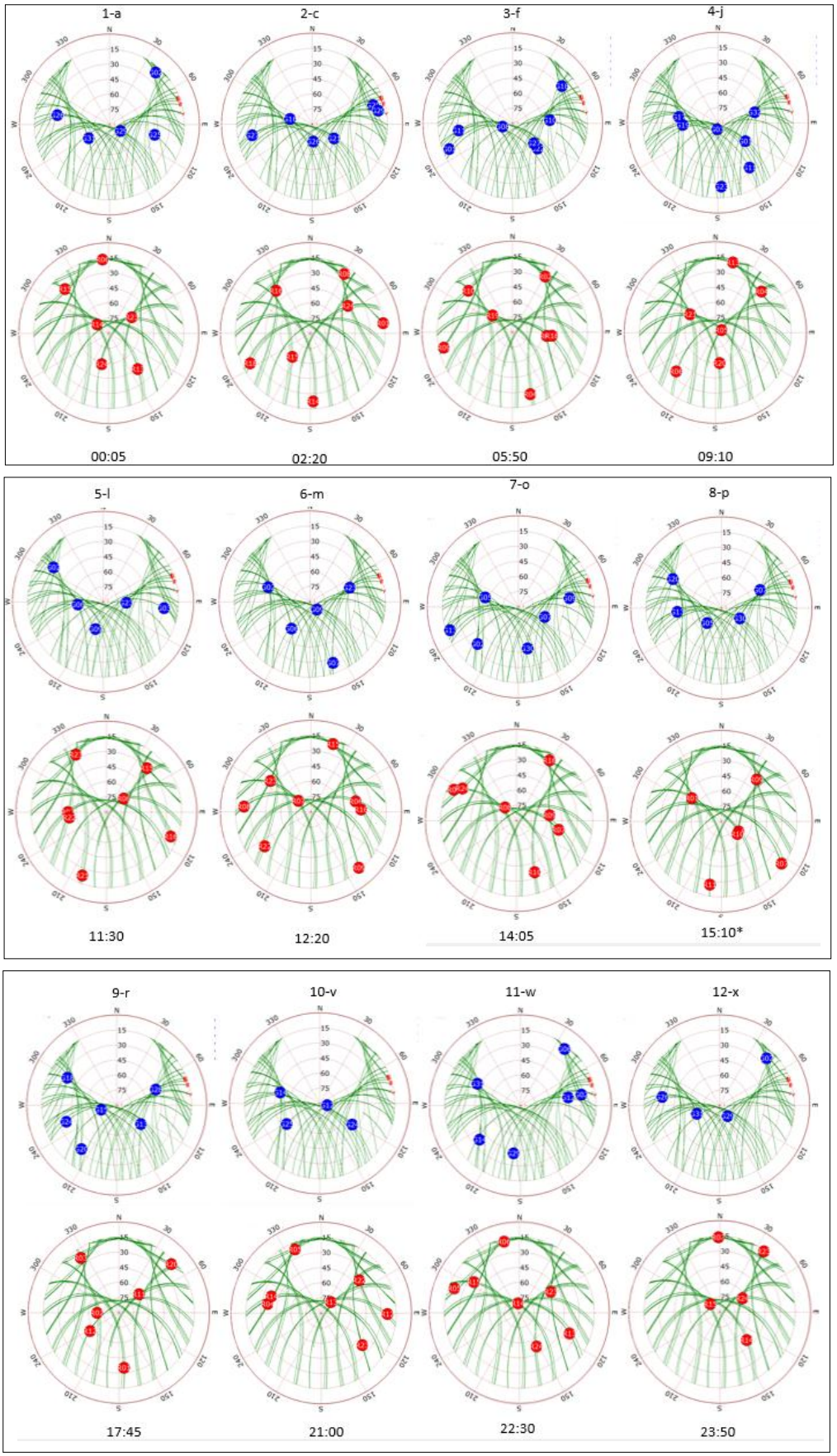


Fig. C.3 Comparison of distributed GPS and GLONASS satellites at the Forth Road Bridge on 09/01/2016.

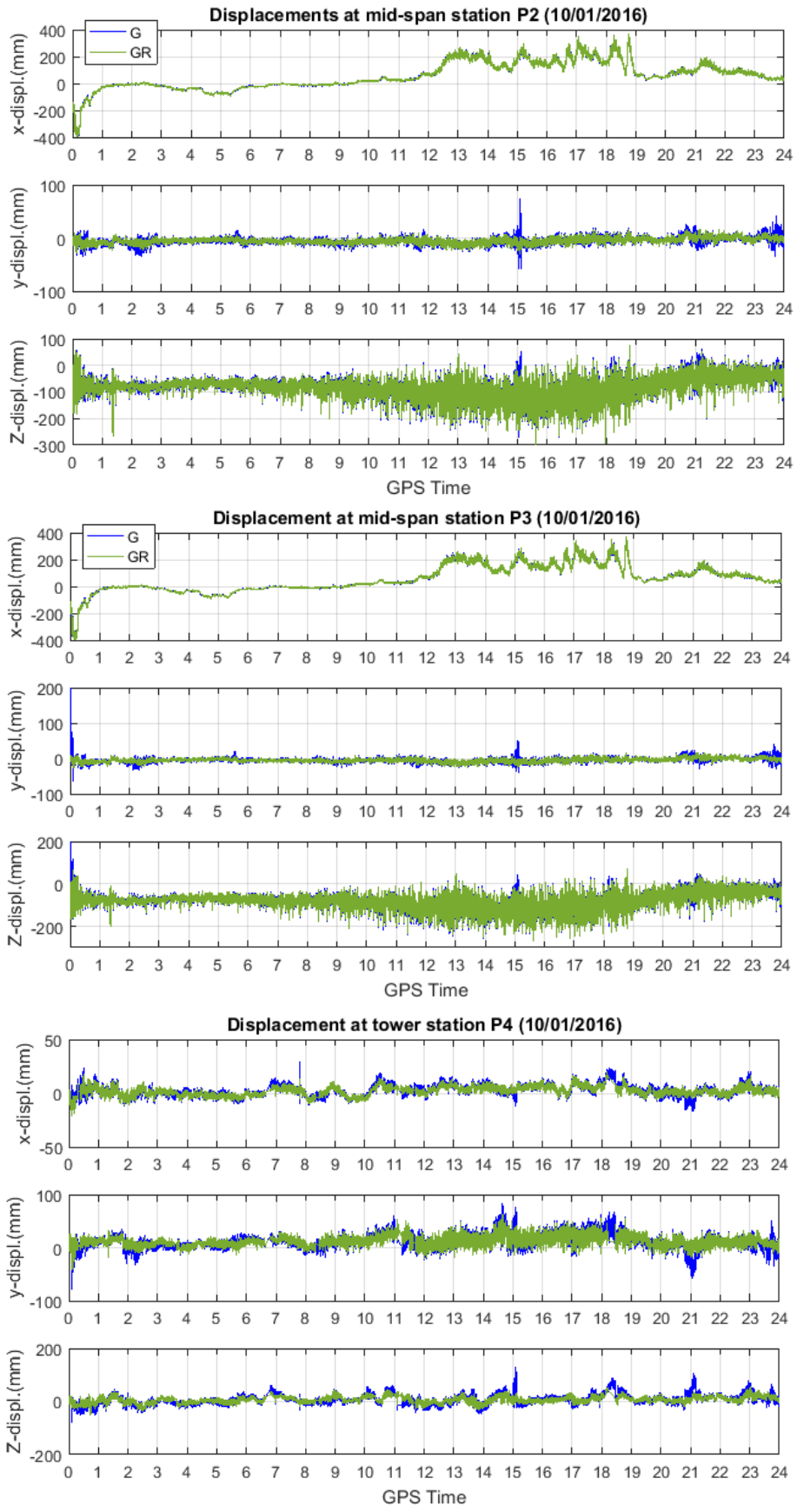


Fig. C.4 Daily time series of displacement compared between GPS-only and combined GPS/GLONASS detected at Forth Road Bridge on 10/01/2016.

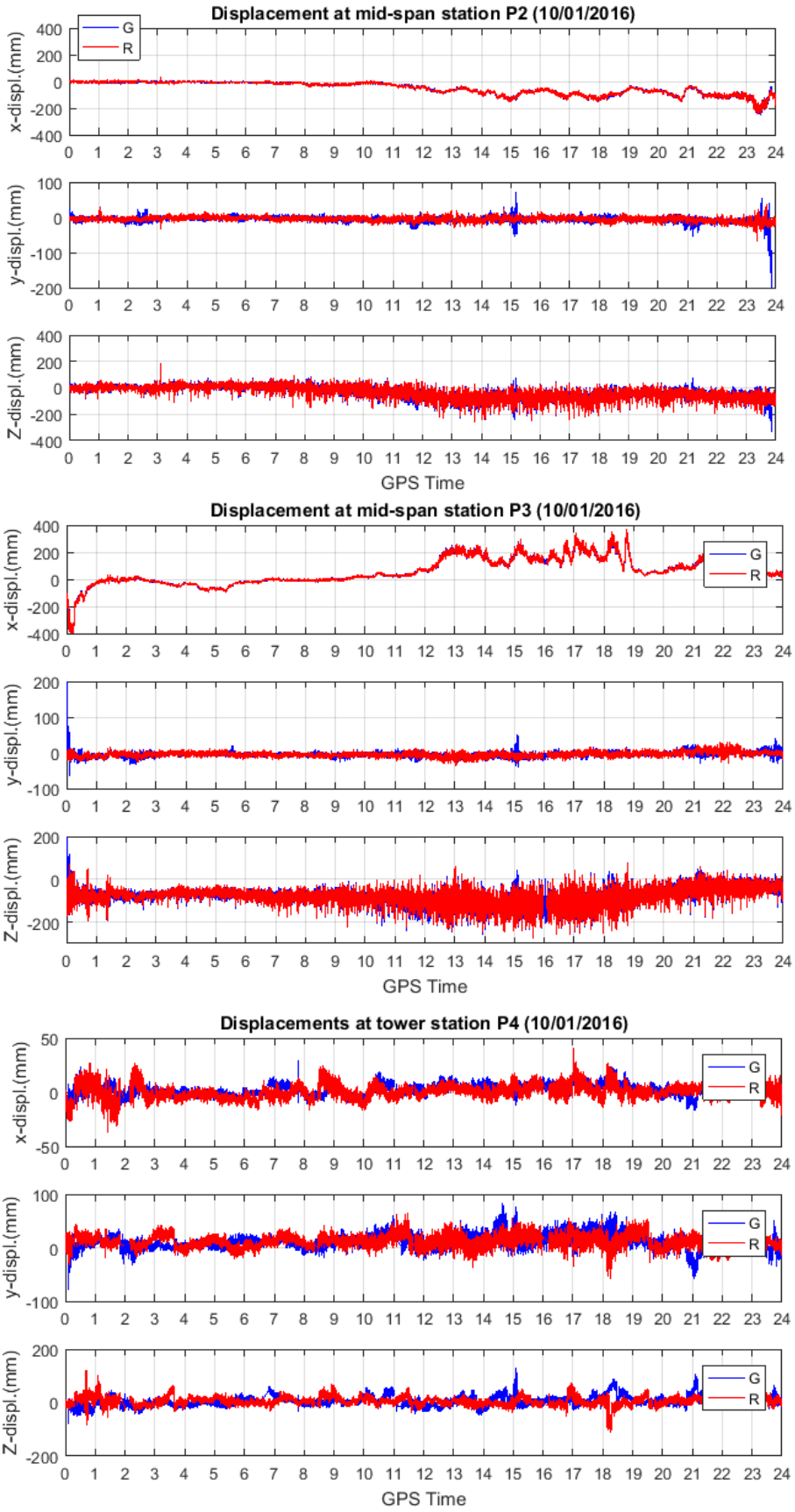


Fig. C.5 Daily time series of displacement compared between GPS-only and GLONASS-only detected at Forth Road Bridge on 10/01/2016.